New Geant4-based Monte Carlo Software for the COMPASS-II Experiment at CERN

Tobias Christian Szameitat

Dissertation

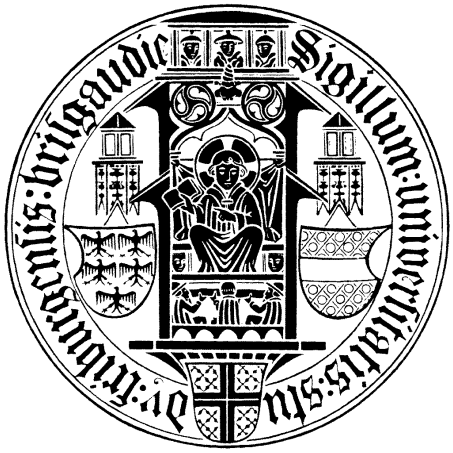

Albert-Ludwigs-Universität Freiburg

Fakultät für Mathematik und Physik

New Geant4-based Monte Carlo Software for the COMPASS-II Experiment at CERN

Dissertation

zur
Erlangung des Doktorgrades
der
Fakultät für Mathematik und Physik
der
Albert-Ludwigs-Universität
Freiburg im Breisgau

vorgelegt von

Tobias Christian Szameitat

aus
Lahr/Schwarzwald

Freiburg, Dezember 2016

Dekan:	Prof. Dr. Gregor Herten
Leiter der Arbeit:	Prof. Dr. Horst Fischer
Referent:	Prof. Dr. Horst Fischer
Korreferent:	Prof. Dr. Karl Jakobs

Tag der Verkündung des Prüfungsergebnisses: 14.02.2017

Contents

1. Introduction

For over 2000 years, mankind has been fascinated by the question of what matter consists of. Over the course of the last century, our notion of the structure of matter has changed considerably. As early as 1911, scattering experiments were carried out in the attempt to unlock the secrets of the substructure of matter. In that year, E. Rutherford succeeded in discovering the atomic nucleus by scattering alpha particles against gold nuclei [1]. With the discovery of the neutron in the year 1932 [2], a preliminary answer to our starting question had been found. The visible matter that surrounds us consists of electrons, protons, and neutrons. The latter two make up the atomic nucleus and are thus subsumed under the term nucleons. Soon, scientists found out that in contrast to electrons, which are point-like elementary particles, nucleons are composite particles with a substructure of their own.

Until the middle of the 20th century, protons, neutrons, and electrons along with photons, muons, neutrinos, and pions were considered to be the only existing elementary particles. Shortly after, an entire array of "strange" new particles were discovered, which were successfully classified according to their properties at the beginning of the sixties. In 1964, M. Gell-Mann [3] and, independently, G. Zweig [4] postulated a model relying on the existence of quarks as elementary building blocks. At the same time, A. Petermann also came up with the idea of fundamental triplet particles [5]. In today's Standard Model of particle physics, there are six kinds of quarks known as flavors and when taking into account their antiparticles and their various color charges, there are 36 different quarks in total. Together with leptons and intermediate particles, they form the fundamental building blocks of matter [6].

Nowadays, the nucleon's substructure can be described by the parton model. Nucleons consist of three valence quarks, which determine the nucleon's quantum properties (e.g. its electric charge). These quarks are "glued" together by gluons, which are the intermediate particles of strong interactions. Gluons can produce quark-antiquark pairs, which are known as sea quarks. These do not influence the nucleon's quantum numbers but they do contribute to its momentum and spin. The naive assumption that valence quarks are the sole contributors to the nucleon spin

was refuted by the EMC[1] experiment at CERN[2] at the end of the 1980s [7]. This unexpected discovery led to the so-called "spin crisis" [8].

The composition of the nucleon's momentum has been studied extensively over the last decades and can be described by parton distribution functions. Questions regarding nucleon spin structure remain, however. Since EMC further experiments at CERN, DESY[3], and SLAC[4] have measured the spin contributions of valence and sea quarks to not add up to the nucleon's spin. Groundbreaking research has been conducted with the COMPASS[5] experiment at CERN, showing that the gluon spin contribution is smaller than expected [9]. The remaining question concerns the determination of the orbital angular momenta of quarks and gluons. A method for direct measurement has not been found yet. The model of generalized parton distribution functions presents a new approach and is introduced in Chapter 2. By exploiting Ji's sum-rule, this model grants access to the total angular momenta of quarks and gluons [10].

Generalized parton distribution functions can be extracted from cross section measurements of exclusive scattering processes like deeply-virtual Compton scattering (DVCS) or hard-exclusive meson production. In 2016/17, the COMPASS-II experiment is focusing on the measurement of the DVCS process $\mu p \to \mu' p' \gamma$. Several upgrades of the spectrometer have been performed in preparation for this extremely challenging measurement. Details of the experimental setup are given in Chapter 3.

Monte Carlo simulations are indispensable for the analysis of such kind of exclusive cross section measurements to take account of acceptance corrections, background estimations, and model predictions. A new Monte Carlo software called TGEANT[6] was therefore developed from scratch in a team of only two developers. TGEANT is based on the framework of Geant4[7] and simulates all aspects of the COMPASS-II experiment. Chapter 4 gives a detailed insight into the event simulation and emphasizes the flexible design philosophy of the software package.

An accurate electromagnetic shower propagation is essential regarding the simulation of DVCS reactions and is therefore optimized in terms of agreement with measurements and software performance. The latter motivates the use of the fast shower parameterization algorithm GFlash in TGEANT. The implementation and tuning of GFlash as well as a new cell-dependent energy calibration method is addressed in Chapter 5.

The simulation of the trigger decision, which is needed in the experiment to distinguish between physically interesting and uninteresting events and which is described in Chapter 6, includes geometrical and technical aspects of the trigger hodoscopes. This opens up the possibility to use TGEANT for optimizations of the trigger system in preparation for the DVCS measurements in 2016/17.

[1] European Muon Collaboration
[2] Conseil Européen pour la Recherche Nucléaire
[3] Deutsches Elektron Synchroton
[4] Stanford Linear Accelerator Center
[5] Common Muon Proton Apparatus for Structure and Spectroscopy
[6] Total Geometry And Tracking
[7] Geometry And Tracking

The new Monte Carlo software was used for the first time for the final analysis of the four-week-long DVCS pilot run in 2012. Chapter 7 focuses on two examples, in which TGEANT was indispensable. An alternative approach for luminosity determination, which strongly relies on the acceptance correction of the experimental apparatus, is presented and the results are compared with the conventional method to validate the new simulation software. Monte Carlo estimates delivered by TGEANT also play a central role for the analysis of the pure DVCS cross section.

In Chapter 8, the possibilities of a measurement of the spin-dependent generalized parton distribution functions using a polarized target are discussed. Such a measurement calls for an upgrade of the COMPASS polarized target with silicon recoil detectors. The kinematical acceptance and the feasibility and precision of a four-momentum reconstruction needs to be studied and optimized using Monte Carlo.

2. Theory

This chapter offers a theoretical overview of the basic concepts needed when studying the substructure of nucleons, as far as they are relevant for this thesis. The nucleon is not a fundamental particle, but is instead composed of other particles, namely quarks, anti-quarks, and gluons. These are the elementary particles that give the nucleon its physical quantities such as its momentum and spin. Deep-inelastic lepton-nucleon scattering is an essential tool to explore the nucleon's substructure.

In the framework of the quark-parton model, the nucleon's substructure is universally described by parton distribution functions. Former experimental measurements have shown that only a part of the nucleon's spin arises from the spin of its constituents. The orbital angular momenta have thus become the focus of present and future studies. Furthermore, the concept of generalized parton distribution functions is motivated and introduced in this chapter. It has been shown that these functions are connected with the total angular momenta of quarks and gluons inside the nucleon. A prominent experimental approach is deeply-virtual Compton scattering. Different experimental techniques using unpolarized or polarized nucleons are presented, granting an access to generalized parton distribution functions.

2.1 Deep-Inelastic Scattering

When studying the nucleon's substructure, the basic concept of high-energy lepton-nucleon scattering is of great importance.

$$l + N \to l' + X \tag{2.1}$$

In a deep-inelastic scattering (DIS) process, a lepton l is scattered on a quark inside the nucleon N. The struck quark and the rest of the nucleon may fragment into one or more hadrons, which are denoted by X. The associated four-vector for the incoming nucleon is p, while k and k' are the four-vectors for the incoming and outgoing lepton, see Fig. 2.1.

The interaction is mediated by a virtual vector boson, with the four-momentum

$$q = k - k'. \tag{2.2}$$

In the case of the kinematics at the COMPASS experiment, the center of mass energy is much less than $M_{Z^0}\mathrm{c}^2$, so only a virtual photon γ^* contributes to the process with an energy of[1]

$$\nu = \frac{p \cdot q}{M} \overset{\text{lab}}{=} E - E', \tag{2.3}$$

where M represents the mass of the nucleon. The fractional energy of the virtual photon is calculable via:

$$y = \frac{p \cdot q}{p \cdot k} \overset{\text{lab}}{=} \frac{\nu}{E}. \tag{2.4}$$

In the laboratory frame, the nucleon is at rest and its four-vector can be written as $p = (M\mathrm{c}, \vec{0})$, whereas the energy of the incoming and outgoing lepton is E and E', respectively. To describe the kinematics of the process, some Lorentz invariants are useful:

$$Q^2 = -q^2 \tag{2.5}$$

is the negative of the squared invariant mass of the virtual photon,

$$W^2\mathrm{c}^2 = (q + p)^2 = M^2\mathrm{c}^2 + 2M\nu - Q^2 \tag{2.6}$$

is the invariant mass of the $\gamma^* p$ system. The dimensionless Bjorken variable x_{Bj} is defined as

$$x_{\mathrm{Bj}} = \frac{Q^2}{2p \cdot q} = \frac{Q^2}{2M\nu}. \tag{2.7}$$

In the Bjorken limit, where

$$Q^2, \nu \to \infty, \text{ with } x_{\mathrm{Bj}} = \text{fixed}, \tag{2.8}$$

the differential cross section of deep-inelastic lepton-nucleon scattering can be expressed as the product of a hard leptonic and a soft hadronic tensor, which are associated with the coupling of the exchanged virtual photon at the upper and lower vertices in Fig. 2.1 [12, 13]:

$$\frac{\mathrm{d}^2\sigma}{\mathrm{d}x_{\mathrm{Bj}}\mathrm{d}y} = \frac{2\pi y \alpha_{\mathrm{em}}^2}{Q^4} L_{\mu\nu} W^{\mu\nu}, \tag{2.9}$$

[1] The common convention $c = \hbar = 1$ is used in the following.

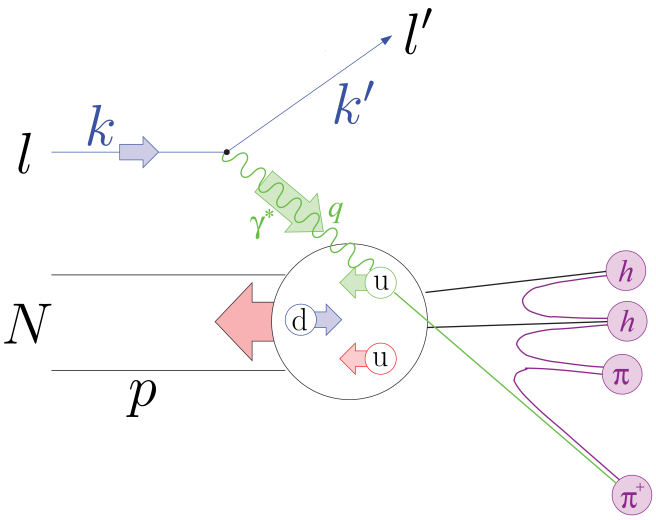

Figure 2.1: Schematic diagram of deep-inelastic lepton-nucleon scattering. Picture adopted from Ref. [11].

where α_{em} is the electromagnetic coupling constant. The leptonic tensor describes the emission of the virtual photon by the incoming lepton and can be calculated explicitly in quantum electrodynamics (QED). The hadronic tensor is the object of interest here, since it includes the description of the structure of the nucleon. Both tensors can be decomposed into a symmetric (S) and an antisymmetric (A) part, where only the latter depends on the spin four-vector s_l of the incoming lepton and the spin four-vector S_N of the nucleon [13]:

$$\begin{aligned} L_{\mu\nu} &= L^{(\mathrm{S})}_{\mu\nu}(k,k') + \mathrm{i}L^{(\mathrm{A})}_{\mu\nu}(k,s_l,k'), \\ W_{\mu\nu} &= W^{(\mathrm{S})}_{\mu\nu}(q,p) + \mathrm{i}W^{(\mathrm{A})}_{\mu\nu}(q,p,S_N). \end{aligned} \tag{2.10}$$

Using Eq. (2.10), the DIS cross section (2.9) becomes

$$\frac{\mathrm{d}^2\sigma}{\mathrm{d}x_{\mathrm{Bj}}\mathrm{d}y} = \frac{2\pi y\alpha^2_{\mathrm{em}}}{Q^4}\left[L^{(\mathrm{S})}_{\mu\nu}W^{\mu\nu(\mathrm{S})} - L^{(\mathrm{A})}_{\mu\nu}W^{\mu\nu(\mathrm{A})}\right]. \tag{2.11}$$

Both the symmetric and antisymmetric part of the hadronic tensor are parameterized in terms of two pairs of structure functions F_1, F_2 and g_1, g_2, which need to be measured in experiments. The symmetric, unpolarized part of the cross section for scattering a lepton on an unpolarized spin-$\hbar/2$ target is written as [13]:

$$\frac{\mathrm{d}^2\sigma}{\mathrm{d}x_{\mathrm{Bj}}\mathrm{d}y} = \frac{4\pi\alpha^2_{\mathrm{em}}}{Q^2x_{\mathrm{Bj}}y}\left\{x_{\mathrm{Bj}}y^2F_1(x_{\mathrm{Bj}},Q^2) + \left(1 - y - \frac{x^2_{\mathrm{Bj}}y^2M^2}{Q^2}\right)F_2(x_{\mathrm{Bj}},Q^2)\right\}. \tag{2.12}$$

From past measurements the structure functions F_1 and F_2 are well-known over a wide range in Q^2 and x_{Bj}. The experimental results for F_2 in dependence of Q^2 for various values of x_{Bj} are shown in Fig. 2.2.

The structure functions g_1 and g_2 can be studied in measurements either with a longitudinally ($\Leftarrow$, $\Rightarrow$) or a transversely ($\Uparrow$, $\Downarrow$) polarized target, where the polarizations of the nucleon are in reference to the lepton beam axis. The difference of two

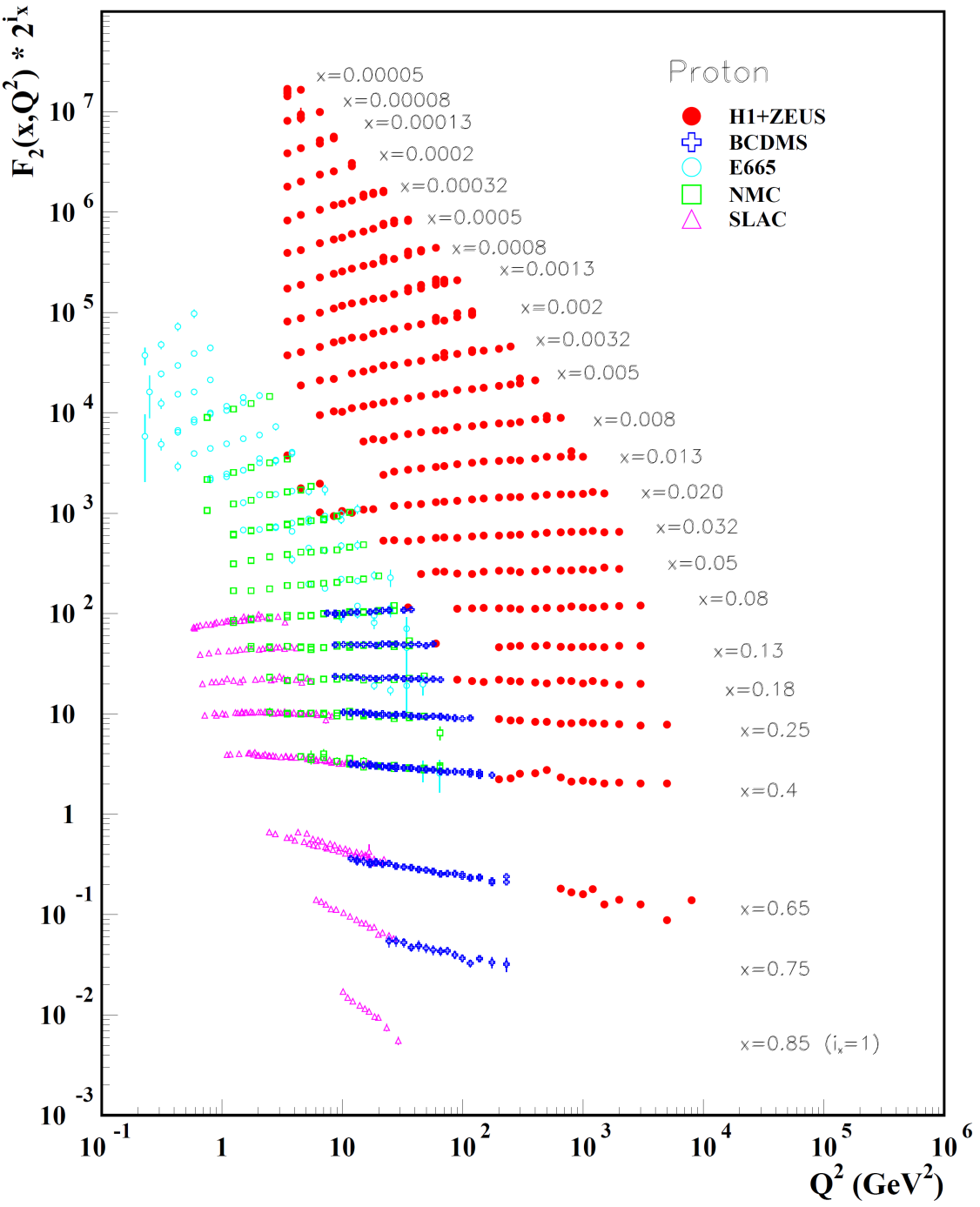

Figure 2.2: Proton structure function F_2 in dependence of Q^2 for various values of x_{Bj}, measured in electromagnetic scattering of electrons and positrons on protons (H1 and ZEUS [14]) and for electrons (SLAC [15]) and muons (BCDMS [16], E665 [17], NMC [18]) on a fixed target. For the purpose of plotting, F_2^{p} has been multiplied by 2^{i_x}, where i_x denotes the number of the x_{Bj}-bin, ranging from $i_{0.85} = 1$ to $i_{0.00005} = 24$ [19]. Note that this figure uses $x = x_{\mathrm{Bj}}$.

cross sections with opposite target spin probes the antisymmetric part of the leptonic and hadronic tensors. For a longitudinally polarized target, the cross section difference reads [13]:

$$\begin{aligned}&\frac{\mathrm{d}^3\sigma^{\leftarrow\Rightarrow}}{\mathrm{d}x_{\mathrm{Bj}}\mathrm{d}y\mathrm{d}\phi} - \frac{\mathrm{d}^3\sigma^{\leftarrow\Leftarrow}}{\mathrm{d}x_{\mathrm{Bj}}\mathrm{d}y\mathrm{d}\phi} \\ &= \frac{4\alpha_{\mathrm{em}}^2}{Q^2}\left\{\left(2-y-\frac{2x_{\mathrm{Bj}}^2y^2M^2}{Q^2}\right)g_1(x_{\mathrm{Bj}},Q^2) - \frac{4x_{\mathrm{Bj}}^2yM^2}{Q^2}g_2(x_{\mathrm{Bj}},Q^2)\right\},\end{aligned} \tag{2.13}$$

where ϕ is the azimuthal angle between the lepton plane spanned by the incoming and outgoing lepton (k, k') and the spin plane spanned by the incoming lepton and the nucleon spin (k, S_N). The cross section difference for a transversely polarized target is [13]:

$$\begin{aligned}&\frac{\mathrm{d}^3\sigma^{\leftarrow\Uparrow}}{\mathrm{d}x_{\mathrm{Bj}}\mathrm{d}y\mathrm{d}\phi} - \frac{\mathrm{d}^3\sigma^{\leftarrow\Downarrow}}{\mathrm{d}x_{\mathrm{Bj}}\mathrm{d}y\mathrm{d}\phi} \\ &= \frac{4\alpha_{\mathrm{em}}^2}{Q^2}\frac{2x_{\mathrm{Bj}}M}{Q}\sqrt{1-y-\frac{x_{\mathrm{Bj}}^2y^2M^2}{Q^2}}\cdot\left\{yg_1(x_{\mathrm{Bj}},Q^2)+2g_2(x_{\mathrm{Bj}},Q^2)\right\}\cos\phi.\end{aligned} \tag{2.14}$$

In Eq. (2.13), g_2 is suppressed by a factor of $1/Q^2$ compared to g_1. Thus, if the target is longitudinally polarized, the cross section difference mainly depends on g_1, which allows a direct measurement. Deep-inelastic measurements of g_1 have been performed in experiments at CERN, DESY, JLab[2] and SLAC. An overview of the world data for protons, deuterons and neutrons is shown in Fig. 2.3. The experimental results for the proton structure function g_1^{p} are presented in Fig. 2.4, where the kinematic coverage of the different experiments is also illustrated.

If the target is transversely polarized, g_1 and g_2 contribute at the same order and their sum can be measured, though the cross section difference is suppressed by a factor of $1/Q$. Experimental results on the measurement of g_2 are presented in Refs. [21–23]. An interpretation of the structure functions F_1, F_2, and g_1 is given by the quark-parton model.

2.2 The Quark-Parton Model

Experimentally it was discovered that the structure functions F_1 and F_2 lose their dependence on Q^2 in the deep-inelastic region over a large range in Q^2, see Fig. 2.2:

$$F_i(Q^2, x_{\mathrm{Bj}}) \to F_i(x_{\mathrm{Bj}}) \tag{2.15}$$

This relation is called Bjorken scaling and was predicted by J. Bjorken in 1968. The quark-parton model arose from an idea by R. Feynman and gives the most intuitive explanation of such scaling relations. In this model, the nucleon is made up by point-like non-interacting constituents that are called partons. Deep-inelastic scattering is seen as the incoherent sum of point-like elastic scattering of quasi-free spin-$\hbar/2$ partons, which can be identified as quarks. The dominant part of the

[2]Jefferson Laboratory

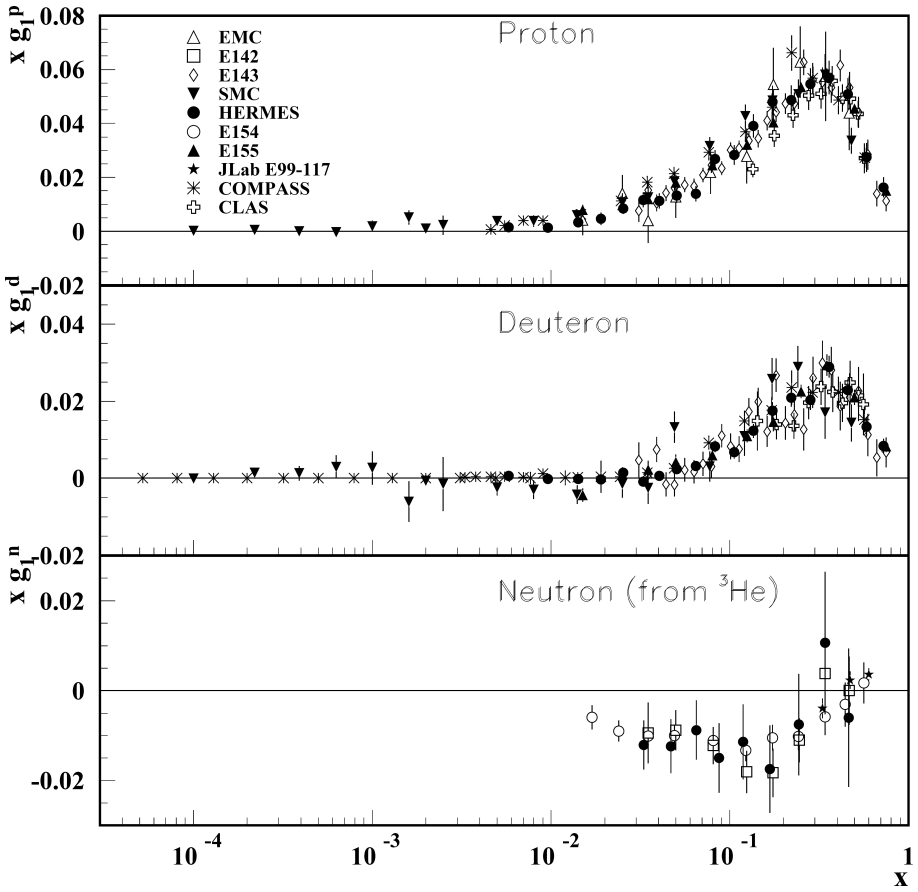

Figure 2.3: Spin-dependent structure function $x_{\mathrm{Bj}}g_1$ in dependence of x_{Bj}, measured at different fixed target experiments with polarized deep-inelastic lepton-nucleon scattering for protons, deuterons and neutrons [19]. Note that this figure uses $x = x_{\mathrm{Bj}}$.

hadronic tensor $W^{\mu\nu}$ comes from the scattering of the virtual photon with a free quark.

If the nucleon is considered in the Lorentz frame, where it is moving with infinite momentum, the transverse momentum and rest mass of all constituents can be neglected. In this frame, relativistic time dilation slows down the rate at which the partons interact with each other during the short time in which the virtual photon interacts with the quark. The partons can be understood as free particles carrying a longitudinal momentum fraction of the nucleon. This momentum fraction is found to be identical with the Bjorken variable x_{Bj} defined in Eq. (2.8) [12, 24]. The probability to find a quark of flavor f inside the nucleon with a momentum fraction within the interval $[x_{\mathrm{Bj}},\, x_{\mathrm{Bj}} + \mathrm{d}x_{\mathrm{Bj}}]$ is defined as $q_f(x_{\mathrm{Bj}})\,\mathrm{d}x_{\mathrm{Bj}}$, where $q_f(x_{\mathrm{Bj}})$ are called parton distribution functions (PDFs). Consequently, $x_{\mathrm{Bj}}q_f(x_{\mathrm{Bj}})$ and $x_{\mathrm{Bj}}\bar{q}_f(x_{\mathrm{Bj}})$ represent the momentum distributions of quarks and anti-quarks, respectively.

2.2.1 Unpolarized PDFs

In the quark-parton model, the double-differential lepton-nucleon cross section can be calculated as a sum of incoherent lepton-quark scattering for all possible types

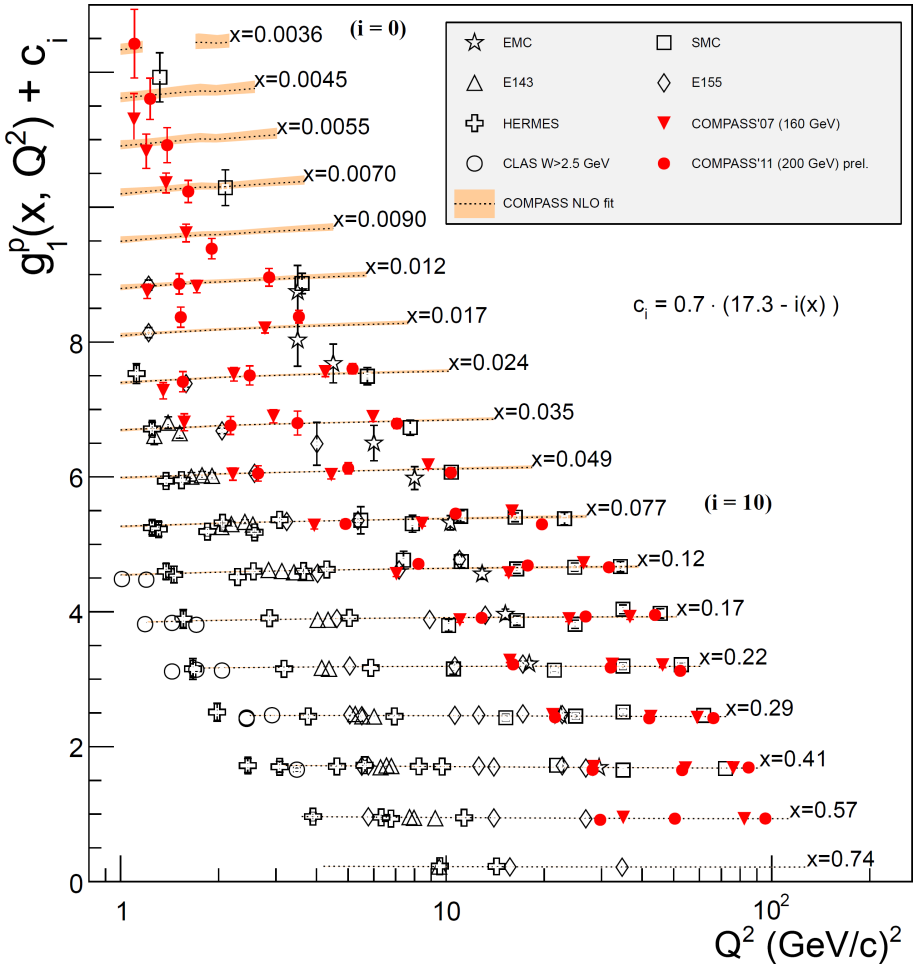

Figure 2.4: World data on the spin-dependent proton structure function g_1^{p} as a function of Q^2 for different values of x_{Bj} [20]. Note that this figure uses $x = x_{\mathrm{Bj}}$.

of quarks with the electric charge $e_f \cdot \mathrm{e}$ with a specific value of x_{Bj}.[3] This implies that the structure functions F_1 and F_2 can be expressed in terms of the PDFs [25]:

$$\begin{aligned} F_1(x_{\mathrm{Bj}}) &= \frac{1}{2} \cdot \sum_f e_f^2 \, (q_f(x_{\mathrm{Bj}}) + \bar{q}_f(x_{\mathrm{Bj}})) \\ F_2(x_{\mathrm{Bj}}) &= x_{\mathrm{Bj}} \cdot \sum_f e_f^2 \, (q_f(x_{\mathrm{Bj}}) + \bar{q}_f(x_{\mathrm{Bj}})) \, . \end{aligned} \tag{2.16}$$

The parton model further predicts:

$$2x_{\mathrm{Bj}} F_1(x_{\mathrm{Bj}}) = F_2(x_{\mathrm{Bj}}), \tag{2.17}$$

which is known as the Callan-Gross relation [26]. This relation has been experimentally confirmed and therefore it follows that the quarks have a spin of $\hbar/2$ [27].

In the quark-parton model, the structure functions solely depend on x_{Bj}, as pointed out in Eq. (2.15). Yet, high precision measurements have shown that F_2 also depends

[3] The elementary charge is denoted by e and e_f represents the fraction of the positron charge a quark with flavor f carries.

on Q^2: The structure function decreases with increasing Q^2 at large values of x_{Bj} and increases with Q^2 at small values of x_{Bj}. This behavior is called scaling violation and can be calculated beyond leading order of perturbative quantum chromodynamics (QCD), where the Bjorken scaling is broken by logarithms of Q^2 [28]. For increasing Q^2, this implies a smaller probability to find a quark with a large momentum fraction in the nucleon and a higher probability for quarks with a small momentum fraction. The scaling violation can be traced back to fundamental processes in QCD and does not indicate the existence of a substructure of the partons: Quarks can emit and absorb gluons, which, in turn, can split into a $q\bar{q}$ pair or emit other gluons. With large Q^2, the resolving power of the virtual photon is increasing and these QCD effects become relevant. The quark and gluon distribution functions in dependence of Q^2 at a fixed value of x_{Bj} can be described by the DGLAP evolution equations [27].

The sum over the momenta of all partons must reconstruct the total momentum of the nucleon. However, an integration over the experimental data on F_2, which represents the momentum carried by the charged partons, namely the quarks and anti-quarks, only explains about 54 % of the nucleon's momentum and hence, a substantial fraction is carried by neutral partons, the gluons, which cannot interact with the virtual photon in leading order of QCD.

2.2.2 Polarized PDFs

In polarized deep-inelastic lepton-nucleon scattering, the helicity of the partons can be analyzed. Analogous to the already introduced quark momentum distributions, the probability to find a quark with the momentum fraction x_{Bj} and a helicity parallel to the nucleon's spin is denoted by $q_f^{\vec{\Rightarrow}}(x_{\mathrm{Bj}})$. The probability to find a quark with the opposite helicity is described with $q_f^{\vec{\Leftarrow}}(x_{\mathrm{Bj}})$. The helicity distribution of the quarks can therewith be expressed as:

$$\Delta q_f(x_{\mathrm{Bj}}) = q_f^{\vec{\Rightarrow}}(x_{\mathrm{Bj}}) - q_f^{\vec{\Leftarrow}}(x_{\mathrm{Bj}}). \tag{2.18}$$

In this context, the unpolarized parton distribution functions may also be written analogously:

$$q_f(x_{\mathrm{Bj}}) = q_f^{\vec{\Rightarrow}}(x_{\mathrm{Bj}}) + q_f^{\vec{\Leftarrow}}(x_{\mathrm{Bj}}). \tag{2.19}$$

The helicity distributions for the anti-quarks are defined in the same way. The spin sum of all quarks and anti-quarks is obtained by the summation over the integrated helicity distribution for all quark and anti-quark flavors:

$$\Delta\Sigma = \sum_f \Delta q_f, \tag{2.20}$$

where Δq_f is the integrated helicity distribution for quarks and anti-quarks with the flavor f:

$$\Delta q_f = \int_0^1 \Delta q_f(x_{\mathrm{Bj}}) + \Delta\bar{q}_f(x_{\mathrm{Bj}})\,\mathrm{d}x_{\mathrm{Bj}}. \tag{2.21}$$

As the structure functions F_1 and F_2 in Eq. (2.16), the spin-dependent structure function g_1 can also be expressed by the polarized parton distribution functions, describing the difference in probabilities for scattering on a quark with the momentum fraction x_{Bj} and a helicity parallel and anti-parallel to the spin of the nucleon [25]:

$$g_1(x_{\mathrm{Bj}}) = \frac{1}{2}\sum_f e_f^2 \left(\Delta q_f(x_{\mathrm{Bj}}) + \Delta\bar{q}_f(x_{\mathrm{Bj}})\right). \tag{2.22}$$

The structure function g_2, on the other hand, has no such interpretation in the parton model and is predicted to be zero. This is a result from the assumption that all transverse momenta of the initial state quarks can be neglected. If this assumption is relaxed, it can be shown in models beyond the quark-parton model that g_2 is non-zero [25].

2.3 The Spin Structure of the Nucleon

From the experimental point of view, one of the key measurements is the integral of g_1 over x_{Bj}. Using Eqs. (2.21) and (2.22), the measured quantity can be written as:

$$\Gamma_1^{\mathrm{p,n}} = \int_0^1 g_1^{\mathrm{p,n}}(x_{\mathrm{Bj}}, Q^2)\,\mathrm{d}x_{\mathrm{Bj}} = \frac{1}{2}\sum_f e_f^2 \Delta q_f. \tag{2.23}$$

For the proton, using the three lightest quark flavors up (u), down (d), and strange (s), Γ_1^{p} can be expressed in terms of $\Delta\Sigma$, the isovector charge a_3, and the octet charge a_8:

$$\Gamma_1^{\mathrm{p}} = \frac{1}{2}\left[\frac{4}{9}\Delta q_{\mathrm{u}} + \frac{1}{9}\Delta q_{\mathrm{d}} + \frac{1}{9}\Delta q_{\mathrm{s}}\right] = \frac{1}{9}\Delta\Sigma + \frac{1}{12}a_3 + \frac{1}{36}a_8, \tag{2.24}$$

where [25]

$$a_3 \equiv \Delta q_{\mathrm{u}} - \Delta q_{\mathrm{d}} \qquad \text{and} \qquad a_8 \equiv \Delta q_{\mathrm{u}} + \Delta q_{\mathrm{d}} - 2\Delta q_{\mathrm{s}}. \tag{2.25}$$

With the knowledge of a_3 and a_8 from neutron and hyperon beta decay plus theoretical calculations of perturbative QCD, Γ_1^{p} can be used to extract $\Delta\Sigma$ which can be interpreted as the fraction of the proton's spin which is carried by the intrinsic spin of its quark and anti-quark constituents.

First measurements of g_1 have been performed in the early 1980's at SLAC by scattering longitudinally polarized electrons on longitudinally polarized protons, which cover a kinematic range of $0.18 < x_{\mathrm{Bj}} < 0.70$ [29]. The measurements were consistent with the predictions from the quark-parton model. In 1988, however, the European Muon Collaboration (EMC) at CERN published a surprising result, leading to the conclusion that the quark and anti-quark contribution to the spin of the proton is significantly smaller than expected [7]. In this experiment, longitudinally polarized muons were scattered on a longitudinally polarized proton target (NH_3) over a larger x_{Bj} range down to $x_{\mathrm{Bj}} = 0.01$. In the following years, a variety of experiments were carried out, refining this result and backing up the EMC findings

that $\Gamma_1^{p,n}$ is very small. For example, the COMPASS experiment measured the sum of the quark and anti-quark contributions to [30–32]:

$$\Delta\Sigma = 0.32 \pm 0.02\,(\text{stat.}) \pm 0.03\,(\text{syst.}) \pm 0.03\,(\text{evol.}), \tag{2.26}$$

obtained by semi-inclusive[4] deep-inelastic muon-proton scattering in a kinematic range of $0.004 < x_{\text{Bj}} < 0.70$. The fact that the result of the EMC experiment was consistent with zero, rather than with $\hbar/2$, became generally known as "spin crisis" [8]. Today we know, that only 32 % of the proton's spin is carried by its quarks and anti-quarks.

A possible decomposition of the nucleon spin was derived by Jaffe and Manohar and can be written as [33]:

$$\frac{J}{\hbar} = \frac{1}{2} = \frac{1}{2}\Delta\Sigma + \Delta G + L_q + L_g, \tag{2.27}$$

where J is the total angular momentum and ΔG the intrinsic gluon spin contribution. Gluons have a spin of $\hbar$. The quark and gluon orbital angular momenta are represented by L_q and L_g, respectively, since partons moving with a fraction x_{Bj} of the nucleon's infinite momentum may nevertheless have small transverse momentum components.

The COMPASS experiment was designed to measure $\Delta g/g$ via the study of the photon-gluon fusion process, where a gluon splits into a $q\bar{q}$ pair, which can interact with the virtual photon. This higher order process offers a possibility to determine the gluon helicity distribution. The cleanest way to tag this process is via open charm production, where a charmed meson is required in the final state, or by detecting two hadrons with a large transverse momentum with respect to the virtual photon direction. The result of this measurement is shown in Fig. 2.5, which leads to the conclusion that

$$\Delta G \lesssim 0.2 \tag{2.28}$$

is rather small and not sufficient to resolve the difference between the small value of $\Delta\Sigma$ and the total angular momentum of the nucleon [9].

The determination of the orbital angular momentum is the final challenge to unravel the spin composition of the nucleon. A way to directly measure the orbital angular momenta of quarks and gluons is still unknown today, but the theoretical framework of generalized parton distributions (GPDs), which is introduced in the following section, contains vital information about the quark and gluon total angular momentum in the nucleon. Ji has derived a sum-rule connecting the forward limit ($t \to 0$) of GPDs $H^{q_f,g}$ and $E^{q_f,g}$ to information about the total angular momentum [10]:

$$\begin{aligned} J^{q_f} &= \frac{1}{2}\lim_{t\to 0}\int_{-1}^{1}\left[H^{q_f}(x,\xi,t) + E^{q_f}(x,\xi,t)\right] x\,dx \\ J^{g} &= \frac{1}{2}\lim_{t\to 0}\int_{0}^{1}\left[H^{g}(x,\xi,t) + E^{g}(x,\xi,t)\right]\,dx. \end{aligned} \tag{2.29}$$

[4] A deep-inelastic scattering process is called semi-inclusive if in addition to the scattered lepton at least one hadron, produced in the current fragmentation region, is detected.

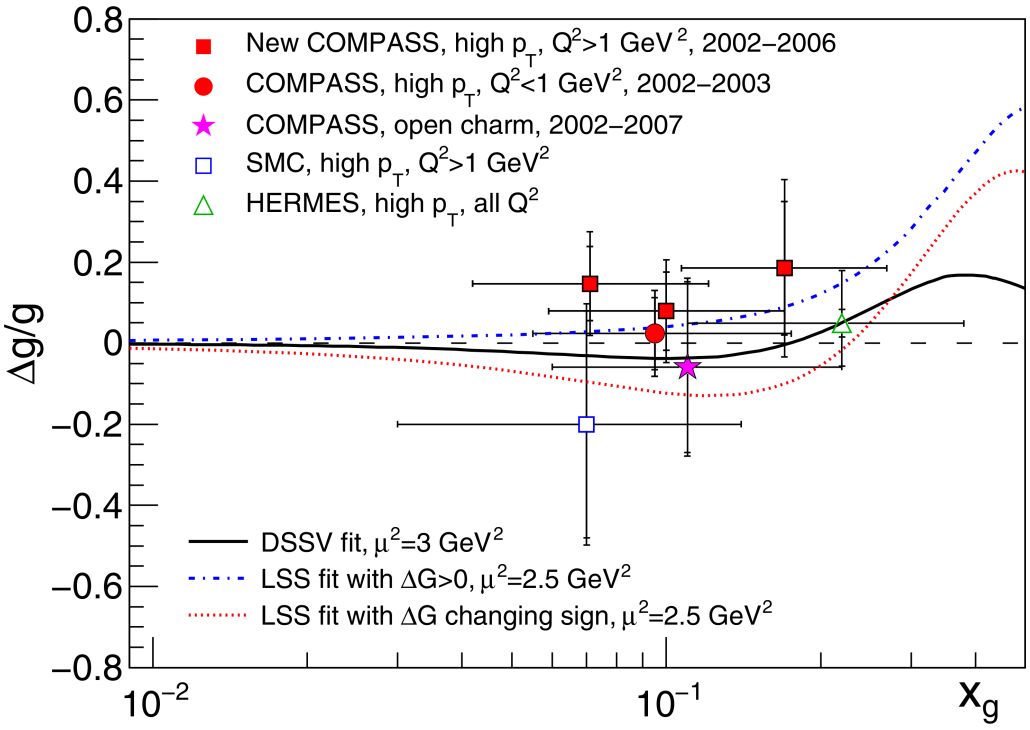

Figure 2.5: Experimental results of the ratio of polarized and unpolarized gluons $\Delta g/g$ in the nucleon and results of NLO QCD analyses of world data [9].

The kinematic variables are defined and discussed in the following section, see Eqs. (2.30) and (2.31).

An experimental access to the GPDs is given by deeply-virtual Compton scattering, which is discussed in Sec. 2.5, as well as by hard-exclusive meson production, where the GPDs need to be extracted from the measured cross sections. An extrapolation of the GPDs into unmeasured regions to $t = 0$ grant access to the total angular momenta of quarks and gluons, thus getting access to orbital angular momenta by exploiting Ji's sum-rule.

2.4 Generalized Parton Distributions

Most knowledge about the internal structure of the nucleon has been discovered by inclusive and semi-inclusive high-energy lepton-nucleon scattering $l + N \to l' + X$. Although PDFs can be extracted from the measurement of these reactions, they only describe single parton distributions because the nucleon, which is the object of interest, is destroyed. Hence, they only depend on the longitudinal momentum fraction x_{Bj} and can only provide a one-dimensional picture of the nucleon.

In order to gain insight into the nucleon's three-dimensional structure, parton correlation functions that encode additional information on how the nucleon as a whole reacts to an outside probe need to be measured. This is only possible if the nucleon stays intact during and after the reaction: $l + N \to l' + N' + X$. Otherwise, the dynamical relationship between the partons would be destroyed.

2.4.1 Properties of the GPDs

One particular process is deeply-virtual Compton scattering $l + N \to l' + N' + \gamma$, cf. Sec. 2.5. Comparable to DIS, such a process can be factorized into a hard, perturbative subprocess and a soft, non-perturbative stage of the interaction as shown in Fig. 2.6 [34]. While the former term can be calculated in QED, the latter is expressed by four generalized parton distribution functions denoted by $H^{q_f,g}$, $\tilde{H}^{q_f,g}$, $E^{q_f,g}$ and $\tilde{E}^{q_f,g}$, which are universal non-perturbative objects. The GPDs are reviewed in Refs. [35–38].

The transformation of a virtual photon into a real photon, as shown in Fig. 2.6, requires a finite momentum transfer given by the invariant Mandelstam variable

$$t = (p - p')^2 = -\Delta^2, \tag{2.30}$$

where p and p' are the associated four-vectors for the incoming and outgoing nucleon. The momentum transfer can have a transverse component, unveiling information about the transverse structure of the nucleon, encoded in the GPDs as further discussed in Sec. 2.4.3. In addition, the GPDs are also dependent on the momentum of the struck parton designated by x and ξ. The momentum fraction of the emitted and reabsorbed parton is represented by $x + \xi$ and $x - \xi$, while x and ξ refer to the average nucleon momentum $(p + p')/2$. In this context, x is the mean longitudinal momentum fraction of the struck parton and is defined in the interval $x \in [-1, 1]$, whereas ξ represents half the difference between the initial and final longitudinal momentum fraction and is related to the Bjorken variable x_{Bj} [40]:

$$\xi = x_{\mathrm{Bj}} \frac{1 + \frac{\Delta^2}{2Q^2}}{2 - x_{\mathrm{Bj}} + x_{\mathrm{Bj}} \frac{\Delta^2}{Q^2}}. \tag{2.31}$$

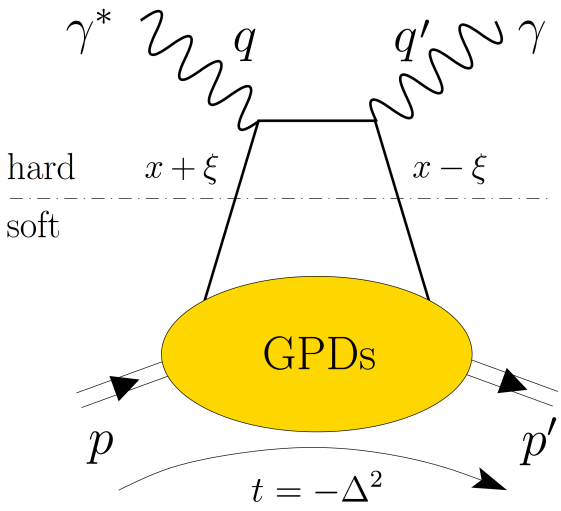

Figure 2.6: Factorization of the deeply-virtual Compton scattering process. The non-perturbative part in the lower blob can be described by the GPDs. Here, the virtual photon interacts with a quark originating from the nucleon. Picture adopted from Ref. [39].

Table 2.1: Properties of the four GPDs H, $\tilde{H}$, E, and $\tilde{E}$.

		Nucleon helicity conservation	flip
Quark helicity	independent	H	E
	dependent	$\tilde{H}$	$\tilde{E}$

The four GPDs only depend on the kinematic variables x, ξ and t. They are defined as an interference amplitude in which a quark having a momentum fraction of $x+\xi$ is taken out of the initial nucleon and created back at a different light-cone space-time point with the momentum fraction $x-\xi$. Their properties are summarized in Tab. 2.1. H and E correspond to vector operators at quark level. In contrast to the axial-vector operators $\tilde{H}$ and $\tilde{E}$, they do not depend on the helicity of the quark. H and $\tilde{H}$ conserve the nucleon helicity (vector and axial-vector transition), whereas E and $\tilde{E}$ flip the nucleon helicity (tensor and pseudoscalar transition) [36].

The "skewness" variable ξ is supported in the interval $\xi \in [0,1]$ as it follows from Eq. (2.31) and the fact that $x_{\mathrm{Bj}} \in [0,1]$. This allows a positive and negative sign for the momentum fraction $x+\xi$ and $x-\xi$ for the active parton, where a negative sign is interpreted in the quark sector as belonging to an anti-quark. As illustrated in Fig. 2.7, there are three options possible, namely the emission and reabsorption of a quark for $x \in [\xi,1]$ or an anti-quark for $x \in [-1,-\xi]$ and the emission of an quark anti-quark pair for the intermediate x region in $x \in [-\xi,\xi]$. In the latter regime, the GPDs probe $q\bar{q}$ and gluon pairs in the nucleon and thus provide a unique tool to study the dynamics of sea quarks or meson distributions.

Gluons are their own anti-particles, which implicates a symmetry property for the gluon distribution functions contrary to the quark distributions: $H^g(x,\xi,t)$ and $E^g(x,\xi,t)$ are even functions of x, and $\tilde{H}^g(x,\xi,t)$ and $\tilde{E}^g(x,\xi,t)$ are odd functions of x.

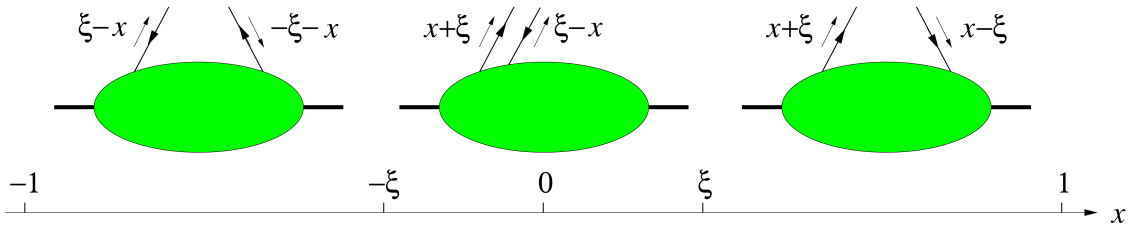

Figure 2.7: The parton interpretation of the GPDs for three possible x intervals. Left: Emission and reabsorption of anti-quarks for $x \in [-1,-\xi]$. Center: Emission of a $q\bar{q}$ pair for $x \in [-\xi,\xi]$. Right: Emission and reabsorption of quarks for $x \in [\xi,1]$ [35].

2.4.2 Relation of the GPDs to Known Distibutions

In the forward limit, where the momentum and the helicity of the incoming and outgoing nucleon become equal,

$$t \to 0 \qquad \text{and} \qquad \xi \to 0, \tag{2.32}$$

the generalized quark distribution functions $H^{q_f}(x,\xi,t)$ and $\tilde{H}^{q_f}(x,\xi,t)$ respectively reduce to the spin-independent and spin-dependent PDFs [35]:

$$\begin{aligned} H^{q_f}(x,0,0) &= q_f(x), \quad \tilde{H}^{q_f}(x,0,0) = \Delta q_f(x) \quad \text{for } x > 0, \\ H^{q_f}(x,0,0) &= -\bar{q}_f(x), \quad \tilde{H}^{q_f}(x,0,0) = \Delta \bar{q}_f(-x) \quad \text{for } x < 0. \end{aligned} \tag{2.33}$$

Figure 2.8 shows a model calculation of the GPD $H^{q_u}(x,\xi,t=0)$ for the u-quark distribution, including the PDF for u- and ū-quarks at $\xi = 0$.

Comparably, the generalized gluon distribution functions coincide with the corresponding gluon PDFs [35]:

$$H^g(x,0,0) = xg(x), \quad \tilde{H}^g(x,0,0) = x\Delta g(x) \quad \text{for } x > 0. \tag{2.34}$$

Note that in the forward limit, the finite momentum transfer onto the final state nucleon is zero, which prevents a spin flip. Consequently, there are no corresponding relations for the nucleon helicity flipping quark or gluon distributions $E^{q_f,g}$ and $\tilde{E}^{q_f,g}$. Hence, they contain unique information about orbital momenta that is only accessible in exclusive reactions as realized by Ji with his sum-rule in Eq. (2.29).

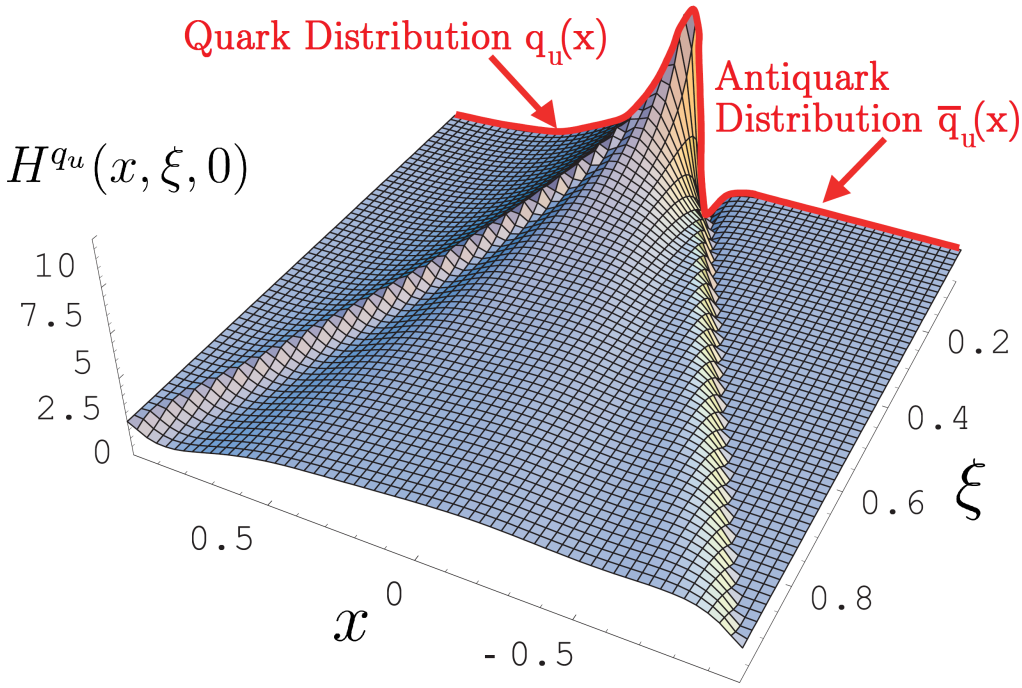

Figure 2.8: Model calculation for the generalized u-quark parton distribution function $H^{q_u}(x,\xi,t=0)$ from Ref. [36]. The red line at $\xi = 0$ corresponds to the usual PDFs for u- and ū-quarks.

Beside the relation to the PDFs in the forwards limit, the four GPDs are also associated with nucleon form factors. At finite momentum transfer, the first moments of the GPDs are related to [10]:

$$\begin{aligned}
\int_{-1}^{+1} dx H^{q_f}(x,\xi,t) &= F_1^{q_f}(t) \\
\int_{-1}^{+1} dx E^{q_f}(x,\xi,t) &= F_2^{q_f}(t) \\
\int_{-1}^{+1} dx \tilde{H}^{q_f}(x,\xi,t) &= g_A^{q_f}(t) \\
\int_{-1}^{+1} dx \tilde{E}^{q_f}(x,\xi,t) &= g_P^{q_f}(t),
\end{aligned} \tag{2.35}$$

where $F_1^{q_f}$ and $F_2^{q_f}$ are the Dirac and Pauli form factors and $g_A^{q_f}$ and $g_P^{q_f}$ the axial and pseudoscalar form factors, respectively. The form factors are independent of ξ and only depend on t.

2.4.3 Impact Parameter Space Interpretation

So far, GPDs were interpreted in momentum space. GPDs also grant access to a phenomenological interpretation of the nucleon structure in three dimensions as shown by the work of M. Burkardt on the impact parameter representation [41, 42]. As the Fourier transform of form factors is associated with the charge distribution in position space, the GPDs contain information about the parton distributions in transverse position space.

In the limiting case $\xi \to 0$, the longitudinal momentum fraction x of the struck parton is the same in the initial and final state. Consequently, the momentum transfer $t = -\Delta^2 = -\Delta_\perp^2$ is purely transverse, and the probability density to find a parton with the momentum fraction x at a distance from the center of momentum in the transverse plane can be interpreted as the Fourier transform of the GPD $H^{q_f}(x, \xi = 0, t)$ [42]:

$$q_f(x, \vec{b}_\perp) = \int \frac{d^2\Delta_\perp^2}{(2\pi)^2}\, e^{-i\Delta_\perp \cdot \vec{b}_\perp}\, H^{q_f}(x, 0, -\Delta_\perp^2), \tag{2.36}$$

where $\vec{b}_\perp$ is named impact parameter, which is defined as the distance to the nucleon's center of momentum $\vec{R}_\perp$, represented as the momentum weighted sum over all transverse parton positions $\vec{r}_\perp$:

$$\vec{R}_\perp = \sum_{i=q,g} x_i \vec{r}_{\perp,i}. \tag{2.37}$$

Note that the uncertainty principle is not an issue here, since the transverse coordinates and longitudinal momentum are probed in separate dimensions. A simple model calculation for the impact parameter dependent PDFs $q_f(x, \vec{b}_\perp)$ is depicted in

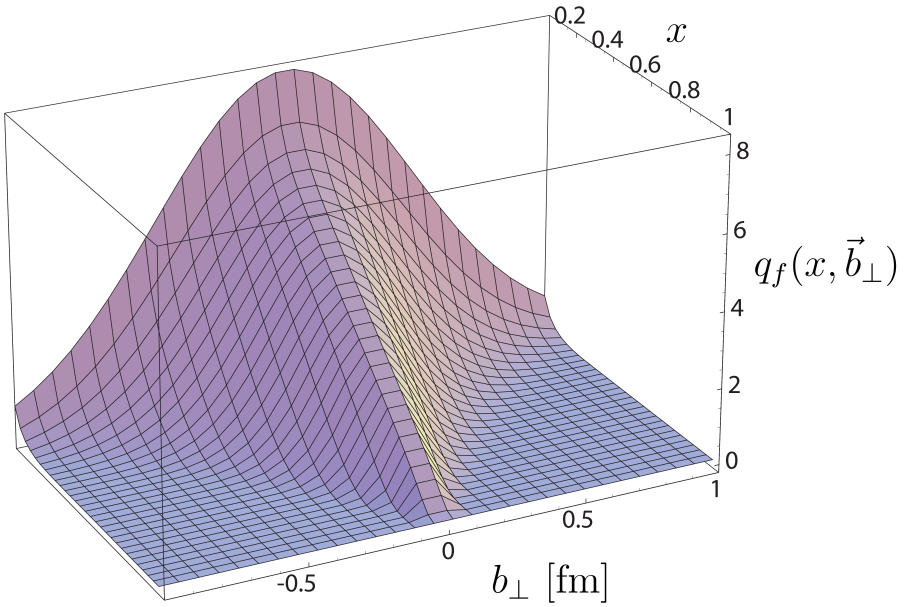

Figure 2.9: Qualitative distribution of the impact parameter dependent PDFs $q_f(x, \vec{b}_\perp)$. Picture adopted from [42].

Fig. 2.9. For $x \to 1$, the center of momentum is defined by the struck quark itself and the distribution converges to zero except for $\vec{b}_\perp = 0$. For smaller x, the sea-quarks and gluons dominate and may appear at larger distances in the transverse plane. This concept allows for a set of tomographic images for a given value of x, which contain information about the dynamics of a slice of the nucleon. Putting all slices together, a three-dimensional image of the nucleon can be obtained. Figure 2.10 illustrates the nucleon tomography for three slices in x. This framework has been extended to nonzero skewness ξ in Ref. [43].

Another important quantity of the GPDs is given for $x = \xi$, where the Fourier transform is connected to the distance $r_\perp$ between the struck parton and the spectator system [44]. At small x_{Bj}, the average $\langle r_\perp^2 \rangle$ is related to the t-slope parameter $B(x_{\mathrm{Bj}})$ and the overall transverse size of the nucleon can be written as

$$\langle r_\perp^2 \rangle \approx 2 \cdot B(x_{\mathrm{Bj}}), \tag{2.38}$$

if the cross section of the exclusive process is parametrized with the simple ansatz:

$$\frac{\mathrm{d}\sigma}{\mathrm{d}t} \propto e^{-B(x_{\mathrm{Bj}}) \cdot |t|}. \tag{2.39}$$

The measurement of the exclusive cross section depending on t, e.g. of the DVCS process, provides an extraction of the t-slope parameter and can, therefore, help to understand the dependence of the nucleon's transverse size to the momentum fraction carried by the struck parton.

2.5 Deeply-Virtual Compton Scattering

In a deeply-virtual Compton scattering (DVCS) process, a high-energy lepton is scattering on a proton target by exchanging a high-energy virtual photon. The

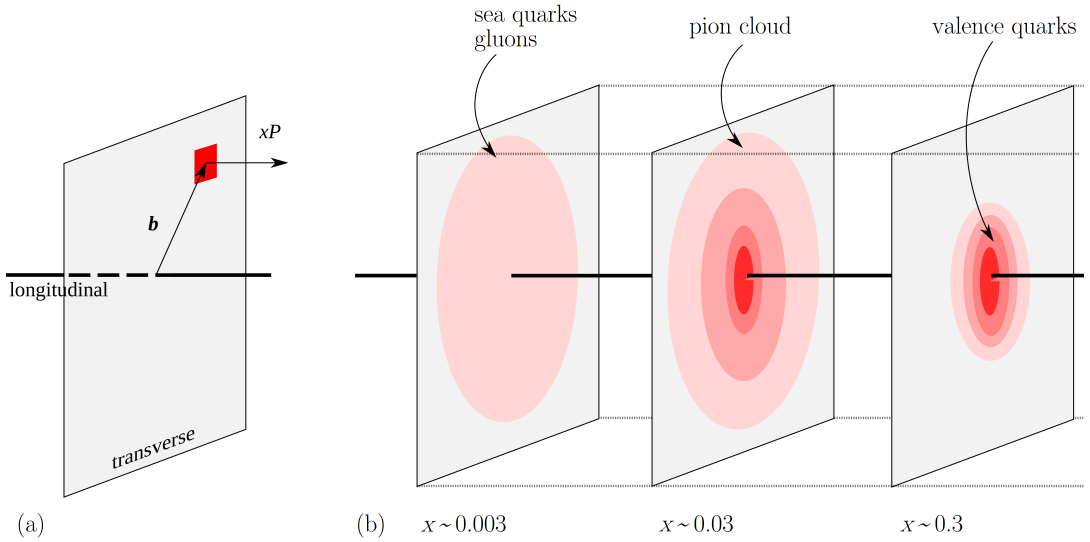

Figure 2.10: Nucleon Tomography: (a) The Fourier transform of the GPD H (Eq. (2.36)) describes the parton distribution function of partons with the momentum fraction x in a transverse distance b from the nucleon's center of momentum. (b) A three-dimensional image of the nucleon can be obtained through different slices in x. In the low x range $x \approx 0.003$, the distribution is dominated by sea-quarks and gluons, while for $x \approx 0.3$ the valence quarks are dominating. Picture adopted from Refs. [39, 45].

initial state of this reaction is similar to DIS. The final state, however, consists of a real photon and a slightly recoiled target nucleon:

$$l + N \to l' + N' + \gamma. \tag{2.40}$$

When studying GPDs, the DVCS process, also referred to as "golden channel", is the cleanest. The reason for this is the production of a real photon in the final state, which is an elementary point-like particle. Other processes that also have a recoiled proton in the final state, such as hard-exclusive meson production, are more complicated to describe due to the presence of a bound meson state.

As shown in Fig. 2.11, the DVCS process has the same initial and final state as the competing Bethe-Heitler (BH) process. The BH process is elastic lepton-nucleon scattering with a real photon emitted by either the incoming or outgoing lepton. This process is well understood and completely calculable in QED.

The full DVCS cross section reads [46, 47]:

$$\begin{aligned}
\mathrm{d}\sigma(lp \to l'p'\gamma) \;\propto\; & \mathrm{d}\sigma^{\mathrm{BH}}_{UU} + e_l\,\mathrm{d}\sigma^{\mathrm{I}}_{UU} + \mathrm{d}\sigma^{\mathrm{DVCS}}_{UU} \\
& + P_l\,S_L\,\mathrm{d}\sigma^{\mathrm{BH}}_{LL} + e_l\,P_l\,S_L\mathrm{d}\sigma^{\mathrm{I}}_{LL} + P_l\,S_L\,\mathrm{d}\sigma^{\mathrm{DVCS}}_{LL} \\
& + P_l\,S_T\,\mathrm{d}\sigma^{\mathrm{BH}}_{LT} + e_l\,P_l\,S_T\,\mathrm{d}\sigma^{\mathrm{I}}_{LT} + P_l\,S_T\,\mathrm{d}\sigma^{\mathrm{DVCS}}_{LT} \\
& + e_l\,P_l\,\mathrm{d}\sigma^{\mathrm{I}}_{LU} + P_l\,\mathrm{d}\sigma^{\mathrm{DVCS}}_{LU} \\
& + e_l\,S_L\,\mathrm{d}\sigma^{\mathrm{I}}_{UL} + S_L\,\mathrm{d}\sigma^{\mathrm{DVCS}}_{UL} \\
& + e_l\,S_T\,\mathrm{d}\sigma^{\mathrm{I}}_{UT} + S_T\,\mathrm{d}\sigma^{\mathrm{DVCS}}_{UT},
\end{aligned} \tag{2.41}$$

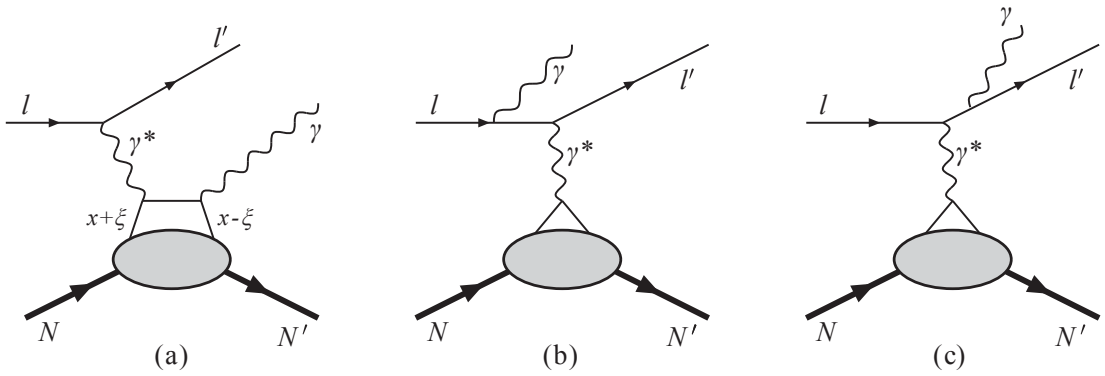

Figure 2.11: Leading order processes of lepton-nucleon scattering for the production of real photons: (a) DVCS, (b) Bethe-Heitler with the real photon emitted by the incoming, and (c) by the outgoing lepton [11].

where, for the sake of simplicity,

$$\mathrm{d}\sigma \equiv \frac{\mathrm{d}^4\sigma(lp \to l'p'\gamma)}{\mathrm{d}x\ \mathrm{d}Q^2\ \mathrm{d}|t|\ \mathrm{d}\phi_{\gamma\gamma^*}}. \tag{2.42}$$

The first subscript in the cross section $\mathrm{d}\sigma$ denotes the polarization of the lepton beam, while the second subscript indicates the polarization of the proton target. The letters U, L, and T stand for unpolarized, longitudinal, and transverse polarization state with respect to the virtual photon direction. The superscript referes to the process. The lepton beam charge and polarization are implied by e_l and P_l. The longitudinal and transverse target polarizations are represented by S_L and S_T. The azimuthal angle $\phi_{\gamma\gamma^*}$ is between the leptonic plane and the plane spanned by the virtual photon and produced real photon, cf. Fig. 2.12. The dependence on the azimuthal angle $\phi_{\gamma\gamma^*}$ is a characteristic feature of the cross section. This equation indicates the large variety of observables accessible with polarized beams or targets.

The DVCS and BH process have an indistinguishable initial and final state. Hence, an interference term (I) needs to be considered in the cross section. The differential cross section can also be written in terms of the DVCS and BH process amplitudes [11]:

$$\frac{\mathrm{d}^4\sigma(lp \to l'p'\gamma)}{\mathrm{d}x\,\mathrm{d}Q^2\,\mathrm{d}|t|\,\mathrm{d}\phi_{\gamma\gamma^*}} \propto |\mathcal{T}_{\mathrm{BH}}|^2 + |\mathcal{T}_{\mathrm{DVCS}}|^2 + \underbrace{\mathcal{T}_{\mathrm{DVCS}}\,\mathcal{T}^*_{\mathrm{BH}} + \mathcal{T}^*_{\mathrm{DVCS}}\,\mathcal{T}_{\mathrm{BH}}}_{\mathcal{I}}, \tag{2.43}$$

where $\mathcal{T}$ denotes the complex scattering amplitude of the corresponding process. The interference term $\mathcal{I}$ provides an access to the real and imaginary part of the DVCS scattering amplitude with the knowledge of the well-understood BH process.

The propagator term of the BH process is proportional to $1/t$, while the propagator term for DVCS goes with $1/Q^2$ [40]. Consequently, the ratio of BH, DVCS, and interference term varies strongly for a given beam energy over the x_{Bj} region, especially for the kinematic domain of the COMPASS-II experiment. As indicated in Fig. 2.13, the BH process dominates in the lower x_{Bj} region. With increasing

x_{Bj}, the amplitudes of both processes are of the same order, while the DVCS process dictates the total cross section in the large x_{Bj} regime. In this case, the DVCS amplitude can be extracted.

2.5.1 Unpolarized Target

For an unpolarized target, $S_L = S_T = 0$ in Eq. (2.41), the differential cross section for muoproduction of real photons can be written as [39]:

$$\frac{\mathrm{d}^4\sigma(\mu p \to \mu' p' \gamma)}{\mathrm{d}x\ \mathrm{d}Q^2\ \mathrm{d}|t|\ \mathrm{d}\phi_{\gamma\gamma^*}} = \mathrm{d}\sigma_{UU}^{\mathrm{BH}} + \left[\mathrm{d}\sigma_{UU}^{\mathrm{DVCS}} + P_l \mathrm{d}\sigma_{LU}^{\mathrm{DVCS}}\right] + e_l \left[\mathrm{Re}\,\mathcal{I} + P_l \mathrm{Im}\,\mathcal{I}\right]. \quad (2.44)$$

At the CERN SPS M2 beam line, where the COMPASS-II experiment is located, the muon beam is naturally polarized due to the nature of parity violation of the pion and kaon decay (see Sec. 3.1). Consequently, a reversal of the beam charge implies a polarization sign change, which makes the COMPASS-II experiment predestinated for the measurement of the beam charge and spin sum and difference. In the following, the beam charge and polarization are denoted by $\overset{+}{\leftarrow}$ and $\overset{-}{\rightarrow}$.

Beam Charge and Spin Sum

The sum of cross sections for separate measurements with opposite charge and polarization of the lepton beam allows to extract certain contributions of the cross section in Eq. (2.44). The beam charge and spin sum for an unpolarized target, denoted by the subscript U [39],

$$\mathcal{S}_U = \mathrm{d}\sigma^{\overset{+}{\leftarrow}} + \mathrm{d}\sigma^{\overset{-}{\rightarrow}} = 2\left(\mathrm{d}\sigma_{UU}^{\mathrm{BH}} + \mathrm{d}\sigma_{UU}^{\mathrm{DVCS}} + e_l P_l \mathrm{Im}\,\mathcal{I}\right), \quad (2.45)$$

contains the BH and unpolarized DVCS contribution and is also sensitive to the imaginary part of the interference term. These cross sections and their $\phi_{\gamma\gamma^*}$-dependence can be calculated beyond leading twist including all twist-3 contributions, where the latter ones are put in curly brackets [40]:

$$\mathrm{d}\sigma_{UU}^{\mathrm{BH}} = \epsilon^{\mathrm{BH}}\left(c_{0,U}^{\mathrm{BH}} + c_{1,U}^{\mathrm{BH}}\cos(\phi_{\gamma\gamma^*}) + c_{2,U}^{\mathrm{BH}}\cos(2\phi_{\gamma\gamma^*})\right), \quad (2.46)$$

$$\mathrm{d}\sigma_{UU}^{\mathrm{DVCS}} = \epsilon^{\mathrm{DVCS}}\left(c_{0,U}^{\mathrm{DVCS}} + \left\{c_{1,U}^{\mathrm{DVCS}}\cos(\phi_{\gamma\gamma^*}) + c_{2,U}^{\mathrm{DVCS}}\cos(2\phi_{\gamma\gamma^*})\right\}\right), \quad (2.47)$$

$$\mathrm{Im}\,\mathcal{I} = \epsilon^{\mathrm{I}}\left(s_{1,U}^{\mathrm{I}}\sin(\phi_{\gamma\gamma^*}) + \left\{s_{2,U}^{\mathrm{I}}\sin(2\phi_{\gamma\gamma^*})\right\}\right). \quad (2.48)$$

The three kinematic factors ϵ^{BH}, ϵ^{DVCS}, and ϵ^{I} are expressed as:

$$\epsilon^{\mathrm{BH}} = \frac{e^6}{x_{\mathrm{Bj}}^2 y^2 t\left(1 + (2x_{\mathrm{Bj}}M/Q)^2\right)^2 \mathcal{P}_1(\phi_{\gamma\gamma^*})\mathcal{P}_2(\phi_{\gamma\gamma^*})}, \quad (2.49)$$

$$\epsilon^{\mathrm{DVCS}} = \frac{e^6}{y^2 Q^2}, \quad (2.50)$$

$$\epsilon^{\mathrm{I}} = \frac{e^6}{x_{\mathrm{Bj}} y^3 t \mathcal{P}_1(\phi_{\gamma\gamma^*})\mathcal{P}_2(\phi_{\gamma\gamma^*})}. \quad (2.51)$$

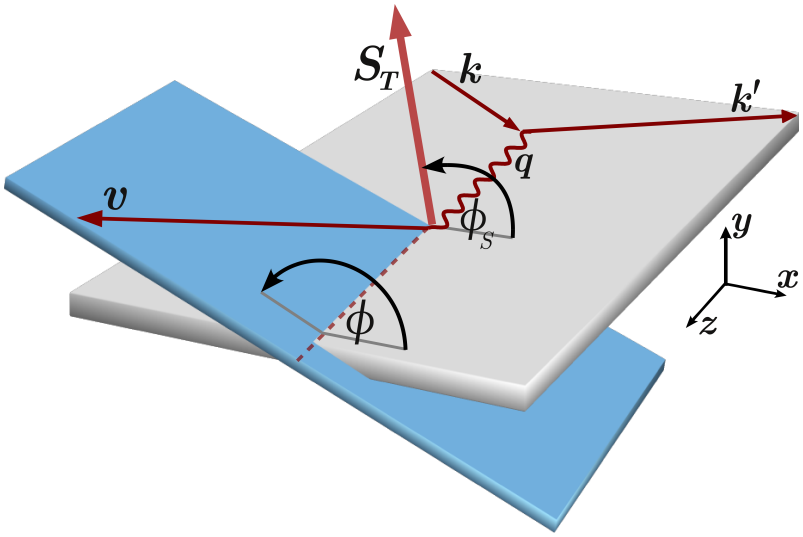

Figure 2.12: Angle definitions according to the Trento convention. Here k, k', q and v represent the three-momentum vectors of the incident and scattered muon, the virtual photon and the final state photon (or meson in the case of hard exclusive meson production). The transverse target spin vector is denoted by S_T [48, 49].

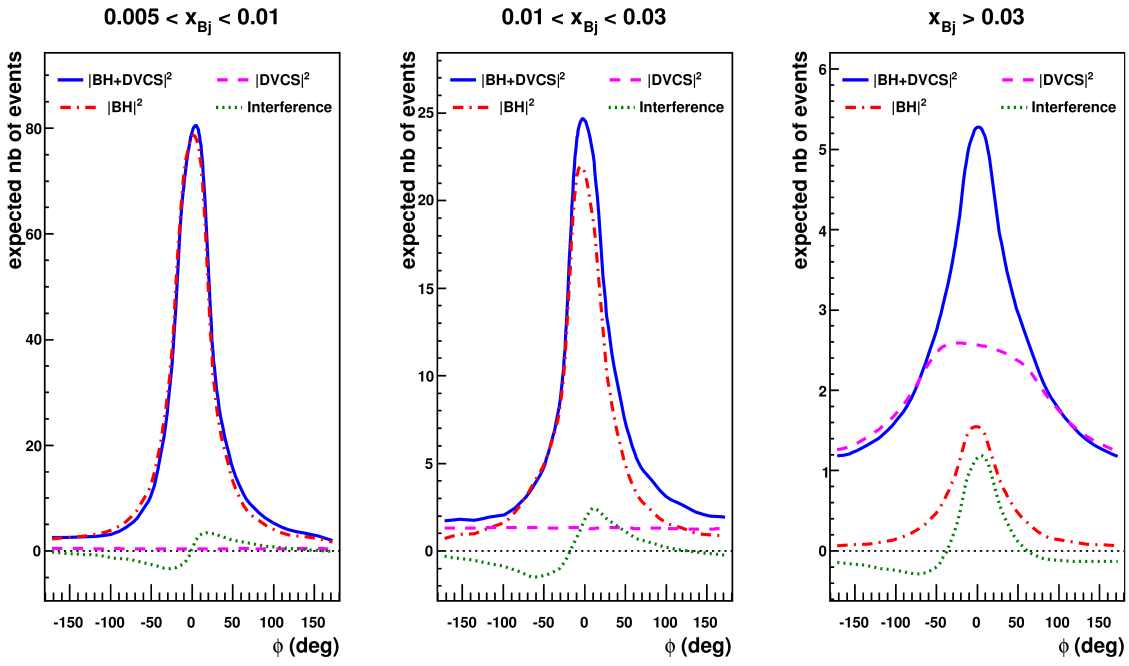

Figure 2.13: Model calculation for three different x_{Bj} regions, showing the expected cross section for DVCS (dashed line), BH (dashed dotted line), and the interference term (dotted line) as a function of $\phi_{\gamma\gamma^*}$. The total cross section is depicted with an continuous line [39].

The kinematic factors of the BH and interference term have an additional $\phi_{\gamma\gamma^*}$-dependence due to the lepton BH propagator [40]:

$$\mathcal{P}_1 = \frac{Q^2 + 2k\cdot(p'-p)}{Q^2} \tag{2.52}$$

$$\mathcal{P}_2 = \frac{t - 2k\cdot(p'-p)}{Q^2} \tag{2.53}$$

The coefficients c_i^{BH} in the BH part of the cross section are expressed solely in terms of the known Dirac and Pauli form factors F_1 and F_2 and are calculable in QED, not only for an unpolarized but also for a transversely or longitudinally polarized target.

The coefficients $c_i^{\mathrm{DVCS,\,I}}$ and $s_i^{\mathrm{DVCS,\,I}}$ are associated with a certain combination of Compton form factors (CFF). A CFF $\mathcal{F}$ is given by the convolution of a perturbatively calculable coefficient function C describing the hard $\gamma^* q$ interaction and the respective GPD F [40]:

$$\mathcal{F}(\xi,t) = \int_{-1}^{1} C(x,\xi)F(x,\xi,t)\,\mathrm{d}x. \tag{2.54}$$

In leading twist, a precise analysis of the $\phi_{\gamma\gamma^*}$-dependence provides $s_{1,U}^{\mathrm{I}}$, which is related to the imaginary part of a combination of the CFF $\mathcal{H}$, $\tilde{\mathcal{H}}$ and $\mathcal{E}$ [40]:

$$s_{1,U}^{\mathrm{I}} \propto \mathrm{Im}\left(\mathcal{C}_U^{\mathrm{I}}\right), \tag{2.55}$$

with

$$\mathcal{C}_U^{\mathrm{I}} = F_1\mathcal{H} + \frac{x_{\mathrm{Bj}}}{2-x_{\mathrm{Bj}}}\left(F_1+F_2\right)\tilde{\mathcal{H}} - \frac{t}{4M^2}F_2\mathcal{E} \approx F_1\mathcal{H}, \tag{2.56}$$

where the last approximation is motivated due to the small kinematic factors before of $\tilde{\mathcal{H}}$ and $\mathcal{E}$ at COMPASS kinematics. Consequently, a precise measurement of the azimuthal angular dependence of the beam charge and spin sum cross section gives at leading order a direct access to the imaginary part of the CFF $\mathcal{H}$. Since the CFF cannot be deconvoluted, models for the GPD H need to be parameterized and adjusted to the experimental data.

An alternative approach is the analysis of the integral of $\mathcal{S}_U$ over the azimuthal angle $\phi_{\gamma\gamma^*}$. In that case, all $\sin(\phi_{\gamma\gamma^*})$-dependent terms cancel,

$$\int \mathrm{Im}\,\mathcal{I}\,\mathrm{d}\phi_{\gamma\gamma^*} = 0, \tag{2.57}$$

and the pure DVCS leading twist contribution $c_{0,U}^{\mathrm{DVCS}}$ can be extracted by subtracting the well-known BH content [40]:

$$c_{0,U}^{\mathrm{DVCS}} \propto \mathcal{C}_U^{\mathrm{DVCS}} \propto \left(\mathcal{H}\mathcal{H}^* + \tilde{\mathcal{H}}\tilde{\mathcal{H}}^*\right), \tag{2.58}$$

with

$$\begin{aligned}\mathcal{C}_U^{\mathrm{DVCS}} = \Bigg\{ & 4(1-x_{\mathrm{Bj}})\left(\mathcal{H}\mathcal{H}^* + \tilde{\mathcal{H}}\tilde{\mathcal{H}}^*\right) - x_{\mathrm{Bj}}^2\left(\mathcal{H}\mathcal{E}^* + \mathcal{E}\mathcal{H}^* + \tilde{\mathcal{H}}\tilde{\mathcal{E}}^* + \tilde{\mathcal{E}}\tilde{\mathcal{H}}^*\right) \\ & - \left(x_{\mathrm{Bj}}^2 + (2-x_{\mathrm{Bj}})\frac{t}{4M^2}\right)\mathcal{E}\mathcal{E}^* - x_{\mathrm{Bj}}^2\frac{t}{4M^2}\tilde{\mathcal{E}}\tilde{\mathcal{E}}^*\Bigg\}\frac{1}{(2-x_{\mathrm{Bj}})^2},\end{aligned} \tag{2.59}$$

where, again, all terms with $\mathcal{E}$ and $\tilde{\mathcal{E}}$ are suppressed by their kinematic factors.

The analysis of the t-dependence of the DVCS cross sections over the experimentally accessible x_{Bj} region can be used to extract the t-slope parameter, cf. Sec. 2.4.3.

Wherever an absolute cross section or the sum of two cross sections needs to be experimentally measured, a trustful Monte Carlo simulation is essential to correct the measured data for the acceptance of the experiment and for an estimate of the background contribution. In particular for the extraction of the t-slope, a subtraction of the BH content from the $\phi_{\gamma\gamma^*}$ integrated cross section sum is indispensable. The new Monte Carlo software for the COMPASS-II experiment is presented in Chapter 4. The software was used for the analysis of the 2012 DVCS pilot run as summarized in Chapter 7.

Beam Charge and Spin Difference

The beam charge and spin difference is analogously given by [39]:

$$\mathcal{D}_U = \mathrm{d}\sigma^{\overleftarrow{\pm}} - \mathrm{d}\sigma^{\overrightarrow{-}} = 2\left(P_l \mathrm{d}\sigma_{LU}^{\mathrm{DVCS}} + e_l \mathrm{Re}\,\mathcal{I}\right), \tag{2.60}$$

in which the BH content drops out and the real part of the interference term is preserved. The two remaining cross section contributions can be calculated beyond leading order and expressed by a combination of CFF [40]:

$$\mathrm{d}\sigma_{LU}^{\mathrm{DVCS}} = \epsilon^{\mathrm{DVCS}}\left(\left\{s_{1,U}^{\mathrm{DVCS}}\sin(\phi_{\gamma\gamma^*})\right\}\right), \tag{2.61}$$

$$\mathrm{Re}\,\mathcal{I} = \epsilon^{\mathrm{I}}\left(c_{0,U}^{\mathrm{I}} + c_{1,U}^{\mathrm{I}}\cos(\phi_{\gamma\gamma^*}) + \left\{c_{2,U}^{\mathrm{I}}\cos(2\phi_{\gamma\gamma^*}) + c_{3,U}^{\mathrm{I}}\cos(3\phi_{\gamma\gamma^*})\right\}\right). \tag{2.62}$$

Regarding twist-2 only, the analysis of the azimuthal angular dependence provides $c_{0,U}^{\mathrm{I}}$ and $c_{1,U}^{\mathrm{I}}$, which are both related to the real part of the CFF combination $\mathcal{C}_U^{\mathrm{I}}$. Again, as in Eq. (2.55), all kinematically suppressed terms are disregarded:

$$c_{0,U}^{\mathrm{I}},\ c_{1,U}^{\mathrm{I}} \propto \mathrm{Re}\left(\mathcal{C}_U^{\mathrm{I}}\right) \propto \mathrm{Re}\left(F_1\mathcal{H}\right). \tag{2.63}$$

Using an unpolarized target, the accurate analysis of the $\phi_{\gamma\gamma^*}$-dependence of the beam charge and spin sum $\mathcal{S}_U$ and difference $\mathcal{D}_U$ grants an access to the real and imaginary part of the CFF $\mathcal{H}$, which is related to the GPD H.

2.5.2 Transversely Polarized Target

In the case of an unpolarized target, the sensitivity to the GPD E is strongly suppressed. The only possibility to access the GPD E is the measurement of the differential cross section for muoproduction of real photons using a polarized target. For a transversely polarized target, denoted by $\Uparrow$ and $\Downarrow$, and a naturally polarized lepton beam, four different cross sections $\mathrm{d}\sigma^{\overleftarrow{\pm},\Uparrow}$, $\mathrm{d}\sigma^{\overleftarrow{\pm},\Downarrow}$, $\mathrm{d}\sigma^{\overrightarrow{-},\Uparrow}$, and $\mathrm{d}\sigma^{\overrightarrow{-},\Downarrow}$ can be measured. These cross-sections have an additional dependence on the azimuthal angle ϕ_S of the transverse target spin vector relative to the lepton scattering plane. New cross section combinations, which are defined as double differences, can be formed to isolate and analyze specific parts of the full cross section.

The beam charge and spin difference between differences of cross sections with opposite target polarizations for a transversely polarized target reads

$$\mathcal{D}_T = \left(\mathrm{d}\sigma^{\overset{+}{\leftarrow},\Uparrow} - \mathrm{d}\sigma^{\overset{+}{\leftarrow},\Downarrow}\right) - \left(\mathrm{d}\sigma^{\overset{-}{\rightarrow},\Uparrow} - \mathrm{d}\sigma^{\overset{-}{\rightarrow},\Downarrow}\right), \tag{2.64}$$

and correspondingly the transverse beam charge and spin sum reads as follows:

$$\mathcal{S}_T = \left(\mathrm{d}\sigma^{\overset{+}{\leftarrow},\Uparrow} - \mathrm{d}\sigma^{\overset{+}{\leftarrow},\Downarrow}\right) + \left(\mathrm{d}\sigma^{\overset{-}{\rightarrow},\Uparrow} - \mathrm{d}\sigma^{\overset{-}{\rightarrow},\Downarrow}\right). \tag{2.65}$$

These cross section combinations and their $\phi_{\gamma\gamma^*}$ and ϕ_S dependence can be calculated. Including all twist-3 contributions, the transverse beam charge and spin difference is given by [39, 40]:

$$\begin{aligned}
\mathcal{D}_T = \quad & 2P_l\epsilon^{\mathrm{BH}}\left(c_{0,T}^{\mathrm{BH}}\,c(0) + c_{1,T}^{\mathrm{BH}}\,c(1) + s_{1,T}^{\mathrm{BH}}\,s(1)\right) \\
& + 2P_l\epsilon^{\mathrm{DVCS}}\left(c_{0,T}^{\mathrm{DVCS}}\,c(0) + \left\{c_{1,T}^{\mathrm{DVCS}}\,c(1) + s_{1,T}^{\mathrm{DVCS}}\,s(1)\right\}\right) \\
& + 2e_l\epsilon^{\mathrm{I}}\Big(c_{0,T}^{\mathrm{I}}\,c'(0) + c_{1,T}^{\mathrm{I}}\,c'(1) + s_{1,T}^{\mathrm{I}}\,s'(1) \\
& \qquad + \left\{c_{2,T}^{\mathrm{I}}\,c'(2) + s_{2,T}^{\mathrm{I}}\,s'(2) + c_{3,T}^{\mathrm{I}}\,c'(3) + s_{3,T}^{\mathrm{I}}\,s'(3)\right\}\Big)
\end{aligned} \tag{2.66}$$

where, for the sake of simplicity, the angular dependency is denoted by the four functions:

$$\begin{aligned}
s(n) &= \sin(n\phi_{\gamma\gamma^*}) \cdot \sin(\phi_{\gamma\gamma^*} - \phi_S), \\
c(n) &= \cos(n\phi_{\gamma\gamma^*}) \cdot \cos(\phi_{\gamma\gamma^*} - \phi_S), \\
s'(n) &= \sin(n\phi_{\gamma\gamma^*}) \cdot \cos(\phi_{\gamma\gamma^*} - \phi_S), \\
c'(n) &= \cos(n\phi_{\gamma\gamma^*}) \cdot \sin(\phi_{\gamma\gamma^*} - \phi_S).
\end{aligned} \tag{2.67}$$

In leading twist, the analysis of the $\phi_{\gamma\gamma^*}$-dependence of $\mathcal{D}_T$ provides $c_{1,T}^{\mathrm{I}}$, which is related to the imaginary part of the CFF combination $\mathcal{C}_{T-}^{\mathrm{I}}$. Neglecting the kinematically suppressed terms,

$$c_{1,T}^{\mathrm{I}} \propto \mathrm{Im}\,\mathcal{C}_{T-}^{\mathrm{I}} \propto \mathrm{Im}\,\left(F_2\mathcal{H} - F_1\mathcal{E}\right), \tag{2.68}$$

such a measurement allows the extraction of both the CFF $\mathcal{H}$ and $\mathcal{E}$ since they contribute on the same level. The full description of the angular dependencies of $\mathcal{S}_T$ and their connections with the CFF combinations can be found in Ref. [40].

The final answer to the spin puzzle, namely the decomposition of the nucleon spin, can only be given with the angular momenta of quarks and gluons. Ji has derived a sum rule (Eq. (2.29)) that connects the total angular momenta with the GPDs H and E, which have to be constrained experimentally by cross section measurements of exclusive reactions. The GPD E, however, can only be accessed by using a transversely polarized target.

The technical challenge to perform such a measurement is the combination of the magnetic field that is necessary during the time needed to polarize the target material and to maintain the target polarization and a recoil proton detector to guarantee the exclusivity of the measurement. A possible solution for a beyond 2020 COMPASS-III experiment is given in Chapter 8.

3. The COMPASS-II Experiment

COMPASS is a fixed target experiment, which is located at the CERN North Area next to Geneva. The purpose of this experiment is the study of hadron structure and spectroscopy. A high-energy muon or hadron beam is scattered off a fixed target, where one or more outgoing particles are detected in coincidence with an incoming beam particle. The experiment can be divided into three sections: the beam line, where the tracks and momenta of the incoming beam particles are measured, the target area, and the spectrometer, which detects outgoing particles. The first spectrometer stage, the large angle spectrometer (LAS), is located downstream directly behind the target. It covers angles of outgoing particles up to 180 mrad. Particles that are scattered or produced at small angles of at most 30 mrad are measured in the second spectrometer stage, the small angle spectrometer (SAS). Each spectrometer stage is equipped with a dipole magnet (SM1 and SM2, respectively), as well as with detector systems optimized for track reconstruction and particle identification.

This chapter presents the setup of 2012 and 2016/17 as it is used for the measurement of deeply-virtual Compton-scattering. Important upgrades of the spectrometer and especially the target region have been performed as outlined in the COMPASS-II proposal [39]. A detailed description of the COMPASS experiment for muon and hadron physics programs can be found in Refs. [50, 51].

A fundamental and indispensable component of the newly developed Monte Carlo software presented in Chapter 4 is an accurate geometrical description of the experimental apparatus. The full COMPASS-II spectrometer with the setup of the 2016/17 measurement is shown in Fig. 3.1. This picture and most of the detector figures shown in the present chapter originate from this new Monte Carlo software named TGEANT. All detector geometries are simulated as detailed as it is possible without slowing down the software performance too much.

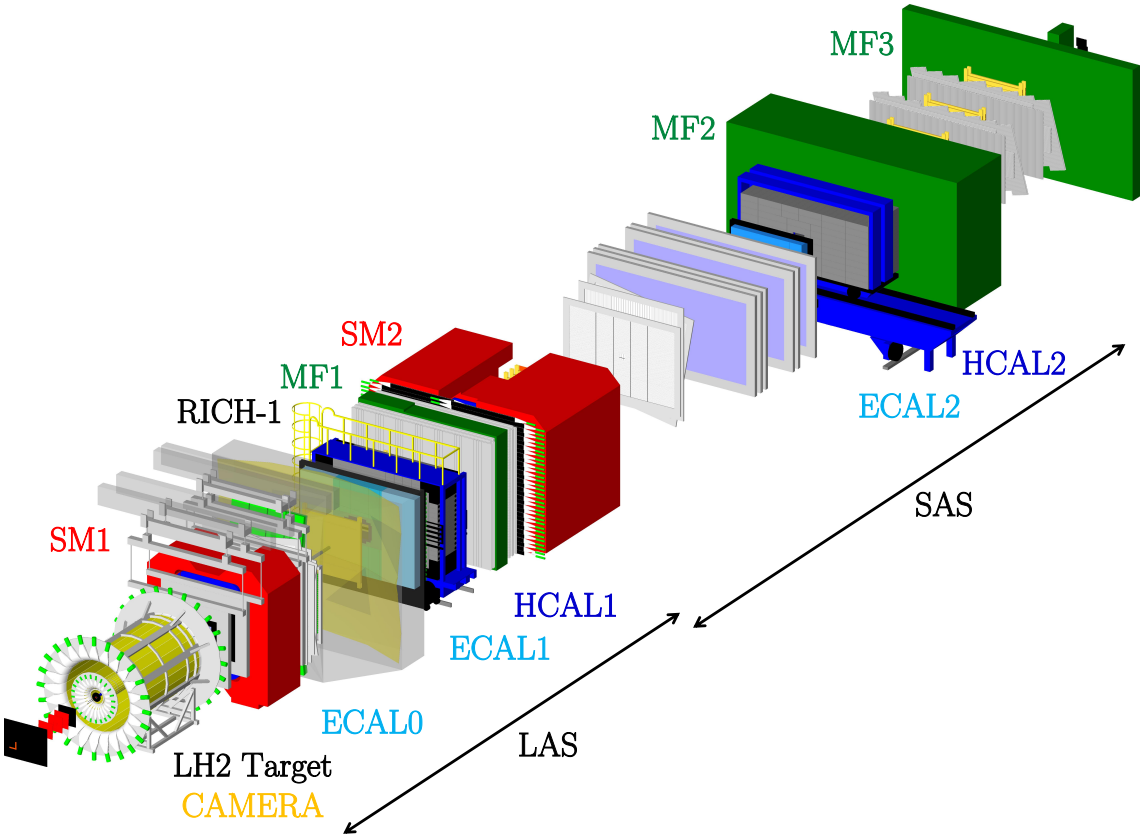

Figure 3.1: Visualization of the 60 m-long COMPASS-II spectrometer from TGEANT. This picture shows the DVCS setup used in 2016/17.

3.1 The Beam Line

The high-energy particle beam used in the COMPASS experiment is provided via the M2 beam line from the Super Proton Synchrotron (SPS) accelerator. The beam type can be selected according to the running physics program. Muon or hadron beam of both charges is available as well as a electron beam with lower intensity. The following section focuses on the muon beam, which is needed for the GPD program.

The SPS accelerates protons to momenta up to 450 GeV/c. Once or twice during a SPS cycle, these protons are extracted onto a fixed beryllium target (T6). The duration of one cycle varies between 33 and 48 s and depends on the number of experiments served by the SPS. The extraction time, which is also called spill, lasts for 4.8 or 9.6 s at the COMPASS experiment. In the reaction of the accelerated protons with nucleons inside the beryllium target, mainly pions are created with a kaon component of about 3.6 %. The intensity of the reaction depends on the thickness of the beryllium, which can be adjusted. After T6, the particles get focused inside a 600 m-long tunnel, where a part of the particles decay by the weak interactions into muons and muon neutrinos: $\pi^+ \rightarrow \mu^+ + \nu_\mu$ and $K^+ \rightarrow \mu^+ + \nu_\mu$ or charge conjugated respectively. The remaining hadron component is stopped by beryllium absorbers at the end of the decay tunnel, while the momentum-selected and focused muon beam is directed through another 250 m-long tunnel leading to the entrance of the experimental hall at ground level. Three 5 m-long dipole magnets (B6) bend

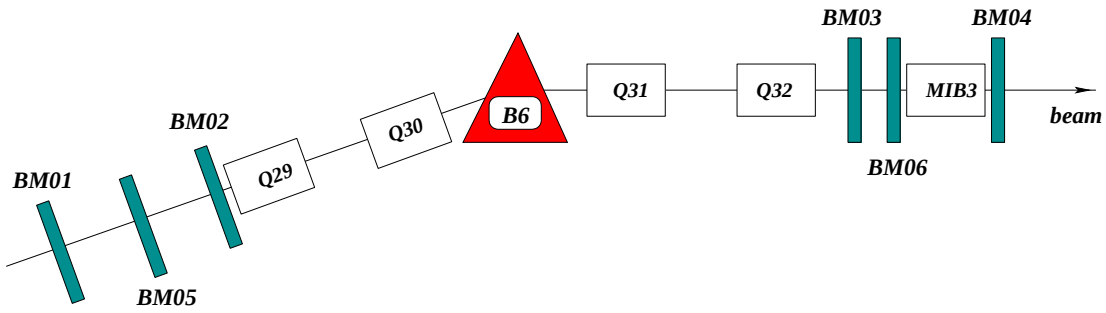

Figure 3.2: Schematic overview of the final part of the M2 beam line including the bending magnet B6 and the beam momentum station BM01-06 [50].

the muon beam and focus it on the target (Fig. 3.2). To maximize the intensity of the muon beam, a momentum deviation of 5 % to the nominal value is accepted. Thus, a precise knowledge of momenta is important. The beam momentum station (BMS), a system of four hodoscopes (BM01 - BM04) and two planes of scintillating fibers (BM05, BM06), is placed up- and downstream of the bending magnets B6 to measure the muon tracks. The momentum can be determined with the known radius of curvature.

In order to study the beam charge asymmetry of the DVCS amplitude, measurements with polarized μ^+ and μ^- beams are performed. The muon beam is naturally polarized due to the nature of parity violation of the pion and kaon decay. A change of sign of the beam charge will also invert the polarization. The degree of polarization depends on the ratio between muon and pion momentum. A polarization of (-80 $\pm$ 4) % can be reached for μ^+ with 160 GeV/c and for decaying particles of 172 GeV/c.

In one spill, up to $2.5{\cdot}10^8$ muons enter the experimental hall. For the GPD measurement, a very precise knowledge of the beam flux and the trajectories of all incoming beam particles is essential. This is accomplished by using scintillating fiber detectors and silicon micro-strip detectors in front of the target.

3.2 The LH_2 Target

In order to study exclusive reactions $\mu p \to \mu' p' \gamma$ in the context of the GPD physics program, a liquid hydrogen (LH_2) target surrounded by a recoil proton detector (see Sec. 3.4.1) is needed. Luminosity depends on the beam flux and the length of the target, which was built with a length of 2.5 m to aim for a luminosity of $10^{32}\,\mathrm{cm^{-2}s^{-1}}$. Due to the transverse size of the μ^+- and μ^- beam profile, the target diameter has a size of 40 mm [52]. The amount of material surrounding the target cell has a strong impact on the lowest possible momenta of the recoiled proton and has been minimized as much as possible to allow protons to escape with a momentum of 260 MeV/c under an angle of 90°. A sketch of the liquid hydrogen target is shown in Fig. 3.3.

A huge challenge is the perfect alignment of the target cell over the full length to reach a maximum homogeneity of the liquid hydrogen and to minimize the amount

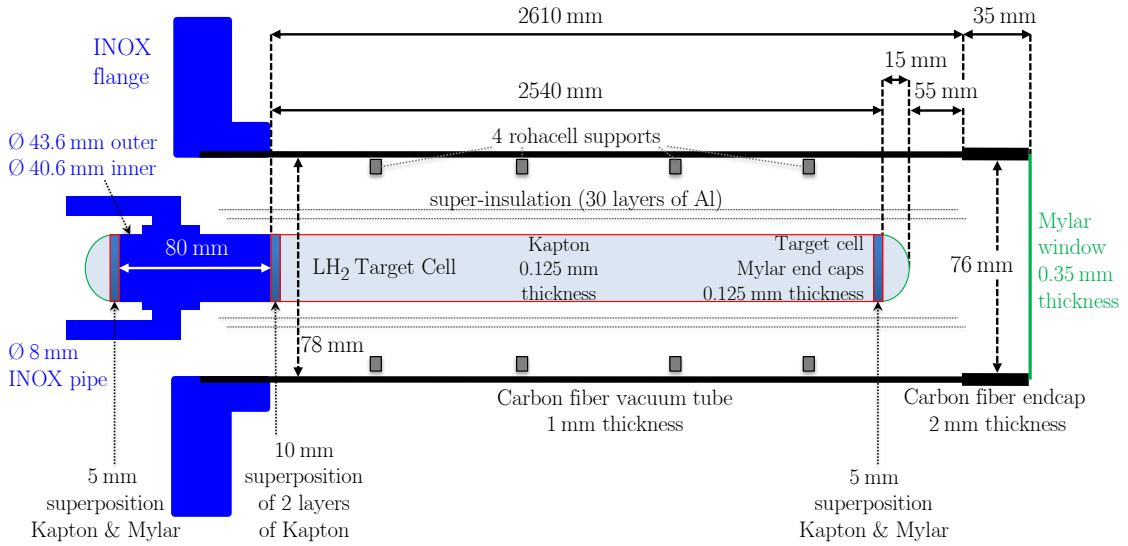

Figure 3.3: Sketch of the liquid hydrogen target (not to scale). Picture adopted from Ref. [52].

of gaseous phase. Following the DVCS pilot run in 2012, the target position and shape was precisely extracted from data using reconstructed vertex positions of deep-inelastic scattering events [53, 54]. This information is important for the data analysis but also for the target description in the Monte Carlo simulation. Especially regarding the simulation of primary vertices a correct target alignment is crucial, as discussed in Sec. 4.2.2.

3.3 Tracking Detectors

The COMPASS-II spectrometer is composed by a large variety of tracking detectors to ensure a precise measurement of particle trajectories. The different detector planes are labeled in Fig. 3.4. Each tracking detector is optimized for its field of application. Detectors in a short distance to the beam axis are exposed to a relatively high radiation dose and particle flux, therefore they need to provide a very good spatial and time resolution. The specification of these detectors differs from the one of the large area tracking detectors, which are installed at a certain distance from the beam axis. The tracking detectors can be separated into three categories:

Very Small Area Trackers

The very small area trackers cover the area near the beam axis up to a radial distance of 2.5 - 3 cm. These detectors need to be radiation hard to resist high particle rates up to $10^5\,\mathrm{mm}^{-2}\mathrm{s}^{-1}$ and they need to have an excellent spatial or time resolution. Scintillating fiber detectors with a time resolution of about 400 ps are in use as well as silicon micro-strip, Pixel-GEM[1] and Pixel-Micromegas[2] detectors with a high spatial resolution.

[1] Gas Electron Multiplier
[2] Micromesh gaseous structure

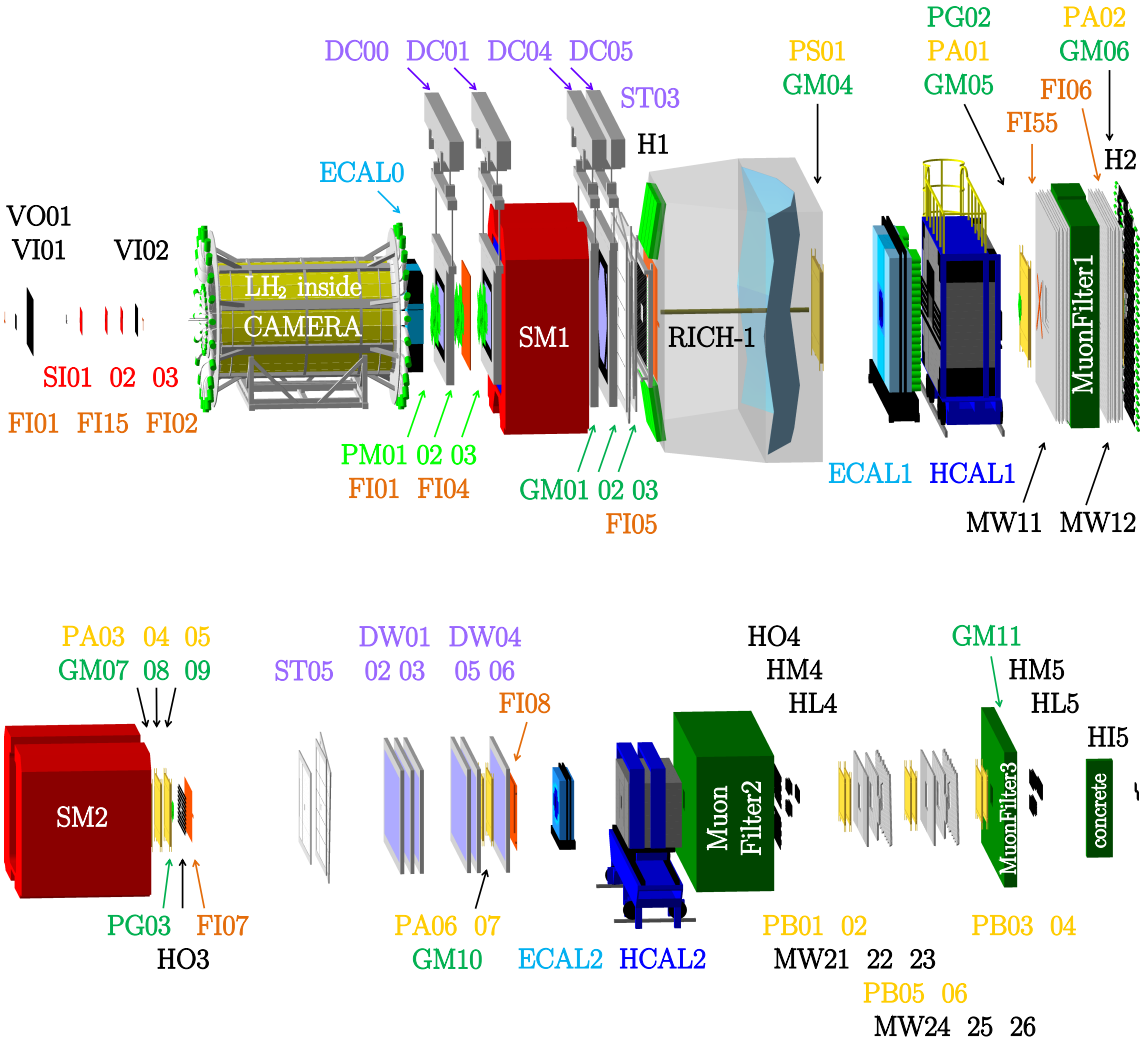

Figure 3.4: Visualization of the LAS (top) and the SAS (bottom) from TGEANT with the labeling of all detector planes. The scales of the two pictures differ. A correctly scaled view of the full COMPASS-II spectrometer with the setup of 2016/17 is shown in Fig. 3.1.

Small Area Trackers

The small area trackers are installed in the intermediate region up to the radial distance of 2.5 - 40 cm. Two types of gaseous detectors are in use here: Micromegas and GEM detectors. They offer a rate stability of up to $10^4\,\mathrm{mm}^{-2}\mathrm{s}^{-1}$ and a spatial resolution higher than 100 µm.

Large Area Trackers

The remaining outer region is covered by the large area drift chambers, the straw detector planes and the multi-wire proportional chambers. Despite the larger wire distances, the large area drift chambers and straw planes reach a good spatial resolution by measuring the drift time.

The small and some of the large area trackers such as the large area drift chambers or multi-wire proportional chambers have a central dead-zone, in which the gas

amplification is disabled, so that they are not not exposed to the very high beam flux. The large area straw detector planes and the muon wall drift chambers, see Sec. 3.4.3, even have a central hole.

3.4 Particle Identification

The COMPASS experiment consists of two spectrometer stages, LAS and SAS, each equipped with a dipole magnet surrounded by a large number of tracking detector planes to measure the trajectories of charged particles with a high redundancy. SM1 and SM2 have an integrated field-strength of 1.0 Tm and 4.4 Tm, respectively. A precise measurement of the radius of curvature allows for a momentum reconstruction but not for a explicit particle identification of all the particles. Especially regarding the exclusive measurement of the DVCS process, the recoiled proton and produced photon need to be detected.

3.4.1 CAMERA Detector

The CAMERA[3] detector, which was newly built for the 2012 DVCS pilot run, is a recoil proton detector. The principle of this detector is based on long scintillator slats forming two concentric rings surrounding the target. This design allows for a time of flight measurement between the two rings as well as a measurement of the energy deposit of recoiled particles. Hence, the inner ring needs to be substantially thinner compared to the outer ring and the support structure needs to be minimized so as not to absorb the particles of interest. The inner ring is shown in Fig. 3.5.

Each ring consists of 24 scintillator elements with light guides and a photo multiplier tube (PMT) readout on both sides. An overview of the dimensions of the

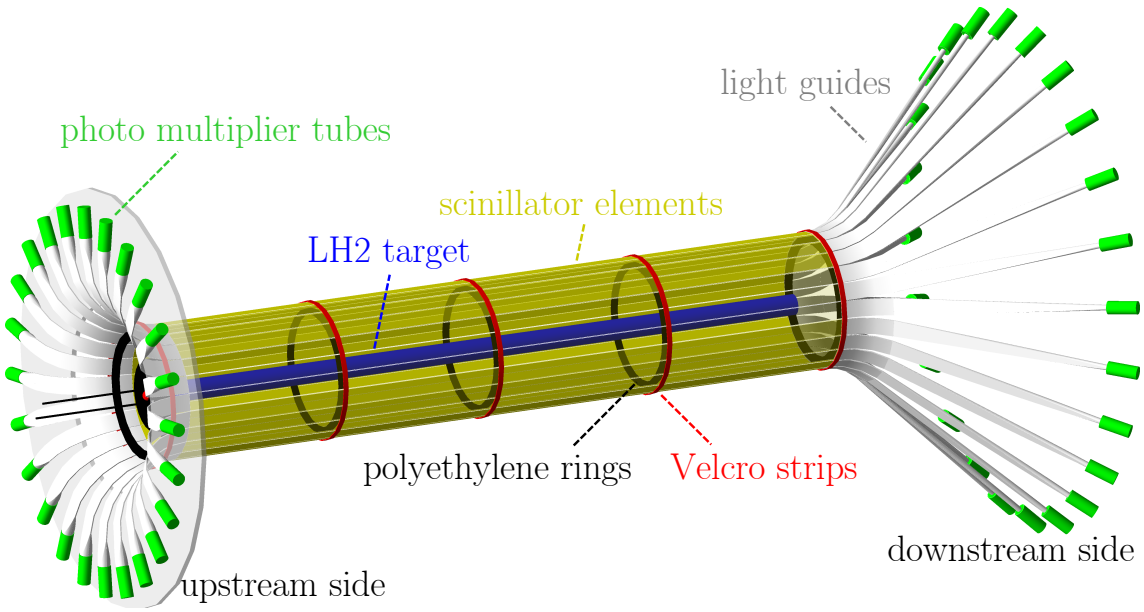

Figure 3.5: The inner ring A of the CAMERA detector with the liquid hydrogen target inside and the mechanical structures for the scintillating slats.

[3]COMPASS Apparatus for Measurements of Exclusive ReActions

Table 3.1: Properties of the CAMERA detector for the inner ring A and the outer ring B.

CAMERA	Ring A	Ring B
Length	275.00 cm	360.00 cm
Thickness	0.40 cm	5.00 cm
Outer trapeze width	6.60 cm	30.28 cm
Inner trapeze width	6.50 cm	28.96 cm
Radius	25.90 cm	114.70 cm
Material	BC408	BC408
PMT	Hamamatsu R10533	ET Enterprises 9823B
Window ∅	51 mm	130 mm
Photo-cathode active ∅	46 mm	110 mm
Time resolution	$\sim$ 380 ps	$\sim$ 175 ps

scintillators is given in Tab. 3.1. Each scintillators cover an azimuth angle of 15°. Both rings are rotated by 7.5° with respect to each other to double the azimuthal angular resolution of the detector. The light guides and PMTs need to be placed outside of the spectrometer acceptance. In particular for the downstream side of the inner ring A, very long light guides with an opening angle of about 45° are used. Due to lack of space on the upstream and downstream side of the CAMERA detector, the PMTs of the outer ring and of the upstream-sided inner ring are mounted orthogonal to the scintillating elements using light guides with a 90° turn.

The two-sided PMT readout also allows for precise measurement of the z position[4] in both rings, which is given by the time difference of the signal measured on the upstream and downstream end of the slat. On account of this, a track reconstruction of recoiled particles is possible if the exact alignment of all 48 scintillator slats in the experimental hall is known. The alignment can be performed using exclusive ρ^0 muoproduction events, $\mu p \to \mu' p' \rho^0 \to \mu' p' \pi^+ \pi^-$. With the help of a kinematic fit, the momentum vector of the recoiled proton can be predicted by the spectrometer measurements of the incoming and scattered muon as well as the two outgoing pions. The predicted momenta are extrapolated to both rings and the intersection points are used to calibrate the measured z positions and azimuthal angles, which are obtained by the pair of slats in the inner and outer ring [55]. The same calibration is also used for the alignment of the CAMERA detector in the Monte Carlo description, where the position and rotation of each scintillator slat is customized.

3.4.2 RICH-1 Detector

A ring imaging Cherenkov detector in the LAS, called RICH-1, serves for the particle identification of charged hadrons. If the velocity of charged particles βc is larger than the speed of light c/n in the local medium with the refractive index n,

[4]The z-axis is defined as parallel to the beam axis.

Cherenkov radiation is emitted under a characteristic angle of $\theta_C = 1/(\beta n)$. Together with a momentum measurement, the particle type can be identified by the measurement of the opening angle of the Cherenkov light cone.

The RICH-1 radiator is filled with C_4F_{10}, which has a refractive index of $n = 1.0015$ at a pressure of 1 atm and a temperature of 25°C. This allows to distinguish between pions, kaons, and protons in the momentum range of 2.5 to 50 GeV/c [56]. The Cherenkov photons that are emitted along the particle's trajectory get reflected by two spherical mirrors and thereby focused as a ring on the readout detectors (Figure 3.6). The radius of the ring correlates with the opening angle of the light cone. In the central part, where the photon rate is higher, multi-anode photo multipliers are in use. Multi-wire proportional chambers with Caesium iodide photocathodes and Thick-GEM detectors are used for the outer part of the readout.

3.4.3 Muon Identification

To separate muons from other particles, so-called muon wall (MW) detector systems are installed at the end of each spectrometer stage. Each MW consists of a large absorber, namely MF1 and MF2, surrounded by several tracking detector planes. These muon filters absorb all particles except the weak interacting muons.

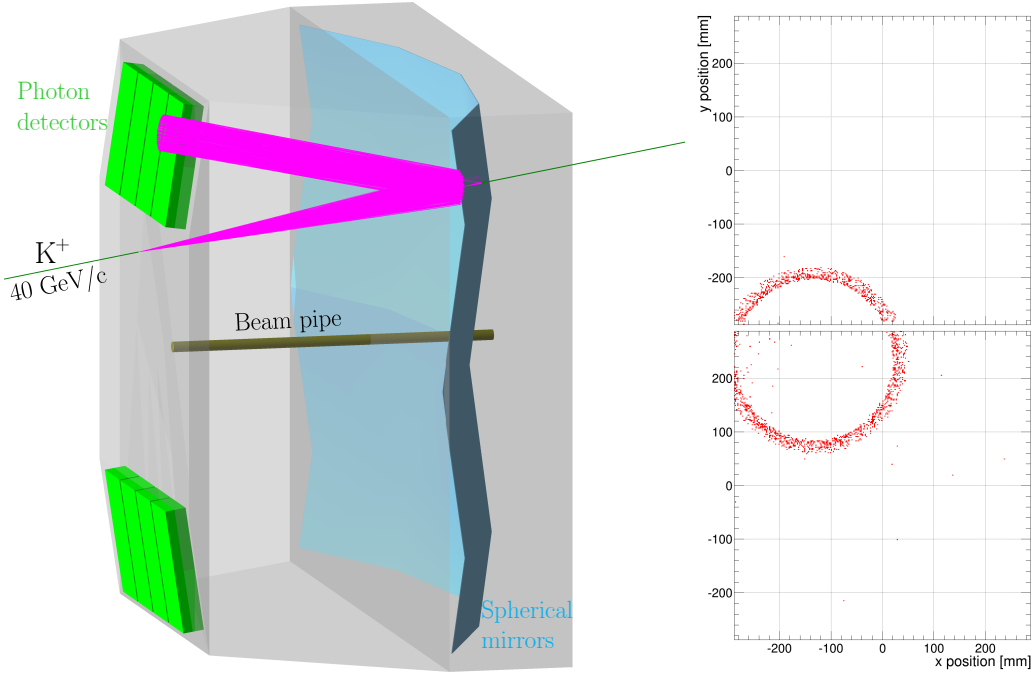

Figure 3.6: Visualization of the RICH-1 detector (left side). In this TGEANT example simulation, a K^+ with a momentum of 40 GeV/c emits Cherenkov radiation in the RICH-1 radiator filled with C_4F_{10}. These photons are reflected by the spherical mirrors to the photon detectors on the upstream side of the detector. The two affected readout channels show the expected circular structure (right side). Note that the detector efficiency was not considered in this simulation. The beam pipe in the center of the RICH-1 radiator is filled with helium to avoid Cherenkov radiation from unscattered beam particles.

Measured particle trajectories that are reconstructed in front of the absorber and behind can be identified as muon tracks.

MW1 is placed at the end of the LAS, directly in front of the second dipole magnet SM2. It consists of a 60 cm thick iron absorber placed between two detector stations. Each station has four drift chambers which are aligned alternately horizontally and vertically. The detector planes and the absorber have a central hole in order not to affect particles that are produced under small angles and detected in the SAS. MW2 is installed at the end of the second spectrometer stage and includes a 2.4 m-thick concrete absorber with several drift and multi-wire proportional chambers behind.

3.4.4 Calorimeters

For the determination of the particle's energy, electromagnetic (ECAL1 and ECAL2) and hadronic (HCAL1 and HCAL2) calorimeters are installed in both spectrometer stages. ECAL1 and ECAL2 are respectively placed in front of HCAL1 and HCAL2. The detection and energy measurement of the outgoing photon in an electromagnetic calorimeter is essential for the measurement of the DVCS process. To enlarge the angular acceptance, a third electromagnetic calorimeter (ECAL0) is installed between the target area and the first dipole magnet SM1. This detector was newly built for the GPD program in the course of the COMPASS-II extension. For the 2012 pilot run, a smaller version of the original design was used, as illustrated in Fig. 3.7.

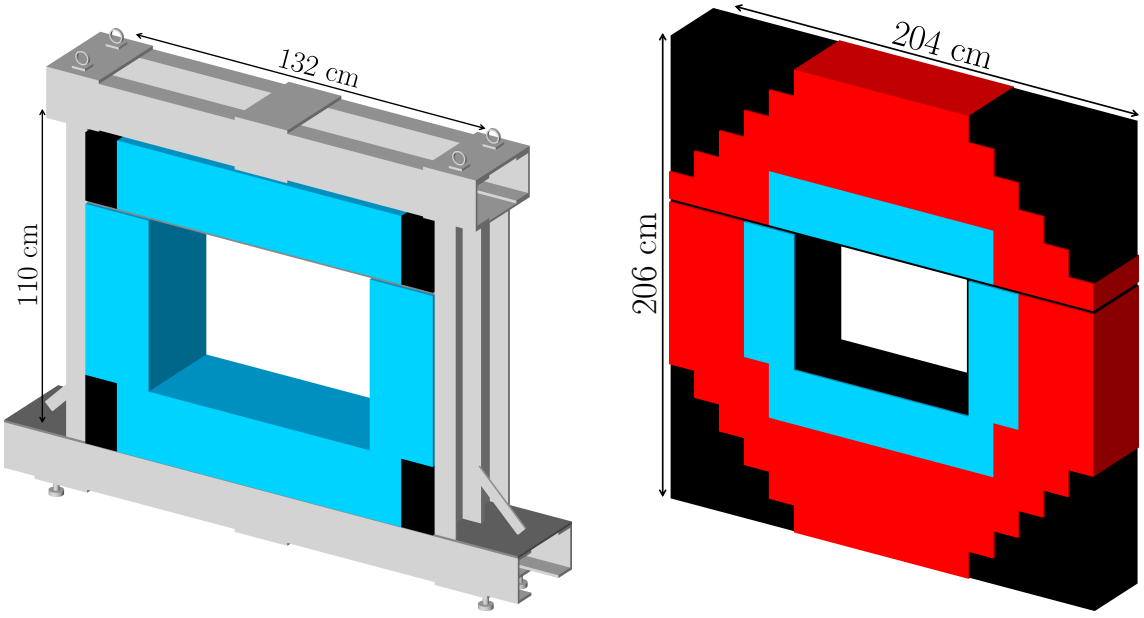

Figure 3.7: Visualization of the electromagnetic calorimeter ECAL0 in 2012 and 2016/17. Left: Small version of ECAL0 used in 2012 with 564 modules. The black-colored modules in the four corners (3×6 modules) were installed without readout. Right: The full size ECAL0 with 1746 modules in total. The modules in light blue color represent the smaller version of 2012, while the modules illustrated in red were added for the DVCS measurement in 2016/17. The black-colored plates are part of the mechanical structure.

The calorimeters are composed of several modules. The number of all modules and their different types are listed in Tab. 3.2. The electromagnetic calorimeter cells are mainly built of lead glass. The interaction of high-energy photons, electrons, or positrons with the lead glass material creates a cascade of secondary particles via electron-positron pair production and bremsstrahlung. The former process is triggered by the photons and the latter by the charged electrons and positrons, which can have a velocity faster than the speed of light c/n in the lead glass material. The emitted Cherenkov photons are detected at the downstream side of the module using a photo multiplier. The intensity of the radiation is proportional to the energy loss of the initial particle and therefore allows an energy measurement. Beside the lead glass modules, several Shashlik modules are installed close to the beam axis. These modules are built as sampling modules, with alternating layers of lead and plastic scintillator, which makes them more radiation resistant. ECAL1 and ECAL2 with the arrangement of the different module types are shown in Fig. 3.8.

The hadronic calorimeters are also composed of sampling modules, but with alternating layers of iron and scintillator. When a high-energy hadron strikes the calorimeter, other hadrons are created due to inelastic scattering off the absorbing material layers so that a hadronic shower results. The important scale characterizing the range of the hadronic shower is the nuclear absorption length, which is significantly greater than the radiation length characterizing the electromagnetic calorimeters. Consequently, the modules of the hadronic calorimeters are built larger than electromagnetic ones. The energy measurement is carried out by the detection of the scintillating light produced in the scintillating layers. The light is guided through optical fibers to the photo multipliers installed at the downstream side of the modules.

3.5 Trigger System

Due to the high luminosity, the COMPASS-II experiment needs to handle huge data rates. A continuous detector readout and data recording is not possible, thus a trigger system is essential to select physically interesting events already on hardware level. The time allowed for the trigger decision is limited to about 1.8 µs, due to the fact that the readout buffers on the front-end electronics is limited. The event reference time together with a synchronous experiment clock is transmitted by a dedicated trigger distribution system.

The trigger system is based on the fast signals of hodoscopes, on the energy measurement of the calorimeters, and on a veto system around the incoming beam axis. The different elements of the trigger system are logically combined to select events depending on the kinematics of the reaction.

3.5.1 Hodoscope Trigger

The COMPASS-II experiment is designed to cover a large range of momentum transfer Q^2. Several pairs of trigger hodoscopes are installed in the experimental hall, all of them cover a specific kinematic region. The layout of the different trigger hodoscopes is shown in Fig. 3.9.

Table 3.2: Electromagnetic and hadronic calorimeters in the COMPASS-II setup.

Calorimeter	Module type	Module material	Module size / cm^2	Module numbers
ECAL0 2012	Shashlik	polystyrene/lead	3.96×3.96	564
ECAL0 2016/17	Shashlik	polystyrene/lead	3.96×3.96	1746
ECAL1	Shashlik	polystyrene/lead	3.82×3.82	232
	Gams	TF1	3.82×3.82	584
	Mainz	SF57	7.50×7.50	572
	Olga	SF5	14.3×14.3	320
				Σ 1708
ECAL2	Shashlik	polystyrene/lead	3.82×3.82	764
	GamsRH	TF1	3.82×3.82	768
	Gams	TF101	3.82×3.82	1440
				Σ 2972
HCAL1	Sampling	polystyrene/iron	14.60×14.20	480
HCAL2	Sampling	polystyrene/iron	19.95×19.95	216

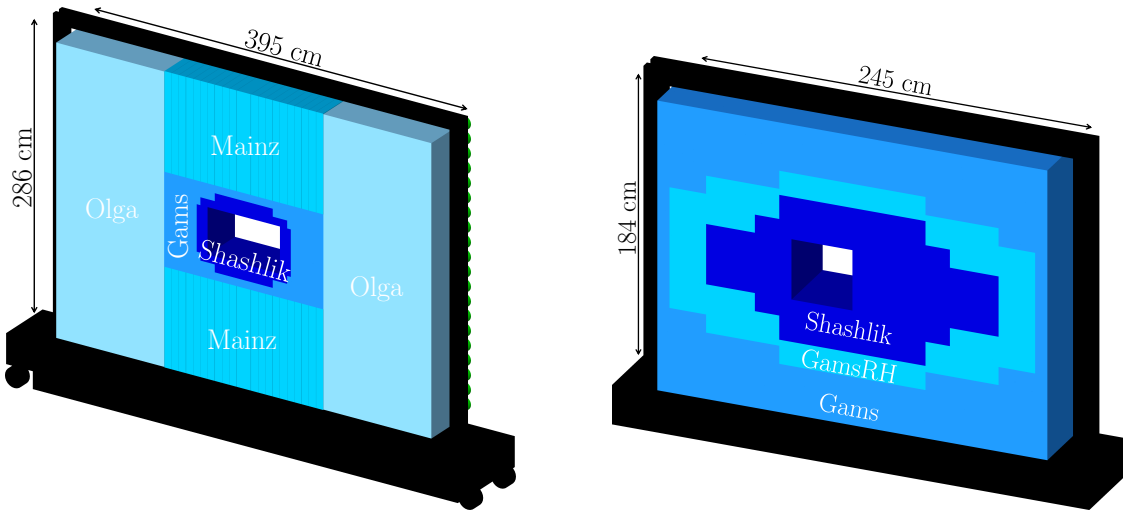

Figure 3.8: Visualization of electromagnetic calorimeters ECAL1 (left) and ECAL2 (right) from TGEANT. The different shades of blue represent the arrangement of the different module types. The central hole for ECAL2 is shifted by 19.15 cm towards the bending direction of the dipole magnets to allow for the unscattered beam to pass without interaction.

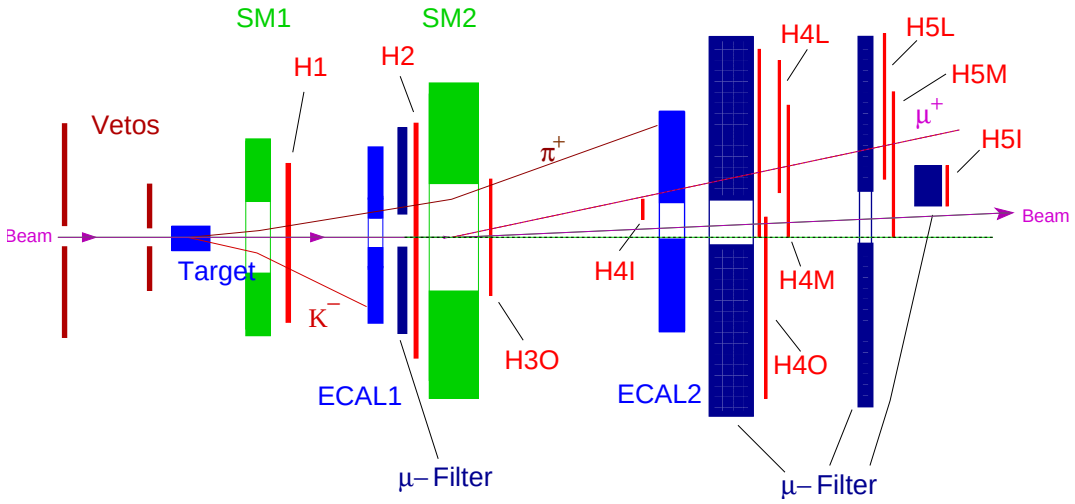

Figure 3.9: Schematic overview of the relevant components of the trigger system [39].

The trigger decision for events with a large $Q^2 > 10\,(\mathrm{GeV/c})^2$ is activated by the detection of the scattered muon. These events are mainly triggered by the outer trigger (OT, hodoscopes H3O and H4O) or the large angle spectrometer trigger (LAST, hodoscopes H1 and H2). These hodoscopes are built of horizontal aligned scintillator slats, which can measure the vertical position of the muon trajectory. The vertical position at the two hodoscope stations at different z positions can be combined to extrapolate the muon track to the target region in the non-bending plane of the two dipole magnets. A coincidence matrix is connected to the trigger system to select combinations that are triggered by muon tracks originating from the target.

At small Q^2, the muons are only slightly scattered during the interaction. In that case, the target pointing method explained above is not feasible. These events are triggered by the ladder trigger (LT), middle trigger (MT) or inner trigger (IT), which are built of vertically aligned hodoscopes to measure the horizontal position of the muon trajectory. The trajectory goes in the same direction as the bending of the two dipole magnets and therefore, a measurement of the energy loss of the scattered muons is possible. Again, a coincidence matrix accounts for all muon tracks originating from the target. An optional feature of some of the small Q^2 triggers is the coincidence with an minimal energy loss in one of the electromagnetic or hadronic calorimeters. This principle is visualized in Fig. 3.10.

To reduce the non-muonic background, the hodoscope stations H4 and H5 are installed behind the muon filters MF2 and MF3. For the DVCS measurement, the important triggers for the exclusive event selection are MT, LT, OT, and LAST without any restrictions on the energy loss in the calorimeters. To increase and optimize the trigger efficiencies for DVCS events, the trigger system and coincidence matrices have been extended and adjusted in preparation for the long DVCS run in 2016/17. This was based on Monte Carlo simulations presented in Chapter 6.

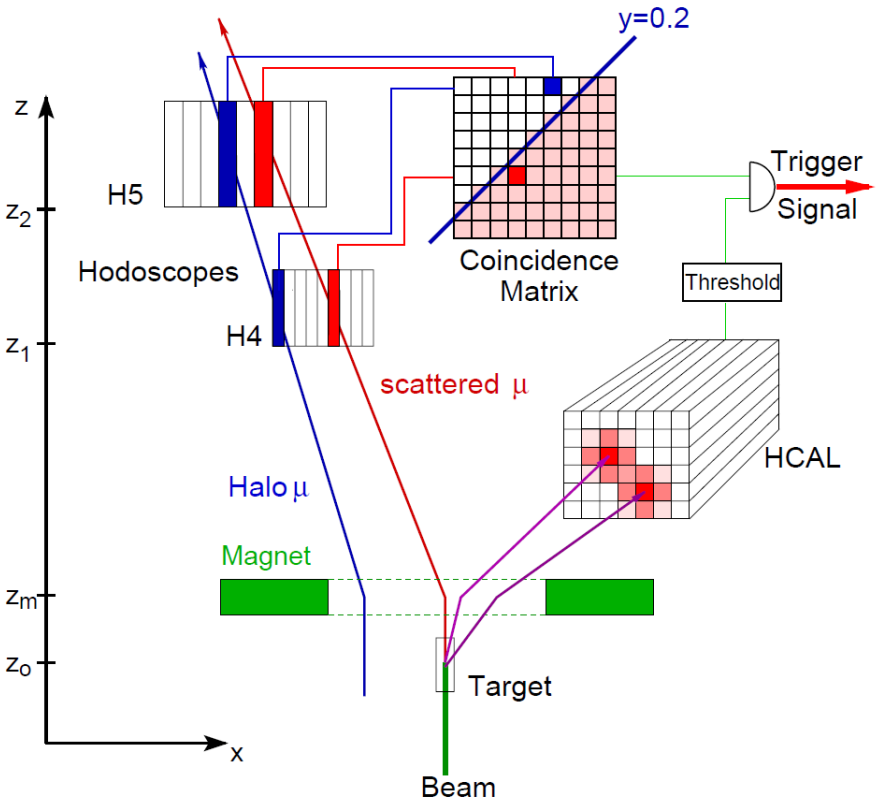

Figure 3.10: Trigger logic for small Q^2 by measuring the energy loss of the scattered muon. The channel combination triggered by a scattered muon originating from the target (red line) is accepted by the coincidence matrix, while the channel combination of a halo muon (blue line) is not. In addition, an energy loss in one of the calorimeters can be forced [57].

3.5.2 Veto Trigger

The muon beam entering the experimental hall has a non-negligible transverse spread, a divergence and a strong halo component. Halo muons do not intersect with the target but may fly through the hodoscope stations and release a trigger. These events are undesired and need to be excluded by a veto system. Three stations of scintillation counters are therefore installed upstream of the target to detect the intense near-beam halo muons, see in Fig. 3.9. The beam muons fly undisturbed through the central holes of the veto counters towards the target.

3.5.3 Proton Trigger

As described in Sec. 3.4.1, the CAMERA detector was installed for the DVCS measurement to detect recoiled protons. The proton trajectory and momentum can be reconstructed by the hit positions in the two barrels and by a time of flight measurement. The integral over the signal strength in the PMTs at both ends of the scintillator is proportional to the energy loss of the crossing particle. In certain kinematic regions, this allows to distinguish between recoiled protons and background events caused by recoiled pions or delta electrons. Figure 3.11 shows a TGEANT Monte Carlo simulation for recoiled protons and pions. The energy loss

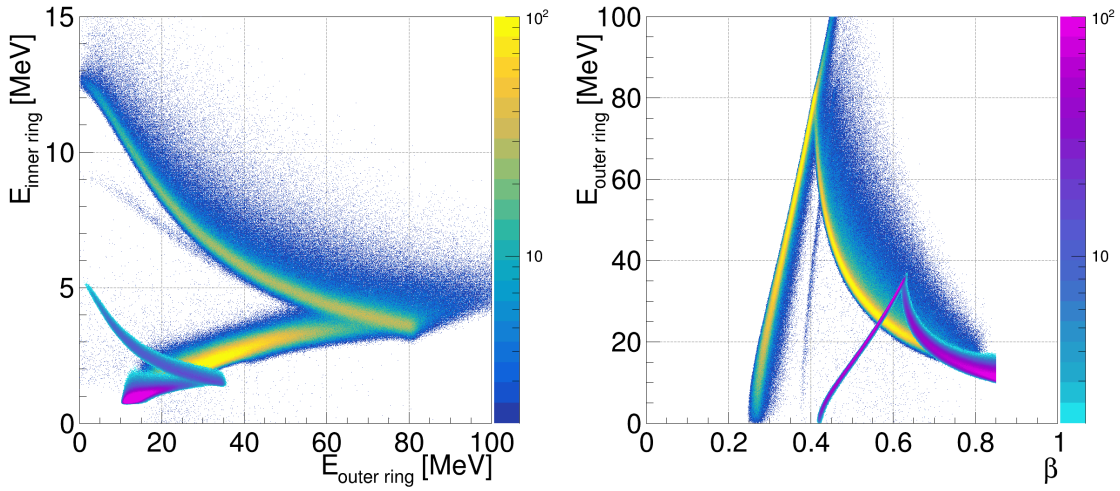

Figure 3.11: TGEANT simulation of recoiled protons and pions that are detected in the CAMERA detector. Left: Energy loss in the inner ring A in correlation with the energy loss in the outer ring B. Right: The energy loss in the outer ring as a function of the velocity at the vertex position inside the liquid hydrogen target. The yellow-colored entries (corresponding to the left-hand side color axis) label the intensity of recoiled protons, generated by the DVCS generator of HEPGen++ [45]. The pions are represented by the violet-colored entries (right-hand sided color axis), generated with a polar angle of 90°. Effects of the mechanical structure, cf. Fig. 3.3 and 3.5, are also slightly visible for the recoiled protons if they traverse the Velcro strips of the inner ring or the rohacell supports of the target.

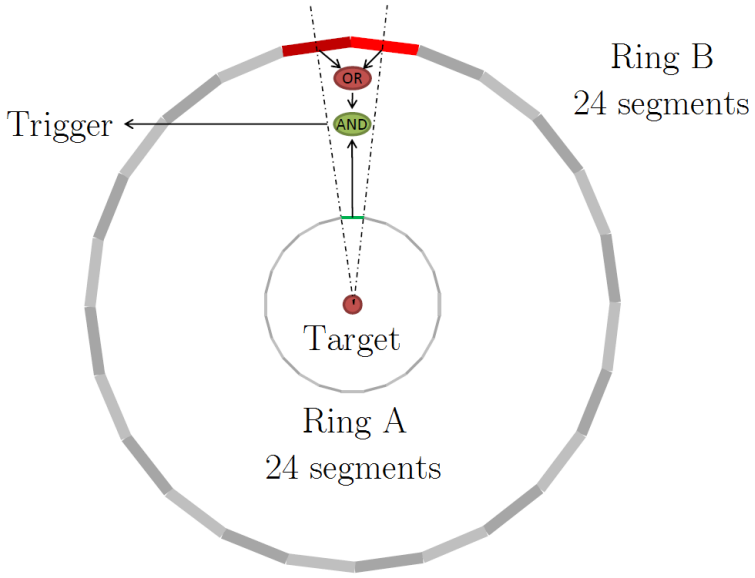

Figure 3.12: Geometric proton trigger principle for a recoiled particle originating from the target. Picture adopted from Ref. [58].

of charged particles in ring A and ring B show significant correlations. Only those events are shown in which the recoiled particle crosses the inner and reaches the outer ring. The same Monte Carlo sample can also be used to plot the energy loss of protons and pions in the outer ring versus the velocity at the vertex position inside the liquid hydrogen target.

This allows to disentangle the proton signal from background in specific kinematic regions. Obviously, the geometric correlation needs to be considered as well, as depicted in Fig. 3.12. A particle track coming from the target can be reconstructed by the correlation of a signal in ring A and in one of the two correlated segments in ring B. Thus, six readout channels are involved in the proton trigger logic for each segment.

Such a recoil proton trigger is only made possible by the use of fast readout electronics. The readout of the 96 PMTs in the CAMERA detector is carried out by 12 GANDALF[5] modules. A TIGER[6] module is used to create the trigger signal.

3.6 Data Acquisition and Reconstruction

3.6.1 Readout and Data Acquisition

The data acquisition system (DAQ) at COMPASS needs to handle more than 250,000 detector channels at trigger rates up to 100 kHz. The analog detector signals are digitized by TDC[7] or ADC[8] units on the front-end boards or directly on the GANDALF or CATCH[9] readout cards. The signals of the GEM and silicon detectors are digitized using the GeSiCA[10] modules.

The data is transferred via optical fibers to FPGA[11] multiplexing cards, where the data can be buffered for one spill. On this stage, the data from the front end boards is buffered and merged into sub events. A FPGA switch distributes these sub events to the multiplexer slaves. These online computers build the final raw-data events and finally transfer them to CASTOR[12] to write them on magnetic tapes [60]. A simplified scheme of the DAQ system is shown in Fig. 3.13.

3.6.2 Data Reconstruction for Real Data and Monte Carlo

For data analysis, the raw-data events saved on CASTOR are processed by the reconstruction software CORAL[13]. The resulting mini data summary trees (mDST files) can finally be analyzed with PHAST[14] [61].

[5] Generic Advanced Numerical Device for Analog and Logic Functions [58]
[6] Trigger Implementation for GANDALF Electronic Readout [59]
[7] Time to Digital Converter
[8] Analog to Digital Converter
[9] COMPASS Accumulate, Transfer and Control Hardware
[10] GEM and Silicon Control and Acquisition
[11] Field Programmable Gate Array
[12] CERN Advanced Storage
[13] COMPASS Reconstruction and Analysis Program
[14] Physics Analysis Software Tools

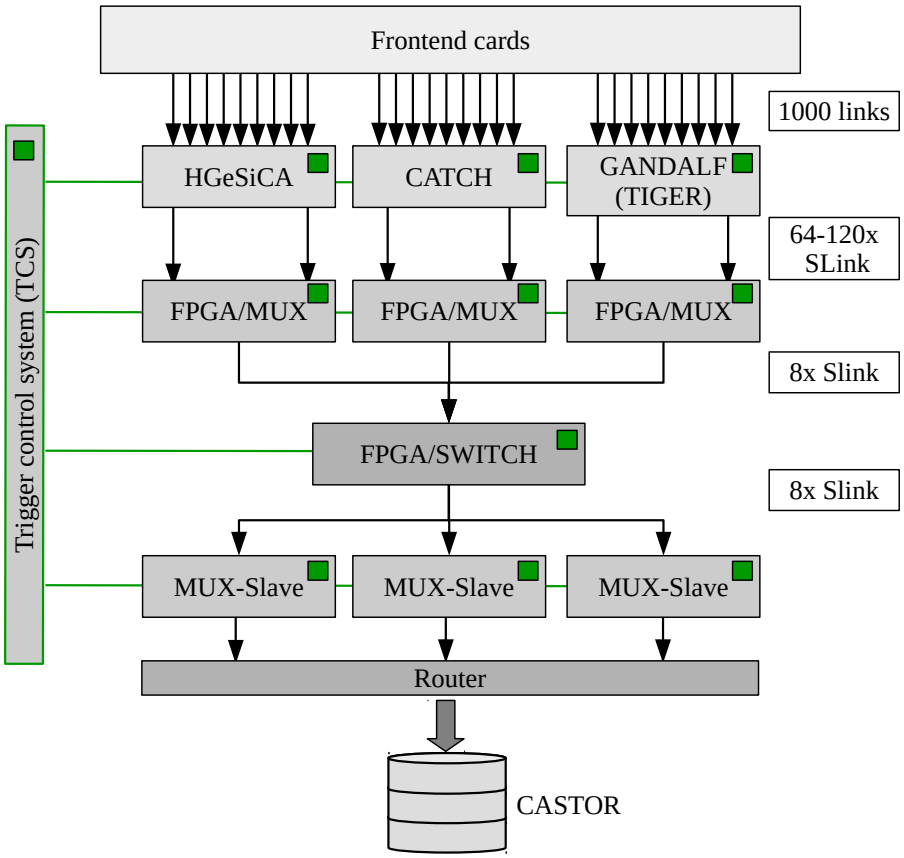

Figure 3.13: A simplified scheme of the readout and data acquisition at the COMPASS-II experiment since 2015. The green boxes mark the components that receive the trigger signal from the TCS [45].

The raw-data events contain binary detector information, such as channel numbers that correspond to certain wires of a detector instead of hit positions in the experimental hall. In this example, the hit positions are the important quantities, so the detector information needs to be decoded first. This is done by the DAQ data decoding (DDD) library. All wire detectors in the COMPASS spectrometer consist of several detector planes. Each plane is rotated with respect to the others, which allows for a hit reconstruction in the detector reference system. Signals on wires that belong to the same hit position in the detector reference system are combined to a cluster. The detector positions are known from specific alignment runs and therefore, a cluster describes a hit position in the experimental hall with a given time stamp. When dealing with calorimeters, the measured signal amplitudes have to be converted to an amount of energy.

The event reconstruction is performed using all cluster information given by the tracking detectors. In the first iteration of track finding, the spectrometer is roughly subclassified into sections with only a slight influence of the magnetic fields. Here, a special Kalman filter algorithm searches for linear segments of particle tracks. Afterwards, the reconstruction algorithm tries to bridge these linear segments through the magnetic fields of the two dipole magnets. Each particle track can be associated with charge and momentum, using the bending direction and curvature in the mag-

netic fields. Particle tracks are also assigned with the sum of traversed radiation lengths, which is used to identify muons. A conclusion about the particle identification for all non-muonic tracks is not yet possible on this stage of the reconstruction. To account on this, measured Cherenkov photons in the RICH-1 detector need to be combined with information on the particle's momentum.

Incoming beam particles are reconstructed using the momentum information given by the BMS detectors and the spatial knowledge obtained from the silicon detectors upstream of the target. Vertices are defined as intersection points of one incoming and one or more outgoing particles. A vertex fitting algorithm is used to find intersections between the reconstructed spectrometer tracks that are extrapolated in upstream direction towards the target area. Each vertex contains information about its position in the experimental hall and all associated particle tracks. A vertex does not necessarily need an associated incoming particle, e.g. a vertex of a decaying K_S^0 is only reconstructed by two outgoing charged tracks. However, a vertex is called primary if its associated incoming particle is part of the beam.

Calorimeter clusters are reconstructed separately using the energy deposit in the different cells. For all calorimeters, a simplified summation algorithm, dubbed Kolosov summation, or a shower fitting algorithm, called Lednev reconstruction, are available. For a better reconstruction of spatially close particle showers in ECAL2, a sophisticated shower fitting algorithm based on the Lednev parameterization is used [62]. In 2012, the Kolosov summation was used for all other calorimeters. Reconstructed calorimeter clusters are associated with (charged) particle tracks in case cluster position and the extrapolated particle track intersect. Consequently, uncorrelated calorimeter clusters originate from neutral particles, such as photons.

After the event reconstruction, all vertices, particle tracks, calorimeter clusters, and RICH information are saved in a mDST file. All raw-data digits measured by the CAMERA detector are stored in addition, since this detector can only be calibrated after the event reconstruction. For the analysis, these raw-data digits are accessed in PHAST to reconstruct recoiled particles tracks in the CAMERA detector.

A very important feature of the COMPASS reconstruction software is the simultaneous use of the software for real data and Monte Carlo events. This excludes systematic uncertainties induced by the event reconstruction. The data flow in both cases is presented in Fig. 3.14. The transferred Monte Carlo information is described in detail in the following chapter. Depending on the detector type, tracking detector hits are digitized and transformed into clusters. At first detector-dependent energy cuts are applied to refuse all low energy Monte Carlo hits that would not result in a measurable signal in the real detector. Afterwards, an acceptance probability for all hits in wire detectors is calculated using the distance of the Monte Carlo hit to the closest detector wires – e.g. a hypothetical Monte Carlo hit in the central hole of a detector would be rejected. A very important element of the Monte Carlo clustering is the smearing of hit position and time stamp according to the time and spatial resolution of the detector. The Monte Carlo clustering for the calorimeter information is described in Chapter 5. All resulting hits and calorimeter clusters are finally processed in the same way as for real data. An additional storage of original

Monte Carlo information, such as detector hits or particle tracks, makes the only difference to real data mDST files.

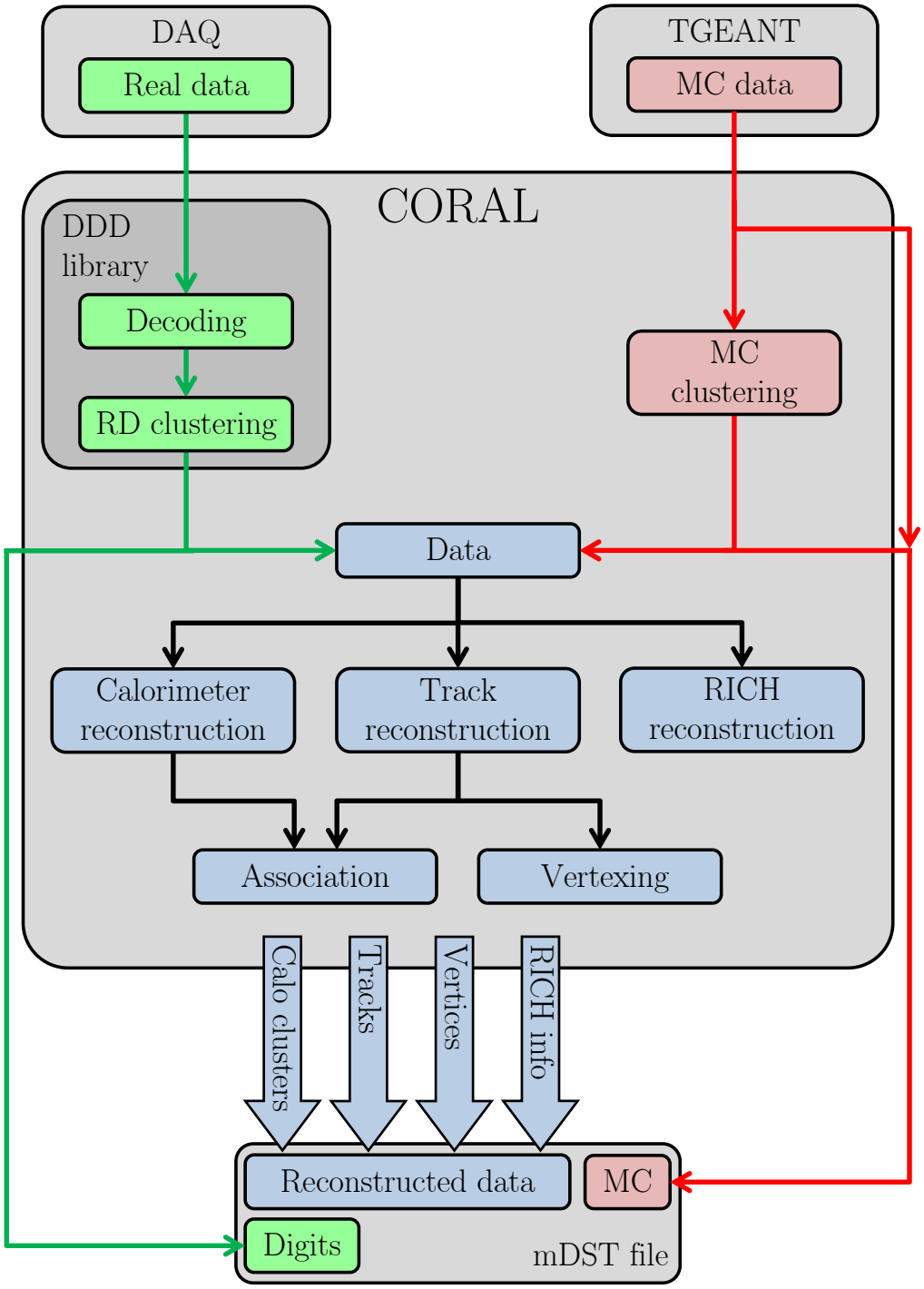

Figure 3.14: Data flow in the COMPASS-II reconstruction software CORAL for real data (green) and Monte Carlo (red). Picture adopted from Ref. [45].

4. TGEANT Monte Carlo Software

Monte Carlo simulations are essential for the analysis of exclusive reactions as measured for the COMPASS-II GPD program. A new Monte Carlo software has consequently been developed and implemented in the COMPASS Monte Carlo chain.

This chapter offers an overview of the new Monte Carlo software package named TGEANT. This software is developed in object-oriented C++ and based on the Geant4 toolkit. TGEANT has extended the basic framework of Geant4 in order to simulate all aspects of the COMPASS-II experiment. A detailed insight into the event simulation is given, including the beam simulation, the realistic vertex generation, and the usage of different event generators. The concepts of sensitive detectors and particle trajectories are further explained. The output of the simulation software, as well as geometry and alignment files are integrated in the reconstruction software and have already been used for a full Monte Carlo production with regard to the analysis of the 2012 DVCS pilot run.

In the first place TGEANT was developed for the GPD program but has been extended so that it can cover all COMPASS physics programs. The concept of application programming interfaces ensures a highly flexible design. The software package also includes a graphical user interface for a simplified usage of TGEANT and a Toolbox, which is used to directly analyze the Monte Carlo output. The latter is extremely useful for any kind of Monte Carlo studies.

4.1 Software Package

The physics program of the COMPASS-II experiment is dedicated to high precision cross section measurements. The measured data is a convolution of physics signals with background contributions and effects related to the experimental acceptance. These effects are introduced by the geometry of the experimental apparatus and by the reconstruction algorithms. The extraction of physics signals requires an extensive knowledge of experimental acceptance and estimations of background effects, which both can only be obtained by Monte Carlo. The contribution of different processes needs to be studied with different event generators and models.

To perform a full Monte Carlo simulation, several aspects need to be taken into account. For a fixed target experiment working with secondary or tertiary beams, such as the COMPASS experiment, an accurate description of the beam phase space is essential to reproduce effects present in real data. While for the simulation of the primary physical interaction a dedicated event generator is used, the transport of all secondary particles through the experimental apparatus and the simulation of their interactions with material and of the detector response is carried out by the Monte Carlo software. The new Monte Carlo software for the COMPASS-II experiment is called TGEANT and makes use of the Geant4 toolkit, which is introduced in Appendix A. The acronym Geant4 stands for "Geometry And Tracking" and is a framework for the simulation of the passage of particles through matter [63–65].

The goal of TGEANT is to simulate the response of the experimental setup for a physical process one wants to study. Basic requirement is an accurate geometry description of the experimental apparatus as presented in the preceding chapter. The implementation of particles and physical models is necessary to simulate the physical interactions of particles with matter and the particle transportation. Geant4 offers data bases, which comprise a huge field of applications for all kinds of particles and processes. In TGEANT, the list of physical processes and particles is optimized to the kinematic range of the COMPASS-II experiment.

TGEANT is delivered in a software package with four other sub-packages, namely the graphical user interface and the Toolbox, both introduced in Sec. 4.5.4 and 4.5.5, as well as the two libraries libSettings and libEvent, which are needed for the data exchange between the different packages. The whole project is maintained in a Git repository on a CERN server. The interplay of the different software packages is presented in Fig. 4.1. As an input, the simulation software TGEANT reads a setup file using the library libSettings. Such a setup file, which relies on the XML[1] format, can be easily created with the graphical user interface. This setup file contains all information TGEANT needs to work with, such as the target and detector alignment or all options related to the beam simulation and primary vertex generation. TGEANT runs the event loop simulation and writes the output on a disk with the help of the event library libEvent. The default file format features a gzip-compressed ASCII file. The TGEANT output files can be either used in CORAL or in the Toolbox. The former case is the standard way of the Monte Carlo reconstruction, while the Toolbox is used particularly with regard to detector studies and tuning.

[1] Extensible Markup Language

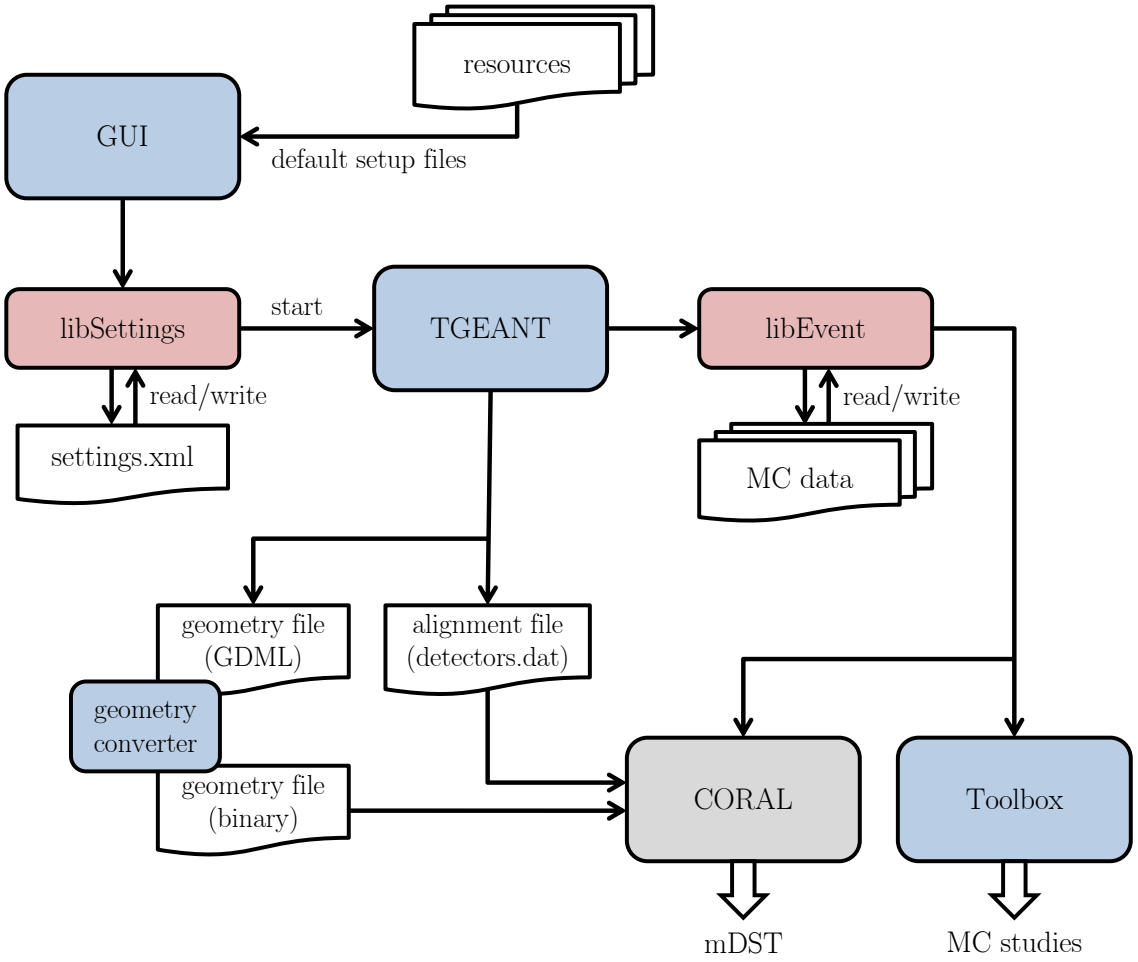

Figure 4.1: Flow chart of the TGEANT software package. The simulation software TGEANT is controlled by a setup file, which is easily created with the graphical user interface. The GUI can draw on different default setup files from the resources folder. The output files can either be analyzed with the Toolbox for the purpose of Monte Carlo studies or processed by CORAL in order to produce mDST files. For the latter case, TGEANT also provides the alignment and geometry files.

4.2 Event Simulation

The event loop in TGEANT is a major part of the simulation software. In a nutshell, one or more so-called primary particles are placed with a given momentum vector in the world volume. After the initialization phase, the event loop is started and primary particles are tracked by the Geant4 algorithm through the experimental setup. During the event loop, new particles can only be created by implemented physical processes. The processes are applied according to their cross sections. Once the event loop has ended, the output of simulated detector responses is processed and saved to disk. The flow chart of the event loop in TGEANT is illustrated in Fig. 4.2.

The following subsections focus on the event loop simulation of the DVCS setup using a muon beam. TGEANT is also able to simulate hadron beams as discussed in Sec. 4.3.

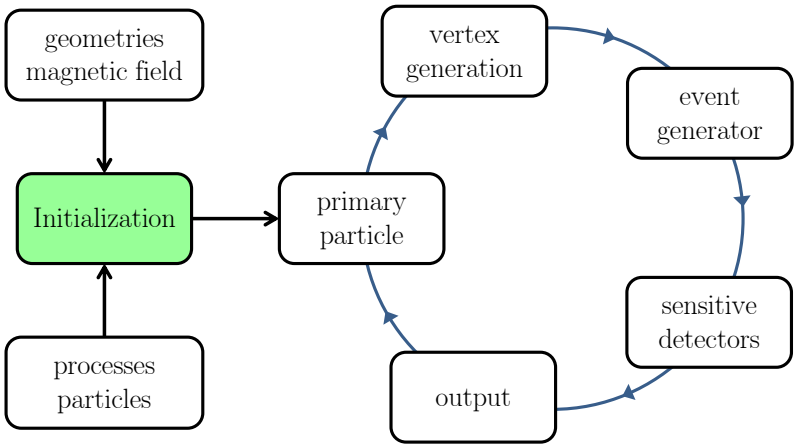

Figure 4.2: Flow chart of the event loop in TGEANT.

4.2.1 Beam Simulation

Regarding the DVCS measurements, delta electrons emitted by the beam muons are the main source of background in the CAMERA detector. A correct simulation of these delta electrons is mandatory. The event loop starts therefore with the incoming beam particle, which is placed at the entrance of the experimental hall. The default position for the DVCS setup is at $z = -9.0\,\mathrm{m}$, but any other position is equally possible as long as it is upstream of the first detector plane[2,3]. In the experiment, the incoming beam particles have a transverse spread and a momentum deviation to the nominal value to maximize the intensity of the muon beam. This is considered in the so-called beam file. The spatial and energy distribution of the μ^+ beam file of 2012 is presented in Fig. 4.3. The beam file contains a binary stream of entries describing the full phase space of a huge number of beam particles, which have been measured in the experiment. Apart from header and footer flags, the beam file contains five entries $x_1 \ldots x_5$ to describe the phase space for each beam particle:

$$\begin{aligned} x &= x_1 \cdot \mathrm{mm} \\ y &= x_2 \cdot \mathrm{mm} \\ s_x &= \sin(x_3 \cdot 10^{-3}) \\ s_y &= \sin(x_4 \cdot 10^{-3}) \\ E_{kin} &= x_5 \cdot \mathrm{GeV} \\ \vec{p} &= \frac{E_{kin}/\mathrm{c}}{\sqrt{1 + s_x^2 + s_y^2}} \begin{pmatrix} s_x \\ s_y \\ 1 \end{pmatrix} \end{aligned} \tag{4.1}$$

The momentum $\vec{p}$ and transverse position coordinates x and y are given by the beam file, but not the z position, which needs to be handed over as a convention.

[2]Technically, TGEANT also allows to start the beam particle downstream of the first detector planes. But the signals of these detectors are required in CORAL to reconstruct the beam trajectory.

[3]The 2.5 m long LH_2 target cell was centered at $z = -1.95\,\mathrm{m}$ in 2012.

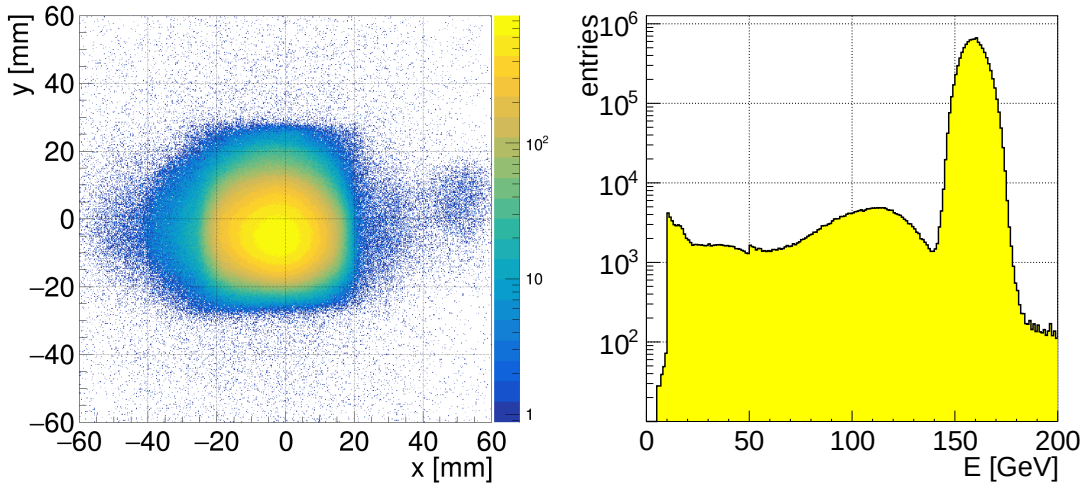

Figure 4.3: Spatial and energy distribution of the 2012 beam file for the μ^+ beam. This beam file has 10^7 entries.

When creating a beam file, reconstructed tracks of beam particles from real data are extrapolated to a given z position. The beam particles are divergent and bent by the dipole magnets. The knowledge of the used z position is therefore very important. For a muon beam the convention $z = 0\,\mathrm{m}$ is normally used. The complete documentation of the beam file format can be found in Appendix B.4. At the beginning of the first event loop, the beam file is loaded. To exploit the full size of the beam file, the beam particle for the first event is randomly chosen, all others follow consecutively.

Extrapolation of Beam File Particles

The primary beam particle is started upstream of the first detector plane and therefore needs to be extrapolated from the beam file position ($z = 0\,\mathrm{m}$) to the beam starting position ($z = -9\,\mathrm{m}$). This is done by a stepping algorithm implemented in the *T4Extrapolate* class. The step size was chosen as $s = 1\,\mathrm{mm}$. Even in the case of an unpolarized target, the magnetic field of the first dipole magnet SM1 cannot be neglected. The stepping algorithm starts at the position of the loaded beam file $\vec{r}_0 = (x, y, z = 0)$ with the inverted momentum $\vec{p}_0 = -\vec{p}$ in order to extrapolate the beam particle backwards.

In each stepping iteration, denoted with the subscript i, the position and momentum of the beam particle gets shifted according to the step length s. The stepping algorithm reads:

$$\begin{aligned} c &= -299.792458 \cdot \frac{\mathrm{MeV/c}}{10^3\,\mathrm{T}\cdot\mathrm{e}\cdot\mathrm{mm}} \\ \Delta\vec{p} &= \left(\vec{p}_i \times \vec{B}(\vec{r}_i)\right) \cdot \frac{c\cdot q\cdot s}{|\vec{p}_i|} \\ \vec{p}_{i+1} &= (\vec{p}_i + \Delta\vec{p}) \cdot \frac{|\vec{p}_i|}{|\vec{p}_i + \Delta\vec{p}|} \\ \vec{r}_{i+1} &= \vec{r}_i + \vec{p}_{i+1} \cdot \frac{s}{|\vec{p}_i|} \end{aligned} \tag{4.2}$$

The magnetic field at the current particle position is denoted by $\vec{B}(\vec{r}_i)$. The conversion factor c considers the system of units used in Geant4 and TGEANT. Natural units are used for the beam energy and momentum. The magnetic field is given in units of 10^3 T and the charge of the beam particle q in units of the elementary charge e, while distances are measured in mm. The negative sign in the conversion factor accounts for the charge conjugation since the beam particle is extrapolated backwards.

To save computing time, the stepping algorithm is replaced by a linear step after the magnetic field is absent (iteration number n). So there is only one calculation left to extrapolate the beam particle backwards to the desired z position:

$$\begin{aligned} \vec{r}_{primary} &= \vec{r}_n + \left(\frac{z - r_{n,z}}{p_{n,z}} \right) \cdot \vec{p}_n \\ \vec{p}_{primary} &= -\vec{p}_n \end{aligned} \tag{4.3}$$

The momentum vector is reinverted again. The algorithm of course works also for extrapolating beam particles in forward direction, e.g. in cases when the z convention of the beam file is located upstream of the desired starting position. The sign of c is inverted in that case.

4.2.2 Primary Vertex Generation

The algorithm to generate a primary vertex in TGEANT is responsible for stopping the primary beam particle and for calling an event generator. Two procedures to trigger the event generator are implemented in TGEANT. The first algorithm, which is called target extrapolation method, fits perfectly to the muon program of COMPASS. The second algorithm was especially designed for pion beams scattered off a setup with a thick target and is discussed in Sec. 4.3.1.

Target Extrapolation Method

The goal of the target extrapolation method is to stop the movement of the primary beam particle at a random position inside the target volume. A flow chart of the target extrapolation method is presented in Fig. 4.4. It is a multi-purpose method to generate vertices within the target volume. A realistic vertex distribution can easily be simulated by using a beam file and a precise target alignment.

To distinguish between usual detector geometries and target volumes, TGEANT uses the *T4TargetBackend* system. Each implemented target geometry is derived from this abstract base class. The target area is the most frequently and most heavily modified component of the COMPASS set-up. So far, five different target geometries have been implemented in TGEANT to cover all physics programs since 2007. The *T4TargetBackend* interface is used to gather information about the target that the algorithm needs to work with. This is exactly the reason why back-end systems are so valuable: the target extrapolation method works regardless of the type of target used. The most important information about a target geometry are the target cells. These have to be registered in the base class. Regarding the 2012 liquid hydrogen target, see Fig. 3.3, this involves liquid hydrogen filled volumes: a 2615 mm-long tube and two spherical end caps on the up- and downstream side. All surrounding

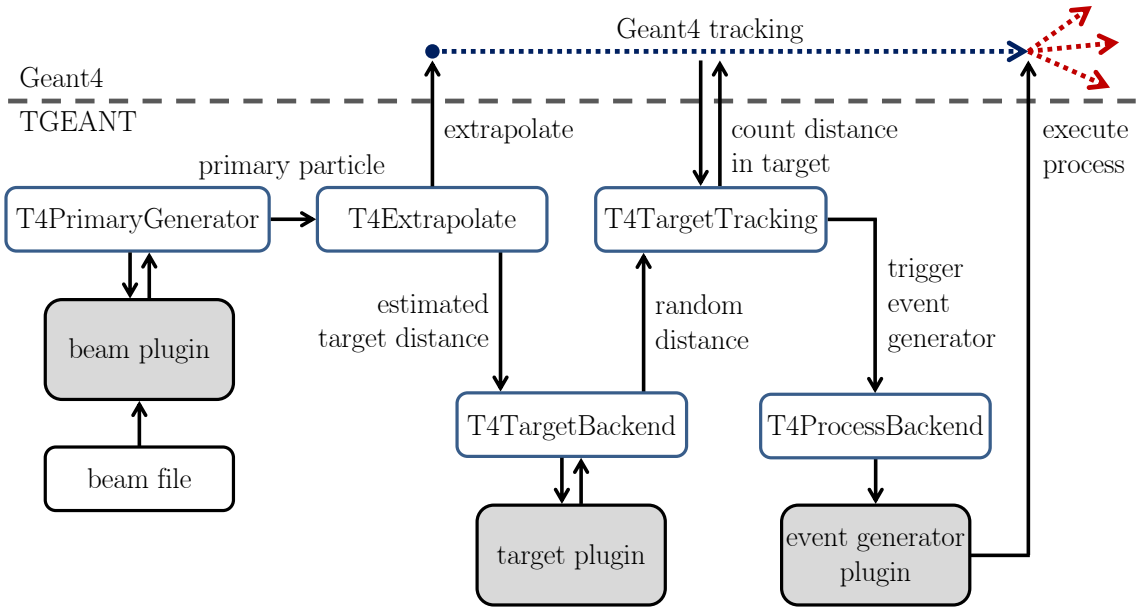

Figure 4.4: Flow chart of the target extrapolation method: The *T4Extrapolate* class extrapolates the primary particle to the desired starting z position. After traversing a random distance inside the target volumes, the beam particle is stopped by the *T4TargetTracking* class. At this point, the event generator is applied. This random distance is dictated by the *T4TargetBackend* derived target class. An estimated distance, which the beam particle is able to traverse in the target volume, is provided by the *T4Extrapolate* class and can be used optionally.

material layers as well as the entrance and exit windows are not marked as active target material and therefore not considered at the vertex generation. In principle, each volume is allowed to be defined as a target, independent of its material or geometrical shape.

The second key module of the target extrapolation method is the *T4TargetTracking* class. This class is derived from a virtual class in Geant4 and overwrites a function to gain control of the particle stepping. In the Geant4 tracking algorithm, a particle track is divided into several steps, cf. Appendix A.3. The *T4TargetTracking* class allows access to information about the particle's state, including the particle's type, the identification number of its track and parent's track after each step. A unique identification of the primary beam particle is therefore possible. The second part of the information carries the particle's current momentum, position, and the length of its last step. Even more interesting is the volume where the particle is actually located. Volumes which are marked as active target can be distinguished from all other volumes. The Geant4 tracking algorithm ensures that each particle track creates an intermediate step at each volume boundary. All this together is used to sum up the exact traversed distance of the primary beam particle inside the active target volumes. Hereby, it makes no difference if the particle has left one cell of the target volumes and reenters another one, e.g. to bridge the gap between two cells. Only the distance within the active target volumes is summed up. This allows to trigger the event generator exactly after the beam particle has traversed a random distance inside the target volumes.

This method is only feasible if the particle's maximum step length inside the target volumes is limited. Usually, the step length varies for each step and depends on the particle type and the implemented physical processes and thus also on the surrounding material. Considering a muon in liquid hydrogen, Geant4 chooses a step length in the order of meters and the muon tracking will most likely only be interrupted by the surface crossing. The maximum step length can be tuned in the TGEANT setup file and should be adjusted to the used target volume. For the 2.5 m-long liquid hydrogen target, a maximum step length of 1 mm is used. A shorter distance would not improve the accuracy of the vertex distribution but increase the number of steps and hence suffer in performance.

Drawing the Random Distance

The random distance that the primary beam particle traverses inside the target volumes before the event generator is triggered needs to be specified in advance. If the beam particle never traverses the chosen distance, the event generator will not be called and the whole event is rejected. A reasonable choice would therefore be a random fraction of the full target length.

The implemented design in TGEANT is much more versatile. The already presented *T4Extrapolate* class is not only able to extrapolate but also to estimate the traversed distance of the beam particle in the target volume. This principle is outlined in Fig. 4.5 with an inclined target. In this regard, it is assumed that effects such as multiple scattering are neglected. This estimation has an accuracy of about 1 mm, which is the step length of the extrapolation algorithm. The last step out of the target is also added so as not to underestimate the distance. This estimate is precise enough to be used instead of the full target length. Using a random fraction makes sure that each beam particle can traverse the chosen distance in the target volume and trigger the event generator[4]. No event needs to be rejected in that case and valuable CPU time can be saved. The method of using a random fraction of the estimated distance is implemented to take care of a target cell that is not perfectly aligned to the beam axis in the experiment. In such a case, it may happen that

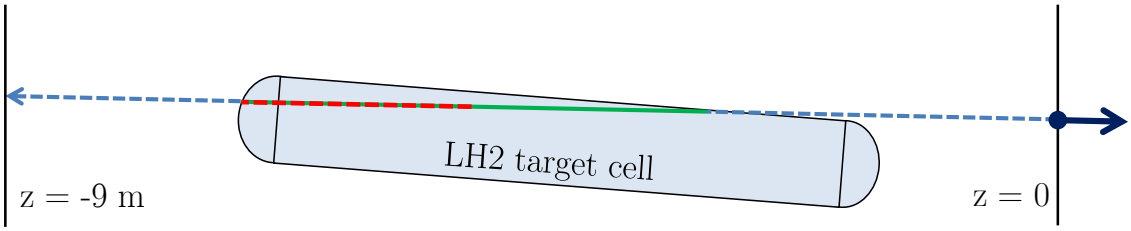

Figure 4.5: Vertex generation with the target extrapolation method. The beam particle loaded from a beam file is extrapolated backwards to the beam starting position at $z = -9\,\mathrm{m}$ (dashed line). During extrapolation, the expected target distance is measured (green line). The vertex will be generated after the beam particle has traversed a random fraction of the expected distance (dashed red line).

[4]This statement is not completely correct. Since the extrapolated target distance is slightly overestimated and the multiple scattering neglected, a small chance remains that the event generator is not triggered. But this is only a factor of 10^{-3} for the DVCS 2012 setup.

some beam particles cannot traverse the full target length. The disadvantage of this method is that each event needs to be weighted on the analysis level according to the estimated distance. Alternatively, TGEANT offers the possibility of drawing a random fraction of the full target length, which does not require any event weights but may waste more CPU time if the target and the beam direction are not perfectly collinear.

4.2.3 Event Generators

Several interfaces for different event generators are already installed in TGEANT and ready to use, see Fig. 4.6. The event generators are implemented as discrete Geant4 processes using the abstract *T4ProcessBackend* base class, which handles the interface to TGEANT. This involves the call of the event generator function and the forwarding of the four-momentum of the incoming beam particle at the vertex position.

During particle tracking, all physical processes that a particle is able to do need to propose a step length: the higher the process probability, the shorter the step length. The shortest step length is selected by the Geant4 tracking algorithm for the particle's next step and the associated process is applied, cf. Appendix A.3. Consequently, the event generator process, which is implemented in TGEANT as a discrete Geant4 process, also needs to propose a step length during particle tracking. To ensure that this process is never applied by chance, the default proposed step length is "DBL_MAX", which is the largest number possible. At the vertex position, however, the proposed step length of the event generator process is changed to zero to ensure that no other process is able to propose a shorter step length and consequently the event generator gets triggered.

The simplified procedure of an event generator can be described as follows. The four-momentum of the incoming beam particle serves as input parameter and the target nucleon is at rest. During the simulated interaction, one or more outgoing particles are generated. The momentum distribution between these final state particles may be a complex procedure and needs to be randomized by the event generator

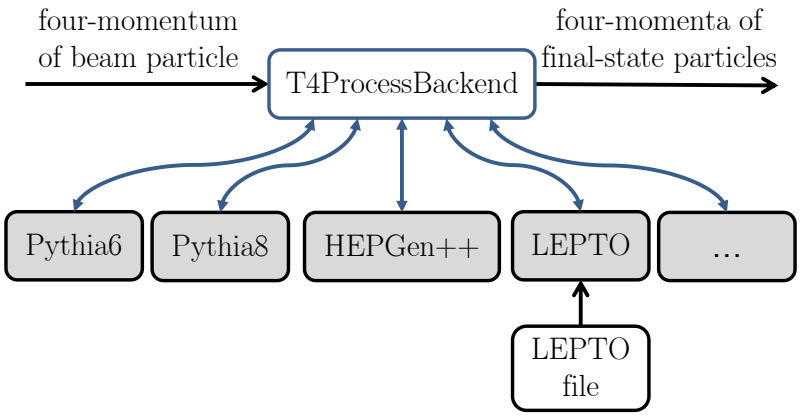

Figure 4.6: Inheritance diagram for the *T4ProcessBackend* base class. The four-momentum of the incoming beam particle is forwarded to the used event generator. The four-momenta of the final state particles are received in return.

according to the cross section of the interaction. At the end, however, the energy and momentum conservation needs to be ensured and TGEANT has to exchange the initial state beam particle with all final state particles.

Event Generators Called by TGEANT

In principle, the complete logic of an event generator can be directly written into the process function. But practically, one wants to use an already existing event generator. The most favored way to apply an event generator is by using its library access as it has been done for HEPGen++, Pythia6 or Pythia8. This allows for the possibility of applying directly the event generator for one event each time the vertex generation method triggers. This method is very beneficial since the energy and momentum direction of the initial beam particle is only known at the randomly chosen vertex position. The kinetic energy can be transferred to the event generator, which simulates one event and then transfers the output to TGEANT. Usually, the event generator aligns the initial beam particle to a conventional beam axis. To also account for the momentum conservation, the whole event is rotated to parallelize the conventional beam axis of the event generator and the momentum direction vector of the incoming beam particle.

Reading External Event Generator Files

The design of an event generator or technical difficulties can preclude the above-mentioned method. In these cases, the event generator needs to be applied independently of TGEANT in advance of the event loop simulation. The event generator prepares an output file that TGEANT needs to read in. The most common output file format for event generators is LEPTO [66], which is described in Appendix B.5.

LEPTO uses a beam file to generate events with varying beam energies. All parameters in Eq. (4.1) are additionally saved in the LEPTO file, which allows TGEANT to use the same beam particle for the beam simulation as LEPTO for the event generation. The vertex generation algorithm remains unchanged and the whole LEPTO event is rotated according to the momentum direction of the initial beam particle at the randomly chosen point of interaction.

There is one inaccuracy in this method that one needs to be aware of. The beam particle should arrive at the vertex position with the same energy as the event was generated. This requires to add the energy loss between the beam starting position and the vertex position in advance before starting the event loop. But this is an impossible task since energy loss is a statistical process. The best one can do is to add the most probable energy loss while extrapolating the beam particle backwards. This energy loss depends on the z position of the vertex, as shown on the left-hand side of Fig. 4.7, and can easily be parameterized with

$$\Delta E = l \cdot \left(\frac{\mathrm{d}E}{\mathrm{d}z}\right)_{\text{Target}} + c, \tag{4.4}$$

where the slope $\mathrm{d}E/\mathrm{d}z$ depends on the target material and is provided by the target class. The offset c accounts for the mean energy loss of the beam particle caused by the material of all detectors upstream of the target. Using constant values for the

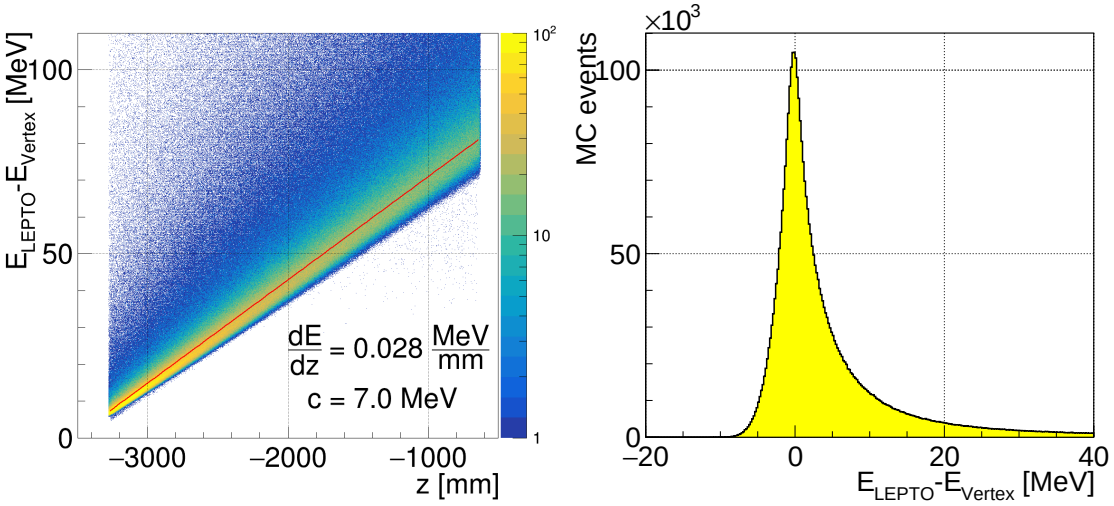

Figure 4.7: Beam energy correction for external event generator files. Left: The energy loss of the beam particle between the beam starting position and the vertex position as a function of z. The extracted slope and offset values can be used to increase the beam energy. This reduces the energy deviation to a negligible scale (right).

slope and the offset is a reasonable assumption due to the fact that the momentum dependence of the mean energy loss can be neglected on the high-energy scale of the beam particles. The slope has to be multiplied with the distance l, which the beam particle traverses inside the target and which is well-known in advance from the target extrapolation method. The addition of ΔE to the kinetic energy of the beam particle reduces the energy deviation to a negligible scale, presented on the right-hand side of Fig. 4.7, which cannot be resolved by the reconstruction software.

4.2.4 Pile-Up

The high beam flux in the experiment can cause reconstruction issues in some cases. For instance, if two beam particles enter the target area in close succession, it may happen that the scattered beam particle is associated with the wrong beam particle. Similar problems can occur in the track reconstruction, especially for detector systems with a lower time resolution or long integration time. These effects need to be considered in Monte Carlo. Besides the primary beam particle, other beam particles are added at the beam starting position. These added particles are generally called pile-up. The number depends on the measured beam flux Φ, which has to be extracted from the data, see Sec. 7.1, and on the time window T. The primary beam particle starts at $t = 0$ by definition. The rate of beam particles is constant over a finite interval of time, thus, the pile-up particles start uniformly distributed in the interval $[-T, T]$. The time window should be chosen according to the timing resolution of the slowest detector components to consider all possible reconstruction issues. The default value is $T = 100\,\text{ns}$ due to the calorimeter systems. The number of pile-up particles that are added to the simulated event follows a Poissonian distribution:

$$\begin{aligned} \bar{x} &= \Phi \cdot 2T \\ n &= \text{RandPoisson}(\bar{x}) - 1, \end{aligned} \tag{4.5}$$

where RandPoisson() is a random number generator that produces integers according to a Poisson distribution. The mean number of particles $\bar{x}$ also includes the primary beam particle, which needs to be subtracted to calculate the number of pile-up particles n. In opposition to the selection of the primary beam particle, all entries in the beam file are valid. This involves beam particles that are intersecting the target as well as the halo, see Fig. 4.8. The ratio between beam and halo is dictated by the beam file, which is extracted from measurements. The pile-up component for the 2012 μ^+ beam file is 4.3 %.

In principle, the pile-up particles do not interact with each other and are therefore independent events. From a technical point of view, the primary beam particles, which trigger the event generator, can be simulated independently of the pile-up. To build the final event, TGEANT offers the possibility of merging the output of one physics event with n pile-up events before the event reconstruction starts. Using this feature, the Monte Carlo production can start before and during the measurement, while the beam flux only serves as input parameter on the reconstruction level. A new data base format has been developed to make fast random access to the stored pile-up events possible. This data base format is described in Ref. [45].

4.2.5 Sensitive Detectors

Sensitive detectors are the key feature of this simulation software. They are the first step to project the Monte Carlo truth on an experimental scale. The full information about all particles on each step is well-known in the simulation. The experimentalist, however, is restricted to the response of the detectors. Technically, a volume in the simulation can be assigned as a *T4SensitiveDetector*. Many sensitive detectors are used in TGEANT, for instance one for each tracking detector channel or calorimeter module. For each particle step inside a sensitive detector, all information about the step, its pre-step, and post-step points are accessible and saved in TGEANT until the end of the event.

All Monte Carlo hits with a chance to be measured in the real experiment need to be recorded and transferred to the reconstruction software. But this statement does

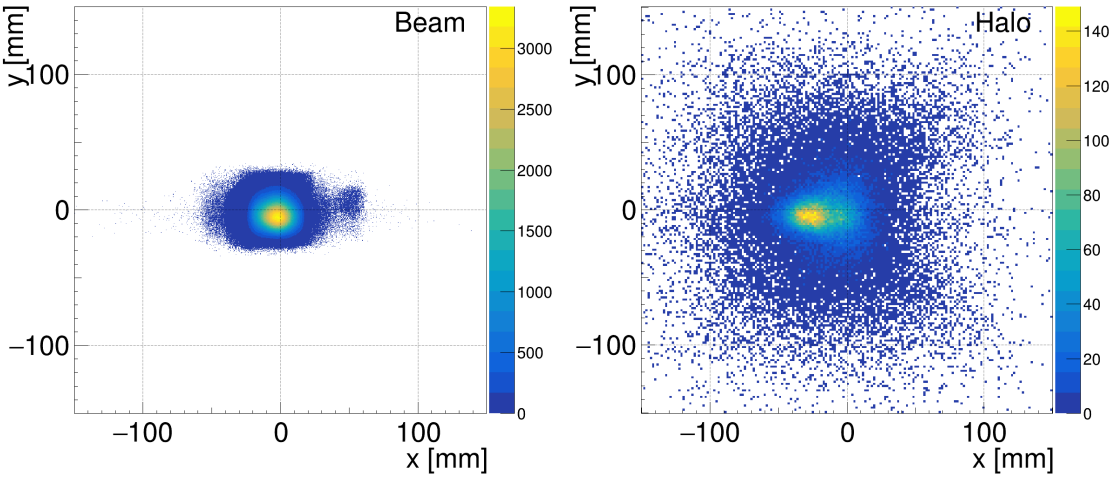

Figure 4.8: Spatial distribution of all beam flagged (left) and all pile-up flagged (right) entries of the 2012 μ^+ beam file.

not refer to the individual steps of a particle hitting a detector and in particular not to the steps of its secondary particles that may have been created. Consequently, the recorded step information in a detector channel needs to be merged. The readout type is used to classify different components of the experimental apparatus, which are processed differently. Figure 4.9 shows the flow chart of the event loop with a focus on sensitive detectors.

Tracking Detector Readout

The tracking detector readout is used for all different detector types in the COMPASS experiment, except for the calorimeter modules and the detectors that are designed to detect optical photons [5].

The number of events a tracking detector may measure depends on its time and space resolution. The consideration of these restrictions is the task of the reconstruction software CORAL. TGEANT therefore delivers all hits, even if they are close in time and space. A hit is defined as the combination of all particle steps inside a sensitive detector that can be traced back to one particle track that enters the detector. Figure 4.10 shows an example in which a sensitive detector has measured nine steps and seven different track ids, which originate from two independent particle tracks. Using the information of the particle's parent track id, all secondary particles that are created in the interaction with the detector material are traced

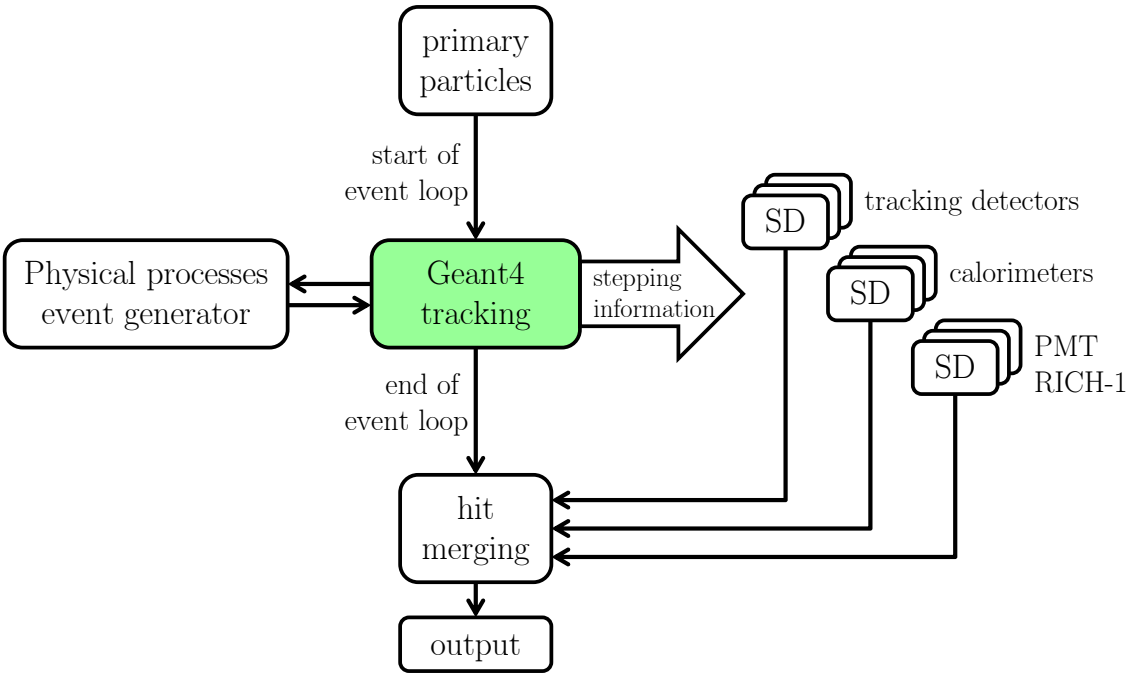

Figure 4.9: Flow chart of the event loop with a focus on sensitive detectors. The event loop begins with the tracking of the primary particles. Secondary particles may be created by physical processes and interact with one of the sensitive detectors (SD), which collect all stepping information. This information is merged for each sensitive detector at the end of the event loop.

[5] Photons that are created by a Cherenkov or scintillation process are called optical photons in Geant4 and are treated as independent particles, cf. Appendix A.1

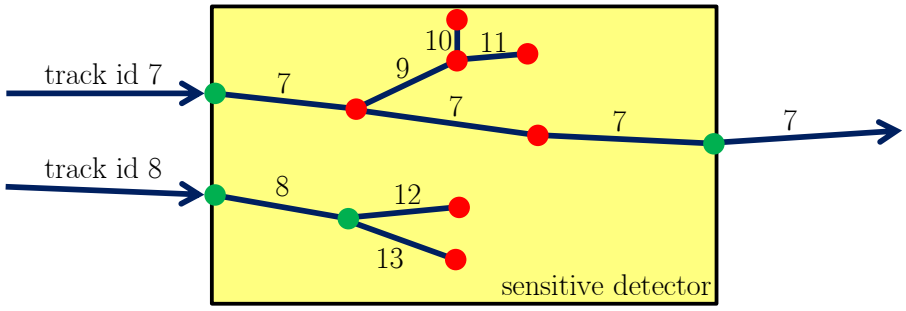

Figure 4.10: Example for the particle-hit-merging in a sensitive detector. Nine steps are measured, which can be tracked back to two incident particles using the track ids and track's parent ids. The green points mark the pre-step and post-step point of the first and last step of the two independent particles.

back to the particle that enters the detector. In the given example, two hits with six and three steps respectively have been measured.

The information of all steps, which are related to one hit, needs to be merged and converted to a tracking hit. The energy deposit is calculated as the sum of energy deposits over all steps. The pre-step point of the incident particle's first step in the sensitive detector, also called primary hit position, provides information on the interaction time, the particle's energy and its momentum direction. The last hit position is defined as the post-step point position of the last step that has the same track id as the incident particle. These points are colored green in the example figure, while all others are colored red. The two hit positions are important for the event reconstruction to calculate the closest distances of the particle trajectory from the nearby anode wires. The full information of a tracking hit is listed in Tab. B.15.

Calorimeter Readout

The different calorimeter modules used in the COMPASS experiment have a lower time resolution as the tracking detectors. The pile-up time window has been chosen accordingly. Consequently, a calorimeter module cannot separate different events from each other. The calorimeter readout only needs to gather information on the total energy deposit in one module, which is calculated as the sum over all particle steps in the respective modules, and on the rising time of the signal, which is obtained from the first particle interaction.

The huge number of secondary particles scales with the energy of the incident particle. The ordering of all secondary particles that derive from one single source as it is done in the tracking detector readout would be a time consuming task and is not needed here. Dispensing with this tracking information allows for the running of the same calorimeter readout algorithm with standard Geant4 tracking and with the fast shower parameterization GFlash. GFlash is described in detail in Chapter 5. In a nutshell, energy spots are distributed all over the calorimeter modules, which are no longer connected by particle tracks. The total energy deposit is calculated as the sum over all energy spots within one module.

4.2.6 Trajectories

An exclusive piece of information about Monte Carlo events is the trajectories of all particles. This information can later be used, for instance, to study the efficiency of the event reconstruction. Table B.16 lists all information of a trajectory object.

During the event loop, all trajectories are temporarily stored. The number of trajectories might get very large in certain circumstances, e.g. in a high-energy particle shower in a calorimeter module. Particularly in this example, only the trajectory of the incident particle has relevance for the analysis. Additionally recording all secondary particles would mean wasting valuable disk storage and processing time in the writing and reading process. For this reason, TGEANT filters and sorts the trajectories at the end of each event loop. The sorting is important since the reconstruction software CORAL needs the trajectories in a specific order because of hard-coded constraints.

Particle trajectories that generate a hit in one of the sensitive detectors need to be saved. In addition, the trajectories of all particles that go out of the primary vertex are considered to be relevant for the event analysis. To provide full information on particle branching, all parent tracks are also added to the list of useful trajectories, as well as the parents' parent tracks, etc. Figure 4.11 illustrates the principle of trajectories selection.

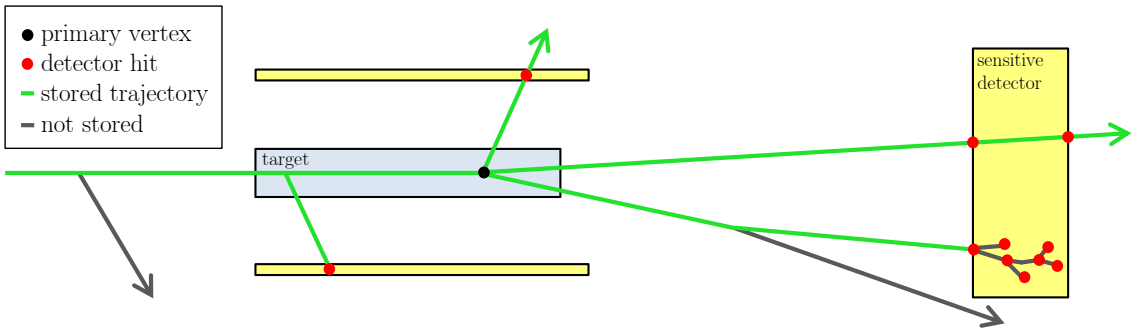

Figure 4.11: Principle of the trajectories selection in an example setup. All particle tracks originating from the primary vertex and all tracks that generate a hit are stored.

4.3 TGEANT with Hadron Beams

In order to optimize the performance of the event simulation while using a hadron beam, a new vertex generation method was developed and added in TGEANT, the so-called hadronic interaction method.

4.3.1 Hadronic Interaction Method

When using a pion beam in combination with the target extrapolation method, cf. Sec. 4.2.2, it may happen that the pion gets destroyed by an inelastic hadronic interaction before the event generator is triggered. In that case, the event gets rejected. The probable loss of an event (and processing time) is highest if the

primary vertex was intended to be at the downstream side of the target. Due to inelastic hadronic interactions, the pion flux and therefore also the number of primary vertices drops exponentially along the beam axis – the same observation is well-known in the experiment and thus also desired in the simulation. To avoid this performance leak, the hadronic interaction method was developed.

The idea is to call the event generator in case the pion would get destroyed due to inelastic hadronic interactions. A special TGEANT process was therefore interposed between the Geant4 tracking algorithm and the inelastic hadronic process table. This process checks whether the primary beam particle gets destroyed during the interaction or not. As long as the initial beam particle survives, the intended hadronic processes are executed. This ensures a realistic simulation of the beam particle propagation, taking into account effects like multiple scattering, energy loss and bending of the target dipole magnet. This method only depends on the material the beam particle crosses. The flow chart of the hadronic interaction method is shown in Fig. 4.12.

4.3.2 Drell-Yan Setup at COMPASS-II

The hadronic interaction method was specially developed for the Drell-Yan measurements at the COMPASS-II experiment in 2014/15. A detailed description of the pion-induced Drell–Yan muon pair production, $\pi^- + p \to \mu^+ + \mu^- + X$, at the COMPASS-II experiment is given in Ref. [39]. In the experiment, a high-energy pion beam is scattered off a polarized ammonia target. A hadron absorber was installed downstream of the target cells to reduce the high secondary particle flux produced by the interaction of the pion beam in the target. A configuration with alternating layers of alumina and stainless steel absorbers was chosen. Inside the absorber, centered on the beam axis, a 120 cm long tungsten plug was installed in

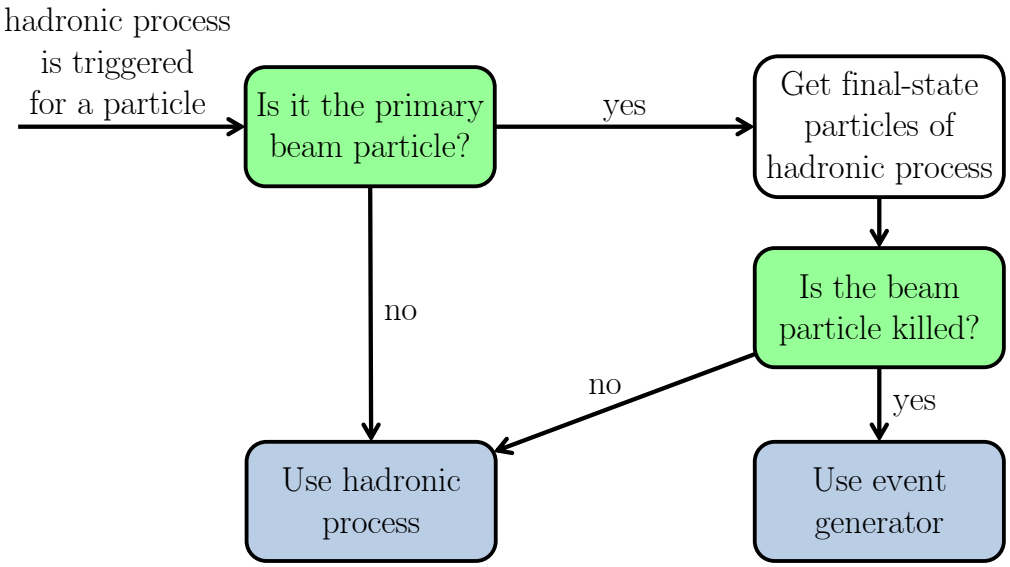

Figure 4.12: Flow chart of the hadronic interaction method. If the primary beam particle gets killed by an inelastic hadronic interaction, the event generator is applied instead. Otherwise, the intended hadronic process is used.

order to stop the non-interacting pion beam. In combination with a 7 cm thin aluminum disc placed in the same cavity 26 cm more upstream, the tungsten target is used to measure unpolarized Drell-Yan events. A visualization of the target area is shown in Fig. 4.13.

In order to simulate a realistic vertex distribution, the target extrapolation method is adequate, but suffers in performance. The pion flux drops exponentially, especially in the tungsten tube that was designed to fully absorb the pion beam. A huge fraction of events would be rejected and only 36 % of the incoming pions would create a primary vertex. The hadronic interaction method avoids this performance leak and allows to simulate Drell-Yan events in all target cells simultaneously.

At COMPASS kinematics, the absorption cross sections for pions depends on the atomic mass number and is proportional to $A^{0.77}$ [67], while the Drell-Yan cross section was observed to be proportional to A by previous experiments [68]. TGEANT stores the material properties of the volume in which the primary vertex was created for each event and therefore allows for the application of an event weight. Regarding the Drell-Yan event selection [69], each event is weighted according to $A^{0.23}$. Figure 4.14 shows the reconstructed vertex distribution from a TGEANT Monte Carlo sample for the 2015 Drell-Yan setup in comparison with real data. The exponential shape in the two ammonia cells or the tungsten plug is clearly visible just as the different scale according to the material properties is. The small amount of vertices

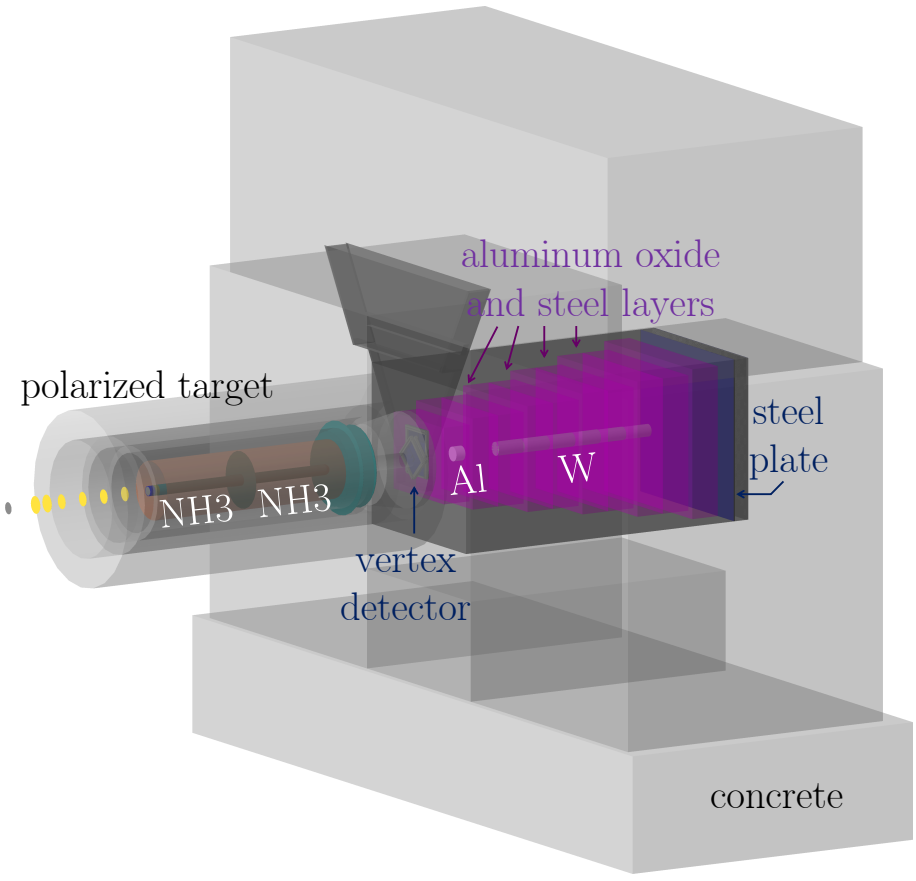

Figure 4.13: Visualization of the target area of the Drell-Yan setup from TGEANT.

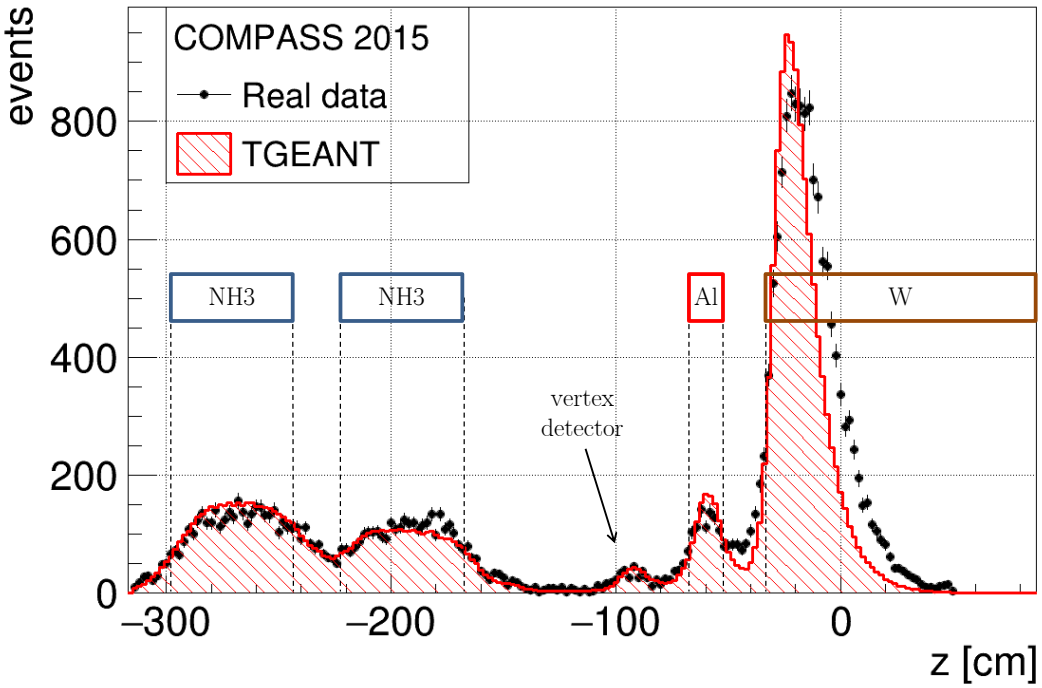

Figure 4.14: Reconstructed vertex distribution from a TGEANT Monte Carlo sample for the 2014/15 Drell-Yan setup in comparison with real data (measured in period W10 in 2015). Picture adopted from Ref. [69].

created by the vertex detector, which is installed between the ammonia target cells and the absorber, is also well reproduced.

4.3.3 Improved Pile-Up Simulation

When simulating a pion beam, a unique feature is implemented in TGEANT. In the experiment, the pion beam always has a fractional amount of muons due to the decay of a pion into a muon: $\pi^- \to \mu^- + \bar{\nu}_\mu$ or charge conjugated respectively when dealing with a π^+ beam. All pile-up pions, emitted at the beam starting position, can decay.[6] Therefore the muon content increases with z, while it is zero at the beam starting position, which is usually selected much more downstream compared to the dipole magnets B6 that bend the beam to the horizontal, cf. Sec. 3.1. A non-negligible muon component is therefore expected at this position. A second muon beam file, which can be loaded in TGEANT in addition, solves this problem: this second beam file needs to describe the muon flux and phase space at the chosen beam starting position.

4.4 Geometry and Alignment Files

Apart from the output of the TGEANT event loop, two more input files are required by the reconstruction software CORAL, namely the geometry and alignment files, thus they need to be provided by the Monte Carlo software.

[6]The primary beam particle can of course also decay, but in that case the event is rejected.

4.4.1 Geometry File

The geometry file describes the TGEANT world volume, including all volumes and material definitions. This file is important for the track reconstruction so that the energy loss and multiple scattering in the different material layers can be accounted for. This file is not only used for the reconstruction of Monte Carlo events but also for real data.

TGEANT features the export of the geometries in a GDML[7] file, which is an application-independent geometry description format based on XML and is therefore also human readable and supported for example in CORAL and ROOT[8]. The disadvantage of this format and of the complexity of the TGEANT geometries is the rather long loading time. The loading of the full COMPASS spectrometer takes about one minute. This delay multiplies in a parallelized Monte Carlo mass production, in which each CORAL job needs to load the geometry file. Moreover, the geometry file is also provided to the analyst using the analysis software PHAST, who also has to cope with this delay. In order to avoid such delays, a ROOT-dependent program is provided to convert the GDML format into a pre-loaded binary ROOT file. The binary ROOT file is no longer human readable, but the loading time drops below one second. A direct export in the binary file was avoided to keep TGEANT independent of ROOT.

4.4.2 Alignment File

The process of digitization and clusterization, cf. Sec. 3.6.2, is a crucial step of the well-known Monte Carlo hits to a detector cluster as it is measured in the experiment. This process is individual for all different tracking detector systems. The input parameters are provided by the alignment file, also inside COMPASS known as “detectors.dat” file. Each detector plane is identified through its identification number and characterized by its position, size, and rotation. Information about the wire alignment is given with the number of wires, their distance apart, and angle with respect to the detector reference system. Central holes or insensitive areas without any readout are described by dead-zones. All these values are related to the geometry and alignment of the detector planes and therefore provided by each detector geometry class of TGEANT. Other values such as one-dimensional efficiency or values describing the timing resolution of a detector plane complement the alignment file. These values are essential for the digitization process in the reconstruction software but are not relevant for the event simulation. TGEANT therefore forwards these values from a database to the alignment file. This data base is based on XML and can easily be created or modified with the graphical user interface of TGEANT. One data base file for each physics program is delivered in the TGEANT resources folder.

The alignment file is only capable of considering one-dimensional efficiencies for each detector plane. To improve the description of spatial anisotropies in the detectors, a new two-dimensional efficiencies data base has been developed and added to the TGEANT-CORAL interface [45].

[7] Geometry Description Markup Language

[8] ROOT is a modular scientific software framework. It provides all the functionalities needed to deal with big data processing, statistical analysis, visualization, and storage [70].

4.5 Design of the Simulation Software

The simulation software package TGEANT is designed highly flexible. Software extensions, which are needed to adapt TGEANT for a new physics program, are easily manageable using the concept of back-end systems. This is the reason why TGEANT, which was developed in the first place for the GPD program, is nowadays used for all COMPASS physics programs.

4.5.1 Back-end Systems

Necessary functionalities that the software needs to be able to execute are combined in the core of TGEANT. This involves for instance the initialization, the concept of the event loop, and the input-output interface. All software extensions are embedded in an object-oriented inherited approach, called back-end system. Although TGEANT is a fairly complicated software, only the self-consistent back-end systems need to be understood in order to begin implementing new features.

A back-end system is a unified application programming interface, which provides virtual functions that are applied by the main program. A new plugin inherits from the abstract base class and implements or overwrites the virtual functions. Back-end systems are designed in such a way that either only one of the plugins is in operation or all of them are registered and called one after the other.

An example for a back-end system in which all plugins are called one after another are the geometries, see Fig. 4.15. Each detector geometry in TGEANT inherits from the abstract *T4BaseDetector* class and needs to implement specific functions. The most important one is called to construct the geometries. Another function is called to gather information on all tracking detectors to create the alignment file. This back-end system is not just an elegant way to loop over all geometries but it is also designed in a user-friendly way, allowing developers to access easily all tools required such as the definition of all materials. A similar approach of back-end system is in operation to implement the magnetic fields. The global magnetic field in the world

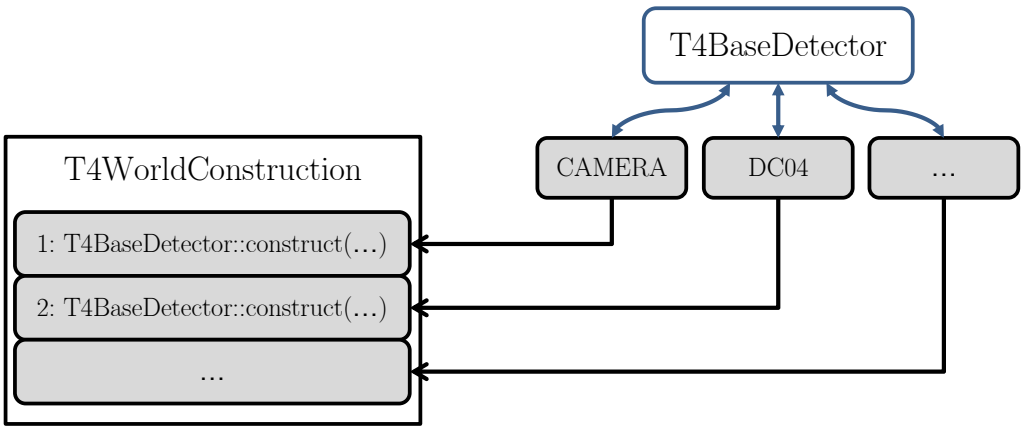

Figure 4.15: Inheritance diagram for the *T4BaseDetector* base class. Each detector geometry inherits from the abstract base class and needs to implement their pure virtual functions. All plugins are registered in the *T4WorldConstruction* class, where the functions of the *T4BaseDetector* class can easily be called.

volume is built up by several independent partial fields. An example of a partial field is the magnetic field of the dipole magnets SM1 or SM2.

Examples for back-end systems, where only one plugin is used are the beam plugins and event generators, as shown in Fig. 4.16. The active plugin is chosen by the input setup file. The *T4PrimaryGenerator* applies the implemented functions of the active beam plugin automatically in the correct order. A developer only has to provide the new functions of the newly added beam plugin. Changes in the core functionalities are not required.

A varying number of beam plugins are installed. The most important one is the beam simulation in combination with an event generator as described in Sec. 4.2.1. The same code base can also be used to only simulate the beam particles without any event generator. This is needed to prepare a data base with pile-up events as discussed in Sec. 4.2.4. Other beam plugins are for example installed to simulate the 40 GeV electron beam that is used for ECAL calibrations (see Fig. 5.1 in the following chapter). Simulations of cosmic muons or a radioactive source helped to characterize the CAMERA detector, as applied in Ref. [71]. Of course, a user can also easily customize the particle type and four-momentum of the primary particle.

4.5.2 Software Structure

The TGEANT software package is divided in five sub-packages, which simplifies matters for the software user. Often a user is only interested in the production of a large TGEANT Monte Carlo sample, which is needed for the analysis of a certain physics channel. Here, only the installation of TGEANT and the two linked libraries is needed. Neither the graphical user interface nor the Toolbox are necessary. This not only saves some computing time during the installation, but also reduces the external software dependencies. A complete dependencies list and several installation guides are well-covered on the TGEANT website [72].

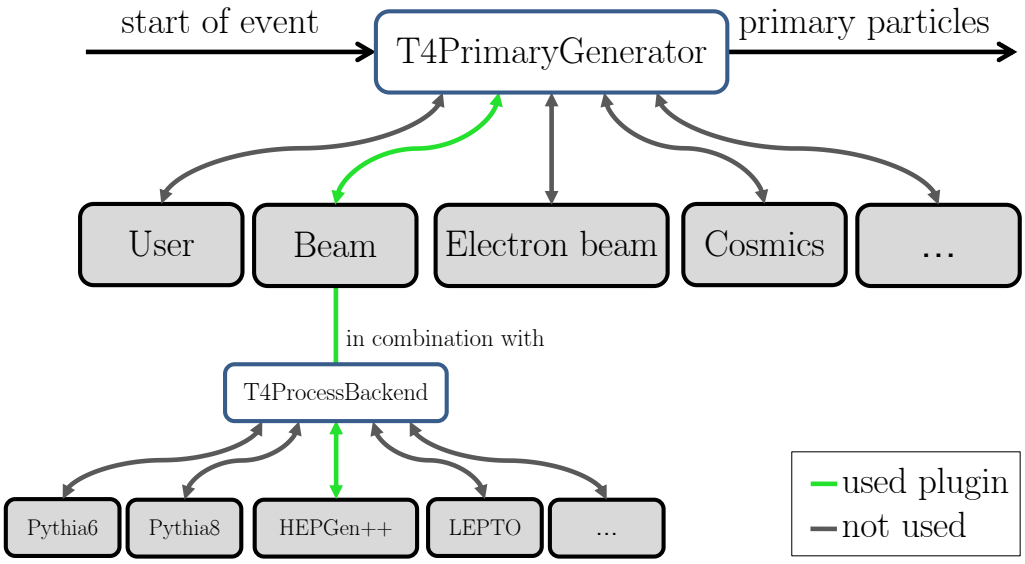

Figure 4.16: Overview of the available beam plugins. Several plugins are installed and the *T4PrimaryGenerator* uses the active one. The beam simulation plugin can be used in combination with a *T4ProcessBackend* plugin.

TGEANT Libraries in CORAL

Usually, a huge amount of Monte Carlo statistics is needed. In order to finish the Monte Carlo production as fast as possible, TGEANT is normally used on different grid computing centers at the same time. The Monte Carlo event reconstruction with the software CORAL is faster by a factor 10 to 20, thus it can be considered to separate the event simulation from the reconstruction. This is also useful under the aspect that CORAL requires its own list of dependencies and may be problematic to install. Essentially, one wants the full reconstructed Monte Carlo statistics stored at one place and not distributed over several grid computing centers. The recommended method would be to concentrate the TGEANT output files on one batch system, wherever CORAL and its dependencies are installed. To run CORAL with TGEANT files, only the two libraries are required. Neither the simulation software TGEANT nor Geant4 are needed. This makes the TGEANT software package easy to use, as it is adapted to the needs of the user.

4.5.3 Pseudo-random Number Generator

A crucial part for the Monte Carlo software, especially in a parallelized mass production, is the pseudo-random number generator. A reliable pseudo-random generator, the James Random [73], is used in Geant4. The algorithm of a pseudo-random number generator starts with a first number, which is called seed. Running the same pseudo-random generator with the same seed will always deliver the same result and has to be avoided during a mass production. Consequently, each TGEANT instance needs an individual seed – assuming TGEANT is running multiple times in parallel on one or more batch systems.

One possibility is to write a unique seed into the setup file for each TGEANT job individually. But that is not an optimal solution from the user's point of view. The basic idea is to only have one default setup file for a Monte Carlo mass production to minimize the potential for problems caused by different setups. Hence, TGEANT needs to generate its own random seed. It is a standard method to randomly initialize a pseudo-random number generator with the time stamp. This approach is swift, but it leads to more than one TGEANT jobs starting concurrently on the same CPU and ending up with the identical seed. The solution for this problem is to read a random seed from the "/dev/random" file, which exists in Unix-like operating systems. The random numbers are generated from an entropy pool. If the entropy pool is empty, the reading will block until additional environmental noise has been gathered. This ensures a very high randomness of the seed at the expense of initialization time.

4.5.4 Graphical User Interface

The graphical user interface is a Qt4-based application, which was designed to easily create and modify TGEANT setup files. The different settings are grouped in several tabs: the general settings that are shown in Fig. 4.17, the detector selection and alignment tab, and the tab for all external input file paths. A full list of all TGEANT settings is given in Appendix B.1. A user can load and modify the different settings for all physics programs with one click. The setup file and

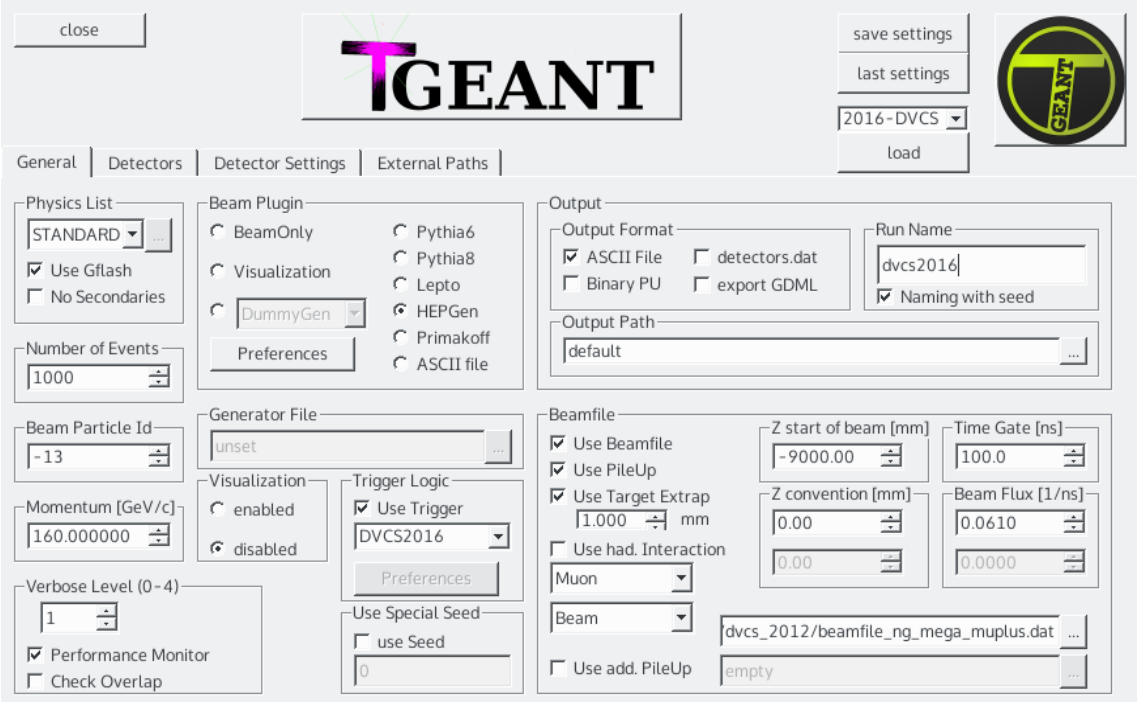

Figure 4.17: Graphical User Interface of TGEANT.

the graphical user interface are designed in such a way that they work without any hard-coded file paths. This ensures that especially the default setup files, which are stored in the resources folder, can be loaded by each user. Absolute file paths that point into the resources folder are automatically exchanged by relative paths starting from the TGEANT installation directory. This is used particularly with regard to all external input files such as the field maps for the dipole magnets.

Furthermore, the graphical user interface is able to load all detector positions from the same alignment file that is used for the real data reconstruction. This is a very useful and easy-to-use tool. During this process, the interface also assesses whether the relevant detector planes have already been implemented. This is extremely helpful if a user wants to add a new physics program into TGEANT. Warnings are printed for detector components that are unknown or if the alignment file is corrupted. For instance, warnings are printed if a detector position needs to be checked to avoid overlaps.

4.5.5 Toolbox

The Toolbox is a special analysis software designed for TGEANT output files. Usually, the TGEANT output is reconstructed by CORAL and analyzed with PHAST. However, there are different fields of applications in which the analysis of the original Monte Carlo output is preferred, such as Monte Carlo studies that are in first instance related to detector geometries. Two examples in which the Toolbox was used for this purpose are presented in Chapter 6.3 and 8.

The Toolbox is designed similarly to PHAST, which is well-known to most users of COMPASS. In PHAST, users write their own “user function”, which is called by the main program. Neither a detailed knowledge of the program sequence nor

of the input-output interface is needed. The Toolbox follows the same approach, but relies on "user classes" instead of "user functions". These plugins are embedded in an object-oriented inherited approach. The abstract base class provides three pure-virtual functions the user has to implement. The first function is called at the beginning of the events and is used for initialization purposes. The second function is called for each event and the third function at the end of the event loop.

The COMPASS Monte Carlo chain with CORAL and PHAST was developed for the reconstruction and analysis of the full experimental setup with already existing detector components. The Toolbox, however, can also analyze Monte Carlo hits from test setups or dummy detectors. This is especially useful for Monte Carlo tunings, as presented in the following chapter.

5. Tuning of the Electromagnetic Calorimeter Simulation

The three electromagnetic calorimeters play a crucial role for the exclusive measurement of the DVCS process and the process of exclusive π^0 production. The detection of the final state photon or the photon pair in the latter case happens with the reconstruction of neutral clusters in the electromagnetic calorimeters. Here, a cluster is defined as neutral if no incident particle track can be associated with the cluster. The reconstruction of the photon's four-momentum only relies on the combination of the vertex and cluster position as well as on the energy measurement. An accurate simulation of the electromagnetic shower propagation is therefore essential.

This chapter starts with an introduction to the simple cluster reconstruction in CORAL, emphasizing the important characteristics the simulation needs to take care of. The fast shower parameterization algorithm GFlash is implemented in TGEANT to accelerate the electromagnetic shower simulation. GFlash always works in combination with standard Geant4 tracking and does not replace it. Adjusting the Geant4 production cuts and tuning the GFlash parameters was necessary. An evolutionary algorithm was developed to optimize the large number of GFlash parameters in an efficient manner. Finally, the new cell-dependent energy calibration is presented.

5.1 Simple Cluster Reconstruction in CORAL

Several cluster reconstruction methods are available in CORAL. This section focuses on the most simplified one, namely the so-called Kolosov reconstruction code, introducing the important characteristics of an electromagnetic shower. This code was in use for the two electromagnetic calorimeters ECAL0 and ECAL1 regarding the reconstruction of real data and Monte Carlo for the 2012 DVCS pilot run. A sophisticated shower fitting algorithm based on the Lednev parameterization was used for ECAL2. The following section refers to the cluster calibration and reconstruction for Monte Carlo events. However, the cluster finding algorithm is the same as for real data. The same algorithm is also used for the hadronic calorimeters, which have less importance for the GPD program and are therefore disregarded in the following.

Energy Calibration

The calorimeter readout of TGEANT provides the energy deposit for all calorimeter modules. As the first step, the Monte Carlo cell energy E_{MC} is calibrated by a factor b provided by the alignment file[1]:

$$E_{\mathrm{calib}} = E_{\mathrm{MC}} \cdot b. \tag{5.1}$$

This linear calibration factor depends on the module type and calorimeter. Usually, it is different for the same module types in different calorimeters, e.g. for Shashlik or Gams modules in ECAL1 and ECAL2. The cells per se are identical, but the typical energies and angles of the incident particles are different for the two calorimeters. The calibrated cell energy E_{calib} enters in the cluster smearing and digitization algorithm. The purposes of the cell-dependent energy calibration are correct cluster energies in the end, which conform to the energies of the incident particles. The calibration is therefore needed to deal with the leaking energy on the backside of the calorimeter modules or the space between the sensitive parts of the different calorimeter modules.

Resolution of the Electromagnetic Calorimeters

The energy measurement in an electromagnetic calorimeter is based on the principle that the released energy of the charged particles, such as the electrons and positrons, is proportional to the energy of the incident particle. A measurement of the signal produced by the charged tracks of the cascade allows for a measurement of the incident particle energy. The shower development is a stochastic process, though the intrinsic energy resolution is given by:

$$\sigma_{\mathrm{stoch}}(E) \propto \sqrt{E}. \tag{5.2}$$

A second contribution to the energy resolution comes from the electronic noise of the readout electronics. This term, σ_{noise}, does not depend on the energy of the particle. The noise contribution therefore increases with decreasing particle energies.

[1]The actual calibration factor written in the alignment file is b^{-1}.

Nonuniformities in the detector geometry and readout systems from the radiation damage and detector ageing or from temperature gradients are considered with the so-called constant term,

$$\sigma_{\text{const}}(E) \propto E, \tag{5.3}$$

which becomes more and more dominant with increasing particle energies. All three effects are considered for each module individually in the Monte Carlo calorimeter reconstruction:

$$E'_{\text{calib}} = E_{\text{calib}} + \sigma_{\text{stoch}}(E_{\text{calib}}) \cdot r_1 + \sigma_{\text{noise}} \cdot r_2 + \sigma_{\text{const}}(E_{\text{calib}}) \cdot r_3, \tag{5.4}$$

where $r_{1...3}$ represent standard Gaussian-distributed random numbers.

Digitization of the Signal

In the experiment, the analog readout signal is converted into a digital signal using ADC cards on the frontend electronics. The energy is sampled in units of E_{sample}. The Monte Carlo reconstruction accounts for that by reducing the calibrated and smeared cell energy E'_{calib} to an integer value d, which is equivalent to the digital signal obtained in the experiment:

$$d = \left\lfloor \frac{E'_{\text{calib}}}{E_{\text{sample}}} \right\rfloor \equiv \max \left\{ d \in \mathbb{Z} \;\middle|\; d \leq \frac{E'_{\text{calib}}}{E_{\text{sample}}} \right\}. \tag{5.5}$$

The symbols $\lfloor\ \rfloor$ indicate the floor function. This integer characterizes the final cell energy E_{cell}, which is used by the cluster finding algorithm, in units of the sampling energy:

$$E_{\text{cell}} = d \cdot E_{\text{sample}}. \tag{5.6}$$

In addition, only modules above a cell-dependent energy threshold are considered in the final sample:

$$E_{\text{cell}} > E_{\text{threshold}}. \tag{5.7}$$

In 2012, the threshold was adjusted to 200 MeV and the digitization constant E_{sample} to 20 MeV for the three electromagnetic calorimeters.

Cluster Finding Algorithm

The final sample of ECAL modules obtained from TGEANT is now comparable to real data and goes through the cluster finding algorithm. Coherent modules are combined to a cluster and the total energy deposit is summed up. The algorithm finds the central module, which has the highest energy deposit of all cells in the cluster. Comparing the energy deposits in neighboring cells then allows for a precise determination of the impact point of the incident particle.

Two quantities are very important for a realistic simulation of the electromagnetic calorimeters: the cluster energy is obtained from the energy deposit sum over all modules that belong to the cluster. A precise energy calibration is therefore essential. The energy calibration has to account for lateral and longitudinal energy leakage as well as for energy loss due to the threshold for low-energy modules. The second quantity is an accurate simulation of the transverse propagation of the shower so that the reconstruction of the cluster position is possible with the same precision as in the experiment.

5.2 GFlash in TGEANT

The computing time needed for the simulation of high-energy electromagnetic showers depends on the number of secondary particles that have to be tracked through the material of the calorimeter modules. This computing time can become very large, since it increases approximately linearly with the energy of the incident particle [74]. Using parameterizations of the longitudinal and radial profiles can speed up the simulation considerably without sacrificing too much precision. The GFlash package allows the parameterization of electron and positron showers in homogeneous and sampling calorimeters. The parameterization is extensively described in Ref. [75].

5.2.1 Parameterization Ansatz

The spatial energy distribution of electromagnetic showers is given by three probability density functions:

$$\mathrm{d}E(\vec{r}) = E\ f(t)\mathrm{d}t\ f(r)\mathrm{d}r\ f(\phi)\mathrm{d}\phi, \tag{5.8}$$

where E is the energy of the first electron or positron at the starting point of the shower. The starting point is defined by the space point where the first bremsstrahlung process occurs. The GFlash parameterization Ansatz was developed for homogeneous and sampling calorimeters. In the latter case, the shower shapes depend in addition on the materials and geometries of the two alternating layers in the sampling modules. The following equations refer to homogeneous calorimeters.

The longitudinal shower depth is denoted by t and measured in units of the radiation length X_0. The average longitudinal shower profiles can be described by a gamma distribution [76]:

$$\left\langle \frac{1}{E}\frac{\mathrm{d}E(t)}{\mathrm{d}t} \right\rangle = f(t) = \frac{(\beta t)^{\alpha-1}\beta\exp(-\beta t)}{\Gamma(\alpha)}. \tag{5.9}$$

The shape parameter α and the scaling parameter β are associated with the center of gravity $\langle t \rangle$ and the maximum depth T of the shower, which can both be measured in units of the radiation length X_0 and the critical energy E_c:

$$\begin{aligned} \langle t \rangle &= \frac{\alpha}{\beta}, \\ T &= \frac{\alpha - 1}{\beta} \propto \ln\frac{E}{E_\mathrm{c}}. \end{aligned} \tag{5.10}$$

The radial distance from the shower axis is denoted by r and measured in Molière units. The average radial energy profile is parameterized in GFlash with a two component Ansatz, in which the profile is separated into a core of the shower and a tail:

$$f(r) = \frac{1}{\mathrm{d}E(t)}\frac{\mathrm{d}E(t,r)}{\mathrm{d}r} = p(\tau)f_\mathrm{core}(r,\tau) + (1-p(\tau))f_\mathrm{tail}(r,\tau), \tag{5.11}$$

with

$$f_i(r,\tau) = \frac{2rR_i^2(\tau)}{(r^2+R_i^2(\tau))^2} \qquad \text{for} \qquad i \in \{\text{core, tail}\}\,. \tag{5.12}$$

Here, $R_{\text{core}}(\tau)$ and $R_{\text{tail}}(\tau)$ represent the median of the core and tail component and $p(\tau) \in [0,1]$ is a probability giving the relative weight of the core component. The variable $\tau = t/T$, which measures the shower depth in units of the depth of the shower maximum, was introduced for a more convenient parameterization. A realistic radial shower profile is key for an accurate simulation of the lateral energy distribution, which is needed for the cluster position reconstruction especially concerning incoming photons. A parameter tuning was therefore needed, as presented in Sec. 5.4.

The azimuthal energy distribution is assumed to be uniformly:

$$f(\phi) = \frac{1}{2\pi}. \tag{5.13}$$

The energy of the incident electron or positron is distributed according to Eq. (5.8) via discrete energy spots in the calorimeter. An energy spot represents an amount of energy that is deposit at the position (t, r, ϕ). The total number of energy spots needed for one shower is obtained by

$$N_{\text{spot}} = 93\ln(Z)E^{0.876}. \tag{5.14}$$

The given numbers correspond to the default GFlash tuning for the liquid argon calorimeter of the H1 experiment as presented in Ref. [75].

The corresponding density distribution function is parameterized according to Eq. (5.9) by a gamma distribution with parameters α_{spot} and β_{spot}, which correlate with the corresponding longitudinal energy profile parameters α and β. The total number of energy spots for a longitudinal interval Δt of the length X_0 is evaluated by integrating the energy spot density distribution over this interval. The number of energy spots for the j'th interval reads:

$$N_{\text{spot}}(t) = N_{\text{spot}} \int_{t_{j-1}}^{t_j} \frac{(\beta_{\text{spot}}t)^{\alpha_{\text{spot}}-1}\beta_{\text{spot}}\exp(-\beta_{\text{spot}}t)}{\Gamma(\alpha_{\text{spot}})}\mathrm{d}t. \tag{5.15}$$

The energy content $\mathrm{d}E(t)$ in the same longitudinal interval Δt can be calculated from the actual longitudinal energy distribution given by Eq. (5.9). This amount of energy is divided into $N_{\text{spot}}(t)$ discrete spots with the energy $E_{\text{spot}} = \mathrm{d}E(t)/N_{\text{spot}}(t)$. The energy spots are distributed radially according to $f(r)$, uniformly in ϕ, and uniformly in the longitudinal interval Δt. Lastly, the energy spots are transformed into the detector reference system.

5.2.2 Implementation in TGEANT

The GFlash algorithm is implemented in the Geant4 toolkit and can therefore be called in TGEANT without any further external software dependencies. However, the parameterization algorithm for sampling calorimeters is directly implemented in TGEANT to enable a parameter tuning and also to fix an error in the Geant4 implementation of the GFlash code.[2]

[2] In the meantime, the bug report was approved and is fixed for newer Geant4 versions. To keep the backwards compatibility for older versions of Geant4, the patched code remains in TGEANT.

The GFlash parameterization is initialized with the homogeneous material individually for each lead glass module and with the two materials and their ratios regarding the sampling modules. Technically speaking, GFlash is not associated with the sensitive detector volumes of the ECAL modules but with regions. The concept of regions is introduced in Geant4 to combine a specific part of an entire detector setup to perform some special functions. Concerning the GFlash implementation, regions are used to trigger the GFlash parameterization. Two important facts need to be considered: GFlash is only triggered for electrons or positrons. The process of pair production with incident photons is performed by Geant4 tracking, thus GFlash is only able to speed up the simulation of sub-showers. GFlash is further only triggered for particle showers that are completely enclosed in the associated region. Otherwise, the usual Geant4 tracking is used and more and more secondary particles are created to form the particle cascade. GFlash may nevertheless be triggered for one of these secondaries, which have less energy compared to the incident electron or positron and are thus enclosed in the GFlash region.

The calorimeter modules in the COMPASS experiment were designed in a way that allows the electromagnetic shower to spread over several modules. GFlash will not be triggered in most cases if the GFlash region is only restricted to the sensitive part of one module and separated from its neighboring cells by the iron case. TGEANT follows another approach and combines all modules of the same kind into one region. This involves the sensitive parts, as well as the iron cases of the modules. The identically structured modules are placed side by side in the two electromagnetic calorimeters ECAL1 and ECAL2, see Fig. 3.8, while ECAL0 only consists of Shashlik modules. This enlarges the different GFlash regions to a maximum and ensures that GFlash is triggered for most of the particle showers. This also means that GFlash is never able to replace the usual Geant4 tracking, especially for particle showers that are close to the region's boundaries or to the central hole of the calorimeter.

The downside of the parameterization is that the material is assumed to be homogeneous in the entire GFlash region, which also includes the iron layers between the modules. The different behavior of the shower propagation in the lead glass material and the iron cases is neglected. Especially regarding the Shashlik modules, additional effects related to the internal mechanical structures, such as the steel rods that are needed to put the different scintillator and lead layers together or the optical fibers to guide the scintillating light to the photo multiplier tubes are neglected and replaced by the parameterization. But these effects are mainly related to the radial shower propagation and the total energy deposit in the sensitive part of the calorimeter. Both problems are solved with the GFlash tuning.

5.3 Geant4 Production Cuts for ECAL Regions

The fast shower parameterization algorithm GFlash always works in combination with the usual Geant4 tracking. Accordingly, both methods need to produce the same results so as not to introduce a position- and energy-dependent bias in the shower simulation. Even more important is that both methods simulate the same shower propagation as in the experiment. An appropriate comparison of the simulation with the experiment can be accomplished by analyzing the 40 GeV electron test

beam data. These measurements were performed at the beginning of the 2012 run in order to calibrate ECAL1. The beam was mostly focused on Gams and Shashlik modules as shown on the left-hand side of Fig. 5.1.

The same situation was simulated to compare the number of cells in one cluster, hereafter referred to as cluster size, with the measurement. The result is presented on the right-hand side of Fig. 5.1. The simulation was repeated with two different values for the production cuts. The concept of production cuts is used in Geant4 as a material-dependent energy threshold for the creation of secondary particles, cf. Appendix A.3. A small value of 50 mm shows a precise agreement with the measured data. Very large production cuts, on the other hand, show the expected behaviour: The full energy of the 40 GeV electron beam is deposited in only one calorimeter module in 94 % of all events. The reason for this are the large production cuts, which prevent the creation of secondary particles. The total energy is therefore treated as an energy deposit of the incident particle in the first cell so that the energy conservation is not violated. The same simulation was also performed with the default parameterization of GFlash. Here, two distributions are visible, which originate from the different shower parameterization in the Gams and Shashlik modules. Both of them are not in agreement with the measurement, which emphasizes the importance of the GFlash tuning.

The simulation with the 40 GeV electron beam shows the influence of the production cuts on the tracking. Higher production cuts speed up the simulation, but become unrealistic at a certain value. In the presented example, the speed advantage of the higher production cuts was a factor of 10^3. A tuning of the production cuts was therefore essential to optimize the performance without sacrificing preci-

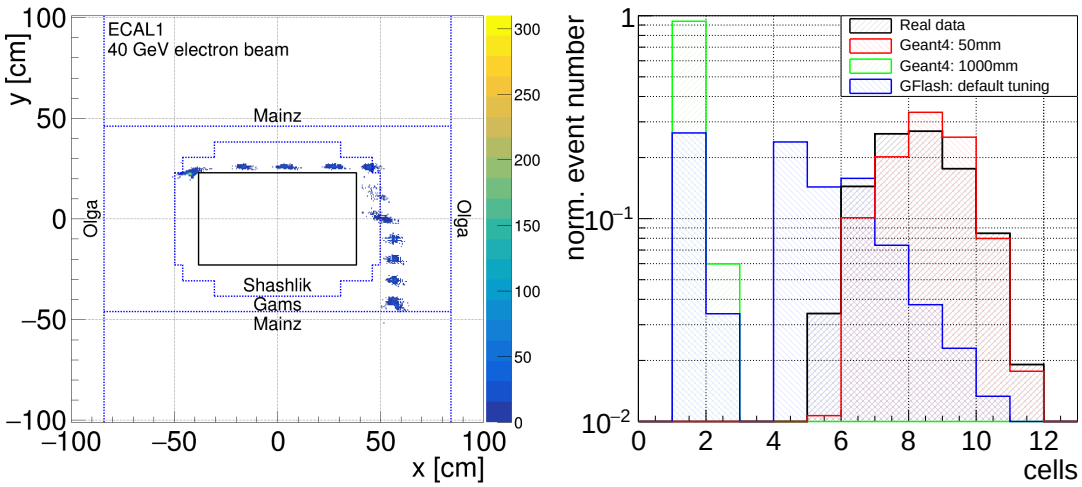

Figure 5.1: Comparison of cluster sizes using a 40 GeV electron beam. Left: Measured cluster positions in ECAL1. The electron beam is mostly focused on Gams and Shashlik modules. The blue dotted lines show the boarders between the different module types. Right: The number of cells for real data in comparison with Geant4 and GFlash. Geant4 with small production cuts shows a good agreement, while higher production cuts and the default tuning of GFlash do not coincide. The two GFlash distributions originate from the different default parameterizations for Gams (smaller mean value) and Shashlik modules.

sion. The results of the production cuts tuning for the Gams modules are presented in this section. The same optimization was also performed for all other modules, namely for the GamsRH, Mainz, Olga, and Shashlik modules. These results are given in Appendix C.1.

The calorimeters ECAL1 and ECAL2 are made of several module types. A particle shower often spreads over different types. To perform a module-independent study of the production cuts, a special test calorimeter is included in TGEANT. This test setup consists of a large grid of 101×101 modules to ensure that the full radial shower propagation is covered[3]. The 40 GeV electron strikes the test calorimeter in the center. The simulation was reiterated for different production cuts. Figure 5.2 shows the number of cells that have measured an energy deposit. The distributions for smaller production cuts up to a value of 250 mm are closely related. For higher values, the number of cells decreases slightly due to the decreasing number of secondary particles. For all production cuts from 400 mm, the particle shower is mainly restricted to the first hit module.

An important quantity when comparing the radial shower propagation is the shower profile. The energy deposit of all 101 modules that are placed in one row is summed up and plotted on the left-hand side of Fig. 5.3[4]. The energy deposit is at maximum for the central row, in which the incident electron strikes, and decreases for all neighboring rows. It is clearly obvious that the shower profile is very similar for production cuts values up to 350 mm. The same situation is also given for the

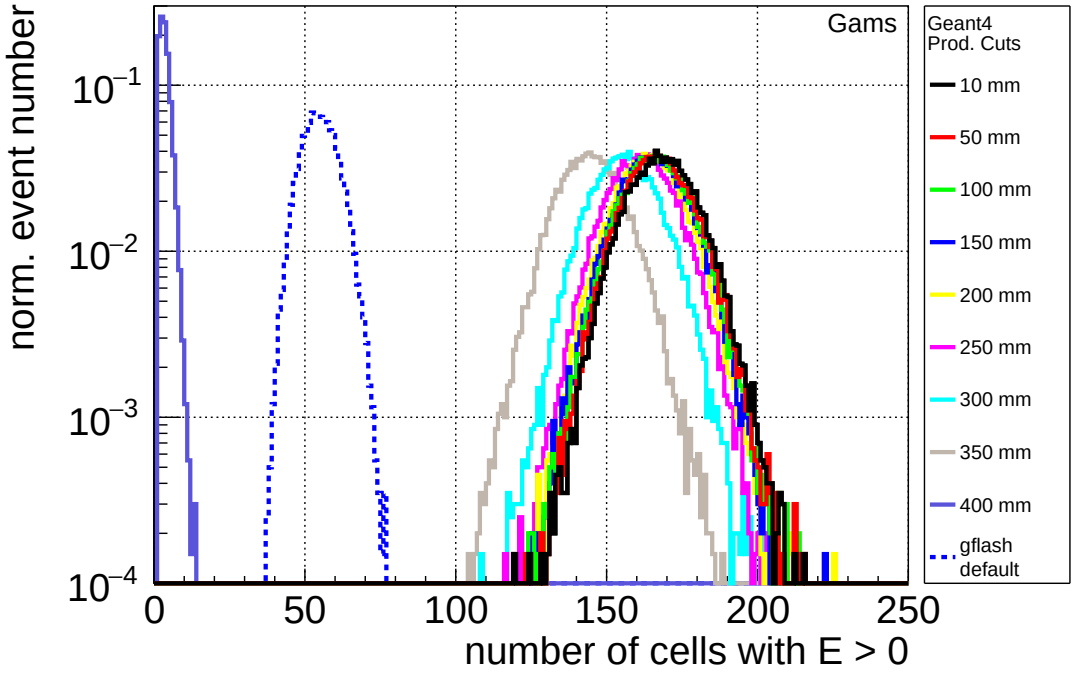

Figure 5.2: Production cuts tuning for Gams modules using a 40 GeV electron beam in the test calorimeter. The number of cells for smaller production cuts decreases with increasing production cuts. The TGEANT default value is 250 mm.

[3]An odd number was chosen to hit the test calorimeter in the center of the central module.
[4]The same diagram is obtained by summing up the columns.

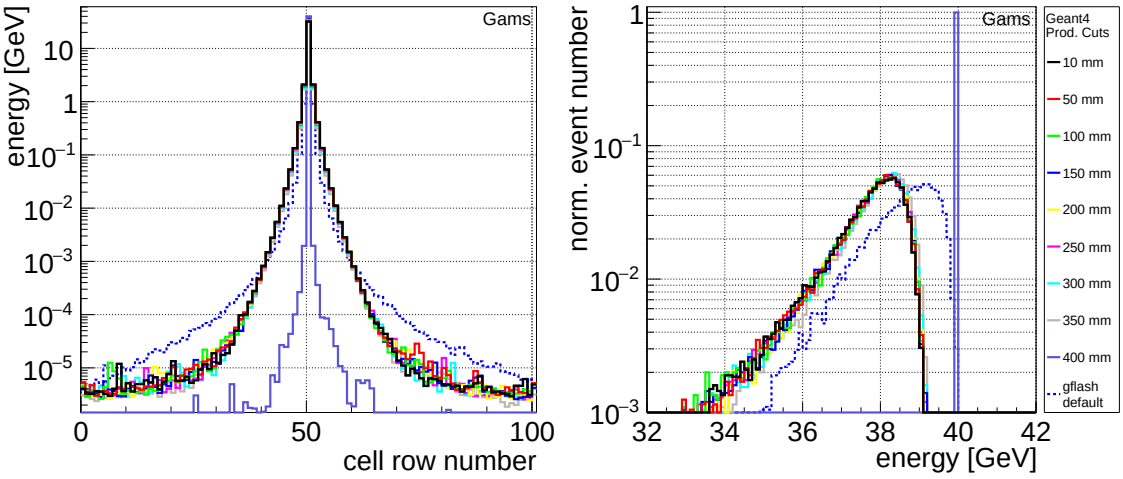

Figure 5.3: Production cuts tuning for Gams modules using a 40 GeV electron beam in the test calorimeter. Left: The energy profile shows the summed energy deposit for a given cell row number. The incident electron hits the test calorimeter in the center at row number 51. Right: The total energy deposit. The chosen default value of 250 mm still gives the same results as for smaller production cuts with the best performance.

total energy deposit, which is shown on the right-hand side of the figure. The expected lateral and longitudinal energy leakage is reproduced by the simulation and the measured energy deposit is below 40 GeV. For higher production cuts, however, the energy deposit matches the energy of the electron. It is therefore very important that the chosen production cuts stay below this threshold.

The new default production cuts for the different ECAL modules are presented in Tab. 5.1. For the Gams modules, a value of 250 mm was chosen, since this value reproduces the same results for the radial shower profile and the number of cells with an energy deposit compared to the smallest production cuts, which have been proven to be in good agreement with the experimental measurement, at the shortest processing time. The same simulations are also presented with the default GFlash tuning in Fig. 5.2 and 5.3. The results are not satisfactory, but the performance boost of a factor of 10 to 50 indicates the need for a GFlash tuning for TGEANT.

5.4 GFlash Tuning

The GFlash algorithm is parameterized by a sizeable number of parameters. A tuning of all parameters results in a very large number of different combination possibilities and has no reasonable chance of success regarding the needed processing time. A tuning of the radial profile was aimed at to obtain the same shower profile as for the new default production cuts of TGEANT. The tuning was repeated for all kind of ECAL modules using a 40 GeV electron beam that strikes the test calorimeter.

5.4.1 Radial Profile Parameterization

The radial probability density function is parameterized with a two component Ansatz according to Eq. (5.11) and (5.12). The two radii $R_{\text{core}}(\tau)$ and $R_{\text{tail}}(\tau)$ as

Table 5.1: Default production cuts for all ECAL modules in TGEANT. The default production cuts produce a realistic shower profile, but the cost of the high precision is the increased processing time. The processing time for a electromagnetic shower simulation is slowed down by a factor of 10^2 to 10^3 compared to the high production cuts, where the incident particle is mostly completely absorbed in the first calorimeter cell. The fast shower parameterization GFlash, however, is able to compensate this loss.

Module	Default Production Cuts		High Production Cuts		GFlash
	cut	t_{default}	cut	t_{high}	t_{GFlash}
Gams	250 mm	6.1 s	400 mm	0.006 s	0.63 s
GamsRH	250 mm	6.0 s	400 mm	0.008 s	0.7 s
Shashlik	50 mm	117 s	150 mm	0.26 s	8.4 s
Mainz	150 mm	5.6 s	250 mm	0.03 s	0.33 s
Olga	300 mm	7.3 s	400 mm	0.02 s	0.14 s

well as the weight of the core component $p(\tau)$ are further parameterized according to the following formulae [75][5]:

$$\begin{aligned} R_{\text{core}}(\tau) &= z_1 + z_2\tau \\ R_{\text{tail}}(\tau) &= k_1 \left\{\exp\left(k_3(\tau - k_2)\right) + \exp\left(k_4(\tau - k_2)\right)\right\} \\ p(\tau) &= p_1 \exp\left\{\frac{p_2 - \tau}{p_3} - \exp\left(\frac{p_2 - \tau}{p_3}\right)\right\}, \end{aligned} \tag{5.16}$$

with

$$\begin{aligned} z_1 &= t_1 \cdot (0.0251 + 0.00319 \cdot \ln E) \\ z_2 &= 0.1162 - 0.000381 \cdot Z \\ k_1 &= t_2 \cdot 0.659 - 0.00309 \cdot Z \\ k_2 &= 0.645 \\ k_3 &= -2.59 \\ k_4 &= t_3 \cdot (0.3585 + 0.0421 \cdot \ln E) \\ p_1 &= t_4 \cdot 2.632 - 0.00094 \cdot Z \\ p_2 &= 0.401 + 0.00187 \cdot Z \\ p_3 &= t_5 \cdot (1.313 - 0.0686 \cdot \ln E). \end{aligned} \tag{5.17}$$

The parameters $z_1 \ldots p_3$ are either constant or functions of $\ln E$ or Z. The given default numbers of GFlash were tuned for the liquid argon calorimeter of the H1 experiment as presented in Ref. [75]. The radial parameterization depends on the longitudinal shower depth τ and on nine different parameters with 16 variables in total. These 16 variables in an unknown parameter space are still very tough conditions for a tuning. The parameter set was therefore further reduced to five parameters $t_{1\ldots5}$. The energy-dependent terms z_1, k_4, and p_3 are scaled with the tuning parameters $t_{1,3,5}$. A second tuning parameter was further needed for both the

[5]For the sake of simplicity, all units are omitted in the following equations. However, the energy E is measured in units of the critical energy E_c and all lengths in units of the radiation length X_0.

tail component and the weight of the core component. The set of tuning parameters has been chosen and extended slightly in order to give a minimal parameter sample with which the tuning algorithm provides very good results. A tuning of material-dependent terms was omitted.

5.4.2 Evolutionary Algorithm

Tuning the radial parameterization is a tough challenge, even with the reduced sample of five parameters. In combinatorial optimization problems, the brute force method is often the only one that finds the optimal solution. This method checks all possible combinations at the expense of a polynomial runtime. Apart from the long runtime, this method deals with the problem of the undefined parameter space, in which the parameters $t_{1...5}$ can take continuous values. An evolutionary algorithm was therefore developed, which is an optimization technique to find a well approximating solution. The evolutionary algorithm is inspired by biological evolution and typically uses the same terminology. It uses the mechanisms of selection, recombination, and mutation to simulate the evolution of all individuals in a population over several generations. Individuals with a higher fitness are preferred in the process of selection. New individuals are created by the process of recombination and mutation. An evolutionary algorithm does not necessarily find the optimal solution of a problem but it provides a very good approximation without having to make any assumptions about the underlying parameter space. Figure 5.4 shows the general scheme of the evolutionary algorithm that was developed for the GFlash tuning.

Initialization

A set of the five parameters $t_{1...5}$ is defined as an individual, which therefore represents a possible solution to the problem. The size of the population is 200 individuals according to the size of the batch system on which the algorithm was

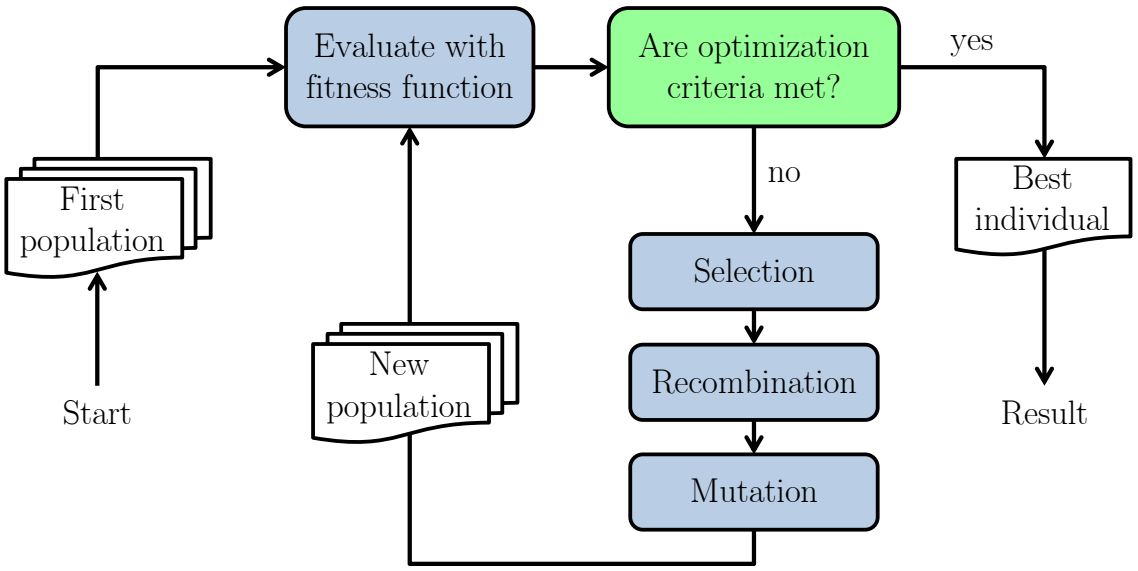

Figure 5.4: General scheme of the evolutionary algorithm that was developed for the GFlash tuning.

running. The first population consists of 200 randomly initialized individuals. The range limit for each parameter is specified between

$$0.2 < t_i < 5, \tag{5.18}$$

to limit the maximal deviation from the GFlash default parameter to a factor of 5. However, the upper and lower bounds are only used for the initialization.

Fitness Function

The shower propagation is simulated with the tuning parameter set of all individuals that represent the current population. To gather a significant amount of statistics for each parameter set, 50k events with the 40 GeV electron beam have been simulated. The quality of each possible solution is determined by a so-called fitness function.

An optimal solution parameterizes the electromagnetic shower in perfect agreement with the simulated shower using Geant4 tracking and the new TGEANT production cuts. This involves the shower profile as well as the cluster size. According to Eq. (5.7), only cells with an energy deposit above the threshold of 200 MeV are taken into account. Energy fluctuations according to the resolution of the calorimeter modules are not considered by the algorithm, since these effects cancel for a large amount of statistics and have no impact on the mean value of the cluster size.

The fitness function $F(t_{1...5})$ assesses the agreement of the shower profile $F_{\text{profile}}(t_{1...5})$ and the agreement of the cluster size distribution $F_{\text{cluster size}}(t_{1...5})$ of GFlash, which uses the given parameter set $t_{1...5}$, in comparison with the ones of Geant4 tracking. The fitness function is defined with the following value range:

$$F(t_{1...5}) = F_{\text{profile}}(t_{1...5}) + F_{\text{cluster size}}(t_{1...5}), \tag{5.19}$$

with

$$\begin{aligned} F_{\text{profile}}(t_{1...5}) &\in [0, 0.7] \quad \text{and} \\ F_{\text{cluster size}}(t_{1...5}) &\in [0, 0.3]\,. \end{aligned} \tag{5.20}$$

The higher the value of the fitness function, the better the parameter set. A result with $F(t_{1...5}) = 1$ represents the optimal solution, but the aim of the evolutionary algorithm is rather to find an excellent approximation.

The agreement of the shower profile F_{profile} is calculated for the five central rows of the shower profile, where most of the energy deposit is expected. It depends on the ratio r_i of the energy deposit of GFlash and Geant4 for each of the five rows with the row number i:

$$r_i = \mathcal{R}\left(\frac{E_{\text{GFlash}}(i)}{E_{\text{Geant4}}(i)}\right) \quad \text{for} \quad 48 \leq i \leq 52, \tag{5.21}$$

using the ratio function

$$\mathcal{R}(x) = \begin{cases} x & \text{for } x < 1 \\ x^{-1} & \text{else} \end{cases} \quad \text{with} \quad \mathcal{R}(x), r_i \in [0, 1]. \tag{5.22}$$

The functional form of the fitness function influences the selective pressure, which characterizes the probability of selecting the best individual of the population compared to the probability of selecting the average individual. If the selection pressure is too low, bad individuals remain in the population and the evolutionary algorithm may converge to a random search. The agreement f_i of the five central rows is therefore only assessed for ratios $r_i > 0.5$:

$$f_i = \begin{cases} (r_i - 0.5) \cdot 2 & \text{for } r_i > 0.5 \\ 0 & \text{else} \end{cases} \quad \text{with} \quad f_i \in [0, 1]. \tag{5.23}$$

The results f_i of the central row and the two neighboring rows are weighted with a factor of 3 or 2 relative to the two outermost rows. The fitness function for the shower profile therefore reads:

$$F_{\text{profile}} = \frac{f_{48} + 2f_{49} + 3f_{50} + 2f_{51} + f_{52}}{9} \cdot 0.7. \tag{5.24}$$

The last term accounts for the defined value range in Eq. (5.20).

The fitness of the cluster size $F_{\text{cluster size}}$ is evaluated in a similar way. The ratio and agreement f are calculated for three bins of the cluster size distribution, which describes the probability of a cluster size. The central bin is defined as the cluster size of the Geant4 distribution with the highest probability and is denoted as j. The agreement of this bin is weighted with a factor of 2 relative to the two neighboring bins:

$$F_{\text{cluster size}} = \frac{f_{j-1} + 2f_j + f_{j+1}}{4} \cdot 0.3. \tag{5.25}$$

Selection, Recombination, and Mutation

All individuals of the current population are rated by the fitness function. The processes of selection, recombination, and mutation are used to build up a new population in order to reiterate the procedure. The procedure can be stopped either after a certain number of generations or when the fitness function of the best individual exceeds a defined upper limit. Typically, about 30 iterations were simulated for each module type. Compared with the brute force method, the total processing time is marginal[6].

The 20 fittest individuals are selected and mutated slightly to preserve their good parameters in the next generation. In the process of mutation, the parameters are modified on percent level according to

$$t_i' = t_i \cdot p \cdot r, \tag{5.26}$$

using a uniformly distributed random number $r \in [-1, 1]$. The obtained parameter sets $t'_{1\ldots5}$ form the 20 first individuals of the new population. The modification parameter p is adjusted to 3 %.

[6] In total, $30 \cdot 200 = 6000$ different individuals were processed for each kind of ECAL module. Using the brute force method, only the combinations of $\sqrt[5]{6000} = 5.70$ different values for each of the five parameters $t_{1\ldots5}$ could have been tested in the same time.

To account for a completely new set of parameters in the next generation, 20 individuals are again initialized randomly within the parameter bounds. This ensures that the algorithm always explores the full parameter space. A pure limitation to the parameter set of the fittest individuals of the last generation would end up in some kind of "inbreeding". This is equivalent to the convergence of the solution to a local optimum.

The rest of the population is generated by the combination of two individuals. The concept of tournament selection shows a good performance. Here, two pairs of individuals are randomly selected from the population. The two fittest individuals of each pair are chosen to combine to two new individuals, which randomly share the parameters of their "parents". The principle of the tournament selection is illustrated in Fig. 5.5. Finally, the parameters of the new individuals are fluctuated with a higher value $p = 5\,\%$.

5.4.3 Results

The evolutionary algorithm was used to tune the GFlash parameters for all electromagnetic module types. Again, the results for the Gams modules are presented in this section, for all others, consult Appendix C.2. Figure 5.6 shows the shower profile obtained from the new tuning parameters in comparison with Geant4 tracking. An excellent agreement could be accomplished for the three central rows or the nine central modules, respectively, which are used in the Kolosov reconstruction algorithm for the impact position determination. The energy deposit for all other modules is 3-4 magnitudes lower. The improvement compared to the default GFlash tuning parameters is remarkable. The second objective of the evolutionary algorithm was the tuning of the cluster size distribution. The convincing results are presented in Fig. 5.7.

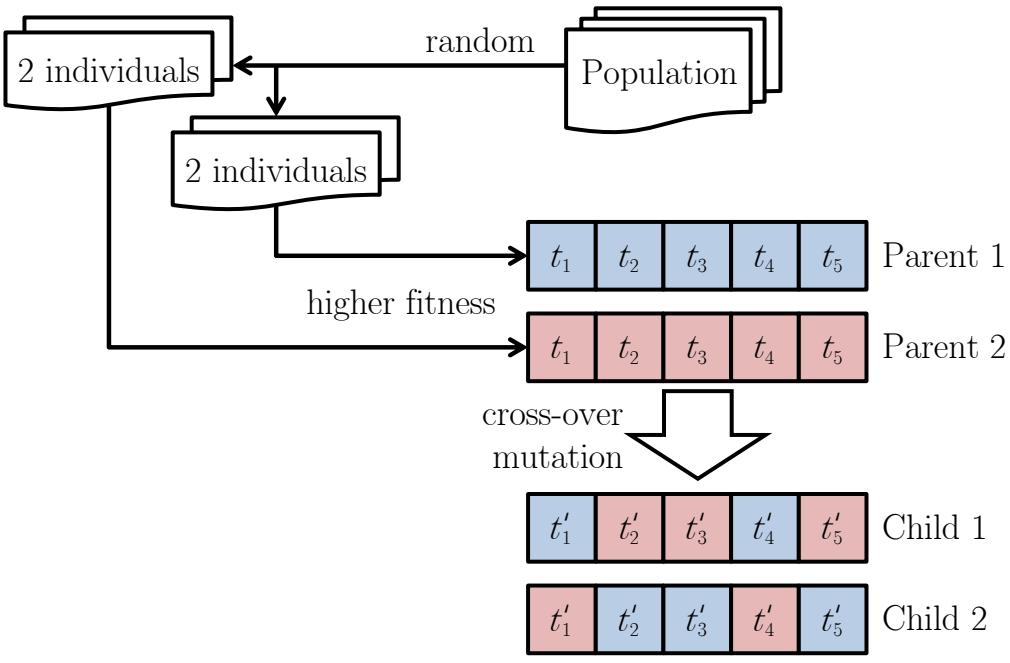

Figure 5.5: Principle of the tournament selection in the evolutionary algorithm.

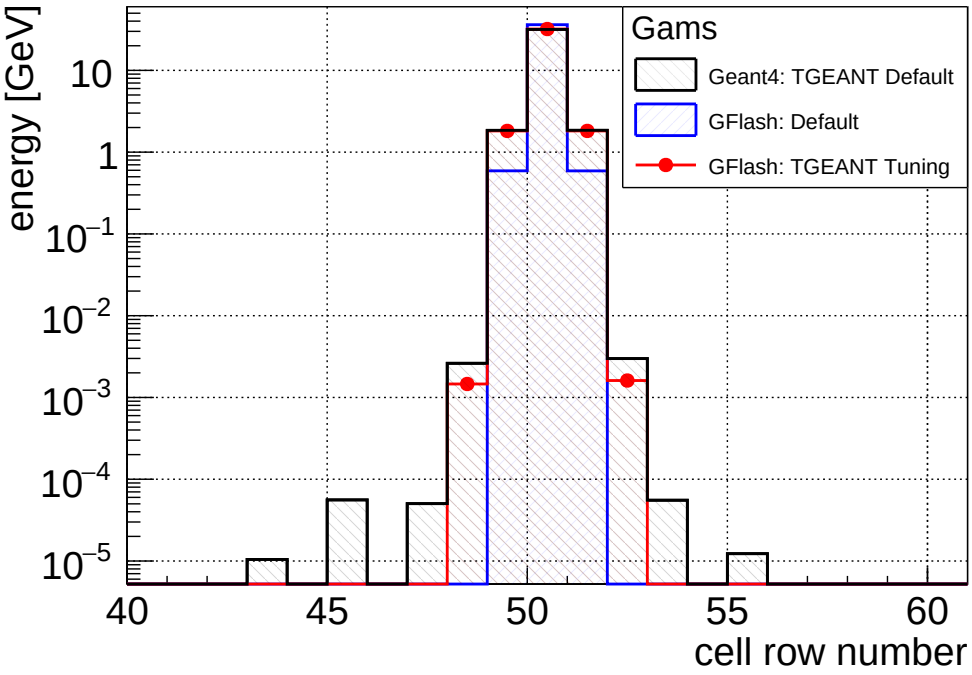

Figure 5.6: Shower profile for Gams modules simulated in the test calorimeter with a 40 GeV electron beam. The tuned GFlash parameterization (red points) shows an excellent agreement with Geant4 tracking (black).

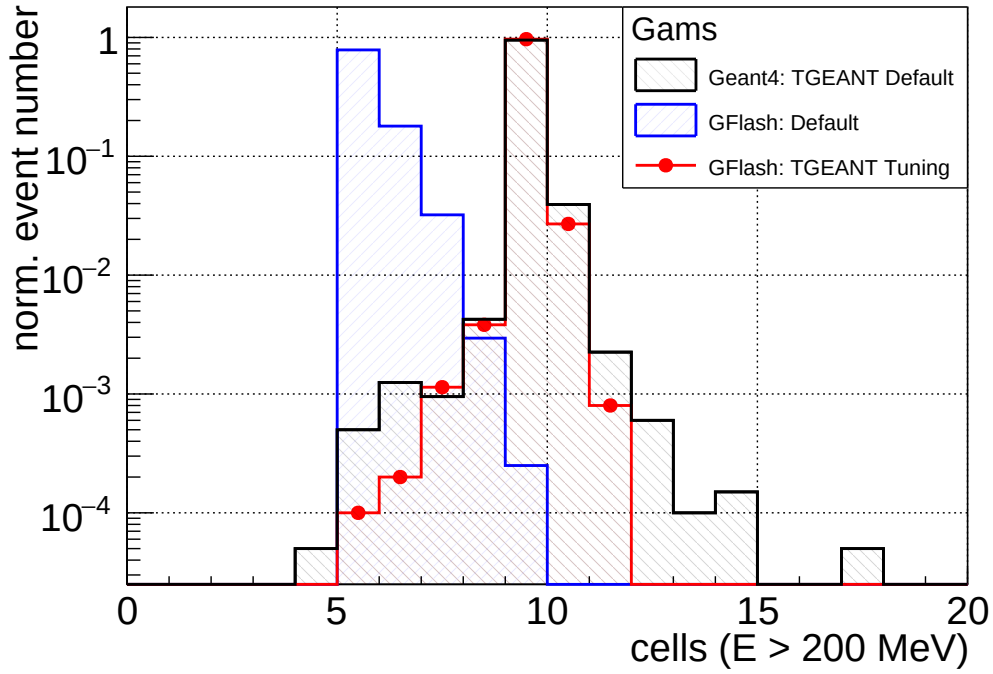

Figure 5.7: Cluster size for Gams modules simulated in the test calorimeter with a 40 GeV electron beam. Only cells with an energy deposit above the 200 MeV threshold are considered here.

Besides the radial shower propagation, the energy deposit in the sensitive part of the calorimeter modules is an important quantity. GFlash distributes discrete energy spots in the GFlash region according to Eq. (5.8). Only energy spots that are placed in a sensitive volume are recognized by the calorimeter readout of TGEANT. The sum of all energy spots within one module gives the total energy deposit for that cell. Unlike the shower profile and cluster size, the cluster energy distribution is not explicitly tuned by the algorithm. An additional energy calibration is therefore needed to scale the mean cluster energy obtained from the new GFlash parameterization according to Geant4 tracking. This energy scaling is implemented in the calorimeter readout and affects only the energy spots that are produced by GFlash and not the energy deposit of particle tracks, which originate from Geant4 tracking. The energy distributions for the different methods are shown in Fig. 5.8. Note that the energy scaling for GFlash only changes the mean cluster energy and not the form of the distribution. But even without the additional scaling, a huge improvement was achieved regarding the new GFlash parameters in contrast to the default ones.

The final tuning parameters for all modules are summarized in Tab. 5.2. The Gams and GamsRH modules are very similar. The size of the modules and the density of the lead glass are identical, only the material composition is slightly different in order to make the GamsRH modules, which are enriched with 0.2 % of cerium, more radiation hard. However, a difference in the shower propagation was neither the result for Geant4 tracking nor for the GFlash parameterization. Consequently, the same tuning parameters are used for both module types. It is also remarkable that the evolutionary algorithm results in similar parameters for

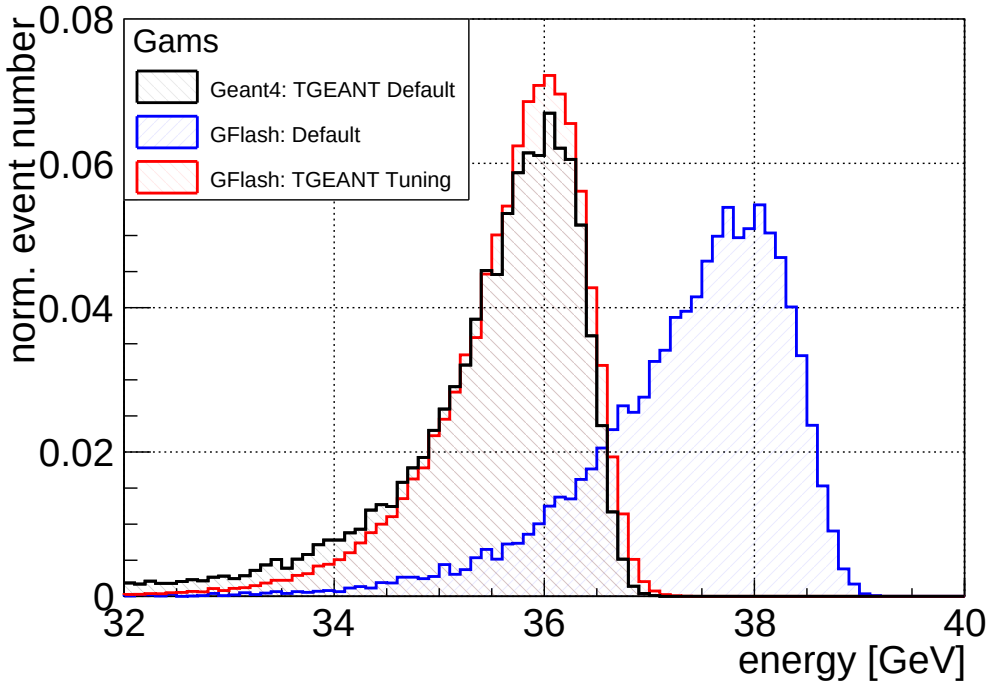

Figure 5.8: Cluster energy for Gams modules simulated in the test calorimeter with a 40 GeV electron beam. The tuned GFlash energy distribution is slightly scaled so as to match the energy distribution of the default Geant4 tracking.

Table 5.2: GFlash tuning parameters for the radial shower distribution and the internal TGEANT energy spot scaling factor.

	t_1	t_2	t_3	t_4	t_5	$\frac{E_{\text{Geant4}}}{E_{\text{GFlash}}}$
Lead glass						
Gams	2.92254	1.30558	1.56211	1.99612	0.401956	0.985
GamsRH	2.92254	1.30558	1.56211	1.99612	0.401956	0.985
Mainz	2.39534	1.2321	1.35387	0.788724	1.575	1
Olga	4.61113	1.84528	2.63962	0.971324	2.24568	1.01
Shashlik						
ECAL0	2.10973	1.56049	0.355487	1.03159	1.30813	0.92
ECAL1/2	2.11428	1.56157	0.355937	1.00855	1.32474	0.974

the two kinds of Shashlik modules. The only difference here is the larger transverse size of the ECAL0 Shashlik modules.

The radial shower parameterization of GFlash was tuned in order to produce the same results as Geant4 tracking with the default TGEANT production cuts. The tuning was performed with a 40 GeV electron beam, but it was also verified for an electron beam with 20 and 80 GeV. Consequently, the full energy range of photon clusters up to 160 GeV is covered, since the first interaction of the photon is always covered by Geant4 tracking.

5.5 Energy Calibration

The simulated energy deposit needs to be calibrated so that it matches the energy of the incident particle after the cluster reconstruction. The diagrams presented in this sections show the results of the energy calibration for all ECAL2 modules. The same figures for the different modules of ECAL2 and all other modules are presented in Appendix C.3. The Monte Carlo sample used here comprises exclusive single photon and π^0 events. Both processes were generated with the HEPGen++ event generator for the analysis of the 2012 DVCS pilot run data.

The standard energy calibration solely relies on one linear calibration factor b, which scales the Monte Carlo energy according to Eq. (5.1). In a first calibration approach, only the calibration factor b was tuned for each module type. A bisection method was used for this purpose. This is a very simple and robust method that finds the best calibration factor by repeatedly bisecting a interval in which the optimum lies. The subinterval is selected according to the energy difference distribution $E_{\text{gen}} - E_{\text{reco}}$, where the energy of the incident particle and the reconstructed cluster energy are denoted by E_{gen} and E_{reco}. If the mean value of the distribution is positive, $E_{\text{gen}} > E_{\text{reco}}$, the upper subinterval is chosen to increase the scaling parameter b and thus the cluster energy. The resulting energy difference distribution with the default calibration procedure for all ECAL2 modules is presented in Fig. 5.9.

The distribution shows an asymmetric behavior, which is a consequence of the energy-dependent leakage of the calorimeter. This is illustrated in Fig. 5.10, which

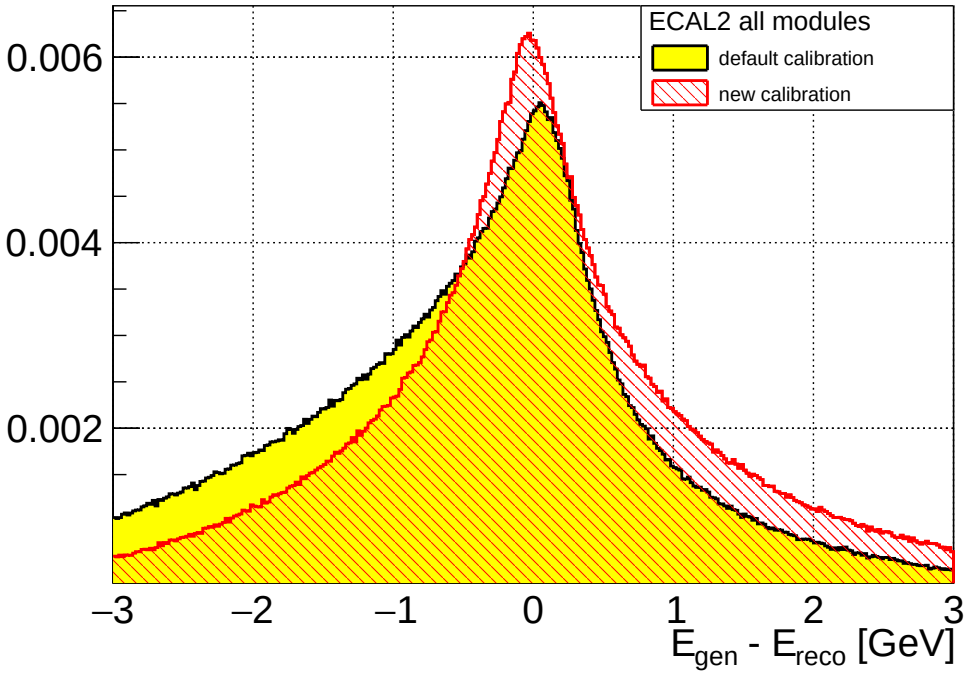

Figure 5.9: Distribution of the energy difference for the default and new ECAL calibration for all ECAL2 modules. The Monte Carlo sample comprises exclusive single photon and π^0 events with the 2012 setup.

shows the energy difference of the incident photon and the reconstructed cluster energy $E_{\text{gen}} - E_{\text{reco}}$ as a function of the photon energy E_{gen}. The calibration factor b was adjusted in order to fit the mean value. The energy difference is positive for the smallest photon energies and decreases to negative values with increasing photon energies. The left plot in Fig. 5.10 shows the most probable values of the energy difference for small intervals of E_{gen}. To account for the energy-dependent leakage of the calorimeter, a new method was developed to calibrate the Monte Carlo cell energy:

$$E_{\text{calib}} = a + E_{\text{MC}} \cdot b + E_{\text{MC}}^2 \cdot c. \tag{5.27}$$

The new calibration factor c adds a quadratic energy dependence. This is needed to correct the longitudinal energy leakage, which increases quadratically with the energy of the incident particle. The second new factor a adds an energy-independent offset that is dominant for lower energies. All three parameters need to be adjusted independently for each kind of module in order to compensate the longitudinal and lateral energy leakage as well as the energy deposit in the outermost cells of the shower, which are below the energy threshold and therefore not considered in the cluster reconstruction.

The new calibration method works iteratively. The most probable energy difference values are fitted according to Eq. (5.27). The result after the first iteration is

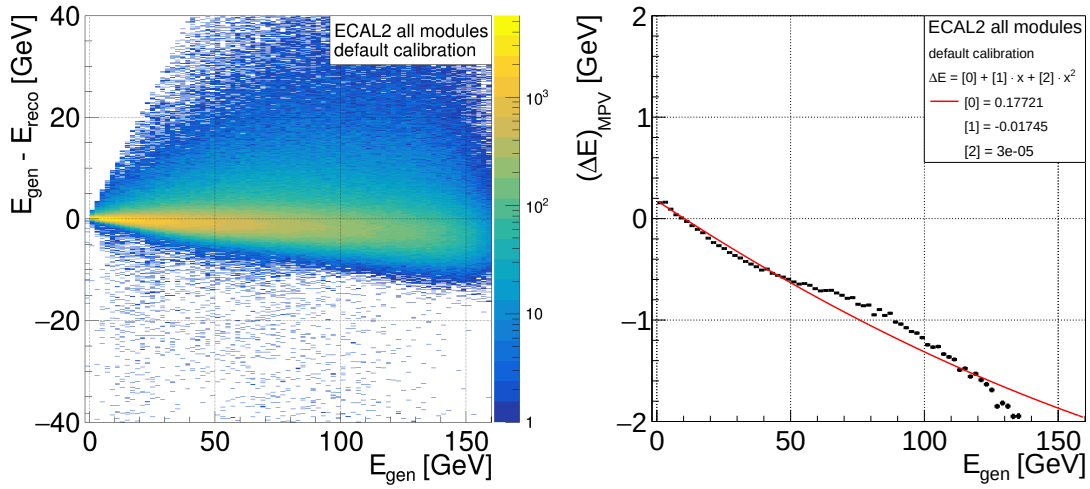

Figure 5.10: Reconstructed cluster energy as a function of the generated energy using the default calibration method. The energy difference is not zero over the full energy scale. The most probable values for the different energies are shown on the right-hand side. The red line shows the result of the fit using Eq. (5.27).

presented on the left-hand side of Fig. 5.10. The obtained fitting parameters $x_{0,1,2}$ are added with a scaling factor to the current parameters after each iteration:

$$\begin{aligned} a_{i+1} &= a_i + x_0 \cdot 0.8 \\ b_{i+1} &= b_i + x_1 \cdot 0.1 \\ c_{i+1} &= c_i + x_2 \cdot 0.8. \end{aligned} \tag{5.28}$$

The scaling factors are needed so as not to overshoot the calibration procedure. A final cluster energy calibration after the cluster reconstruction would be technically much simpler. In this case, a scaling factor is not necessary and only one iteration would be sufficient. But this violates the equal treatment of Monte Carlo and real data. The cell-wise energy calibration before the cluster reconstruction is therefore indispensable.

The result of the new calibration method after 10 iterations is presented in Fig. 5.11. Although the structure of the electromagnetic calorimeters is quite complex, with a variety of different module types and a central hole, the results of the new calibration method are extremely satisfactory. The same also holds for the energy difference distribution that is shown in comparison with the default calibration method in Fig. 5.9. A symmetric distribution was achieved. The final energy calibration factors for all modules are listed in Tab. 5.3.

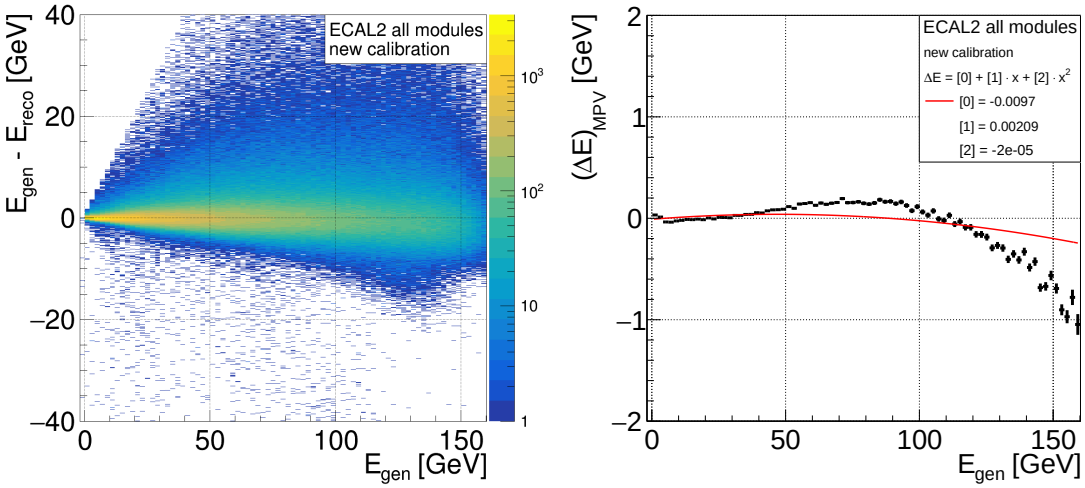

Figure 5.11: Reconstructed cluster energy as a function of the generated energy for ECAL2 using the new calibration method. The most probable values for the different energies are shown on the right-hand side. The red line shows the result of the fit using Eq. (5.27).

Table 5.3: Energy calibration parameters of the new calibration method.

	a [GeV]	b^{-1}	c [GeV^{-1}]
ECAL0			
Shashlik	0.008555	0.822936	-0.00436835
ECAL1			
Shashlik	0.035421	0.903328	-0.00029262
Gams	0.046408	0.924021	-0.00061808
Mainz	0.028876	0.976197	-0.00001672
Olga	-0.000131	0.959805	-0.00028311
ECAL2			
Shashlik	0.081229	0.914545	0.00010977
Gams	0.133243	0.917406	0.00169120
GamsRH	0.131134	0.914713	0.00118497

6. Trigger Simulation and Optimization for the 2016/17 DVCS Run

Trigger logic simulation is a very important part of the new Monte Carlo software. In the experiment, events are only recorded if the readout of detector signals is triggered. Different trigger systems are in use simultaneously, each of them covering a specific kinematic region. The events are flagged with the trigger bit of the activated trigger systems that allows for an event selection in the analysis. TGEANT needs to simulate the trigger system in order to provide a comparability with the real data.

This chapter addresses the topic of trigger simulation in TGEANT. The flexible design of the software also enables using the trigger simulation in the reconstruction software CORAL. A combination of the trigger simulation with the hodoscope and trigger efficiencies is made possible by this unique feature.

In preparation for the long DVCS run in 2016/17, an optimization of the trigger system was performed. This involved changes of the hodoscope geometries as well as optimizations of the alignment and of the trigger matrices. These modifications were based on Monte Carlo studies with TGEANT and are presented at the end of this chapter.

6.1 Trigger Simulation

Trigger simulation is a crucial part of the event loop to keep the comparability of the Monte Carlo sample with real data. Like most of the features in TGEANT, the trigger system is also based on back-end systems. The trigger plugin, which needs to be customized for each physics program and year of measurement, defines all input parameters. These are for example the coincidence timing windows of the hodoscope stations or the trigger bit positions of the different trigger systems. Several trigger plugins are provided, which are optimized for different physics programs at the COMPASS experiment. The following section focuses on the trigger simulation for the GPD program as it is used for 2012 and 2016/17, which solely relies on the hodoscope systems, cf. Sec 3.5. The important kinematic regions are covered by the middle (MT), ladder (LT), outer (OT), and large angle spectrometer trigger (LAST). Several other triggers are also in use during the measurement, such as a random trigger or a pure calorimeter trigger. These triggers, however, are of no interest for the data analysis and are therefore not simulated.

The trigger simulation is performed at the end of the event loop. At first, the time t_{hit} for all hodoscope hits is converted into a so-called reduced time t_{red} that is independent of the detector position:

$$\begin{aligned} d &= \left| \vec{x}_{\text{hit}} - \begin{pmatrix} 0 \\ 0 \\ z \end{pmatrix} \right| \\ t_{\text{red}} &= t_{\text{hit}} - \frac{d}{\text{c}}. \end{aligned} \tag{6.1}$$

The distance d between the detector hit position $\vec{x}_{\text{hit}}$ and the beam starting position, which is located on the beam axis at z, is calculated first. The hodoscope system is designed to measure coincidences of intersecting muon tracks in two planes that are installed at different positions in the experimental hall. The muons are highly relativistic due to their large momenta. The time of flight for the distance d is therefore calculated with the speed of light c and subtracted from the hit time t_{hit} to get an estimate at which time the incident particle would have been at the beam start position assuming that it is a muon. This method is extremely helpful since it works independently from the hodoscope positions and is used to consider the timing delays that are installed in the experiment to bring the signals of two planes in coincidence.

The event loop starts with the primary beam particle at $t = 0$. The reduced time for the scattered muon is therefore always $t_{\text{red},\,\mu'} \approx 0$ and it can be used to filter out pile-up particles that start outside the timing window $t_{\text{pile-up}}$:

$$|t_{\text{red}}| < t_{\text{pile-up}}. \tag{6.2}$$

This timing window is used to simulate the time gate of the trigger system in the COMPASS experiment. The evaluation of the timing window around $t = 0$ is not an imbalance in favor of Monte Carlo. It rather takes into account that the trigger signal in the experiment sets the time of the physically interesting interaction to zero as well.

The next step of the trigger simulation verifies if there are any coincidences. Each hit in the upstream plane of the hodoscope system is combined with all hits in the downstream plane. A combination is accepted if the following two criterias are fulfilled. The reduced hit times for the upstream and downstream located hodoscope planes, t_{up} and t_{down}, need to be recorded within the coincidence time window t_i for the corresponding hodoscope system:

$$|t_{\text{up}} - t_{\text{down}}| < t_i \qquad \text{for} \qquad i \in \{\text{MT, LT, OT, LAST}\}\,. \tag{6.3}$$

The second criterion is the geometrical correlation of the hit pair. This is tested with trigger matrices. The hodoscope planes of the different hodoscope systems are constructed with up to 32 channels. The trigger matrices $\mathcal{M}$ are therefore quadratic with 32 rows and columns. The entries of the matrices are Boolean values, whereby an accepted hit combination is stored as 1 and a rejected combination as 0. The trigger logic therefore checks for the entry $\mathcal{M}_{ud}$, where u and d are the channel numbers of the upstream and downstream plane.

The trigger mask for the event is made up of different trigger bits, listed in Tab. 6.1. The trigger logic for the DVCS pilot run in 2012 is illustrated in Fig. 6.1. In the case of the target pointing method as it is used for LAST and OT, the vertical positions of the muon tracks are measured with horizontal scintillator slats. The matrix shape is therefore diagonal. A triangular coincidence matrix is used for the energy loss trigger. Regarding the middle trigger, the vertical scintillator slats, which are needed for the energy loss trigger, are supplemented by horizontal slats in order to reduce the fake trigger rate released by particles with small angles the middle trigger has to deal with. All coincidence time windows are listed in Tab. 6.2. The proton trigger, which was not used in the analysis of the 2012 data, is simulated only with the geometrical correlation.

6.2 Trigger Efficiencies

Efficiencies of the hodoscope slats have an influence on the trigger mask of the event and need therefore to be considered in the trigger simulation. Efficiencies, however, should rather be taken into account on the level of the event reconstruction than in TGEANT. For that reason, the source code of the trigger simulation is part of the library libEvent that is linked in CORAL. At the beginning of the event reconstruction, the trigger mask is optionally renewed.

The efficiencies of the different hodoscope channels can be extracted from the real data measurement. In a nutshell, pure calorimeter trigger events are selected. Here a

Table 6.1: Trigger bits for the 2012 DVCS pilot run.

Trigger System	Trigger Bit Position
CAMERA	0
MT	1
LT	2
OT	3
LAST	9

Table 6.2: Coincidence time windows of the trigger logic for the DVCS pilot run in 2012.

Trigger System	Timing Window
$t_{\text{pile-up}}$	10 ns
t_{MT}	4 ns
t_{LT}	6 ns
t_{OT}	8 ns
t_{LAST}	15 ns

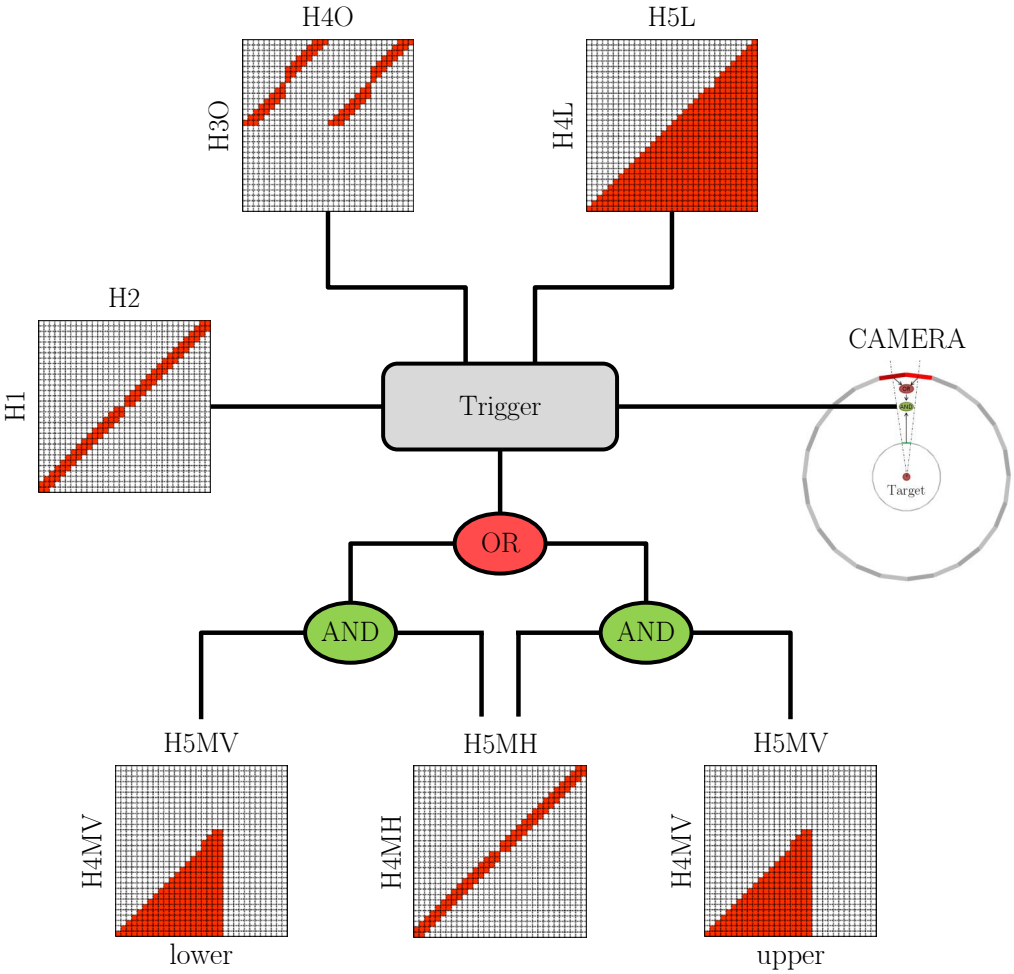

Figure 6.1: Trigger logic for the DVCS pilot run in 2012. Hit combinations in the upstream and downstream planes of a hodoscope system are analyzed for their geometrical correlation using the trigger matrices. The red-colored entries in the trigger matrices label the accepted channel combinations. Regarding the middle trigger, an additional coincidence between the vertical and horizontal system is requested. Picture adopted from Ref. [77].

minimal energy deposit in one of the hadronic calorimeters is required. In addition, a vertex inside the target cell and the scattered muon need to be reconstructed. The scattered muon is extrapolated to the different hodoscope planes for all selected events. The number of extrapolated tracks N_{extrap} is counted for each hodoscope channel. The efficiency ϵ for a channel is obtained by

$$\epsilon = \frac{N_{\text{hit}}}{N_{\text{extrap}}}, \tag{6.4}$$

where N_{hit} is the number of extrapolated tracks with an associated hit. For 2012, a list of hodoscope efficiencies for each channel was provided by Ref. [78]. The efficiencies are transferred to CORAL via the input options file, which also involves other TGEANT related extensions and which is presented in Appendix B.3.

Technically speaking, the efficiencies for the hodoscope channels are used to modify the trigger matrices $\mathcal{M}$. The Boolean values are replaced by floating-point numbers. For each hodoscope channel efficiency the corresponding row or column in the trigger matrix is scaled with the efficiency. A uniform random number $r \in [0, 1]$ decides that the hit pair triggers if the following condition is fulfilled:

$$r < \mathcal{M}'_{ud} = \mathcal{M}_{ud} \cdot \epsilon_u \epsilon_d \cdot \epsilon'_{ud}. \tag{6.5}$$

A trigger condition consequently depends on the efficiencies of both hodoscope channels ϵ_u and ϵ_d.

This method is also capable of considering inefficiencies that originate from the electronic devices that are used in the experiment for the fast trigger decision. The efficiencies for each channel combination, which are denoted by ϵ'_{ud}, can be adjusted individually. This feature can for example also be used to correctly simulate changing trigger efficiencies in different periods of data recording.

6.3 Optimization for the 2016/17 DVCS Run

In preparation for the long DVCS run in 2016/17, a new design for the central holes of the two outer trigger hodoscopes has been planned with the aim of closing previously existing acceptance holes. The layouts of the two planes, as they have been used for the 2012 DVCS pilot run, are shown in Fig. 6.2 and 6.3.

HO3 is installed behind the second dipole magnet SM2. It consits of 16 horizontally aligned scintillator slats with a length of 2.5 m, which are split into two parts with 8 channels each. The gap in-between offers space for two more scintillator slats. To further increase the size of the central hole, plexiglass light guides cut of the four innermost scintillator slats.

HO4 is installed more downstream directly behind the second muon filter, cf. Fig. 3.4. The total size of the hodoscope is therefore larger to cover the same angular acceptance as the hodoscope HO3. It is split into two halves, which have a small overlap of 10 cm, limiting the maximal length of the scintillators to 2.5 m. The central hole of H04 is asymmetric and shifted by 40 cm in bending direction of the two dipole magnets (shown on the right-hand side in Fig. 6.3). The bending direction is horizontal and also parallel to the alignment of the scintillator slats. The central two slats in non-bending direction are omitted.

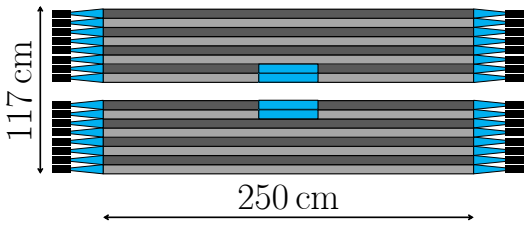

Figure 6.2: Layout of the trigger hodoscope HO3 as used in the DVCS pilot run in 2012. In the central part of the innermost four hodoscopes, plexiglass light guides are installed to increase the size of the central hole. The high rate of the unscattered muon beam would otherwise significantly lower the trigger efficiency for these four scintillator slats. HO3 is shown in the same scale as HO4 in Fig. 6.3. Picture adopted from Ref. [79].

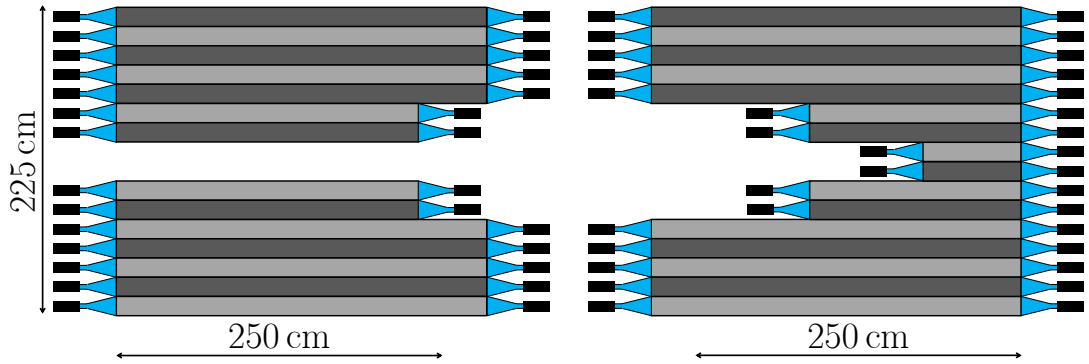

Figure 6.3: Layout of the trigger hodoscope HO4 as used in the DVCS pilot run in 2012. The two halves of the hodoscope, which are shown here apart, are installed in the experimental hall with an overlap of 10 cm. The scale of the picture is the same as for HO3 in Fig. 6.2. Picture adopted from Ref. [79].

6.3.1 Setup for the Simulation

A special setup for the simulation was used in order to optimize the geometries of the two outer hodoscope planes. This setup only includes the relevant parts of the COMPASS spectrometer that are needed for a correct simulation of the hodoscope-based trigger system. These are: the LH_2 target, the two dipole magnets SM1 and SM2, as well as all hodoscopes. The LH_2 target is used in combination with a muon beam file in order to simulate a realistic vertex distribution. Especially the vertex distribution along the beam axis z has a strong influence on the angular acceptance of the different trigger systems. This is further discussed in Sec. 6.3.3. The two magnets are essential for a correct simulation of the muon bending. The alignment of all components is the same as in 2012. All other detector systems are not needed for the geometrical studies of the hodoscopes, thus deliberately omitted here to accelerate the performance of the event simulation. Consequently, the photon track, which would be absorbed by the electromagnetic calorimeter, is not considered at all in this study.

The analysis is performed with the Toolbox. The event reconstruction adds no systematic bias to the track reconstruction of the scattered muon. This also ap-

plies to the omitted detector systems the muon has to cross. The analysis for these kinds of geometrical studies is therefore only related to the Monte Carlo output. The purpose of this study is mainly the optimization of the central holes of the two outer trigger hodoscopes for the DVCS measurement in 2016/17. The used event generator is the exclusive single photon generator of HEPGen++. The simulated events are weighted according to the DVCS cross section model that is implemented in HEPGen++ [45]. This model is based on an adaption of the original FFS model, which has been modified for the kinematical range of the COMPASS-II experiment [80–82]. The kinematics used for this Monte Carlo study are restricted to the following limits:

$$\begin{aligned} 1.0\,(\mathrm{GeV/c})^2 < \quad & Q^2 < 20.0\,(\mathrm{GeV/c})^2 \\ 0.005 < \quad & x_{\mathrm{Bj}} < 0.27 \\ 0.05 < \quad & y < 0.9. \end{aligned} \tag{6.6}$$

These are the same kinematic regions as used in the analysis of the 2012 DVCS pilot run data [83]. The trigger simulation works with the same timings and trigger matrices as used in 2012. All optimizations are therefore with respect to the settings of the pilot run.

To measure all muon tracks at the z positions of the two outer trigger hodoscopes, two dummy detectors[1] are added to the setup, which have no central holes and are able to detect all the crossing muons. The spatial frequency distributions of the muon tracks at the two hodoscope positions are presented in Fig. 6.4 with the full event sample. The azimuthal angle for the scattered muon is generated uniformly, while in the laboratory frame the polar angle θ depends on the kinematic variables [25]:

$$Q^2 \overset{\mathrm{lab}}{=} \frac{4EE'}{\mathrm{c}^2} \sin^2\left(\frac{\theta}{2}\right) = \frac{(1-y)\cdot E^2}{\mathrm{c}^2} \sin^2\left(\frac{\theta}{2}\right). \tag{6.7}$$

A minimal polar angle θ_{min} follows from the lower limits of $Q^2 = 1.0\,(\mathrm{GeV/c})^2$ and $y = 0.05$. The decreasing event numbers for increasing θ angles is a consequence of the Rutherford cross section. Both effects in combination with the bending of the two dipole magnets are clearly visible in Fig. 6.4. The x-axis is defined horizontal, the y-axis vertical. The bending direction of the magnetic field goes in positive x direction.

6.3.2 Geometrical Modifications of the Outer Trigger

Two aspects concerning the geometrical modifications of the outer trigger hodoscopes are important here. First of all, the number of physically interesting events that are recorded in the experiment should be maximized. This means that the number of simulated events without any trigger mask should be minimized. However, the technical realization also needs to be kept in mind. Especially in close distance to the beam axis, a high particle flux in a hodoscope channel lowers the efficiency significantly. The new central holes of the two outer trigger hodoscopes have been

[1] A dummy detector consits of air and uses the same readout as a tracking detector with the difference that a dummy detector can also detect particles that do not deposit any energy such as photons. This readout is not in use for an analysis-oriented Monte Carlo production, though it is very useful for Monte Carlo studies.

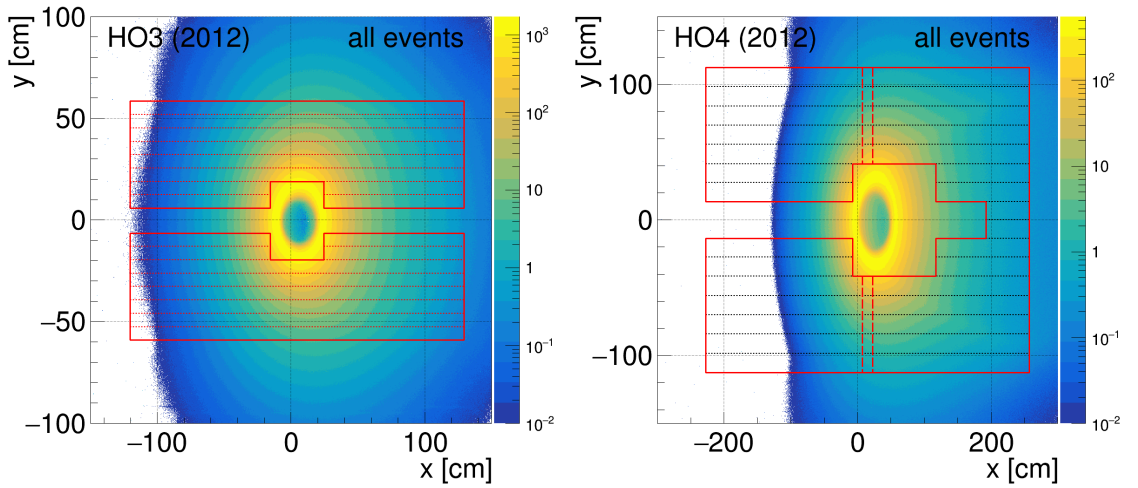

Figure 6.4: Spatial frequency distribution of the scattered muons at the z position of HO3 (left) and HO4 (right). The red lines show the shapes of the two hodoscopes for 2012, the red dotted lines the horizontal scintillator slats. The two halves of HO4 are installed with a small overlap, which is illustrated with the dashed lines. The event sample is weighted according to the DVCS model in HEPGen++. The distribution covers five magnitudes on the z-axis, with a lower limit at 10^{-2}. The event count for the white-colored bins is therefore $< 10^{-2}$.

designed in order to trigger all events that are not already triggered by another system while also minimizing the required particle flux.

Middle Trigger Events

Figure 6.5 shows the spatial frequency distribution of the scattered muons for all middle trigger events. The scintillator slats of the middle trigger hodoscopes (HM4 and HM5) are smaller than the ones of the outer trigger hodoscopes and installed vertically and closer to the beam axis. H4M is installed directly behind HO4 and perfectly covers the acceptance hole on the large x side (right-hand side of the central HO4 hole in Fig. 6.5). However, the central hole on the small x side is 6 cm too large as illustrated with blue lines in the figure. Consequently, the four existing scintillator slats on the negative x side of the hodoscope have been replaced with longer slats.

A significant part of the scattered muon tracks that realease the middle trigger cross the scintillators of HO3. For that reason, the new central hole was increased in y direction by two slats, reducing the particle flux in these two channels. The central parts of the two affected scintillator slats have been removed and replaced by plexiglass light guides. The spatial coverage of the middle trigger also allows to slightly enlarge the new central hole in horizontal direction. The new design of the central hole of HO3 is indicated by black-colored dashed lines in Fig. 6.5. The hole has also been moved in positive x direction.

Ladder Trigger Events

The same diagrams for all ladder trigger events are presented in Fig. 6.6. The vertical scintillator slats of the ladder trigger hodoscopes are installed in bending

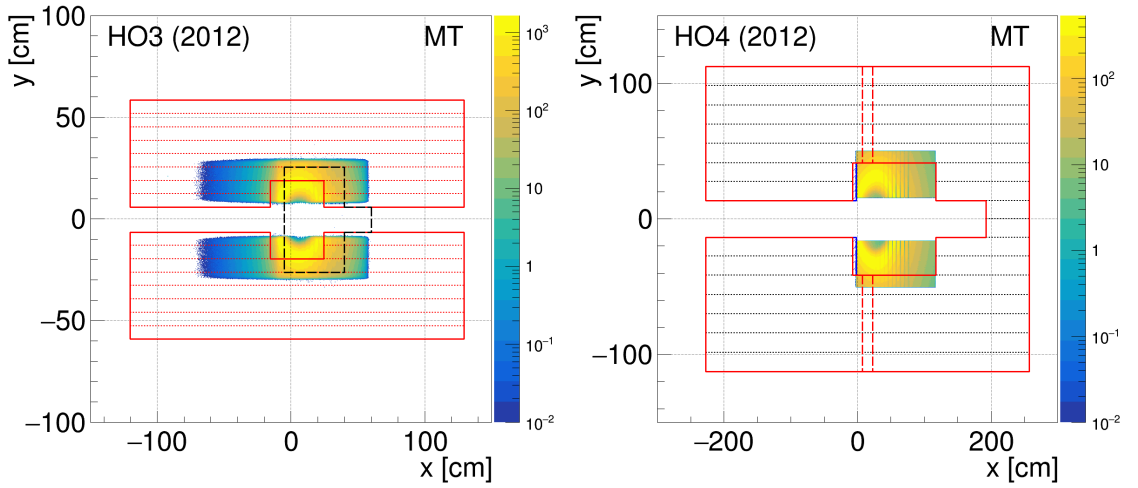

Figure 6.5: Spatial frequency distribution of the scattered muons at the z position of HO3 (left) and HO4 (right) for all middle trigger events. The red lines indicate the shapes of the two hodoscopes for 2012. The black-colored dashed lines illustrate the new central hole of HO3 for 2016/17. The blue lines show the acceptance hole between HO4 and the middle trigger hodoscopes.

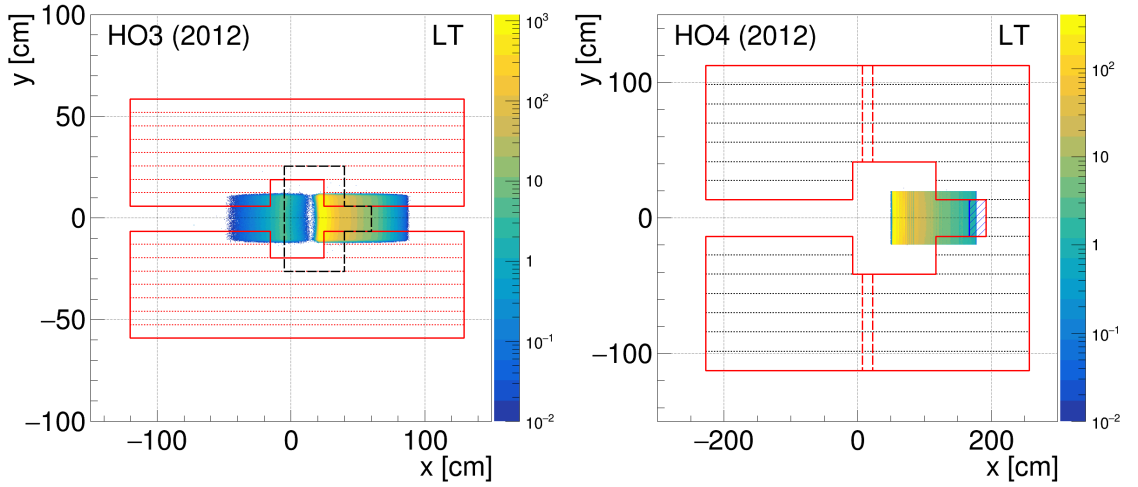

Figure 6.6: Spatial frequency distribution of the scattered muons at the z position of HO3 (left) and HO4 (right) for all ladder trigger events. The red lines indicate the shapes of the two hodoscopes for 2012. The black-colored dashed lines illustrate the new central hole of HO3 for 2016/17. The blue lines show the acceptance hole between HO4 and the ladder trigger hodoscopes.

direction and centered in vertical direction at $y = 0$. For this purpose, the length of the two new central scintillator slats of HO3 are built shorter on the positive x side, since this side is already covered by the ladder trigger. Here, the technical challenge is the installation of the intermediate light guides. To maintain the double-sided readout, central slabs, which are placed very close to the beam axis, are usually individually connected with a high reflective foil to create an air light guide. However, their mechanical stability is only ensured on short distances. For the two new central slabs of HO3, a combination of an air light guide for the central part and a plexiglass light guide has therefore been installed.

The spatial frequency distribution of HO4 reveals that the two short scintillator slats on the large x side need to be enlarged to close the gap to the end of the ladder trigger. Two new scintillator slats have been installed.

Large Angle Spectrometer Trigger Events

All events that are prompted by the large angle spectrometer trigger are shown in Fig. 6.7 for the sake of completeness. The two LAST trigger hodoscopes H1 and H2 are both installed in the large angle spectrometer, directly in front of the RICH-1 detector and SM2. The size of their central hole perfectly fits the size of the two outer trigger hodoscopes.

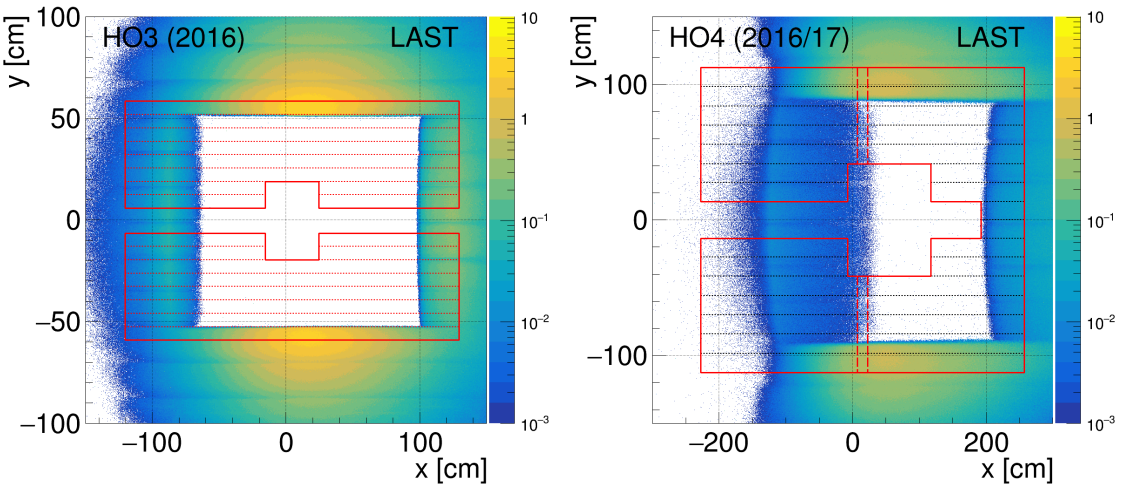

Figure 6.7: Spatial frequency distribution of the scattered muons at the z position of HO3 (left) and HO4 (right) for all large angle spectrometer trigger events. The events are weighted according to the DVCS model in HEPGen++. The red lines indicate the shapes of the two hodoscopes for 2012. The distribution covers four magnitudes on the z-axis, with a lower limit at 10^{-3}. The event count for the white-colored bins is therefore $< 10^{-3}$.

Optimized Outer Trigger Design for 2016/17

All remaining scattered muon tracks that are not activated by the middle, ladder, and large angle spectrometer trigger should be detected by the outer trigger. New central slats have therefore been installed for both hodoscopes. The hole of HO3 has been enlarged and shifted towards bending direction. The scintillator slats of HO4

have been replaced in order to close the acceptance holes to the middle and ladder trigger hodoscopes. The optimized design of HO3 and HO4 are presented together with all remaining scattered muon tracks in Fig. 6.8.

To also allow for a measurement of the scattered muon tracks that are generated in close proximity to the beam axis with a small θ angle, cf. Eq. (6.7), the new central slats of HO4 on the non-bending side, which is not covered by the ladder trigger system, needs to be installed as close as possible to the beam axis. A lengthening of the scintillators is problematic due to the fact that the slats are read out on both sides with photo multiplier tubes. The photo multiplier tubes cannot be installed very close to the beam axis because of the high particle rate, thus a new design has been developed and installed. Each of the two new central scintillator slats has been extended by three smaller scintillator slats. Each of the six scintillator extensions has an individual length so as to portray the circular spatial frequency distribution of the scattered muons. The readout of the new elements is performed with silicon photo multiplier chips [84].

New Alignment for the Ladder Trigger

In non-bending direction, the new design of the HO4 central hole allows for a detection of all scattered muons with a polar angle down to θ_{min}. In bending direction, however, the scattered muons with small polar angles need to be detected either by the middle or the ladder trigger hodoscopes. Figure 6.8 reveals that some of these muons are not detected, thus the two ladder trigger hodoscopes need to be moved in x direction by $-3\,\text{cm}$ towards the central hole.

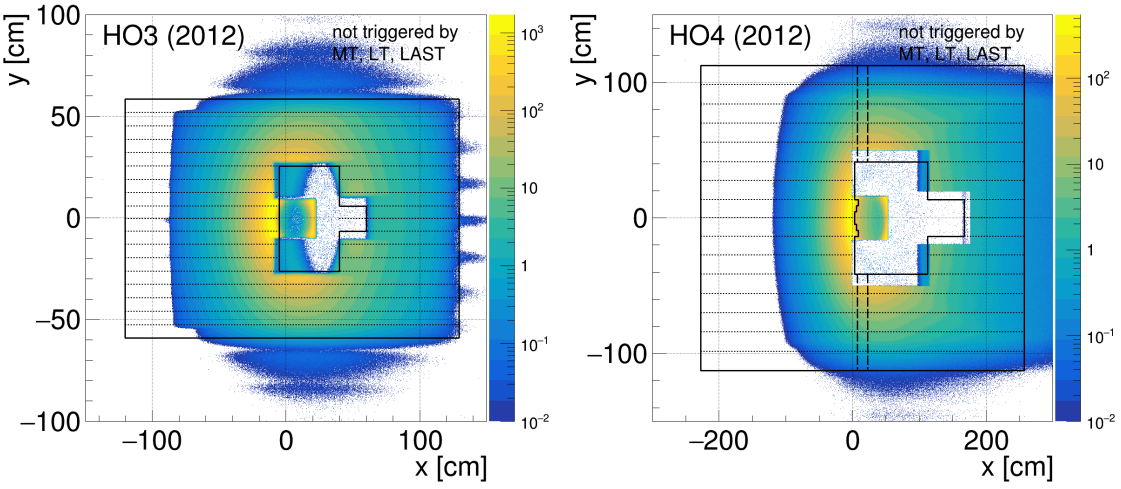

Figure 6.8: Spatial frequency distribution of the scattered muons at the z position of HO3 (left) and HO4 (right) that are not triggered by the middle, ladder, or large angle spectrometer trigger systems with the alignment of 2012. The design of the new central holes for the two outer trigger hodoscopes was optimized in order to measure these muon tracks. The new design for 2016/17 is indicated by the black lines. For the sake of clarity, the trigger simulation is performed with optimized trigger matrices.

6.3.3 Modified Trigger Matrices

A closer look at the spatial frequency distributions for the middle and ladder trigger hodoscopes reveals some irregularities. These are most visible for HO4, which is installed in close distance to the middle and ladder trigger hodoscopes HM4 and HL4. An optimization of the trigger matrices solves this problem. The reason for this discrepancy is the length and position of the LH_2 target, which was newly constructed for the GPD program at COMPASS-II. The target cell extends over $z \in [-3261\,\text{mm}, -646\,\text{mm}]$, while the trigger system was originally designed for a shorter target length of 2 cells, each with a length of 60 cm, installed at $z = 0$. Consequently, the accepted channel combinations needs to be adjusted according to the new target position and also to the longer target length.

Figure 6.9 shows all scattered muon tracks at the position of HO4 that are not triggered by any hodoscope systems for the old design of 2012 and the new design of 2016/17 with the optimized trigger matrices. The trigger matrices of the outer and large angle spectrometer trigger have already been changed in preparation for the Drell-Yan run in 2014/15.

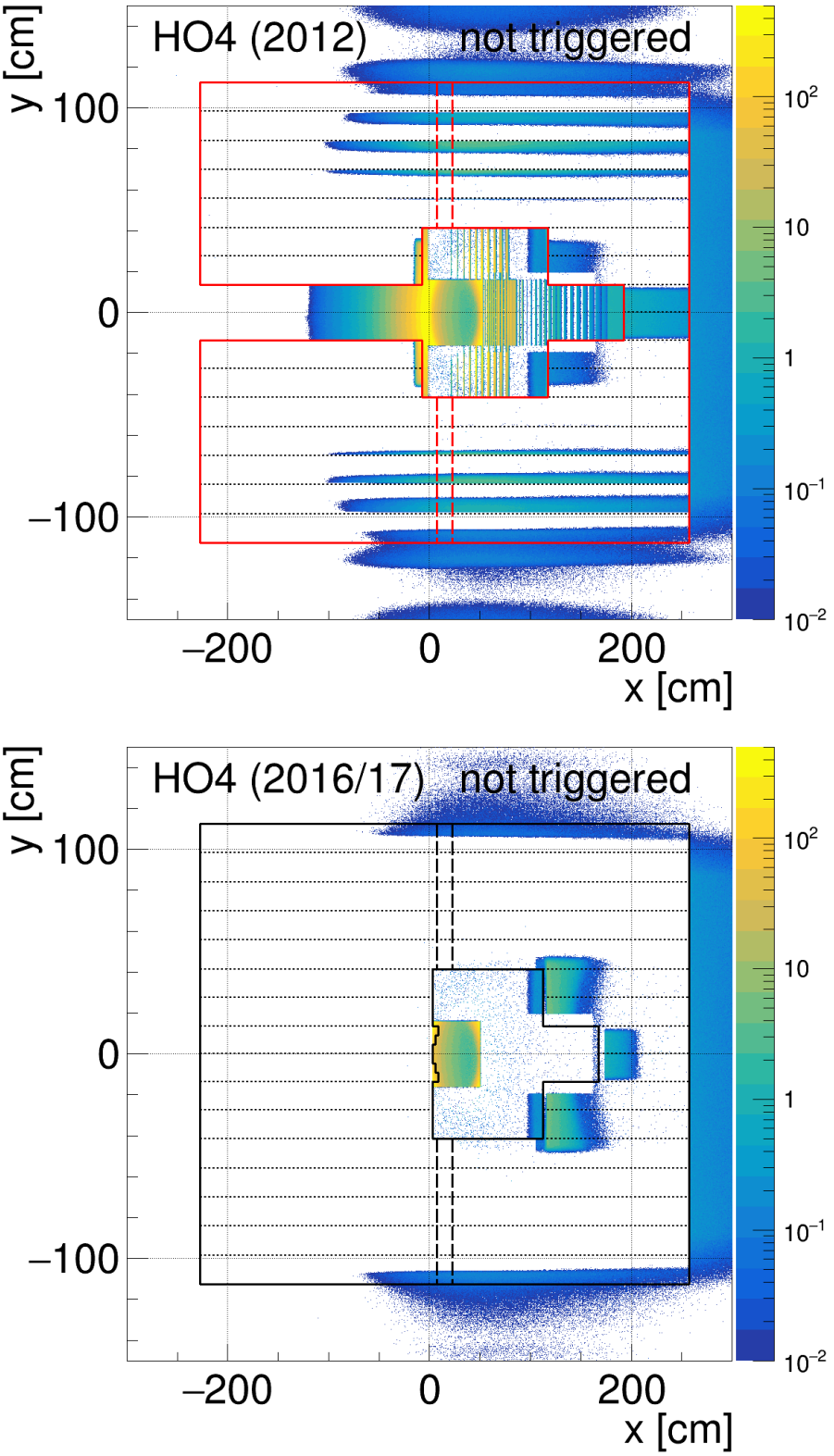

Figure 6.9: Spatial frequency distribution of the scattered muons at the z position of HO4 that are not triggered. The old design of 2012 is shown on top, the new design with the optimized trigger matrices is presented on bottom. The events are weighted according to the DVCS model in HEPGen++. Both plots are normalized to the same scale.

7. Usage of TGEANT for the Analysis of 2012 DVCS Pilot Run Data

In 2012, the setup of the COMPASS-II experiment was upgraded in preparation for the four-week-long DVCS pilot run. This chapter presents two examples of the data analysis in which the new Monte Carlo software TGEANT was successfully used for the first time.

A good knowledge of luminosity is essential for absolute cross section measurements and was therefore precisely measured using the beam flux counting method. A cross-check of these measurements was done with an alternative approach, which uses the structure function F_2 and which is strongly dependent on the acceptance of the experimental apparatus. The good agreement of both methods confirms, in reverse conclusion, the correct acceptance determination provided by TGEANT.

The new Monte Carlo software is also a crucial component of the exclusive single photon production analysis. Such an analysis is not possible without an acceptance correction, the π^0 background estimation, or the calculation and normalization of the Bethe-Heitler contribution.

7.1 Luminosity Determination for the 2012 DVCS Pilot Run

Luminosity is defined as the ratio of the production rate of scattering events $\mathrm{d}E/\mathrm{d}t$ to the interaction cross section σ:

$$\mathcal{L} = \frac{1}{\sigma}\frac{\mathrm{d}N}{\mathrm{d}t}, \tag{7.1}$$

which has the dimension of events per time per area. The integrated luminosity

$$L = \int \mathcal{L}\mathrm{d}t = \int \frac{1}{\sigma}\frac{\mathrm{d}N}{\mathrm{d}t}\mathrm{d}t = \frac{N}{\sigma} = \frac{N_{\mathrm{detected}}}{\sigma \cdot A} \tag{7.2}$$

is obtained by integrating the luminosity $\mathcal{L}$ over time. The number of measured events N_{detected} of a scattering reaction with the cross section σ depends on the acceptance A of the experimental apparatus and the integrated luminosity L. The wanted statistics can only be achieved by increasing the luminosity $\mathcal{L}$ or by extending the duration of the measurement.

In fixed target experiments, the integrated luminosity is connected to the particle flux Φ and the particle density $\rho_{\mathrm{T}} l_{\mathrm{T}}$ of the target, where ρ_{T} is the density of the target material and l_{T} the target length:

$$\mathcal{L} = \Phi \cdot \rho_{\mathrm{T}} l_{\mathrm{T}}. \tag{7.3}$$

The particle flux is equal to the rate of particles $\mathrm{d}N_{\mathrm{beam}}/\mathrm{d}t$ that pass the target:

$$\Phi = \frac{\mathrm{d}N_{\mathrm{beam}}}{\mathrm{d}t} \approx \frac{\Delta N_{\mathrm{beam}}}{\Delta t}, \tag{7.4}$$

where the last approximation becomes true if the rate of beam particle is constant over a finite interval in time.

7.1.1 Beam Flux Determination using Random Trigger Events

According to Eq. (7.4), a muon flux measurement at the COMPASS experiment is performed by counting all reconstructed beam tracks for all random trigger events during one spill:

$$\begin{aligned} \Delta N_{\mathrm{beam}} &= \text{number of reconstruced beam tracks,} \\ \Delta t &= \text{number of random trigger attemps} \times \Delta t_{\mathrm{RT}}. \end{aligned} \tag{7.5}$$

The time window of a random trigger event is denoted by Δt_{RT}. In the COMPASS experiment, a radioactive β^+ source is used as random trigger, where the decay $^{22}\mathrm{Na} \rightarrow {}^{22}\mathrm{Ne} + e^+ + \nu_e$ is measured.

The incoming beam particles are measured by the silicon and fiber detectors upstream of the target cell in combination with a momentum measurement provided by the BMS detectors. A beam track is classified as a reconstructed beam track if it crosses the entire target cell, is measured within Δt_{RT}, and if it has a momentum between 140 GeV/c and 180 GeV/c.

7.1.2 Luminosity Calculation using the F_2 Structure Function

The inclusive differential DIS cross section, which is given in Eq. (2.12), can be reformulated and expressed as [18]:

$$\frac{\mathrm{d}^2\sigma}{\mathrm{d}x_{\mathrm{Bj}}\mathrm{d}Q^2} = \frac{4\pi\alpha_{\mathrm{em}}^2}{Q^4 x_{\mathrm{Bj}}} F_2(x_{\mathrm{Bj}}, Q^2) \left\{ 1 - y - \frac{Q^2}{4E^2} + \left(1 - \frac{2m_\mu^2}{Q^2}\right) \frac{y^2 + Q^2/E^2}{2\left(1 + R(x_{\mathrm{Bj}}, Q^2)\right)} \right\}, \tag{7.6}$$

where m_μ is the muon mass and $R(x_{\mathrm{Bj}}, Q^2)$ is the ratio of the $\gamma^* p$ total cross section for longitudinal and transverse photon polarizations [25]:

$$R(x_{\mathrm{Bj}}, Q^2) \equiv \frac{\sigma_L}{\sigma_T} = \frac{F_2(x_{\mathrm{Bj}}, Q^2)\left(1 + 4M^2 x_{\mathrm{Bj}}^2/Q^2\right)}{2x_{\mathrm{Bj}} F_1(x_{\mathrm{Bj}}, Q^2)} - 1. \tag{7.7}$$

According to Eq. (7.2), the integrated luminosity can be obtained by measuring N_{detected} events, for which the absolute cross section is already known. The absolute cross section can be calculated as an integration over a phase space interval Ω of the double-differential cross section from Eq. (7.6):

$$\sigma(\Omega) = \int_\Omega \frac{\mathrm{d}^2\sigma}{\mathrm{d}x_{\mathrm{Bj}}\mathrm{d}Q^2} \mathrm{d}x_{\mathrm{Bj}}\mathrm{d}Q^2. \tag{7.8}$$

The phase space interval Ω is the region in x_{Bj} and Q^2 the analysis is restricted to. $F_2(x_{\mathrm{Bj}}, Q^2)$ is obtained from the Tulay's fit to the world data, which completely includes the phase space region Ω [85]. For the ratio $R(x_{\mathrm{Bj}}, Q^2)$, a parameterization called R1998 is used [86]. The integrated luminosity therefore reads:

$$L = \frac{1}{\sigma(\Omega)} \sum_{i=1}^{N_{\mathrm{detected}}} \frac{\eta_i}{A_i}, \tag{7.9}$$

where η_i denotes the radiative correction factor and A_i the acceptance of the i'th event. Consequently, the acceptance, which is obtained by using TGEANT, is a key feature of this method. The Monte Carlo sample was produced with the LEPTO event generator for μ^+ and μ^- beam, see Sec. 7.2.1. The analysis is accurately described in Ref. [87]. Additional corrections for the DAQ and veto dead times are also applied.

7.1.3 Comparison of the Two Methods

Figure 7.1 presents the comparison for the flux determination of both methods as a function of the spill number for a typical μ^+ and μ^- run (number 108284 and 108336). The flux is specified as the number of beam particles that have been measured in one spill. The results of the beam counting method using random trigger events are taken from Ref. [88]. The statistical precision of this method depends on the number of counted beam particles during one spill, which is large compared to the number of measured DIS reactions, and thus yields lower statistical uncertainties. The flux measurements for each spill of both methods are consistent

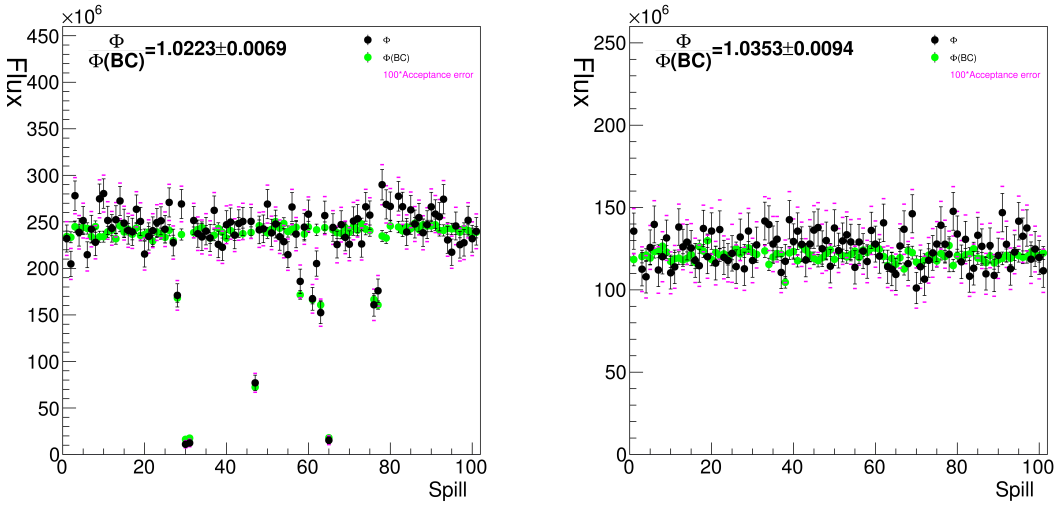

Figure 7.1: Spill-wise comparison of the flux determination results of the two methods for the μ^+ run 108284 (left-hand side) and the μ^- run 108336 (right-hand side). The statistical uncertainties from counting the events are drawn black. The acceptance uncertainties for the method using the structure function F_2 and the acceptance determination from TGEANT are drawn stacked (magenta) and scaled with a factor of 100. The systematic uncertainty of 5.4 % is not depicted [87].

within their statistical uncertainties. However, a systematic deviation of the two methods is visible. The average flux values per run differ by about 3 %, which cannot be explained by the statistical uncertainties.

The relative systematic uncertainty of the second method, which relies on counting the inclusive scattering events using the structure function F_2, is estimated to 5.4 %, where 5.0 % are assigned to the chosen Tulay model for F_2 and 2.0 % account for the radiative corrections η. The systematic uncertainty of the acceptance correction is negligibly small. Within their statistical and systematic uncertainties, both methods are consistent over the full period of measurements. This cross-check proves that the beam flux measurements are correct but also shows the acceptance determination of TGEANT to be accurate.

7.2 Monte Carlo Estimates for Exclusive Single Photon Production

Monte Carlo estimates are indispensable for the analysis of exclusive single photon or pion productions. A large Monte Carlo production with TGEANT was therefore provided. The following subsections roughly summarize the exclusive single photon analysis for the DVCS pilot run data from 2012, with a special focus on the use of the new Monte Carlo software and its agreement with the measurements. A detailed description of the analysis is given in Refs. [83, 89].

7.2.1 Monte Carlo Production for 2012

The measured particle flux directly serves as an input parameter for the Monte Carlo mass production with TGEANT, which was performed with the 2012 DVCS

Table 7.1: TGEANT Monte Carlo mass production for the analysis of the 2012 DVCS pilot run. The events were simulated without pile-up, which was added before the reconstruction in CORAL. The average processing times per event therefore do not differ for μ^+ and μ^- for the same event generator. The total processing time refers to TGEANT only.

Event Generator	Model	Beam particle	Statistics	Processing time avg./event	total
LEPTO		μ^+	86,516,309	5.31 s	5317 d
LEPTO		μ^-	99,624,225		6123 d
HEPGen++	γ (DVCS/BH)	μ^+	7,697,451	15.65 s	1394 d
HEPGen++	γ (DVCS/BH)	μ^-	12,249,968		2219 d
HEPGen++	$\pi^0 \to \gamma\gamma$	μ^+	9,470,633	17.31 s	1897 d
HEPGen++	$\pi^0 \to \gamma\gamma$	μ^-	8,166,514		1636 d
HEPGen++	$\rho^0 \to \pi^+\pi^-$	μ^+	9,233,747	7.02 s	750 d
HEPGen++	$\omega \to \pi^+\pi^-\pi^0$	μ^+	6,368,890	10.75 s	792 d
HEPGen++	$\phi \to K^+K^-$	μ^+	6,532,990	5.94 s	449 d
			Σ 245,860,727		Σ 20577 d

setup. The alignment was imported from the real data alignment file that was used for the 2012 data reconstruction. The Monte Carlo production incorporates deep inelastic muon-proton scattering using the event generator LEPTO and several exclusive processes generated by HEPGen++. Table 7.1 gives an overview of the full production. The important processes for the analysis of exclusive single photon production are the DVCS and BH generator as well as the exclusive π^0 generator. All processes, except for ρ^0, ω, and ϕ, were generated with μ^+ and μ^- beam, since the rate of pile-up particles differ and is higher for μ^+ beam, cf. Fig. 7.1.

The TGEANT production was processed on the grid computing centers in Karlsruhe (GridKA) and Lyon (IN2P3). A total processing time of about 56 years was needed to provide an appropriate statistics for the four-week-long DVCS run. The average duration for the event reconstruction is approximately 0.8 s per event, which results in an additional processing time of 6.2 years.

7.2.2 Exclusive Single Photon Selection

In 2012, only middle, ladder, and outer trigger events are used. The kinematic variables are restricted to the limits given in Eq. 6.6. In order to select exclusive single photon production events $\mu p \to \mu' p' \gamma$, the measured and simulated events need to fulfill the following criteria.

The vertex position needs to be reconstructed inside the target using the incoming and scattered muon, whose four-vectors are denoted by k and k'. Only the scattered muon can be identified by the track reconstruction of the COMPASS experiment, since the recoiled proton scatters outside of the spectrometer acceptance and the photon needs to be detected in one of the three electromagnetic calorimeters.

All reconstructed ECAL clusters are therefore inspected for a minimal cluster energy. The threshold values are adjusted for each ECAL individually according

to the expected photon energy distribution. All clusters with an associated track are rejected and exactly one neutral cluster is forced. The photon's four-vector q' is obtained from the reconstructed cluster and vertex positions as well as from the measured cluster energy.

The proton is traced in the CAMERA detector and identified by a measurement of the z positions in geometrically correlated rings. An additional time of flight measurement allows for a determination of the recoiled proton four-momentum p'.

Exclusivity Variables

With the use of the CAMERA detector, the kinematics are overdetermined, which permits a comparison of the spectrometer prediction of the recoiled proton four-momentum $p'_{\text{spec}} = k + p - k' - q'$ and the measurement with the CAMERA detector p'. The differences between the azimuthal angles $\Delta\phi$ and transverse momenta Δp_{T}, which are measured either by the spectrometer or the CAMERA detector, are defined as:

$$\begin{aligned} \Delta\phi &= \phi(p'_{\text{spec}}) - \phi(p'), \\ \Delta p_{\text{T}} &= |p_{\text{T}}(p'_{\text{spec}})| - |p_{\text{T}}(p')|, \end{aligned} \tag{7.10}$$

where the transverse momenta are measured with respect to the direction of the incident muon. Another exclusivity criterion is a minimal requirement for the missing mass, which is calculated from the four-momentum balance of all incoming and outgoing particles:

$$M_X^2 \mathrm{c}^2 = (k + p - k' - p' - q')^2 . \tag{7.11}$$

The vertex position inside the target cell is known from the measurement of the incident and scattered muon and can be used in combination with the measured hit position in the outer ring B to estimate the z position in the inner ring A. The difference Δz_{A} is defined as the difference between the measured and estimated z positions in the inner ring:

$$\Delta z_{\text{A}} = z_{\text{A, measured}} - z_{\text{A, estimated}}. \tag{7.12}$$

These four exclusivity variables are used to apply exclusivity conditions to remove non-exclusive events from the selected sample. Their distributions are shown in Fig. 7.2, in comparison with the TGEANT Monte Carlo estimate for the BH and DVCS contribution as well as the π^0 background. The normalization of the π^0 background estimate and the BH contribution are discussed in the following sections. The total weight of the Monte Carlo events is calculated according to:

$$w = \omega_{\text{BH}} + \sqrt{0.6} \cdot \omega_{\text{I}} + 0.6 \cdot \omega_{\text{DVCS}}. \tag{7.13}$$

Since there is no DVCS model yet that perfectly fits the amount of DVCS events, the weights of the DVCS and interference term are scaled with respect to the DVCS weights from the FFS model in HEPGen++.

An excellent agreement of the four exclusivity variables with the measured data was achieved with the new Monte Carlo description of the COMPASS experiment. The kinematic distributions of Q^2, x_{Bj}, and ν of the final event sample are presented in Fig. 7.3. TGEANT estimates the kinematic distributions accurately.

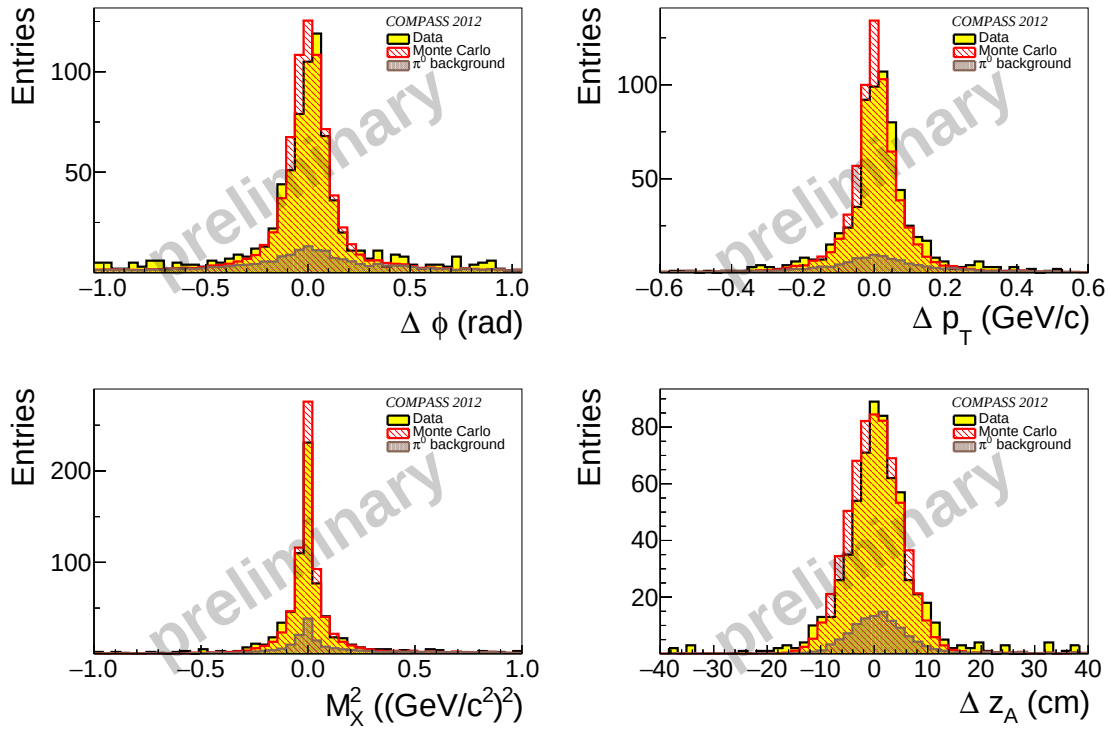

Figure 7.2: Exclusivity variables $\Delta\phi$ (top, left), Δp_{T} (top, right), M_X^2 (bottom, left), and Δz_{A} (bottom, right) for the analysis of the exclusive single photon production with the 2012 DVCS pilot run data. The real data is presented in yellow. The whole Monte Carlo estimate is shown in red while the π^0 contamination is shown in grey [90].

7.2.3 π^0 Background Estimate

The main source of background contribution come from exclusive π^0 ($\mu p \to \mu' p' \pi^0$) and SIDIS π^0 production. For these events, one photon of the π^0 decay is wrongly identified as the exclusive single photon candidate because either the energy of the second photon is below the energy threshold or the second photon is absorbed or emitted outside the acceptance of the electromagnetic calorimeters.

The former case, also referred to as visible leaking π^0 signal, can be extracted from the event sample. These events are used to normalize the two Monte Carlo contributions, which can be either studied by the HEPGen++ exclusive π^0 generator or by LEPTO. The invariant mass distribution for the two γ systems is shown in Fig. 7.4, where the two Monte Carlo contributions are individually normalized to the data. The two contributions are renormalized afterwards according to the ratio that reproduces the experimental data best. Studies have shown that HEPGen++ contributes with 10 % and LEPTO with 90 % [83].

The invisible π^0 background on the other side can only be estimated by Monte Carlo and cannot be extracted from the measurement. The mixed ratio of the LEPTO and HEPGen++ sample therefore provides an estimate for the complete π^0 background, which is crucial for the extraction of the pure DVCS cross section.

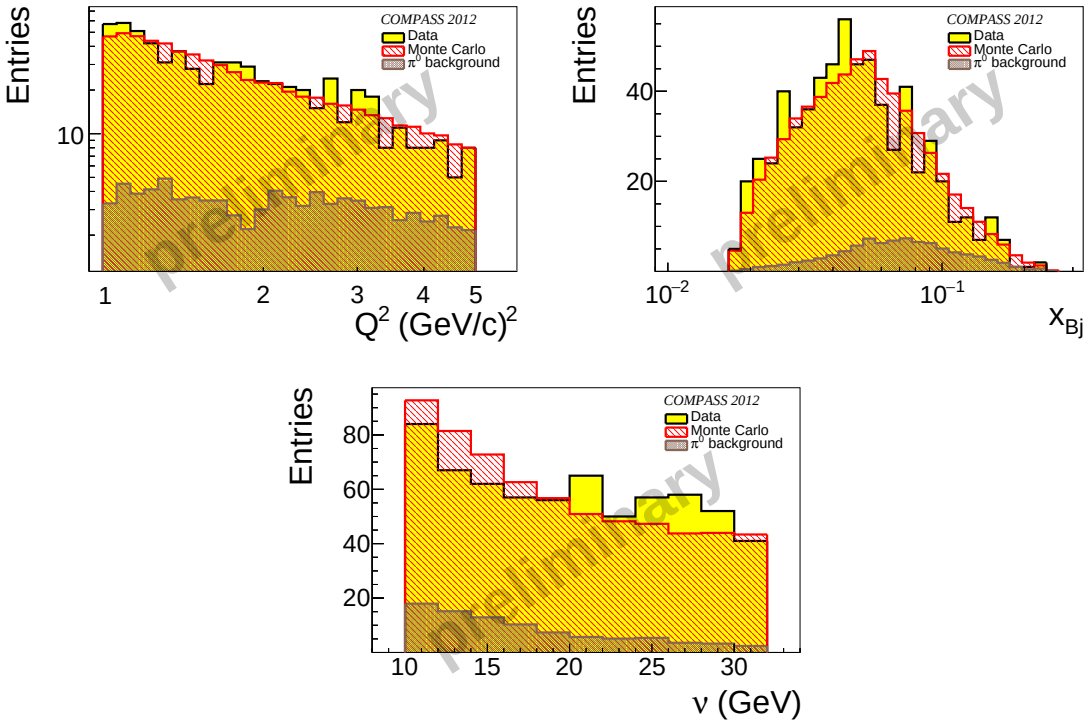

Figure 7.3: Kinematic distributions of Q^2, x_{Bj}, and ν for the analysis of the exclusive single photon production analysis with the 2012 DVCS pilot run data. The real data is presented in yellow. The whole Monte Carlo estimate is shown in red while the π^0 contamination is shown in grey [83].

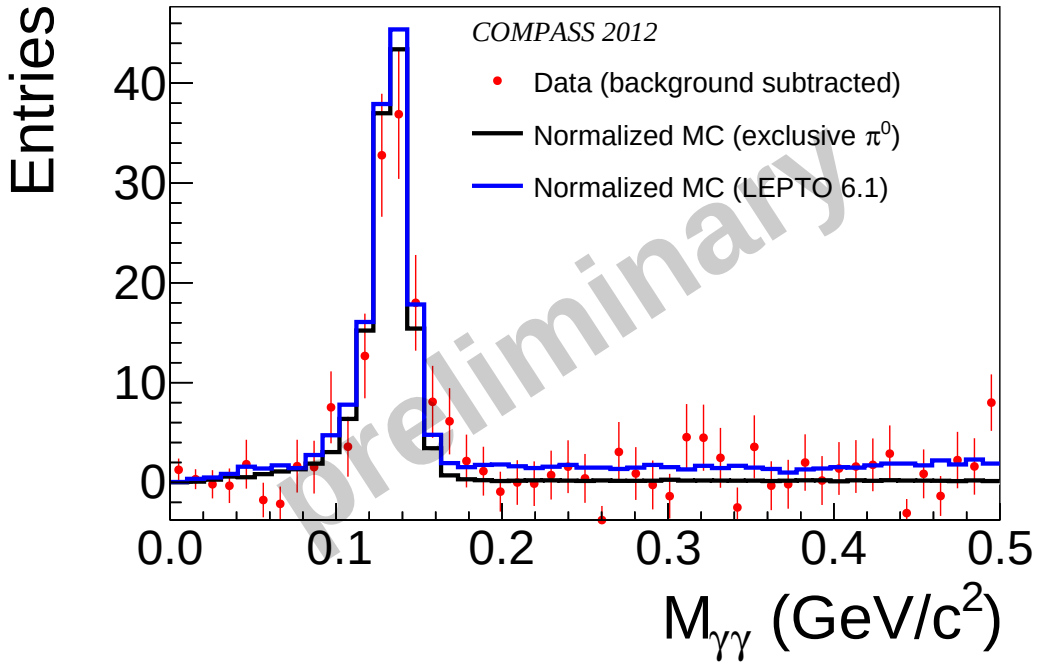

Figure 7.4: Invariant mass of the $\gamma\gamma$ system for the 2012 DVCS pilot run data. The single photon candidate is combined with all other photons below the DVCS energy tresholds of the electromagnetic calorimeters. The HEPGen++ and LEPTO Monte Carlo are individually normalized to the data [83].

These estimates require an accurate description of detector geometries, which is given by TGEANT.

7.2.4 Estimate of the Bethe-Heitler Contribution

The amount of BH Monte Carlo needs to be normalized to extract the pure DVCS cross section. According to the model calculations for BH, DVCS, and interference term (cf. Fig. 2.13) the BH contribution dominates in the lower x_{Bj} region or respectively for high values of ν for the kinematics of the COMPASS-II experiment. The BH Monte Carlo can either be normalized to the background-subtracted signal in the lower x_{Bj} region or alternatively by scaling the Monte Carlo luminosity to the luminosity of the data.

The Monte Carlo luminosity can be calculated as the ratio of the sum of all event weights, where $\omega_{\mathrm{BH},\,i}$ is the BH weight of the i'th event and N_{events} the size of the event sample, and the integral over the differential BH cross section in the phase space interval Ω_{MC} that was used for the Monte Carlo production:

$$L_{\mathrm{MC}} = \frac{\sum_{i=1}^{N_{\mathrm{events}}} \omega_{\mathrm{BH},\,i}}{\int\limits_{\Omega_{\mathrm{MC}}} \frac{\mathrm{d}^4\sigma_{\mathrm{BH}}}{\mathrm{d}\nu\,\mathrm{d}Q^2\,\mathrm{d}t'\,\mathrm{d}\phi_{\gamma\gamma^*}} \mathrm{d}\nu\,\mathrm{d}Q^2\,\mathrm{d}t'\,\mathrm{d}\phi_{\gamma\gamma^*}}. \tag{7.14}$$

A detailed technical discussion about the calculation procedure of the Monte Carlo luminosity can be found in Ref. [45].

7.2.5 Pure DVCS Cross Section

For high values of x_{Bj} or small values of ν, however, a subtraction of the BH contribution and π^0 contamination from the measured signal gives an access to the pure DVCS cross section. As outlined in Sec. 2.5.1, the COMPASS-II experiment is predestinated for a measurement of the beam charge and spin sum S. The integral of S over the azimuthal angle $\phi_{\gamma\gamma^*}$ allows to extract the pure DVCS contribution, since the $\sin(\phi_{\gamma\gamma^*})$-dependent interference term cancel in leading twist-2. The contribution of the coefficient c_0^{DVCS} is selected, cf. Eq. (2.58), which allows for a study of the Compton form factors $\mathcal{H}$ and $\tilde{\mathcal{H}}$.

To obtain absolute cross sections, the acceptance of the experimental apparatus for the DVCS process needs to be calculated. Figure 7.5 shows the acceptance as a function of Q^2, $-t$, and ν, provided from TGEANT. These tools enable a study of the pure DVCS cross section and its t-dependence. The slope $B(x_{\mathrm{Bj}})$ of the exponential t-dependence of the t-differential DVCS cross section are connected to the transverse size of the nucleon, cf. Eq. (2.38) and (2.39). The results of the analysis for the 2012 pilot run data are presented in Ref. [89].

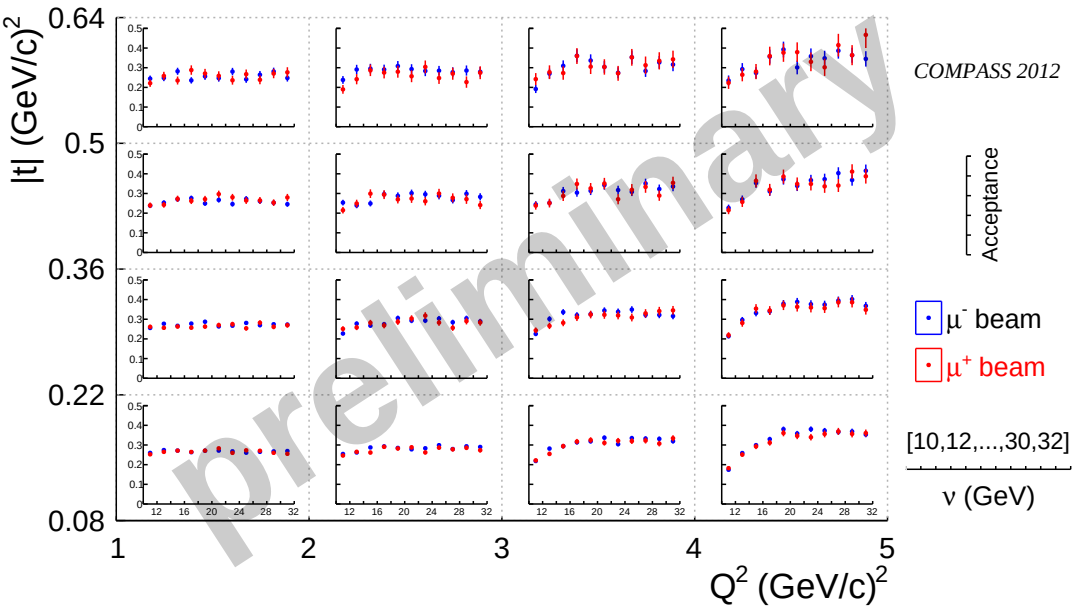

Figure 7.5: Acceptance for the DVCS process as a function of Q^2, $-t$, and ν. In a bin of Q^2 and $-t$, each plot shows the acceptance as a function of eleven equidistant bins of ν [90].

8. Monte Carlo Studies for a Measurement of the GPD E with a Polarized Target

Measuring differential cross sections of exclusive single photon productions in polarized lepton-nucleon scattering using a polarized target is the only possibility to get a sensitivity to the CFF $\mathcal{E}$. Such exclusive cross section measurements are key to constrain the GPD E, which are needed as further input to unravel the spin puzzle by using Ji's sum rule.

The COMPASS facility is capable of using highly polarized μ^+ and μ^- beams. The results of the DVCS pilot run in 2012 prove the capability of the spectrometer to identify exclusive single photon events, as presented in the preceding chapter. In 2016/17, COMPASS-II is going to measure the DVCS cross section using an unpolarized liquid hydrogen target surrounded by the CAMERA detector. An upgrade of the COMPASS polarized target with recoil detectors allows for studies of the spin-dependent GPDs as part of a possible beyond 2020 COMPASS-III measurement.

Such a measurement poses a huge technical challenge. In order to detect recoiled protons, the recoil detector needs to be accommodated inside the target magnet volume. A momentum reconstruction in such an environment is only possible when using silicon detectors and the $\mathrm{d}E/\mathrm{d}x$ technique. An answer to the feasibility of this project can only be given by Monte Carlo simulations. The results of a first study are presented in this chapter.

8.1 COMPASS Polarized Target Equipped with Silicon Recoil Detectors

For studies of the spin-dependent GPDs, a polarized target equipped with recoil detectors is required. The COMPASS polarized target and the CAMERA detector cannot be combined for this purpose because all low energy recoiled protons will be absorbed in the materials that surround the polarized target cells. Therefore a new recoil detector needs to be developed and installed inside the target magnet volume.

A technical drawing of the polarized target is shown in Fig. 8.1. The target cell in the center of the magnet can either be divided into two cells with the same length or three cells, where the inner one has twice the length of the outer ones. For a measurement with polarized protons, the solid state target is filled with irradiated ammonia (NH_3) embedded in liquid helium (LHe). The target cells are separated by microwave stoppers and surrounded by a microwave cavity. The target material is polarized in a 2.5 T solenoid field along the beam direction, using the method of dynamic nuclear polarization [92]. After achieving a stable polarization in the longitudinal direction, a 0.5 T dipole field is used to rotate the target spins adiabatically

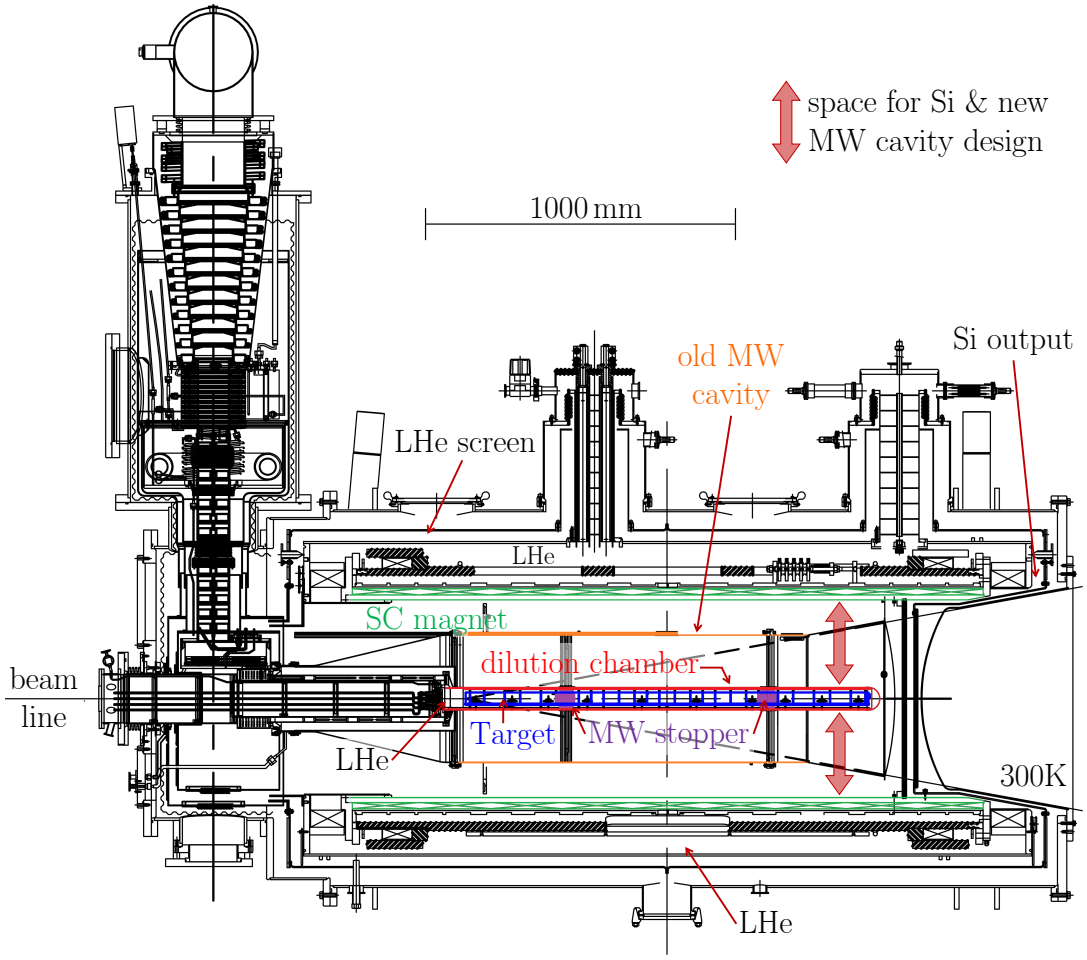

Figure 8.1: Sketch of the COMPASS polarized target. A new design of the microwave cavity provides space for two rings of silicon detectors. Picture adopted from Ref. [91].

into the transverse direction. The polarizations in neighboring cells are opposite, which allows for a simultaneous measurement with both polarization states. A mixture of liquid ^{3}He and ^{4}He is used to cool down the target cells to 50 mK. The superconducting magnet is cooled down with liquid ^{4}He.

The new recoil detector needs to work in the environments of a longitudinal and transverse magnetic field of about 0.5 - 2.5 T, a low temperature of about 5 K as well as a vacuum of about 10^{-6} mmHg. Silicon detectors are the most capable detectors that work in such environments. In order to minimize the influence of the microwave and to provide space for the recoil detector and input-output connections, a new design of the microwave cavity with a smaller radius and thinner thickness is needed. Due to the small space available between the new microwave cavity and the superconducting magnet, a time of flight measurement as for the CAMERA detector is not feasible. Hence, the momentum reconstruction of the recoiled protons needs to be performed by measuring the energy loss in the silicon detectors.

The proposed design for the new recoil detector, which is studied in this chapter, comprises two rings of silicon detectors installed in the free space between the new microwave cavity and the superconducting magnet. A front view of the setup with the magnetic dipole field from TGEANT is shown in Fig. 8.2. Subject of the Monte Carlo studies are mainly the kinematical acceptance and the feasibility of the four-momentum reconstruction of the recoiled proton. The geometrical aspects

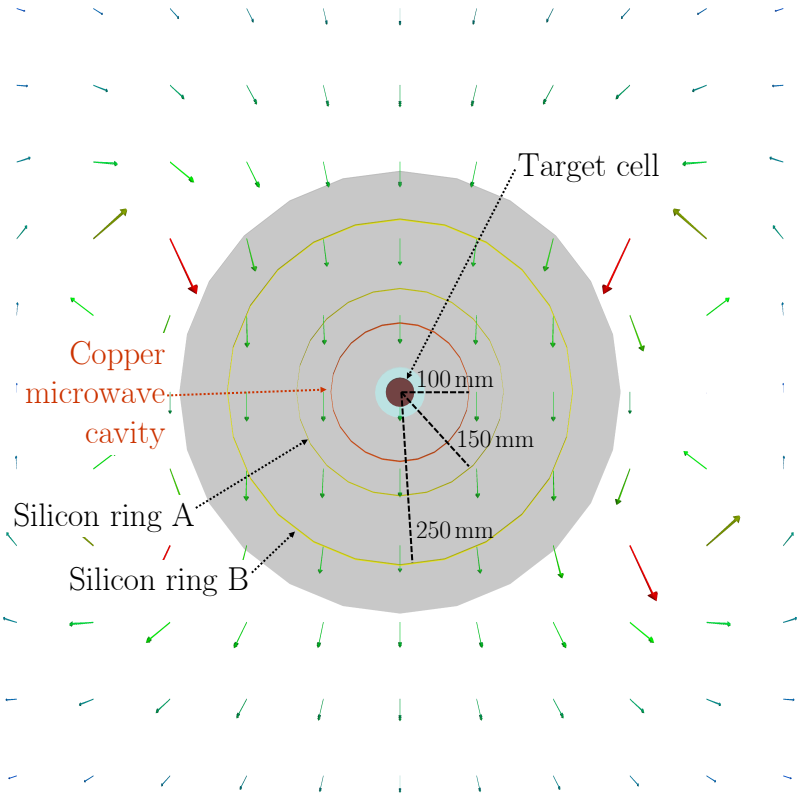

Figure 8.2: Proposed recoil detector design with two layers of silicon detectors inside the target magnet volume. The picture shows the front view of the setup from TGEANT with the magnetic dipole field. The grey-colored volume illustrates the space inside the target magnet volume, while the magnet itself is not shown.

are discussed in the following section, the momentum reconstruction technique and the influence of the silicon strip size is presented in Sec. 8.3.

8.2 Studies of the Kinematical Acceptance

A crucial characteristic of the new target design is the kinematical acceptance. A proton identification and four-momentum measurement is only possible if the recoiled proton crosses the inner and reaches the outer ring. Furthermore, the produced photon and the scattered muon need to be detected in the spectrometer to preserve the exclusivity of the measurement. The Monte Carlo studies presented in this section mainly focus on the kinematical acceptance of the new target design, thus it is only required that the outgoing photon leaves the target cells and target structure. The acceptance of the spectrometer, which is not changed in these studies and therefore constant, is not considered.

The setup of the simulation only includes the modified polarized target with the two silicon rings and the new cavity design as well as the magnetic dipole field. In addition, a dummy detector downstream of the target structure is used to detect all scattered muons and outgoing photons. This is equivalent to a perfect spectrometer acceptance. The DVCS event generator of HEPGen++ is restricted to the following kinematical range:

$$\begin{aligned} 1.0\,(\mathrm{GeV/c})^2 < \quad & Q^2 < 20.0\,(\mathrm{GeV/c})^2 \\ 0.005 < \quad & x_{\mathrm{Bj}} < 0.27 \\ 0.05 < \quad & y < 0.9 \\ & -t < 0.64\,(\mathrm{GeV/c})^2. \end{aligned} \tag{8.1}$$

A key feature of the setup is the lower limit of $-t$, which depends on the material layers the proton has to cross. Table 8.1 summarizes all material layers starting from

Table 8.1: Material thicknesses and properties of the different layers inside the polarized target. A recoiled proton at the center of the target cell with a polar angle of 90° has to cross these layers, except for the outer ring B. The given numbers describe the reference setup.

Material	Thickness [mm]	Density [g/cm^3]
NH_3/LHe	20*	0.58
PCTFE	0.6	2.1
LHe	14.2	0.1451
Kevlar	0.85	1.44
LHe	0.55	0.1451
Epoxy	0.6	1.2
Copper cavity	0.6*	8.96
Silicon Ring A	0.3*	2.33
Silicon Ring B	1.0*	2.33

* modified in Monte Carlo studies

the center of the target cell to the outer silicon ring B. The quoted numbers describe the setup that is used as a reference setup to all modifications that are described in the following. The expected kinematical distributions and mean values of Q^2, x_{Bj}, y, and $-t$ for this reference setup are presented in Fig. 8.3. The purpose of the new design is a lower limit of $-t$ that is as close as possible to the value achieved with the LH_2 target and the CAMERA detector. Here, Monte Carlo studies have shown that the geometrical design of the target and detector system is able to reconstruct protons with a lower limit of $-t_{\mathrm{min}} = 0.066\,(\mathrm{GeV/c})^2$. The minimum is defined as the value at which 20 % of all protons survive. However, this number only considers geometrical aspects and not the reconstruction efficiency for the time of flight measurement for these low momenta protons. Only events with $-t > 0.08\,(\mathrm{GeV/c})^2$ are therefore used in the analysis of the 2012 pilot run.

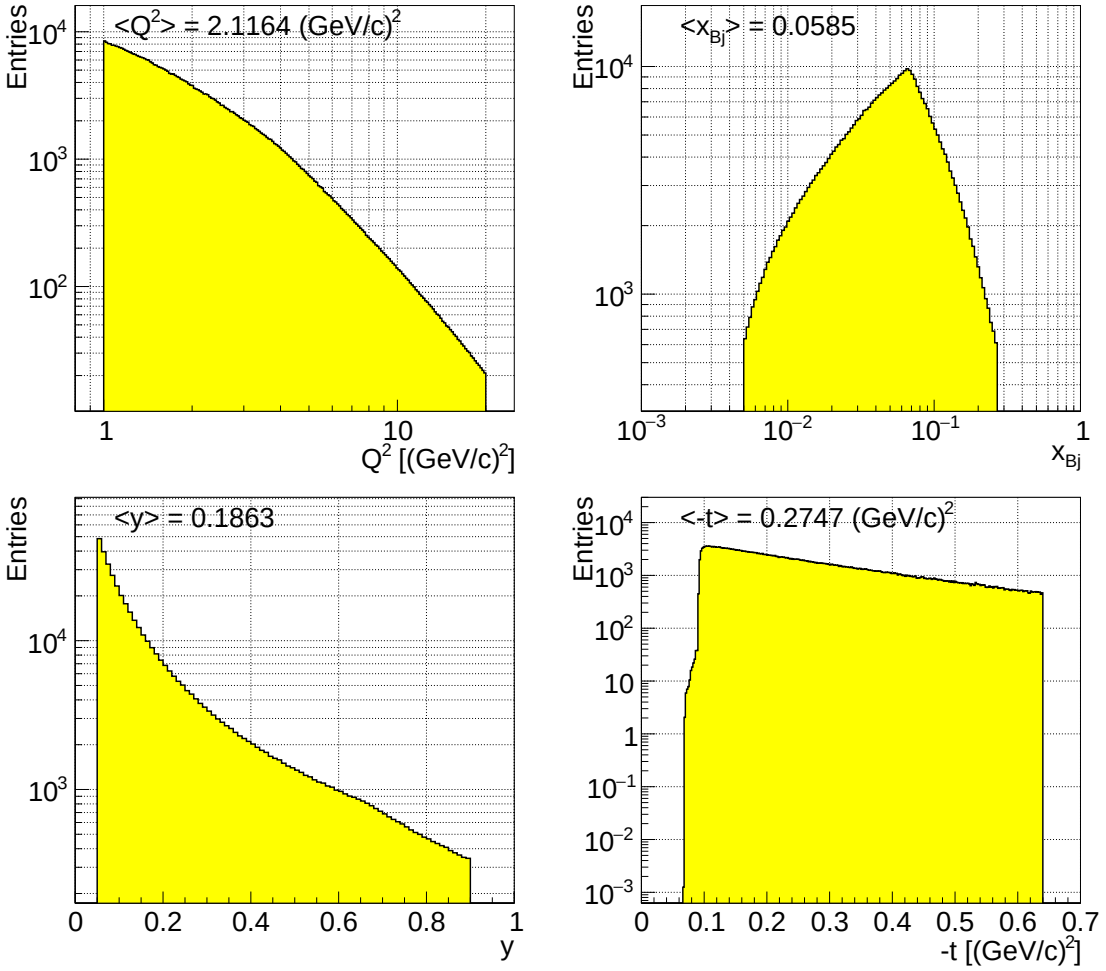

Figure 8.3: Reconstructed kinematical distributions and mean values of Q^2, x_{Bj}, y, and $-t$ for the reference setup, which is described in Tab. 8.1. The DVCS event generator of HEPGen++ is restricted to the kinematical limits given in Eq. (8.1). The lower limit of $-t$, however, is limited due to the material layers the recoiled proton needs to cross.

8.2.1 Modifications of the Target Radius

The lower limit of reconstructed protons for the reference setup is $-t_{\text{min}} = 0.0917\,(\text{GeV/c})^2$. The greatest influence has the distance the proton needs to traverse in the target cell, which is filled with a mixture of solid NH_3 and LHe. It is therefore worth to consider reducing the radius of the target cell in order to decrease the lower limit of $-t$. Technically, this is not a problem since the polarized target was originally used in earlier COMPASS measurements with a smaller radius of 1.5 cm. A smaller target radius has not only the advantages of an increasing number of protons that can be measured but also an increasing number of photons that survive, since their absorption probability is highest in ammonia. The downside of this approach is the fact that luminosity decreases with a smaller target area.

Figure 8.4 shows a typical beam profile for a μ^+ beam at the center of the target. The beam file that was used for this simulation was generated from measured beam tracks of 2012. Bending effects of the target dipole magnet, which were missing in 2012, are correctly considered by the extrapolation algorithm of TGEANT. The target is assumed to be perfectly aligned in the center of the beam. This allows to calculate the ratio of beam tracks inside the target area as a function of the target radius. This luminosity factor has to be multiplied with the ratio of detected events to obtain a combined efficiency, which can be used to compare different setups.

Note that an event counts as detected if the recoiled proton is measured in the inner and outer silicon ring and the photon is able to leave the target structure. This number of events is normalized to the number of generated events and is called proton and photon survival probability. These numbers are appropriate for comparisons, but they are not used to give absolute estimates since they strongly depend on the used kinematic ranges of the event generator, especially the lower limit $-t_{\text{HEPGen++}}$, which needs to be below the geometrical limit $-t_{\text{min}}$ of the setup.

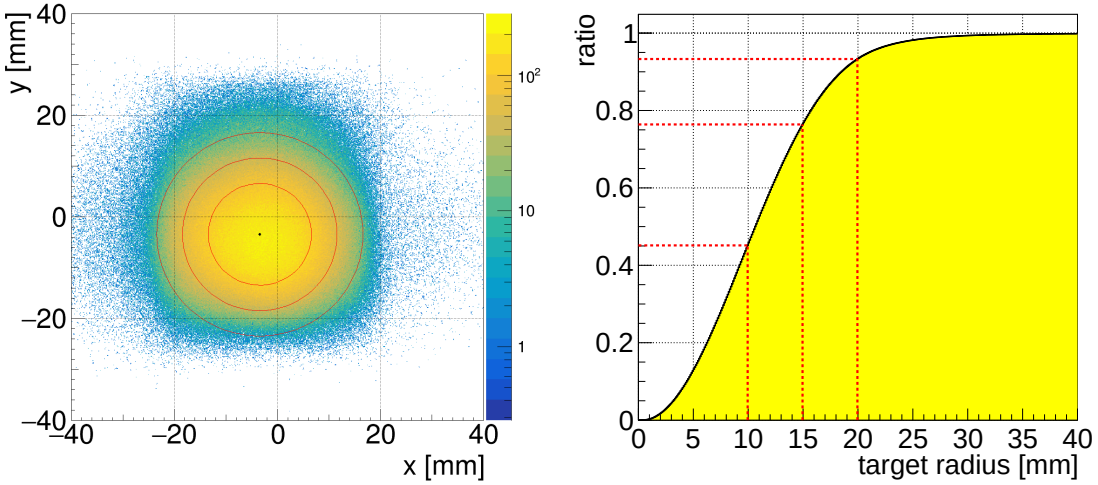

Figure 8.4: Calculation of the luminosity factor as a function of the target radius. Left: Typical beam profile for a μ^+ beam. The target center is located at the center of the beam (black dot). Three different target radii with 10, 15, and 20 mm are highlighted by red lines. Right: The ratio of beam particles inside the target area is calculated as a function of the target radius.

Table 8.2 compares the results of the reference setup with a target radius of 20 mm and two setups with smaller target radii of 15 and 10 mm. As expected, the survival probability increases and the lower limit of $-t$ decreases for smaller target radii. TGEANT only generates events if the beam particle triggers the event generator inside the target volume, thus the survival probability needs to be scaled by the luminosity factor. Going to 15 mm radius lowers slightly the combined efficiency but is worth the gain of protons with lower momenta. The kinematic distributions for the two setups with smaller target radii are presented in Fig. D.1 and Fig. D.2.

8.2.2 Modifications of the Microwave Cavity Design

A measurement with the current design of the microwave cavity is not feasible due to the huge thickness of 1 mm and the lack of space if the radius of the cavity is not reduced. The technical challenge is the reduction of thickness while maintaining mechanical stability. A smaller radius may increase the stability and allow for a smaller thickness, but also lowers the acceptance of photons that leave the target at larger polar angles. Technical studies on feasibility are definitively needed, but Monte Carlo studies can still yield estimates on the absolute scale of the kinematical influence.

The Monte Carlo simulation was repeated for different thicknesses and radii of the microwave cavity. A smaller thickness reduces the lower limit of $-t$, but not as much as the target radius. As expected, the changed cavity radius has no influence on the proton but on the photon absorption. The main priority for the new microwave cavity design is to reduce thickness. Table 8.3 summarizes the lower limit of $-t$ and the combined detection efficiency for several modifications of the setup. Only one material layer was changed with respect to the reference setup to keep the comparability. More detailed tables are presented in Appendix D.

The last material layer that has an influence on proton absorption is the inner silicon detector ring. The thickness of the inner ring in the reference setup is 300 µm. Smaller values increase the kinematic acceptance but lower the momentum resolution due to worse energy measurement as discussed in the following section.

8.3 Four-Momentum Reconstruction of the Recoiled Proton

The new detector needs to be able to measure space coordinates of recoiled particles and their momenta. As already discussed in the introduction of this chapter, the momentum reconstruction of recoiled protons needs to be performed with the $\mathrm{d}E/\mathrm{d}x$ technique. The mean energy loss of a proton in the inner and outer silicon detector is correlated and each can be expressed as a function of the momentum, as illustrated in Figure 8.5. Since energy loss is a statistical process, the precision of this method depends on the relative uncertainty of the energy deposit measurement and hence on the thicknesses of the silicon layers. The feasibility of this technique can only be studied by Monte Carlo and is presented in Sec. 8.3.1.

Each silicon detector ring is made of two layers of silicon strip detectors, which are placed orthogonally to build up a grid of pixels. Each ring is able to measure

Table 8.2: Kinematic limits and detection efficiencies for different target radii. All other material layers remain unchanged with respect to the reference setup (radius of 20 mm). The survival probabilities are normalized to the generated HEPGen++ sample and are therefore dependent on the generator cuts. The luminosity factors are extracted from Fig. 8.4.

NH3 Radius	10 mm	15 mm	20 mm
$p_{\min}/(\mathrm{MeV/c})$	278.3	287.1	307.2
$-t_{\min}/(\mathrm{GeV/c})^2$	0.0758	0.0817	0.0917
$p+\gamma$ survival probability norm. to generated sample	47.1%	45.0%	40.8%
Luminosity factor	45.1%	76.4%	93.3%
Combined efficiency	21.2%	34.4%	38.1%

Table 8.3: Summary of all geometry modifications. Only one material layer was modified, while all others remained unchanged with respect to the reference setup. The combined detection efficiency includes the luminosity factor and the survival probability of the proton and photon, which depends on the generator cuts.

Setup changes w.r.t reference	$-t_{\min}$ $[(\mathrm{GeV/c})^2]$	Combined efficiency
Reference setup	0.0917	38.1%
NH3 target radius 15 mm	0.0817	34.4%
NH3 target radius 10 mm	0.0758	21.2%
Cu Cavity Thickness 0.5 mm	0.0907	38.6%
Cu Cavity Thickness 0.4 mm	0.0895	39.3%
Cu Cavity Thickness 0.3 mm	0.0876	39.7%
Cu Cavity Thickness 0.2 mm	0.0866	40.3%
Cu Cavity Radius 90 mm	0.0917	37.8%
Cu Cavity Radius 80 mm	0.0917	37.3%
Cu Cavity Radius 70 mm	0.0917	36.8%
Ring A Thickness 200 µm	0.0913	38.3%
Ring A Thickness 250 µm	0.0915	38.2%
Ring A Thickness 350 µm	0.0919	38.1%
CAMERA	0.0656	56.6%

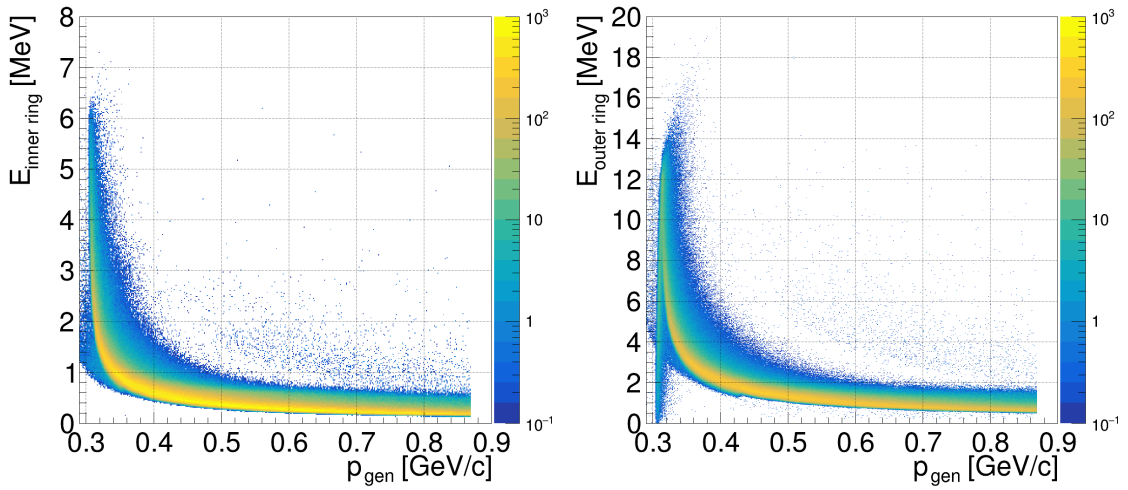

Figure 8.5: Energy deposit in the inner (left) and outer (right) silicon ring as a function of the proton momentum at the vertex position.

the azimuthal angle ϕ and the z position of the so-called pixel the proton has traversed. The resolution of the space coordinates can be expressed as a resolution of the azimuthal angle ϕ and polar angle θ of the recoiled proton at the vertex position. This resolution mainly depends on the size of the silicon strips z and ϕ. Modifications of the strip sizes and their influence on the four-momentum reconstruction are discussed in Sec. 8.3.5.

Smaller strip sizes, however, require more readout channels, which scale linearly with the dissipated power. Due to the low temperature environments, the dissipated power should be reduced to a minimum. A maximum in the range of 10 W can be handled to not disturb the system. First estimates allow for strip sizes of 10 mm in z and 5° in ϕ [93].

8.3.1 Momentum Reconstruction Method

A new design-independent momentum reconstruction method was developed, which allows for a fast momentum reconstruction for different setups with modified geometries or strip sizes. This method relies on calculated mean energy losses as a function of the proton's momentum and polar angle.

The mean rate of energy loss of a proton with the velocity βc in a material layer with the density ρ, the atomic number Z, atomic mass number A, and the mean excitation energy I is well-described by the Bethe-Bloch equation:

$$-\left\langle \frac{dE}{dx} \right\rangle = \frac{1}{4\pi\epsilon_0^2}\frac{z^2e^4}{m_e c^2}\frac{N_A Z\rho}{A}\frac{1}{\beta^2}\left[\frac{1}{2}ln\left(\frac{2m_e c^2\beta^2\gamma^2 T_{\max}}{I^2}\right)-\beta^2\right], \tag{8.2}$$

where $T_{\max} = 2m_e c^2\beta^2\gamma^2$ is the maximum energy transfer possible in a single collision, ϵ_0 the vacuum permittivity, N_A the Avogadro number, e and m_e the electron charge and rest mass respectively, $\gamma = (1-\beta^2)^{-1/2}$ the Lorentz factor, and $z = 1$ the charge number for a proton.

For the momentum spectrum of the recoiled proton, the mean energy loss is strongly dependent on the proton's momentum. In order to calculate the mean

energy loss in a material layer with the thickness l, the layer is divided into n slices and the mean energy loss is calculated iteratively for all n slices taking into account the changing proton momentum. This can be done for the complete momentum spectrum of the proton, starting at the center of the target cell, going through all material layers, and stopping either in the outer silicon ring or if the proton is at rest. However, the effective thickness l' of a material layer the proton has to traverse depends on the polar angle θ:

$$l' = l/\sin(\theta). \tag{8.3}$$

The calculations need to be repeated for all possible θ angles. Figure 8.6 shows the energy loss of the recoiled proton in the outer silicon ring plotted versus the energy loss in the inner ring. A limited selection of calculated curves for the mean energy losses over the full spectrum of possible proton momenta are shown for different polar angles. Higher values of energy deposit come into effect for larger polar angles and small proton momenta.

The momentum reconstruction technique relies on the measured energy deposit in the inner and outer ring as well as on the measured polar angle. The measured energy losses are compared with the calculated mean energy losses for the measured θ angle and the closest distance to the curve is calculated. For this point on the calculated curve, the momentum is already known and assigned to the recoiled proton.

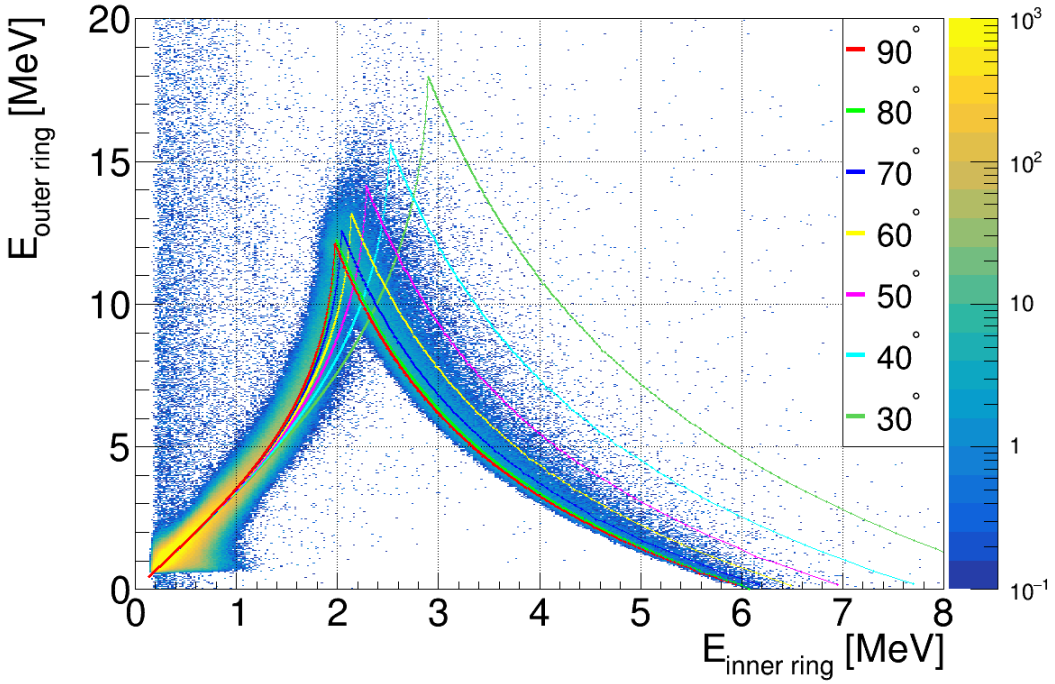

Figure 8.6: Energy loss of the recoiled proton in the outer and inner silicon ring. The calculated curves show the expected mean energy loss for different polar angles θ. The relation to the proton momentum can be extracted from Fig. 8.5.

8.3.2 Polar Angle Reconstruction Method

The space resolution of the silicon detectors in z direction has an influence to the reconstructed polar angle θ and therefore on the momentum reconstruction, which depends on θ. In the setup of the simulation, the two silicon rings are implemented as cylinders with a radius of $r_A = 150\,\text{mm}$ and $r_B = 250\,\text{mm}$ and with a length of 154 cm. The hit position of the recoiled proton, which is perfectly known in the Monte Carlo, needs to be digitized first. The cylinders are segmented into a grid of pixels and the Monte Carlo hit information is replaced with the pixel position the proton has traversed. The reference strip sizes are $\Delta z = 10\,\text{mm}$ and $\Delta\phi = 5°$. The two measured z positions of the two pixels in the inner and outer ring, $z_{A,\,\text{pixel}}$ and $z_{B,\,\text{pixel}}$, can be used to calculate the reconstructed θ angle:

$$\theta = \tan^{-1}\left(\frac{r_B - r_A}{z_{B,\,\text{pixel}} - z_{A,\,\text{pixel}}}\right). \tag{8.4}$$

This method neglects the influence of the magnetic dipole field and can be further improved, but it still gives an upper limit for a possible θ resolution for a given z strip size. Figure 8.7 shows the standard deviation of the measured θ angle as a function of the proton momentum. As expected, the resolution is worse for smaller proton momenta since the influence of the dipole field increases. The same simulation can be repeated without the magnetic dipole field, which gives an estimate for the lower limit of the θ resolution for the reference setup with a z strip size of 10 mm. The tendency for small momenta remains because of the multiple scattering of the protons inside the target material. Neglecting the magnetic field and the target material, the standard deviation is only dictated by the chosen z strip size.

The reconstructed θ angle is used for the momentum reconstruction and is assumed to be the same for all material layers of the target. The influence of the dipole field is therefore neglected again, but a repeated simulation without the dipole field reproduces the same relative uncertainties of the momentum reconstruction for proton momenta $p_{\text{gen}} > 350\,\text{MeV/c}$. Figure 8.8 presents the upper and lower limit of the momentum reconstruction for the reference setup. The increasing relative uncertainty for higher momenta is explained by the fact that the mean energy loss of the proton converts to a minimum value with increasing velocity, cf. Fig 8.5. A momentum reconstruction using the energy deposits is therefore less accurate.

Note that the silicon detectors are implemented in the simulation as perfect cylinders. The support structure and readout electronics is still missing in the description, which will also have an influence on the recoiled protons. Another important factor is the missing energy resolution of the silicon detectors. Detector studies about the performance of silicon detectors at the low temperatures inside the target magnet volume need to be considered. Anyway, Monte Carlo studies have shown that a momentum resolution with a precision of 5 - 10 % is feasible with the new design, which is comparable with the momentum resolution of the CAMERA detector. It has been shown in the analysis of the 2012 pilot run data that the precision for higher momenta can be further improved by using the predicted spectrometer information of the recoiled proton p'_{spec} and a kinematic fit [83].

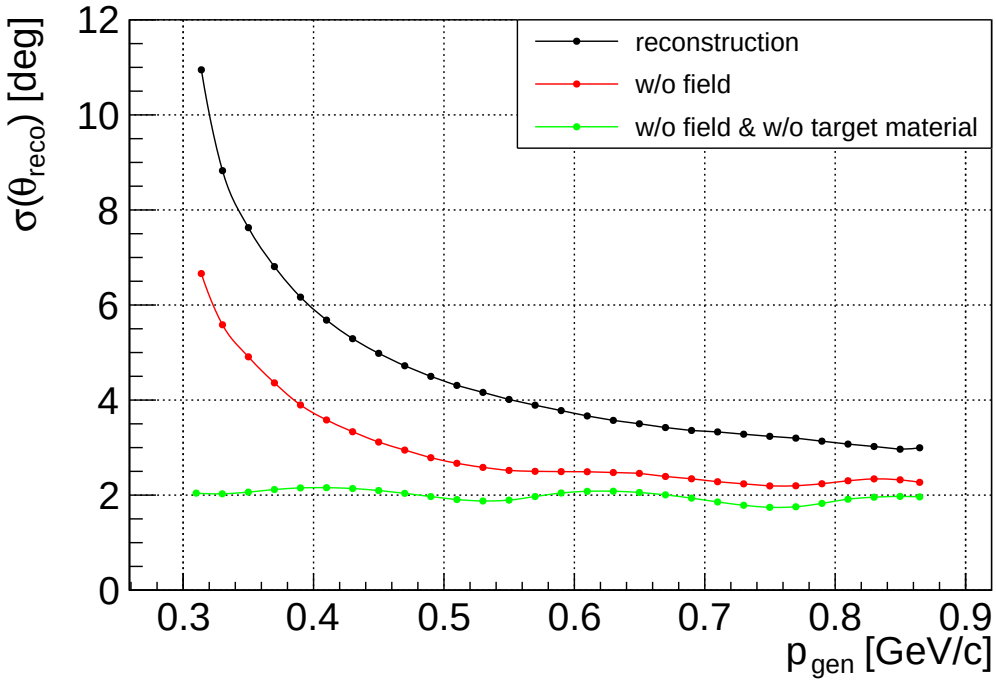

Figure 8.7: Standard deviation of the reconstructed polar angle θ as a function of the proton momentum at the vertex position. The black curve shows the obtained resolution for the reference setup. The influence of the magnetic dipole field (red) and the target material (green) are shown in comparison.

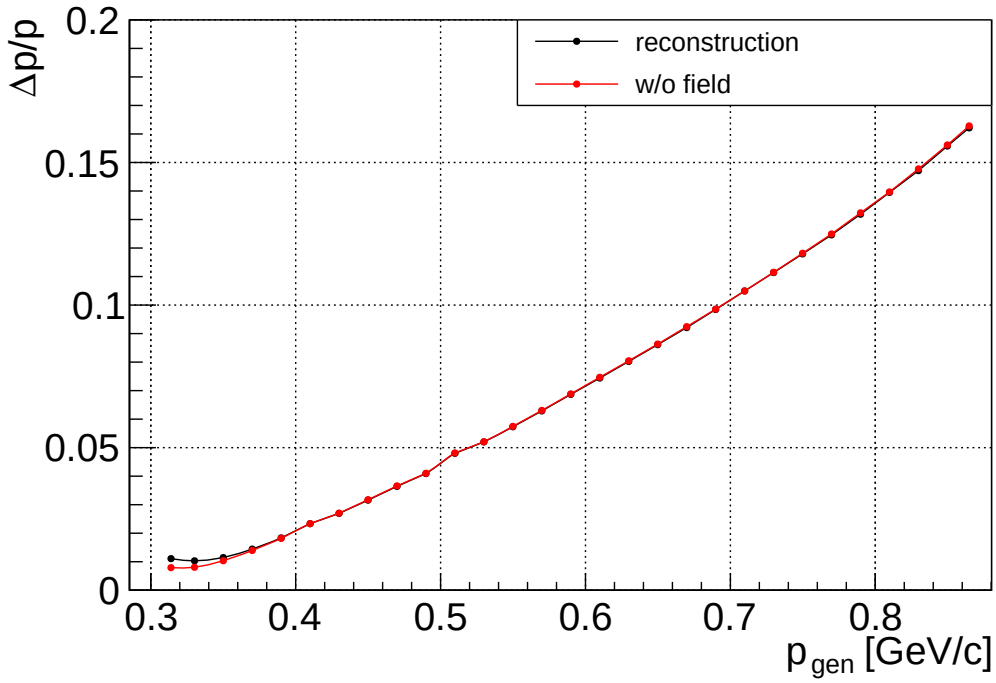

Figure 8.8: Relative uncertainty of the momentum reconstruction method as a function of the proton momentum at the vertex position. The black curve shows the obtained momentum resolution for the reference setup with a z strip size of 10 mm. The results for the same Monte Carlo simulation without the magnetic dipole field are represented by the red curve.

8.3.3 Azimuthal Angle Reconstruction Method

The reconstruction of the azimuthal angle relies on the ϕ strip size. Unlike for the CAMERA detector, both silicon rings cannot be rotated by $\phi/2$ with respect to each other since the readout electronics need to be installed orthogonally between both rings for such a setup.

The ϕ angle is reconstructed as the mean value of the ϕ position of the traversed pixels in the inner and outer ring. The mean value of the difference between the real ϕ angle of the recoiled proton at the vertex position and the reconstructed value is shown as a function of the reconstructed azimuthal angle in Fig. 8.9. If the proton flies in the same direction as the magnetic dipole field ($\phi_{\text{gen}} = 0°$ and $\phi_{\text{gen}} = 180°$), the dipole field bends the proton only along the z direction (for $\theta < 90°$) and has therefore no influence in ϕ direction. The discrepancy between reconstructed and generated angles reaches its maximum for $\phi_{\text{gen}} = \pm 90°$ and can be described by a skewed sine modulation:

$$f(\phi_{\text{reco}}) = \phi_{\text{gen}} - \phi_{\text{reco}} = c_0 \cdot \sin(c_1 \cdot \phi_{\text{reco}}) + c_2 \cdot \phi_{\text{reco}}. \tag{8.5}$$

The coefficients $c_{0\ldots2}$ have been extracted from a fit and can be used to correct the reconstructed azimuthal angle:

$$\phi'_{\text{reco}} = \phi_{\text{reco}} + f(\phi_{\text{reco}}). \tag{8.6}$$

Note that the linear term with the coefficient c_2 is needed because f is a function of ϕ_{reco} and not of ϕ_{gen}.

The calculation of the standard deviation of the reconstructed azimuthal angle as a function of the proton momentum at the vertex position has been repeated for the reference setup with a ϕ strip size of 5° to investigate the influence of the magnetic dipole field and the target material, see Fig. 8.10. The improved ϕ reconstruction method that uses the correction function f comes very close to the expected standard deviation for the same setup without a dipole field. The reconstruction is worse for small proton momenta due to process of multiple scattering in the target material. A simulation without dipole field and target material gives the smallest possible value of $\sigma_{\min}(\phi) = 5°/\sqrt{12} = 1.44°$.

8.3.4 Modification of the Silicon Thicknesses

The uncertainty of the momentum reconstruction depends on the energy measurement in the silicon detectors. A larger thickness of the inner ring improves the momentum resolution but also increases the lower limit of $-t$ (and vice versa). For the outer ring, however, the only limitation for the thickness of the silicon layer is dictated by technical issues and the available space inside the target magnet volume. The Monte Carlo studies presented in Fig. 8.11 give an estimate for the expected relative uncertainty of the momentum reconstruction for different thicknesses of the inner and outer silicon ring. To keep the comparability, only the thickness of one ring was modified with respect to the reference setup. The greatest improvement for the momentum resolution, especially for larger proton momenta, is gained by increasing the size of the outer ring.

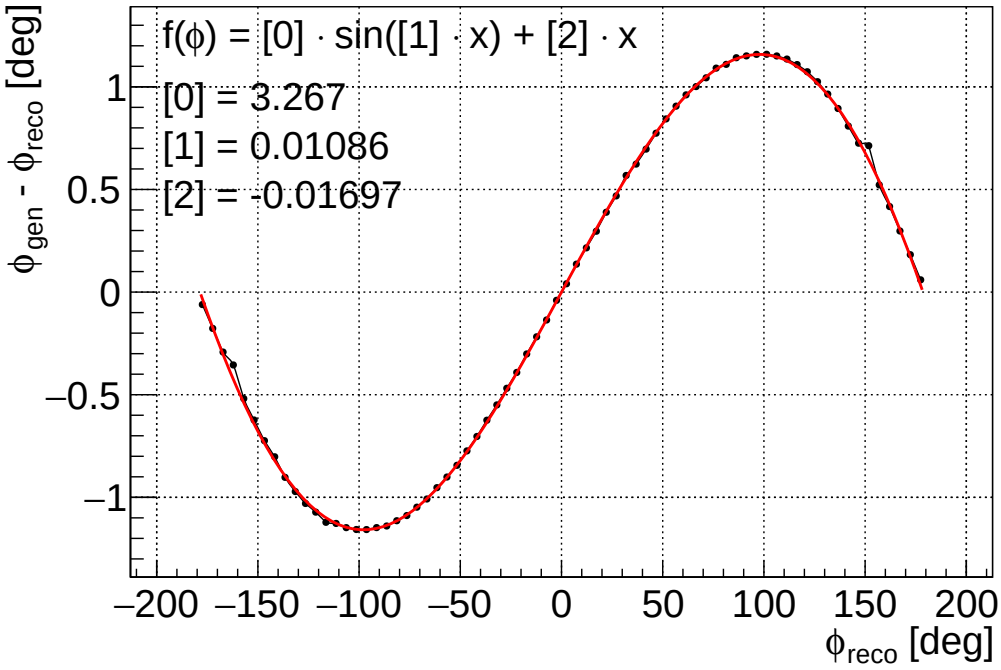

Figure 8.9: Sine-modulated correction function for the azimuthal angle.

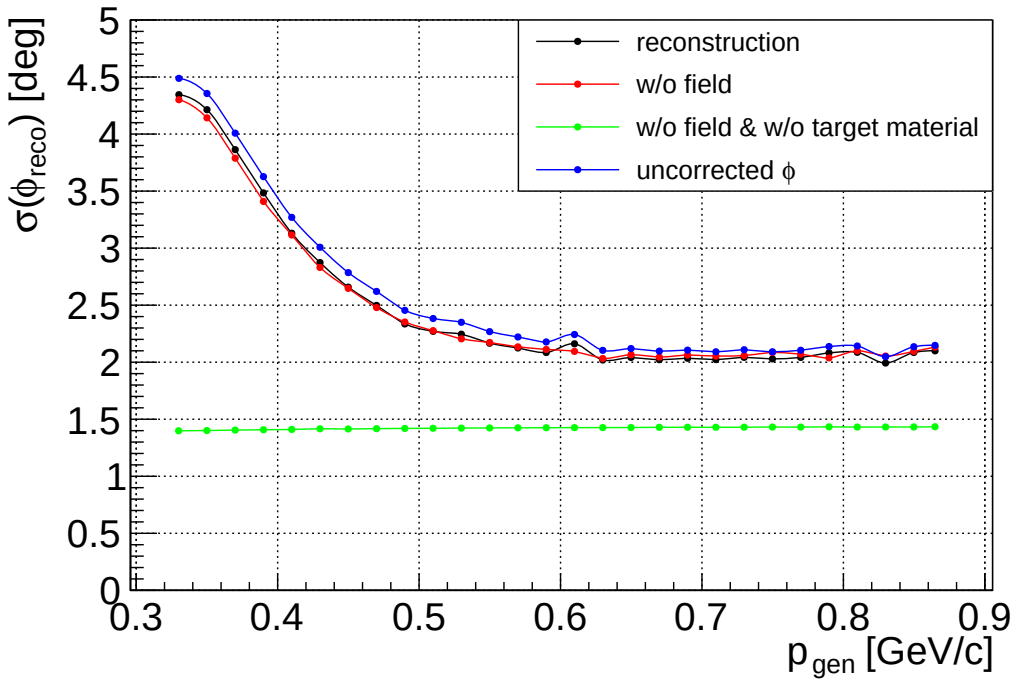

Figure 8.10: Standard deviation of the reconstructed azimuthal angle ϕ as a function of the proton momentum at the vertex position. The black curve shows the obtained resolution for the reference setup with the applied ϕ correction. The influence of the magnetic dipole field (red) and the target material (green) are shown in comparison. The expected standard deviation without correction factor is presented in blue.

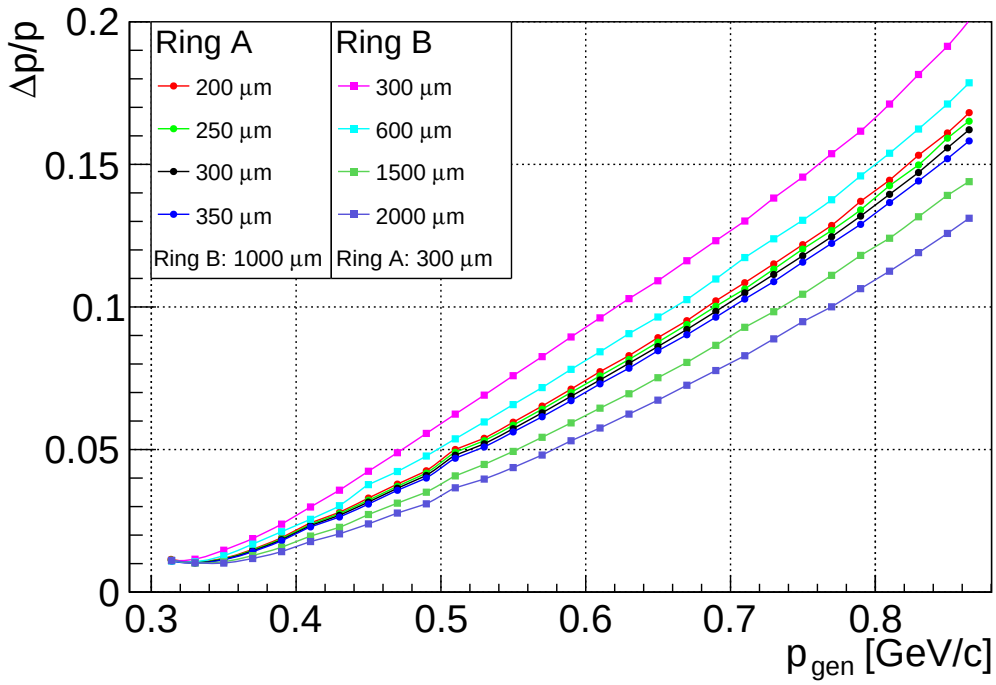

Figure 8.11: Relative uncertainty of the momentum reconstruction as a function of the proton momentum at the vertex position for different silicon detector thicknesses. The black curve shows the momentum resolution for the reference setup. For all other curves, either the thickness of the inner ring or the outer ring was modified.

8.3.5 Modification of the Silicon Strip Sizes

The number of readout channels has a major influence on the technical feasibility of this project due to the dissipated power of the readout electronics. The number of silicon strips is therefore limited and it is important to optimize the available resources. The z strip size has a strong influence on the momentum and polar angle resolution, while the ϕ strip size dictates the azimuthal resolution.

The influence of the z strip size is investigated in Fig. 8.12 and 8.13. The relative uncertainty of the momentum resolution shows no significant variation if the number of readout channels is increased by a factor of 10 ($z = 1\,\text{mm}$) or reduced by a factor of 2 ($z = 20\,\text{mm}$). However, effects of the θ resolution are clearly apparent. Reducing the z strip size to 5 mm seems reasonable, while a further improvement from 5 to 1 mm is not that effective.

The standard deviation of the reconstructed azimuthal angle for different ϕ strip sizes is studied in Fig. 8.14. For proton momenta at the vertex position $p_{\text{gen}} \gtrsim 600\,\text{MeV/c}$, the standard deviation converts to a minimal value. At that range, a ϕ strip size of 5° gives the same azimuthal standard deviation as the CAMERA detector with $\sigma_{\text{CAMERA}}(\phi) = 7.5°/\sqrt{12} = 2.17°$.

8.3.6 Summary

The Monte Carlo studies presented in this chapter are the first step for a proposal for a beyond 2020 measurement of GPD E at COMPASS-III. These studies show the

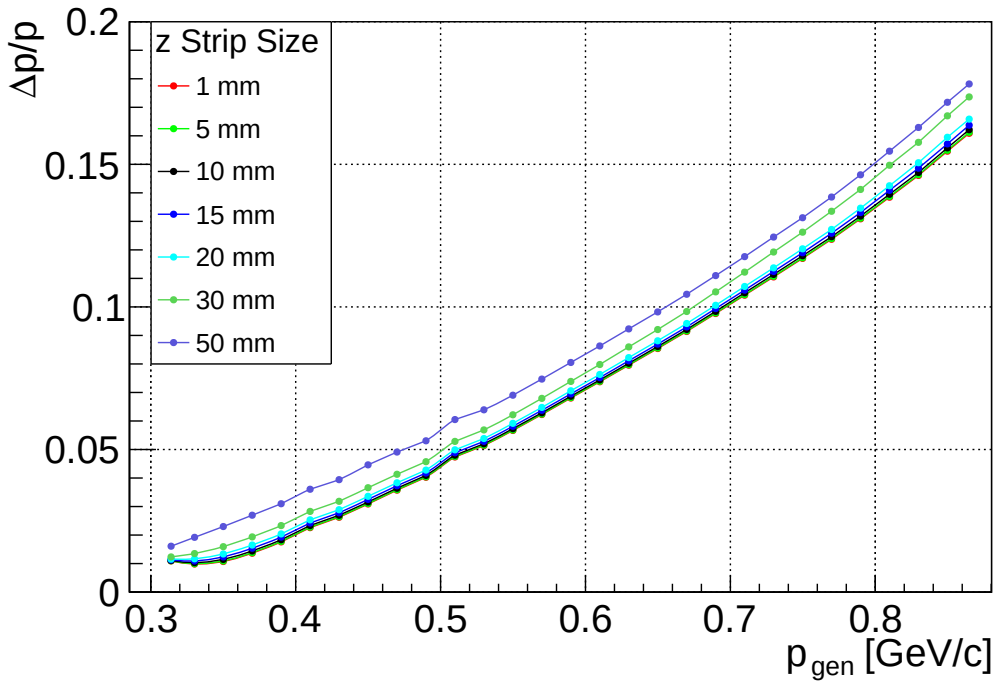

Figure 8.12: Relative uncertainty of the momentum reconstruction as a function of the proton momentum at the vertex position for different z strip sizes. The black curve shows the momentum resolution for the reference setup.

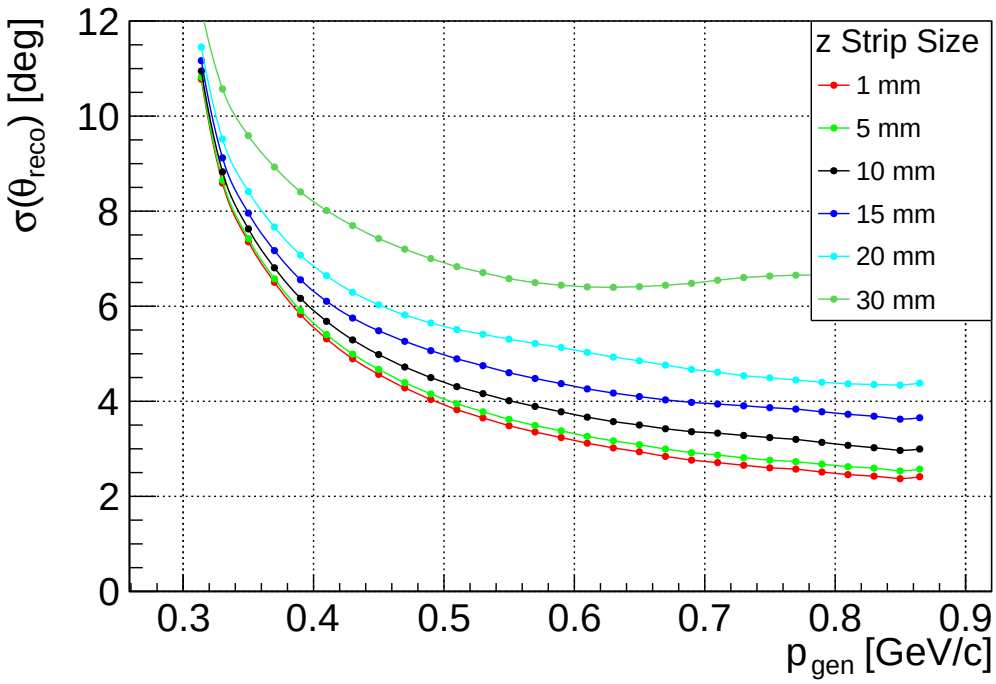

Figure 8.13: Standard deviation of the reconstructed polar angle θ as a function of the proton momentum at the vertex position for different z strip sizes. The black curve shows the θ resolution for the reference setup.

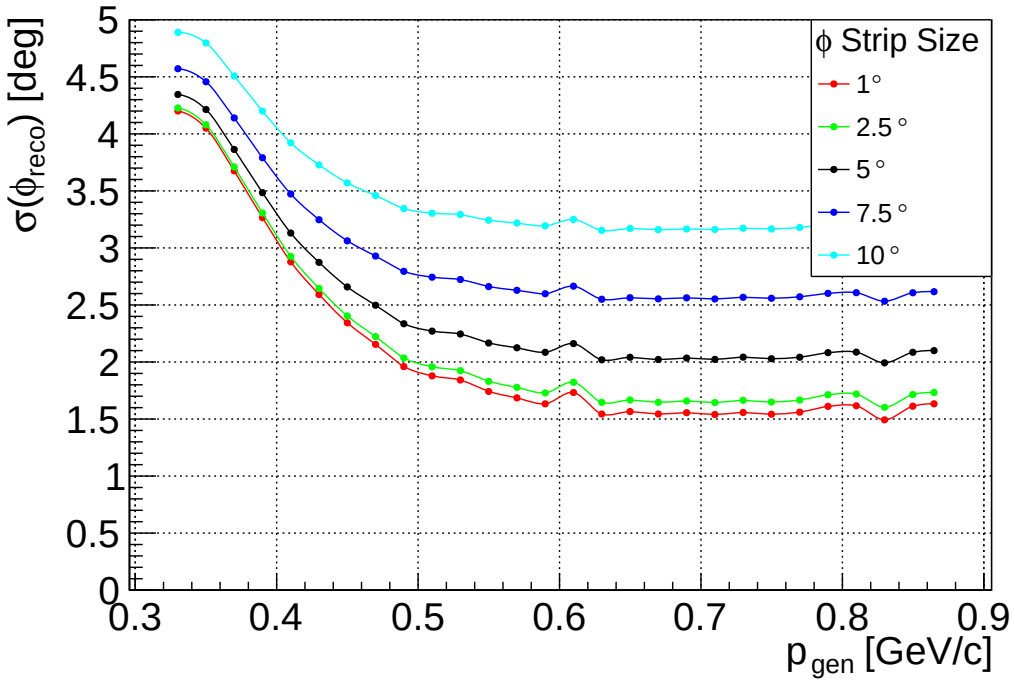

Figure 8.14: Standard deviation of the reconstructed azimuthal angle ϕ as a function of the proton momentum at the vertex position for different ϕ strip sizes. The black curve shows the ϕ resolution for the reference setup.

feasibility of a four-momentum reconstruction of the recoiled proton with two silicon layers installed inside of the magnet volume of the polarized target. A momentum measurement with a precision of 5 - 10 % can be accomplished with silicon thicknesses of 0.3 and 1.0 mm. This precision is competitive to the one obtained in 2012 with the LH_2 target and CAMERA detector.

The resolution of the polar and azimuthal angle strongly depends on the size of the silicon strip detectors, but the total number of readout channels is restricted to not exceed the total power limit of 10 W. Technical studies related to the readout of the silicon detectors are needed to get an estimate for a maximum number of possible channels. However, the influence of different strip sizes, which are close to the allowed reference setup with strip sizes of 10 mm in z and 5° in ϕ, on the four-momentum resolution were given to optimize the detector layout. The resolution of both angles also correlates with the proton momentum and gets worse for smaller momenta due to multiple scattering and bending effects. The latter effect has been studied to give upper and lower limits of the resolution.

9. Conclusion and Outlook

This thesis comprises the development of the new Geant4-based Monte Carlo Software TGEANT for the COMPASS-II experiment. TGEANT was optimized primarily for the GPD program, including a tuning of the electromagnetic shower simulation and a software model of the trigger system, but has since been extended to cover all other physics programs. It has become a standard in the COMPASS-II Monte Carlo chain and has been used by almost all recent analyses.

The new Monte Carlo software was developed in object-oriented C++, with the software package including a graphical user interface for simplified usage and a Toolbox for a direct analysis of the Monte Carlo output. The highly flexible design of the software, based on application programming interfaces, allows for a universal simulation of different physics programs. Two vertex generation algorithms have been developed and linked with different event generators. The presented target extrapolation method fits perfectly to the muon program, while the hadronic interaction method considers the changing phase space and decreasing flux of a pion beam. With TGEANT it is possible for the first time to simulate a vertex distribution that describes the measured data exactly by using a combination of a realistic beam simulation and accurate target alignment.

The COMPASS-II experiment is equipped with three electromagnetic calorimeters in order to detect the single photons that are produced in deeply-virtual Compton scattering and the photon pairs resulting from π^0 decays. A realistic simulation of the electromagnetic shower propagation is essential for determining the impact point of the incident particle with the same precision as in the experiment. The computing time needed for the simulation of a particle cascade increases approximately linearly with the energy of the incident particle. The fast shower parameterization algorithm GFlash was therefore implemented in TGEANT to speed up the simulation of electromagnetic showers. Furthermore, a module-dependent tuning of the Geant4 production cuts was performed as well as an adjustment of the radial shower parameterization. The GFlash parameter set was efficiently optimized using an evolutionary algorithm. A correct energy calibration of the reconstructed

electromagnetic calorimeter clusters over the full energy range of the COMPASS-II experiment was achieved with a new energy-dependent calibration method.

The trigger system in the experiment is essential to distinguish between physically interesting and uninteresting events and needs to be simulated accordingly. A software model of the COMPASS trigger system was developed for each physics program, taking into account the geometrical and temporal coincidences of the hodoscope trigger systems. The design of the trigger simulation was further improved to also consider detection efficiencies of the hodoscope scintillators and efficiencies of the trigger system. In 2016/17, the COMPASS-II experiment is going to measure differential cross sections of deeply-virtual Compton scattering. In preparation for this measurement, Monte Carlo studies with TGEANT were crucial for optimizing the central holes of both outer trigger hodoscopes and for realigning all other hodoscopes. In this process, the trigger matrices were also improved.

The new simulation software was used for the first time in the final analysis of the 2012 DVCS pilot run. A profound understanding of the experimental acceptance and background estimates is key to measure absolute cross sections and can only be obtained with Monte Carlo. The acceptance estimations of TGEANT have been validated in a luminosity measurement using the structure function F_2. This alternative approach strongly relies on the acceptance of the experimental apparatus and is in excellent agreement with the conventional beam flux counting method. The simulation was indispensable for extracting the exponential t-dependence of the t-differential DVCS cross section [89] and the analysis of the cross section of exclusive π^0 production process [94]. Results of the analysis of the Drell-Yan measurements in 2014/15 using TGEANT are also in preparation [95]. In conclusion, the new Monte Carlo software has been validated and is well-prepared for the analysis of the measured data of the 2016/17 run.

The 2016/17 run aims at the measurement of the unpolarized deeply-virtual Compton scattering cross section. The spin-dependent generalized parton distribution functions in the unexplored kinematical domain of the COMPASS experiment can only be accessed in measurements of transverse target spin asymmetries. The polarized target that was used in the COMPASS experiment leaves no space for a recoil detector inside the magnet volume. However, a new design of the microwave cavity allows for the installation of two layers of silicon detectors. Only by using TGEANT, it was possible to study the feasibility of this design. The kinematical acceptance and the four-momentum reconstruction are key features of the setup. Monte Carlo estimates were given for all possible geometrical arrangements and sizes of the silicon strip detectors to optimize the final detector design, taking into account the available resources. These studies form the basis of a proposal for a COMPASS-III measurement beyond 2020.

A. Geant4 Toolkit

The simulation software TGEANT is based on the Geant4, whose acronym stands for "Geometry And Tracking" and which is a framework for the simulation of the passage of particles through matter [63–65].

A.1 Geometries and Materials

Geant4 offers a huge field of applications, although it is not a complete simulation software but rather a basis on which users can build their own simulation software. Basic requirement for a Monte Carlo simulation software such as TGEANT is the geometry description of the experimental apparatus. Geant4 offers a back-end system in which the users can implement their own detector geometries. Each detector is made of a number of volumes. Each volume is described by its shape and its physical characteristics, namely the material of the volume. A volume is always placed inside another volume. The largest volume is called the world volume and represents the experimental hall of the COMPASS experiment in TGEANT.

A various selection of different solid shapes are available in Geant4. Even more complex geometries can be constructed by the combination of two volumes and by a three-dimensional rotation. Two solid shapes can be added, subtracted, or intersected. This offers a huge flexibility to recreate all detector geometries used in the COMPASS experiment in an accurate manner as presented in Chapter 3.

The physical characteristics of the volumes are defined with the material properties. This involves the density and the macroscopic quantities such as radiation length, mean free path, or energy loss ($\mathrm{d}E/\mathrm{d}x$). In TGEANT, multiple ways are used to define a material. Some commonly used materials are already available in the Geant4 material database. Others are defined as a mixture of already existing materials, where the density of the mixture has to be specified as well as the mixing ratio of its components. The third approach to define a new material is to use its density and chemical formula.

In TGEANT, the materials and surfaces of the solid shapes can optionally be linked with optical properties. These are needed for a simulation of the emission of

scintillating light, e.g. in the slats of the CAMERA detector, or Cherenkov photons inside the RICH-1 radiator, as shown in Fig. 3.6. Photons that are created by these processes are called optical photons and are treated as independent particles in Geant4. The wavelength-dependent refractive index and the absorption length are the important quantities that have to be added to the properties table of the respective material. A realistic simulation of the photon dispersion through several volumes is possible with the concept of optical surfaces.

A.2 Physical Processes and Particles

The implementation of particles and physical models is mandatory to simulate the physical interactions of particles with matter and the particle transportation. Geant4 offers data bases, which comprise a huge field of applications, for all kinds of particles and processes. The energy range spans from eV to TeV scale. Each physical model comes with a data base including cross sections valid in a certain energy range. It is obvious that a user has to select only the relevant physical models to keep the performance of the software and combine them to cover the desired energy range. In TGEANT, the list of physical processes and particles is optimized to the kinematic range of the COMPASS-II experiment.

Particles are defined by their mass, charge, spin, and also their lifetime and all decay modes. They are subclassified into leptons, bosons, mesons, baryons, and short-lived particles. Geant4 also differentiates the particles by their lifetime. For stable particles and particles with a very small probability to decay in a detector such as photons, electrons, protons, and neutrons the decay cannot be treated by Geant4. Particles with a lifetime $\geq 10^{-14}$ s, such as muons or charged pions, are called long-lived particles. In contrast to the short-lived particles, they may travel a finite length in the simulation. The π^0 or η particles, two examples of short-lived particles, decay instantaneously. A K^0 is immediately converted into a K^0_L or K^0_S, which decay according to their life time and decay modes.

The physical models that are implemented in TGEANT can be loaded in three steps. Depending on the user's goal of applications, it is beneficial to enable or disable parts of the physics list to optimize the performance of TGEANT. The first stage includes all electromagnetic interactions of the defined particles and their decay channels. The electromagnetic physics tables are sufficient to simulate a particle shower of a photon in an electromagnetic calorimeter or the energy loss of recoiled protons in the scintillator slats. A charged pion, however, would fly undisturbed through all detectors and calorimeters. Consequently, the standard physics list in TGEANT also includes hadronic interactions that are based on Fritiof and Bertini models. A more detailed discussion about the implementation of physical models in Geant4 is given in Ref. [74]. The full physics list also includes optical processes such as scintillation or Cherenkov radiation at the expense of runtime. TGEANT also offers the possibility to confine the optical processes to separate detectors, e.g. to enable the Cherenkov radiation in the RICH-1 detector and disable the scintillation process for the slats of the CAMERA detector and trigger hodoscopes.

A.3 Particle Tracking

Particle tracking is the main feature of the Geant4 toolkit. This entails the simulation of the particle transportation through matter and involves detector geometries, magnetic fields, physics interactions, and hits in the detectors.

The trajectory of a particle is divided into small steps. The starting point of a step is called pre-step point, while the ending one is called post-step point. At each point, a Geant4 algorithm is used to calculate the behavior of the particle. All calculations are based on Monte Carlo techniques. As long as the particle has enough kinetic energy, all the continuous processes the particle is able to do are applied first. This includes multiple scattering, ionization, and bremsstrahlung. The particle's energy loss is calculated as the sum of all contributing processes. Afterwards, all discrete processes are called, e.g. the different decay channels for a non-stable particle. Each process calculates and proposes a step length: the higher the process probability, the shorter the step length. In addition, the distance to the next volume boundary is calculated. The shortest step length is used for the particle's next step. During each step, secondary particles may have been created. All secondary particles are tracked individually. At the end of each step, the position and momentum vector of the particle are updated. Each step point is also flagged with the internal event time. The duration between the pre-step and post-step point is exactly the time of flight.

This mechanism has been proven to be very beneficial. A particle can never pass over a complete material layer and a particle step is always enclosed within one volume. This allows the user to calculate the complete energy deposit of the particle trajectory within one volume, which is an essential property of a sensitive detector. In addition, the particle's entrance and exit points are known. For each step, the step length is newly calculated depending on the surrounding material. Consequently, a much longer step length can be used for muons inside a vacuum than for muons inside layers of a detector plane. This flexibility optimizes the performance of the simulation. As described in Sec. 4.2.2, it is still useful to limit the step length for certain particles and regions in the experimental setup.

The number of secondary particles that are created during a step can be controlled by production cuts. Only secondary particles above the production cut are created and tracked through the Geant4 world until they are at rest with a kinetic energy of zero, while all others are not created. In order not to violate energy conservation, the energy of an omitted particle is treated as an energy deposit in the current volume. The production cut is not defined as an energy threshold for secondary particles but as a distance. A particle gets created only if it has enough kinetic energy to traverse a given distance in the surrounding medium. Consequently, the energy threshold for secondary particles depends on the material. The production cuts can be optimized for different particle types and detector regions. In TGEANT, for instance, the muon filter absorbers are combined into one region. Here, computing time for tracking of secondary particles that are unable to leave the absorber can be economized. On the other hand, an accurate simulation of an electromagnetic calorimeter is crucial, especially for the analysis of DVCS. Consequently, the production cuts for the different module types in the three electromagnetic calorimeters were optimized, as discussed in Chapter 5.

B. Data Formats

B.1 TGEANT Settings File

The TGEANT settings are put into several categories. The settings file of TGEANT is based on the XML format. The reading and writing functions are part of the library libSettings, which is linked in the graphical user interface and TGEANT. If the settings file is loaded in TGEANT, a consistency check for all settings is performed.

Table B.1: General settings of the TGEANT settings file. The following information is stored in the T4SGeneral object.

T4SGeneral	Type	Description
physicsList	string	Physics List: “EM_ONLY”, “STANDARD”, or “FULL”
useGflash	bool	Enable fast shower parameterization GFlash for ECAL regions
useVisualization	bool	Enable OGL visualization
useSeed	bool	Use custom seed
seed	long int	Custom seed
runName	string	Output name for all output files
outputPath	string	Output file path “default” = current directory
saveASCII	bool	Save standard TGEANT output file
saveBinary	bool	Save binary pile-up file
saveDetDat	bool	Create alignment file
exportGDML	bool	Create geometry file
useTrigger	bool	Enable trigger simulation
triggerPlugin	string	Name of the trigger plugin: “Hadron2008”, “SIDIS2011”, “Primakoff2012”, “DVCS2012”, “DY2014”, “DY2015”, or “DVCS2016”

namingWithSeed	bool	Add seed as suffix to output files
verboseLevel	int	Specify the amount of console output (0-4)
usePerformanceMonitor	bool	Enable CPU time measurements
checkOverlap	bool	Check overlaps between geometries For developers only, CPU-intensive
productionCutsGlobal	double	Global production cuts for secondaries
productionCutsGams	double	Production cuts in Gams modules
productionCutsRHGams	double	Production cuts in GamsRH modules
productionCutsMainz	double	Production cuts in Mainz modules
productionCutsOlga	double	Production cuts in Olga modules
productionCutsShashlik	double	Production cuts in Shashlik modules
productionCutsHcal	double	Production cuts in HCAL modules
noSecondaries	bool	Deactivate production of secondaries
colorTheme	int	Color theme for terminal (0-2)
simplifiedGeometries	bool	Simplified geometries without internal or invisible structures, only for visualization
noMemoryLimitation	bool	Disable memory monitor that stops TGEANT if the memory exceeds 2GB
useSplitting	bool	Enable the output file splitting Useful on batch systems with limited quota
eventsPerChunk	int	Number of events per split output file
useSplitPiping	bool	Enable file list writing for all finished split output files

Table B.2: Beam settings of the TGEANT settings file. The following information is stored in the T4SBeam object.

T4SBeam	Type	Description
numParticles	uint	Number of events to simulate
beamParticle	int	PDG ID for incoming beam particle
beamPlugin	string	Name of beam plugin: “BeamOnly” – only primary beam particle “VisualizationMode” – no particles “PYTHIA” – beam and Pythia6 “PYTHIA8” – beam and Pythia8 “LEPTO” – beam and LEPTO file reading “HEPGEN” – beam and HEPGen++ “Primakoff” – beam and Primakoff gen. “ascii” – beam and ASCII file generator “DummyGen” – stop beam at prim. vertex “User” – user-defined momentum-vector “Cosmics” – simulation of cosmic muons “ElectronBeam” – electron calib. beam “PhotonBeam” – longitudinal photon beam “PhotonCone” – conical photon beam “EcalCalib” – ECAL calibration setup “EventGen” – HEPGen++ without beam

beamEnergy	double	Total energy of incoming beam particle
useBeamfile	bool	Use the beam file
beamFileType	string	Allowed beam file particles: "Beam", "Halo", or "Both"
beamFileBackend	string	Name of the beam file backend "Muon" or "Pion"
beamFileZConvention	double	z position convention of the beam file
beamZStart	double	Beam start z position
usePileUp	bool	Enable pile-up simulation
beamFlux	double	Pile-up beam flux
timeGate	double	Time gate for pile-up
useAdditionalPileUp	bool	Enable additional pile-up simulation Additional muon beam file for pion beam
additionalPileUpFlux	double	Additional pile-up beam flux
beamFileZConvention-ForAdditionalPileUp	double	z position convention of the additional beam file
useTargetExtrap	bool	Enable the target extrapolation method
targetStepLimit	double	Step limitation for target region
useHadronicInteraction-EGCall	bool	Enable hadronic interaction method

B.1.1 Additional Beam Plugin Settings

Depending on the chosen beam plugin, some additional settings may be needed.

Table B.3: Additional HEPGen++ settings of the TGEANT settings file. The following information is stored in the T4SHEPGen object and is needed if TGEANT runs with the "HEPGEN" beam plugin. This plugin initializes and calls HEPGen++ [45].

T4SHEPGen	Type	Description
target	string	Target nucleon
IVECM	int	Switch for physics program
LST	int	Switch for diffractive dissociation
CUT	double[14]	Lepto soft cuts
THMAX	double	Scattered muon acceptance $\theta_{\max}$
alf	double	Value of the parameter for A dependence
atomas	double	Average atomic mass of the target
probc	double	Fraction of coherent events
bcoh	double	Slope of nuclear form factor
bin	double	Slope for production of a nucleon
clept	double	Lepton beam charge
slept	double	Lepton beam polarization
B0	double	Param. for x_{Bj}, t correlation (DVCS only)
xbj0	double	Param. for x_{Bj}, t correlation (DVCS only)
alphap	double	Param. for x_{Bj}, t correlation (DVCS only)
TLIM	double[2]	Generation ranges for t

usePi0_transv_table	bool	Switch between old and new π^0 table

Table B.4: Additional "User" plugin settings of the TGEANT settings file. The following information is stored in the T4SUser object.

T4SUser	Type	Description
position	double[3]	Start position of the primary particle
momentum	double[3]	Momentum direction of the prim. particle
useRandomEnergy	bool	Enable random energy selection
minEnergy	double	Minimal total energy
maxEnergy	double	Maximal total energy

Table B.5: Additional "Cosmics" plugin settings of the TGEANT settings file. The following information is stored in the T4SCosmic object.

T4SCosmic	Type	Description
angleVariation	double	Variation of the cosmics momentum direction
positionX	double	Mean x position of cosmics
positionZ	double	Mean z position of cosmics
variationX	double	Variation of x position
variationZ	double	Variation of z position

B.1.2 External File Paths

The design of the writing function ensures that the file paths to all external files that are stored in the TGEANT resources folder are stored as relative file paths. It is therefore possible to use the same settings files on different installations.

Table B.6: External file path settings of the TGEANT settings file. The following information is stored in the T4SExternalFiles object.

T4SExternalFiles	Type	Description
beamFile	string	Beam file path
beamFileForAdditional-PileUp	string	Additional beam file path
localGeneratorFile	string	Event generator file path (e.g. LEPTO)
triggerMatrixInnerX	string	IT coincidence matrix
triggerMatrixOuterY	string	OT coincidence matrix
triggerMatrixLadderX	string	LT coincidence matrix
triggerMatrixMiddleX	string	MT coincidence matrix (X)
triggerMatrixMiddleY	string	MT coincidence matrix (Y)
triggerMatrixLAST	string	LAST coincidence matrix
libHEPGen_Pi0	string	$\pi^0 \rightarrow \gamma\gamma$ table for HEPGen++

libHEPGen_Pi0_transv	string	$\pi^0 \to \gamma\gamma$ transv. table for HEPGen++
libHEPGen_Rho	string	$\rho^+ \to \pi^0\pi^+$ table for HEPGen++
visualizationMacro	string	Macro file for OGL visualization
detectorEfficiency	string	Data base to write alignment file
calorimeterInfo	string	Alignment file for calorimeter modules

B.1.3 Detector Alignment

All detectors in the COMPASS experiment are aligned individually in TGEANT. Each detector plane has its own entry in the settings file, except for detector planes that are mechanically fixed. For the sake of clarity, the alignment options are separated from the general, beam, and external file path options for the default settings file that is stored in the TGEANT resources folder. The minimal requirement for the alignment of a detector plane is summarized in a T4SDetector object, more complicated components of the setup require additional information and therefore extend this object.

Table B.7: General detector alignment settings of the TGEANT settings file.

T4SDetector	Type	Description
useDetector	bool	Place detector in TGEANT world
name	string	Detector name
position	double[3]	Detector position
useMechanicalStructure	bool	Build mechanical structures

Table B.8: Alignment settings of the TGEANT settings file for all magnets.

T4SMagnet	Type	Description
T4SDetector		General detector options
scaleFactor	double	Magnetic field scale factor
useField	bool	Enable magnetic field
fieldmapPath	string	Path to field map
current	int	Current to be written in the alignment file

Table B.9: Alignment settings of the TGEANT settings file for the CAMERA detector, which can optionally be aligned using a detector calibration file.

T4SRPD	Type	Description
T4SDetector		General detector options
useOptical	bool	Enable optical physics, CPU-intensive
useSingleSlab	bool	Build only one scintillator For detector studies only
useCalibrationFile	bool	Use calibration file for detector alignment
calibrationFilePath	string	Path to detector calibration file

Table B.10: Alignment settings of the TGEANT settings file for the RICH-1 detector.

T4SRICH	Type	Description
T4SDetector		General detector options
useOptical	bool	Enable optical physics, CPU-intensive
visibleHousing	bool	Invisible RICH-1 radiator For visualization purposes only
gas	string	Gas inside the RICH-1 radiator "C4F10" or "N2"

Calorimeter Modules

The electromagnetic and hadronic calorimeters are composed of several modules. Modules of the same kind are placed block-wise and are arranged in columns and rows. The position of the first module (with the smallest x and y position) is given, all others are placed successively. These settings are stored in the alignment file for calorimeter modules, see Tab. B.6.

Table B.11: Alignment settings of the TGEANT settings file for calorimeter modules.

T4SCAL	Type	Description
detectorId	int	Detector ID of first module
moduleName	string	Module names: "GAMS", "RHGAMS", "MAINZ", "OLGA", "SHASHLIK", "ECAL0", "HCAL1", "HCAL2"
nRow	int	Number of rows
nCol	int	Number of columns
position	double[3]	Position of first module

The T4SCAL object also includes some additional information that is needed to write the alignment file but is not used in TGEANT and therefore omitted here.

B.2 TGEANT Output File Format

The TGEANT output is composed of different objects, including the different aspects of the event simulation, such as sensitive detector output, trajectories, or event generator information.

Table B.12: T4Event object of the TGEANT output file. This object contains the complete TGEANT event output.

T4Event	Type	Description
beamData	T4BeamData	see Tab. B.13
tracking	vector<T4HitData>	see Tab. B.15
trigger	vector<T4HitData>	
calorimeter	vector<T4HitData>	
rich	vector<T4RichData>	see Tab. B.17
pmt	vector<T4PmtData>	see Tab. B.18
trigMask	int	Trigger mask
processingTime	double	Processing time

Table B.13: T4BeamData object of the TGEANT output file. This object combines all Monte Carlo information that is not used for the event reconstruction in CORAL and that is directly transmitted to the analysis software PHAST.

T4BeamData	Type	Description
vertexPosition	double[3]	vertex position [cm]
vertexTime	double	Geant4-time of vertex [ns]
generator	int	TGEANT internal generator flag
aux	double	Auxiliary option
x_bj	float	Bjorken variable
y	float	Transmitted energy fraction
w2	float	Invariant mass of $\gamma^* p$ system $[(\mathrm{GeV/c^2})^2]$
q2	float	Q^2 $[(\mathrm{GeV/c})^2]$
nu	float	Absolute energy transfer [GeV]
uservar	float[20]	User variables of the event generator
lst	int[40]	LST parameters of the event generator
parl	float[30]	PARL parameters of the event generator
cut	float[14]	CUT parameters of the event generator
nBeamParticle	uint	Number of event generator particles
vector<T4BeamParticle>		see Tab. B.14
nTrajectories	uint	Number of trajectories
vector<T4Trajectory>		see Tab. B.16
T4PySubs		Pythia6 options (optional)
T4PyPars		Pythia6 options (optional)

Table B.14: T4BeamParticle object of the TGEANT output file.

T4BeamParticle	Type	Description
k[0]	int	K-code
k[1]	int	PDG particle ID
k[2]	int	Origin line number
k[3]	int	Daughter particle line number (begin)
k[4]	int	Daughter particle line number (end)
p[0]	float	Momentum p_x [GeV/c]
p[2]	float	Momentum p_y [GeV/c]
p[3]	float	Momentum p_z [GeV/c]
p[4]	float	Total energy [GeV]
p[5]	float	Particle mass [GeV/c^2]

Table B.15: T4HitData object of the TGEANT output file.

T4HitData	Type	Description
detectorName	string	Detector name
detectorId	int	Detector ID
channelNo	int	Channel number
trackId	int	Track ID of incident particle
particleId	int	PDG ID of incident particle
particleEnergy	double	Energy of incident particle [MeV]
time	double	Geant4-time [ns]
beta	double	β of incident particle
energyDeposit	double	Total energy deposit [MeV]
hitPosition	double[3]	Average hit position [mm]
primaryHitPosition	double[3]	Primary hit position [mm]
lastHitPosition	double[3]	Last hit position [mm]
momentum	double[3]	Momentum of incident particle [MeV/c]

Table B.16: T4Trajectory object of the TGEANT output file.

T4Trajectory	Type	Description
trackId	int	Track ID of trajectory
parentId	int	Parent's track ID
particleId	int	PDG particle ID
position	float[3]	Start point of trajectory [mm]
time	float	Creation Geant4-time [ns]
momentum	float[3]	Momentum at start point [MeV/c]

B.2.1 RICH-1 Readout

The RICH-1 readout is designed to detect the Cherenkov photons on the detectors installed on the upstream side of the RICH-1 radiator and is only working if the optical processes are enabled. The information listed in Tab. B.17 is saved in the TGEANT output file for each optical photon hit.

The processing time of one event strongly correlates with the number of particle tracks. The simulation of optical processes is therefore only useful if the readout of the RICH-1 detector is relevant for the analysis. When simulating with the 2012 DVCS setup, the RICH-1 readout is switched off.

Table B.17: T4RichData object of the TGEANT output file.

T4RichData	Type	Description
detectorName	string	Detector name
detectorId	int	Detector ID
photonHitPosition	double[3]	Photon hit position (global system) [mm]
photonProduction-Position	double[3]	Photon production position [mm]
momentumMother-Particle	double[3]	Momentum of the photon's parent particle [MeV/c]
parentTrackId	string	Parent's track ID
photonEnergy	double	Photon energy [MeV]
time	double	Geant4-time [ns]
xPadPosition	double	x pos. in the detector ref. system [mm]
yPadPosition	double	y pos. in the detector ref. system [mm]
cerenkovAngle	double	Cherenkov angle of the prod. process [rad]

B.2.2 PMT Readout

Table B.18: T4PmtData object of the TGEANT output file. This object is used to save the output of the simulation of a photo multiplier tube readout with the GANDALF module. Detailed information about this object is given in [96].

T4PmtData	Type	Description
detectorName	string	Detector name
detectorId	int	Detector ID
channelNo	int	Channel number
randomTime	double	Random start time of GANDALF sampling [ns]
firstEventTime	double	Geant4-time of first photon [ns]
nsPerBin	int	Inverse sampling rate in [ns]
windowSize	int	Sampling time window
digits	vector<int>	Simulated sampling signal

B.3 CORAL Options for TGEANT

The event reconstruction software CORAL is controlled with an option file. To allow for a reconstruction of TGEANT events, special options are added to the CORAL interface. The standard options are listed in Tab. B.19. Other TGEANT modules can be enabled optionally:

- Trigger simulation in combination with hodoscope efficiencies (Tab. B.20 and Sec. 6.2)
- Two dimensional tracking detector efficiencies (Tab. B.21)
- External pile-up addition (Tab. B.22 and Sec. 4.2.4)
- New ECAL calibration method (Tab. B.23 and Sec. 5.5)
- ECAL noise simulation (Tab. B.24)
- EPIC calibration (Tab. B.25)

Table B.19: Standard CORAL options for reconstruction of TGEANT events.

CORAL Option	Argument	Description
CsTGEANTFile file	file path	TGEANT output file
mDST file	file path	CORAL output file
detector table	file path	Alignment file from TGEANT
CsGDMLGeometry file	file path	Geometry file from TGEANT
CsTGEANT RunNumber	number	Specify a Monte Carlo run number (optional)

Table B.20: CORAL options for enabling the TGEANT trigger simulation during the event reconstruction. The efficiencies of the hodoscope channels are transmitted by a list of channel numbers and efficiencies.

CsTGEANT Option	Argument	Description
TriggerPlugin	Plugin name: “DVCS2012” “DY2014” “DY2015” “DVCS2016”	Enables the trigger simulation in CORAL
TriggerMatrixInnerX	file path	IT coincidence matrix
TriggerMatrixMiddleX	file path	MT coincidence matrix (X)
TriggerMatrixMiddleY	file path	MT coincidence matrix (Y)
TriggerMatrixLadderX	file path	LT coincidence matrix
TriggerMatrixOuterY	file path	OT coincidence matrix
TriggerMatrixLast	file path	LAST coincidence matrix
		Efficiencies of hodoscope channels:
TriggerEfficI4X_dn	list	HI4 (lower)
TriggerEfficI4X_up	list	HI4 (upper)
TriggerEfficI5X_dn	list	HI5 (lower)
TriggerEfficI5X_up	list	HI5 (upper)
TriggerEfficM4X_dn	list	HM4X (lower)

TriggerEfficM4X_up	list	HM4X (upper)
TriggerEfficM4Y	list	HM4Y
TriggerEfficM5X_dn	list	HM5X (lower)
TriggerEfficM5X_up	list	HM5X (upper)
TriggerEfficM5Y	list	HM5Y
TriggerEfficL4X	list	HL4
TriggerEfficL5X	list	HL5
TriggerEfficO3Y	list	HO3
TriggerEfficO4Y1	list	HO4 (bending direction)
TriggerEfficO4Y2	list	HO4 (non-bending direction)
TriggerEfficLast1	list	H1
TriggerEfficLast2	list	H2

Table B.21: CORAL options for enabling the two dimensional tracking detector efficiencies module. Detailed information about this module is given in [45].

CsTGEANT Option	Argument	Description
2DEfficDB	file path	2D efficiencies data base (.sqlite)
2DEfficYear	name	Identifier flag for selecting a efficiency map, can be used to identify different periods
2DEfficAcceptNearbyYears	YES	Load most detailed efficiency map even if this map is from another period

Table B.22: CORAL options for enabling the external pile-up addition module. Detailed information about this module is given in [45].

CsTGEANT Option	Argument	Description
ExternalPileUp	1	Enable the external pile up addition module
ExternalPileUpFlux	flux	Particle flux in number per ns
ExternalPileUpTGate	time gate	Time gate in ns of pile-up
ExternalPileUpFileList	file path	List of binary pile-up files
ExternalPileUpCache	1	Copy the loaded binary file to a local folder
ExternalPileUpCacheFolder	file path	Local folder for caching the binary pile-up file

ECAL Options

Table B.23: CORAL options for enabling the improved ECAL calibration method, which is presented in Sec. 5.5. The two calibration values a and c are transmitted by the CORAL option file, while the linear calibration value b is written in the alignment file.

CsTGEANT Option	Argument	Description
AddCalib_-		
ECAL0_Shashlik	a c	ECAL0 Shashlik
ECAL1_Shashlik	a c	ECAL1 Shashlik
ECAL1_Gams	a c	ECAL1 Gams
ECAL1_Mainz	a c	ECAL1 Mainz
ECAL1_Olga	a c	ECAL1 Olga
ECAL2_Shashlik	a c	ECAL2 Shashlik
ECAL2_Gams	a c	ECAL2 Gams
ECAL2_GamsRH	a c	ECAL2 GamsRH

Table B.24: CORAL options for enabling the ECAL noise simulation module. Detailed information about this module is given in [45].

CsTGEANT Option	Argument	Description
EcalNoise	1	Enable the ECAL noise simulation module
EcalNoiseFile	file path	ECAL noise data base
EcalNoiseRate	rate	Average number of clusters to add per event

Table B.25: CORAL options for enabling the EPIC calibration module. EPIC is a cell-dependent π^0 mass calibration software for electromagnetic calorimeters [97], which can be used alternatively or additionally to the new ECAL calibration method.

CsTGEANT Option	Argument	Description
EPICCalib	bool	Enable EPIC calibration
EPIC_ECAL0	file path	EPIC calibration file for ECAL0
EPIC_ECAL1	file path	EPIC calibration file for ECAL1
EPIC_ECAL2	file path	EPIC calibration file for ECAL2

B.4 Beam File Format

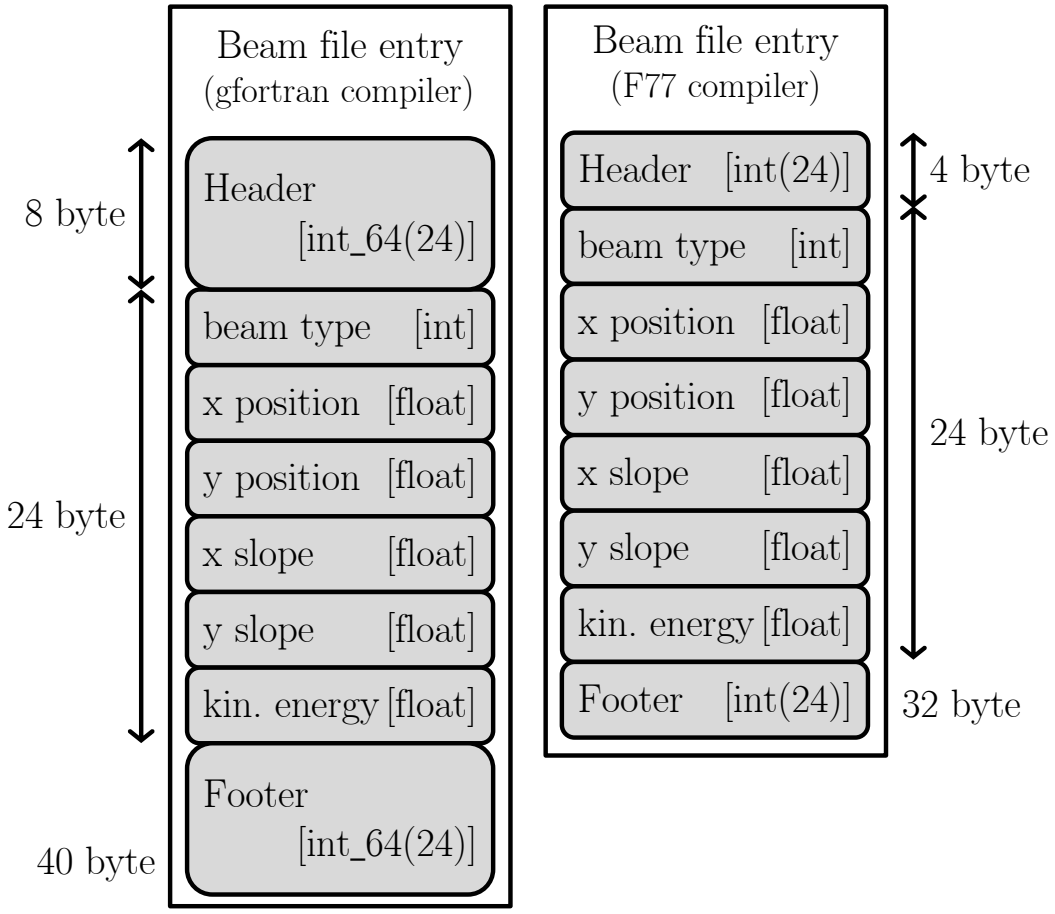

Figure B.1: The beam file format used at COMPASS. The left diagram shows the gfortran-compatible header sizes with a total entry size of 40 byte, the right diagram depicts the old F77-compatible one with a total size of 32 byte. Header and footer flags are identified by the number 24. TGEANT can identify and read both beam file formats. The beam type is used to classify the beam particles: particles intersecting the target are separated from the halo. TGEANT offers the option to consider this value, but this is not obligatory, since a primary vertex is always generated inside the target volume.

B.5 LEPTO Output Format

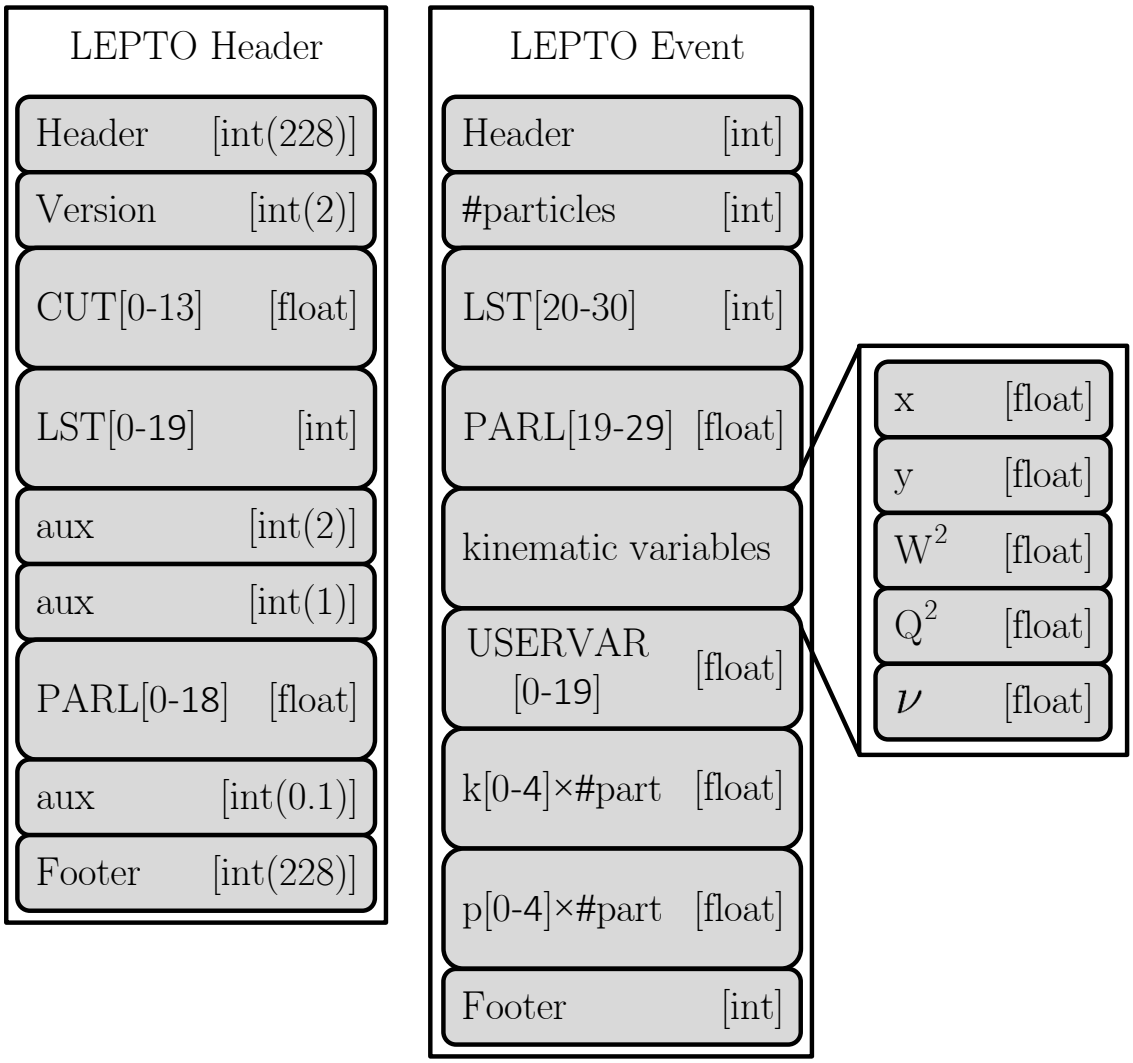

Figure B.2: The LEPTO output format version 2. The header at the beginning of the LEPTO file defines all global parameters such as the kinematic soft-cuts, which are stored in the CUT array, and the first part of the LST and PARL arrays. Header and footer flags are identified by the number 228. The LEPTO events are stored successively. The size of the event block depends on the number of particles.

C. Results of the ECAL Tuning

Chapter 5 describes the tuning of the ECAL simulation in TGEANT. Important is an adjustment of the Geant4 production cuts for all ECAL modules, a tuning of the radial GFlash parameterization parameters, and an energy-dependent calibration for all ECAL modules using three parameters. For the sake of clarity, only the results for one kind of ECAL module are given in the chapter. All other results are summarized in this appendix.

C.1 Production Cuts for ECAL Regions

The tuning of the production cuts is presented for all Gams modules in Sec. 5.3. The following figures present the final results for all other modules:

- GamsRH, Fig. C.1
- Mainz, Fig. C.2
- Olga, Fig. C.3
- Shashlik, Fig. C.4

Note that the production cuts are a purely material-dependent quantity, thus a separation between different electromagnetic calorimeters is not needed.

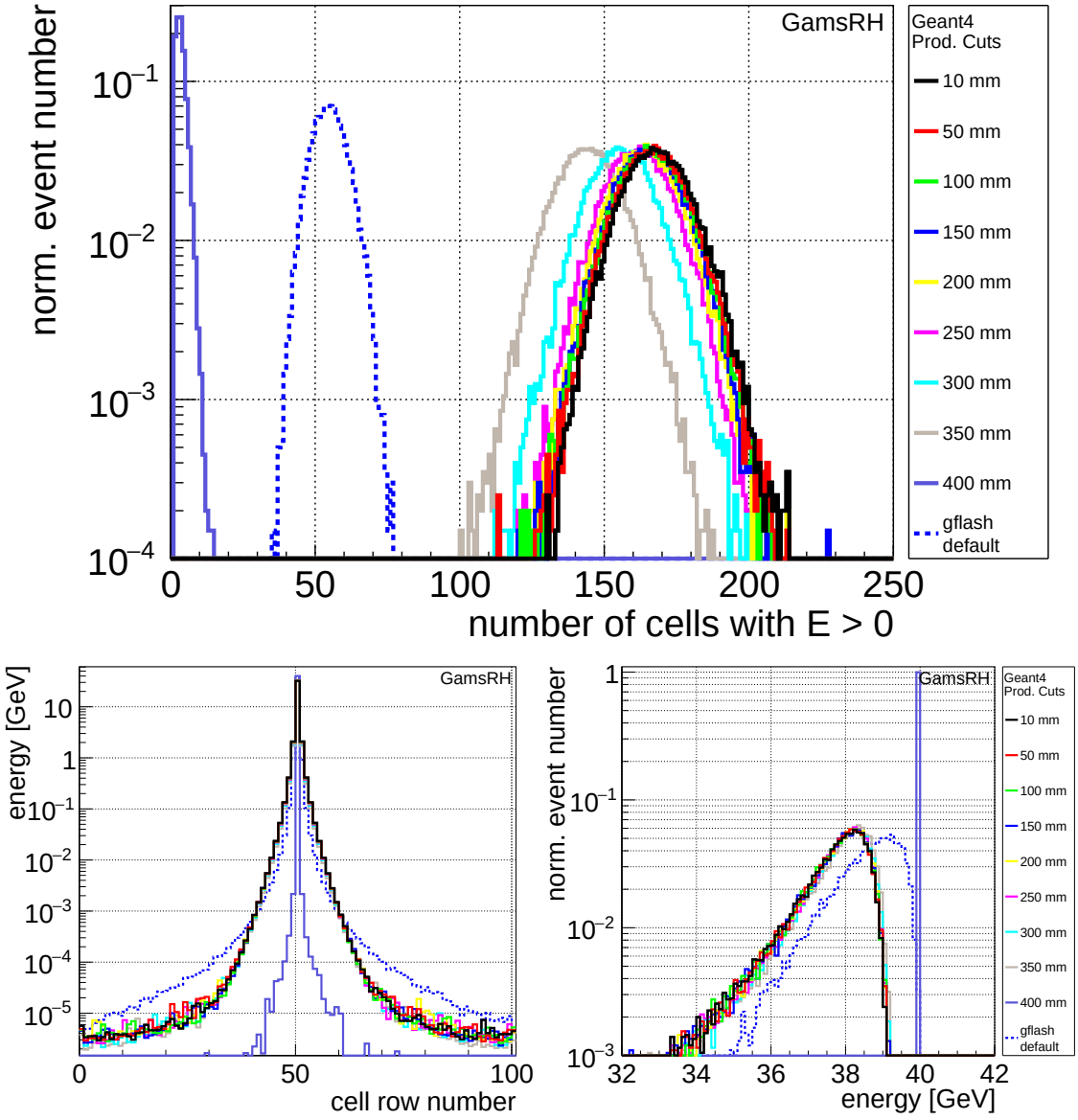

Figure C.1: Production cuts tuning for GamsRH modules using a 40 GeV electron beam in the test calorimeter. Top: Number of cells with an energy deposit. Bottom: Energy profile (left) and measured energy deposit (right). The new default production cuts for GamsRH modules are 250 mm.

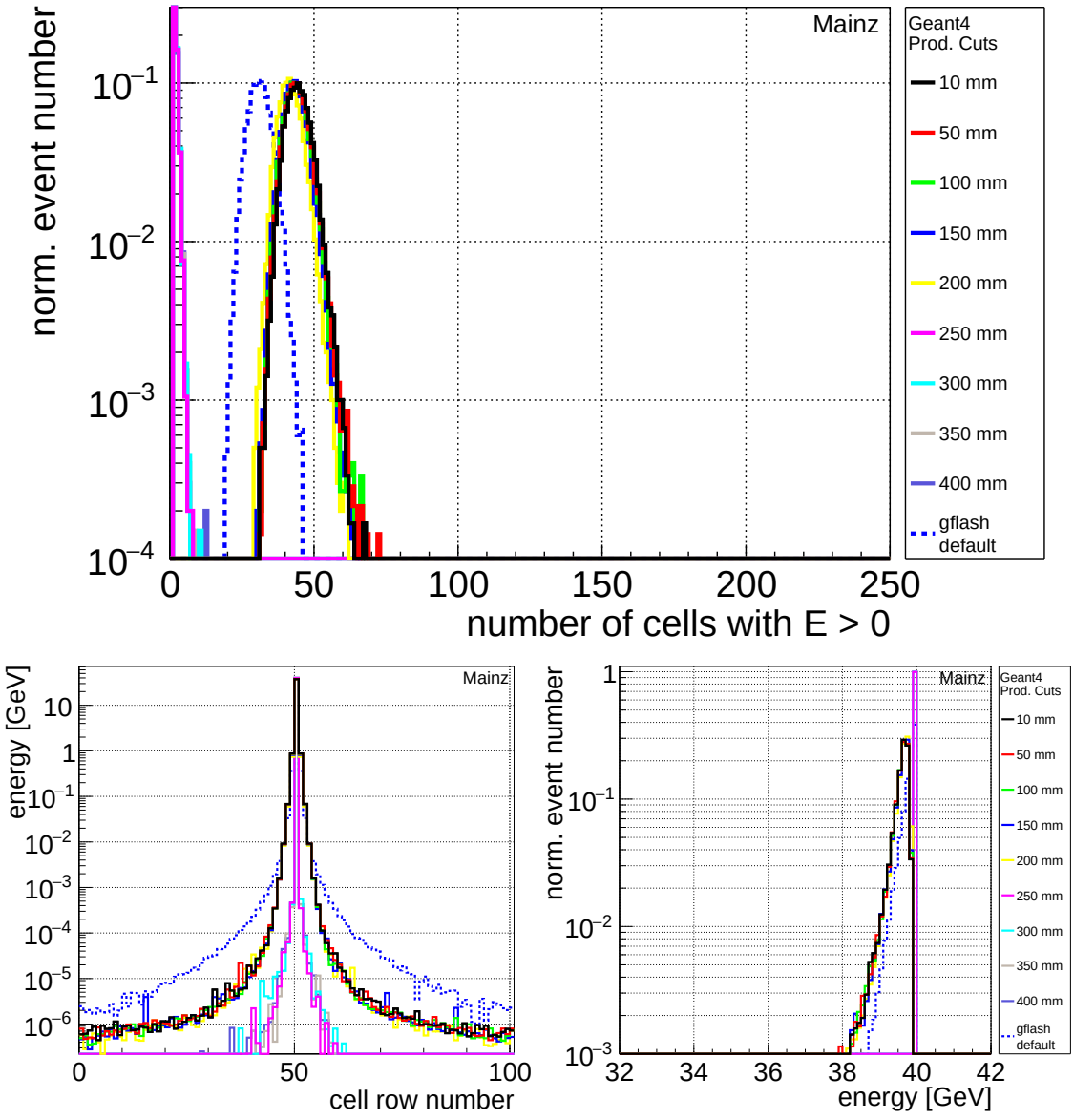

Figure C.2: Production cuts tuning for Mainz modules using a 40 GeV electron beam in the test calorimeter. Top: Number of cells with an energy deposit. Bottom: Energy profile (left) and measured energy deposit (right). The new default production cuts for Mainz modules are 150 mm.

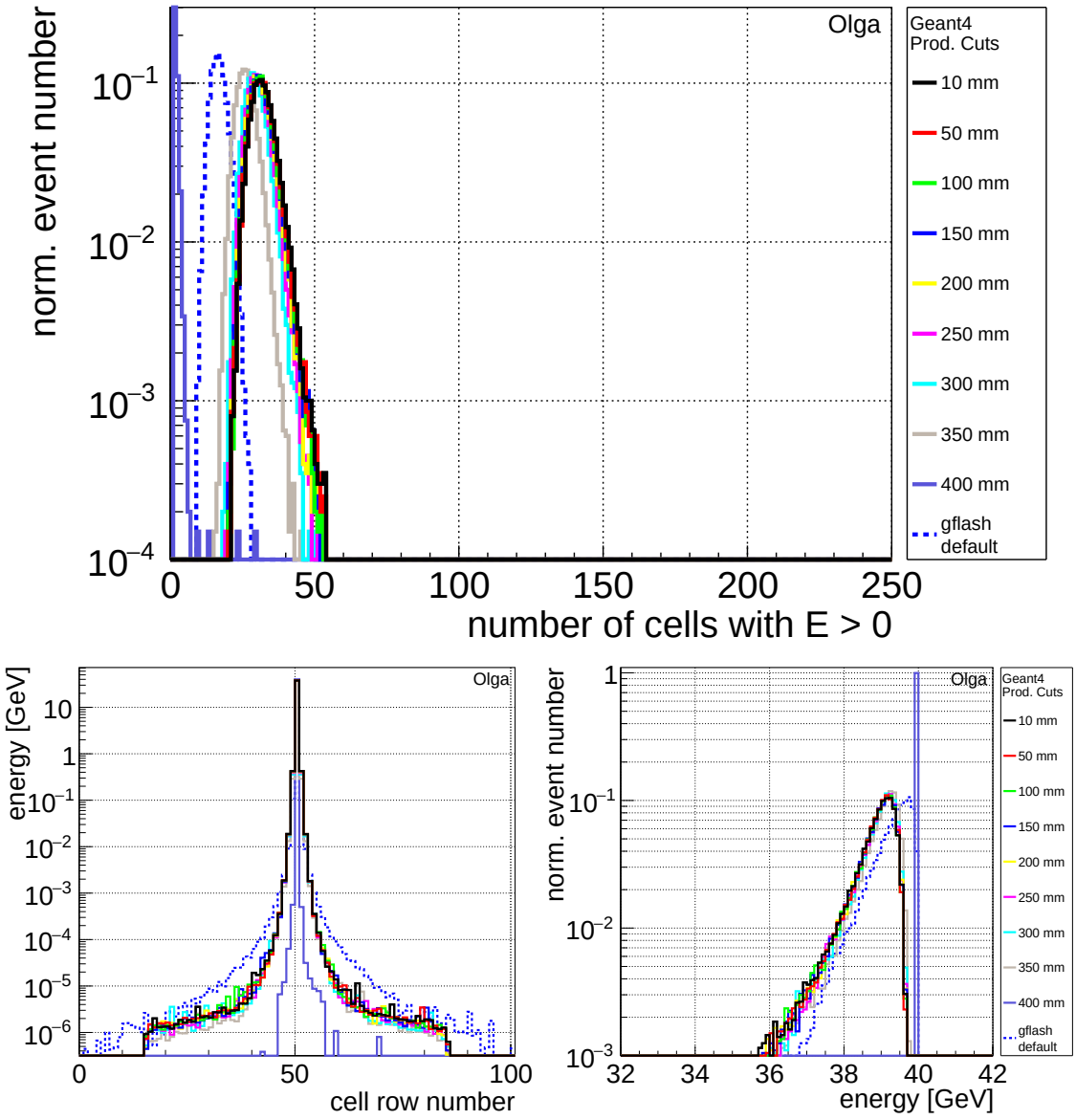

Figure C.3: Production cuts tuning for Olga modules using a 40 GeV electron beam in the test calorimeter. Top: Number of cells with an energy deposit. Bottom: Energy profile (left) and measured energy deposit (right). The new default production cuts for Olga modules are 300 mm.

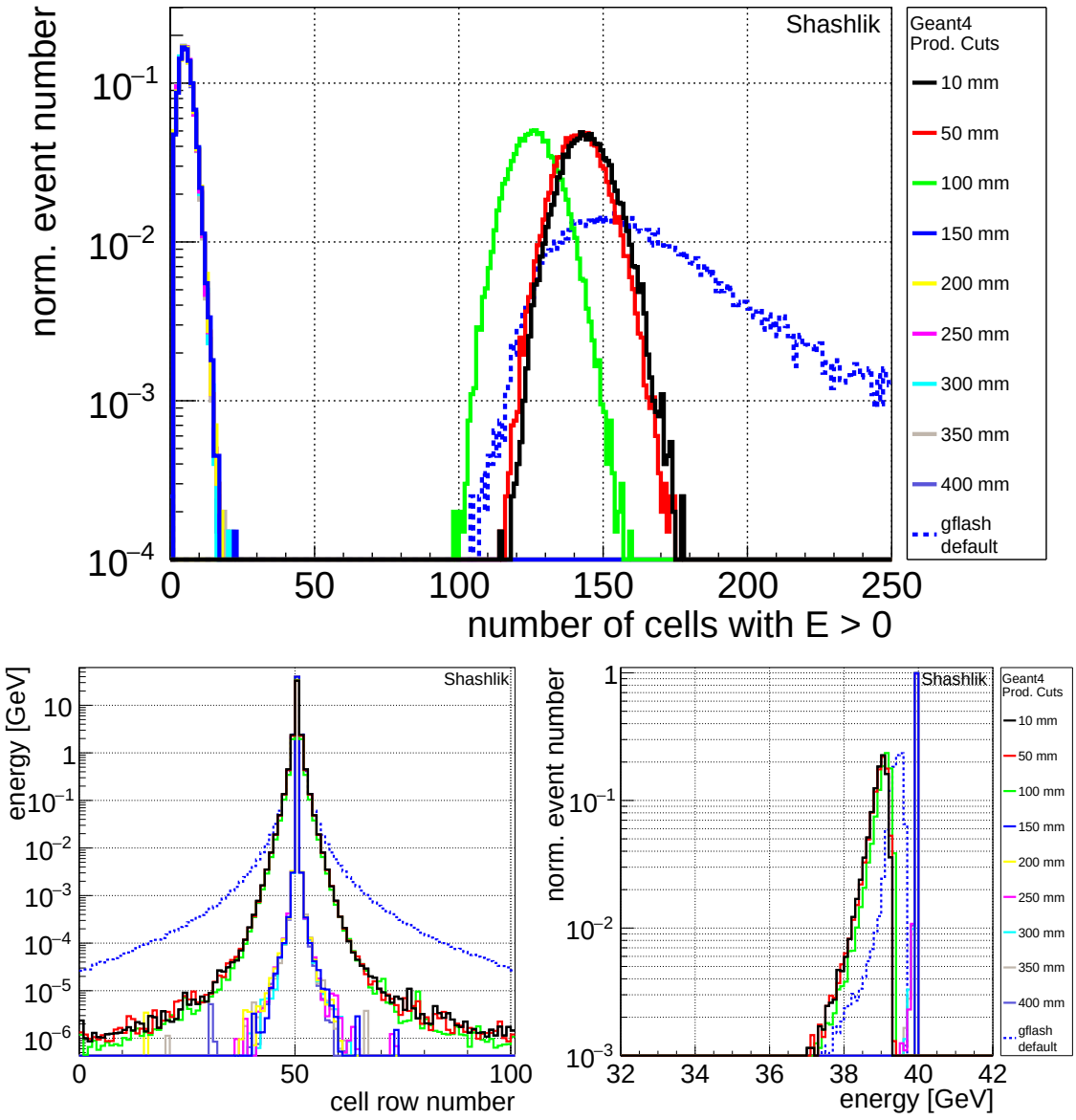

Figure C.4: Production cuts tuning for Shashlik modules using a 40 GeV electron beam in the test calorimeter. Top: Number of cells with an energy deposit. Bottom: Energy profile (left) and measured energy deposit (right). The new default production cuts for Shashlik modules are 50 mm.

C.2 GFlash Tuning

The GFlash tuning for TGEANT is described in Sec. 5.4, presenting the results for all Gams modules. The results for all other modules are shown in the following figures:

- GamsRH, Fig. C.5
- Mainz, Fig. C.6
- Olga, Fig. C.7
- Shashlik, Fig. C.8

Note that the GFLash parameterization only depends on the material properties of the ECAL module. A separation between different electromagnetic calorimeters is therefore not needed.

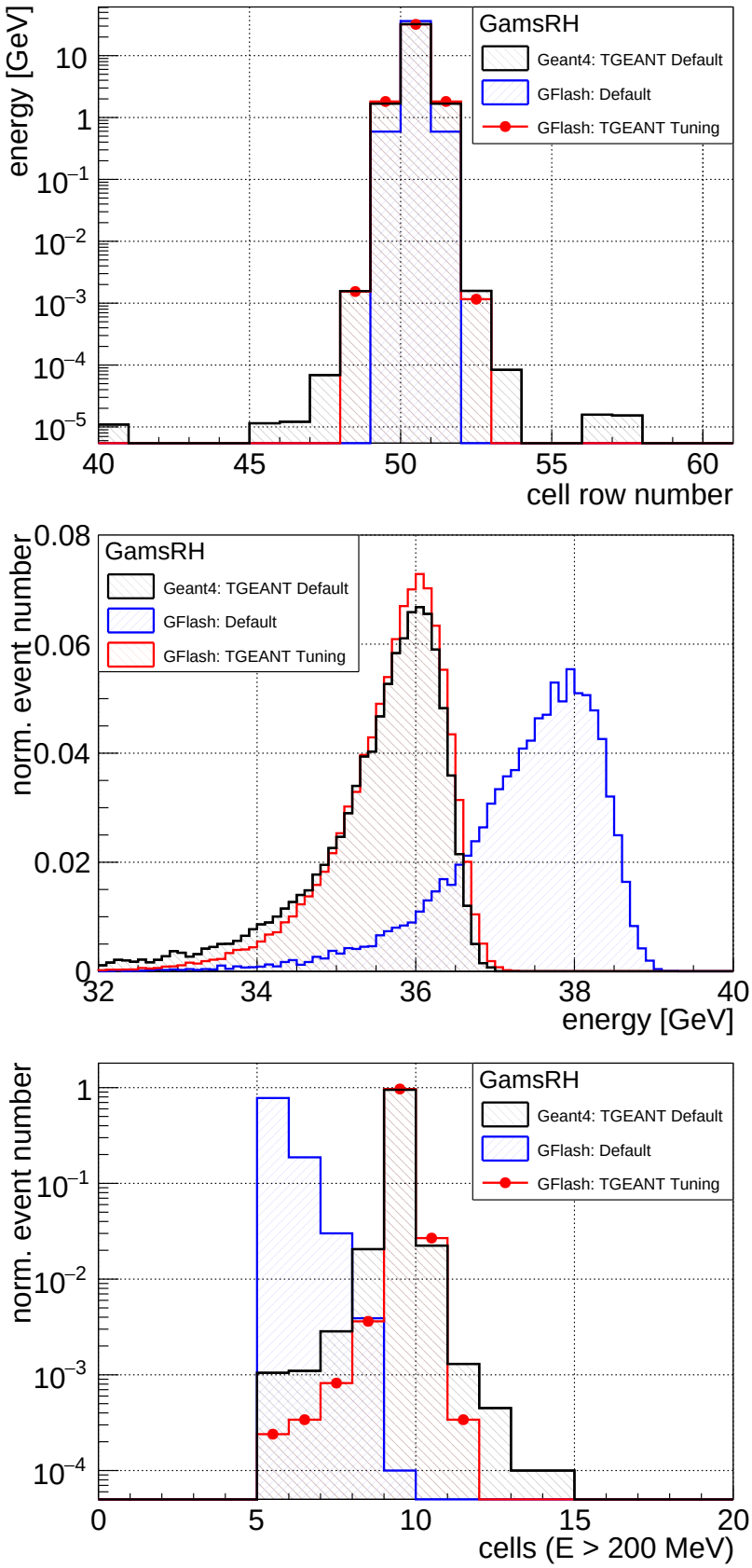

Figure C.5: Results of the GFlash tuning for GamsRH modules. Top: Energy profile simulated in the test calorimeter with a 40 GeV electron beam. Center: Energy calibration. Bottom: Number of cells above the 200 MeV threshold.

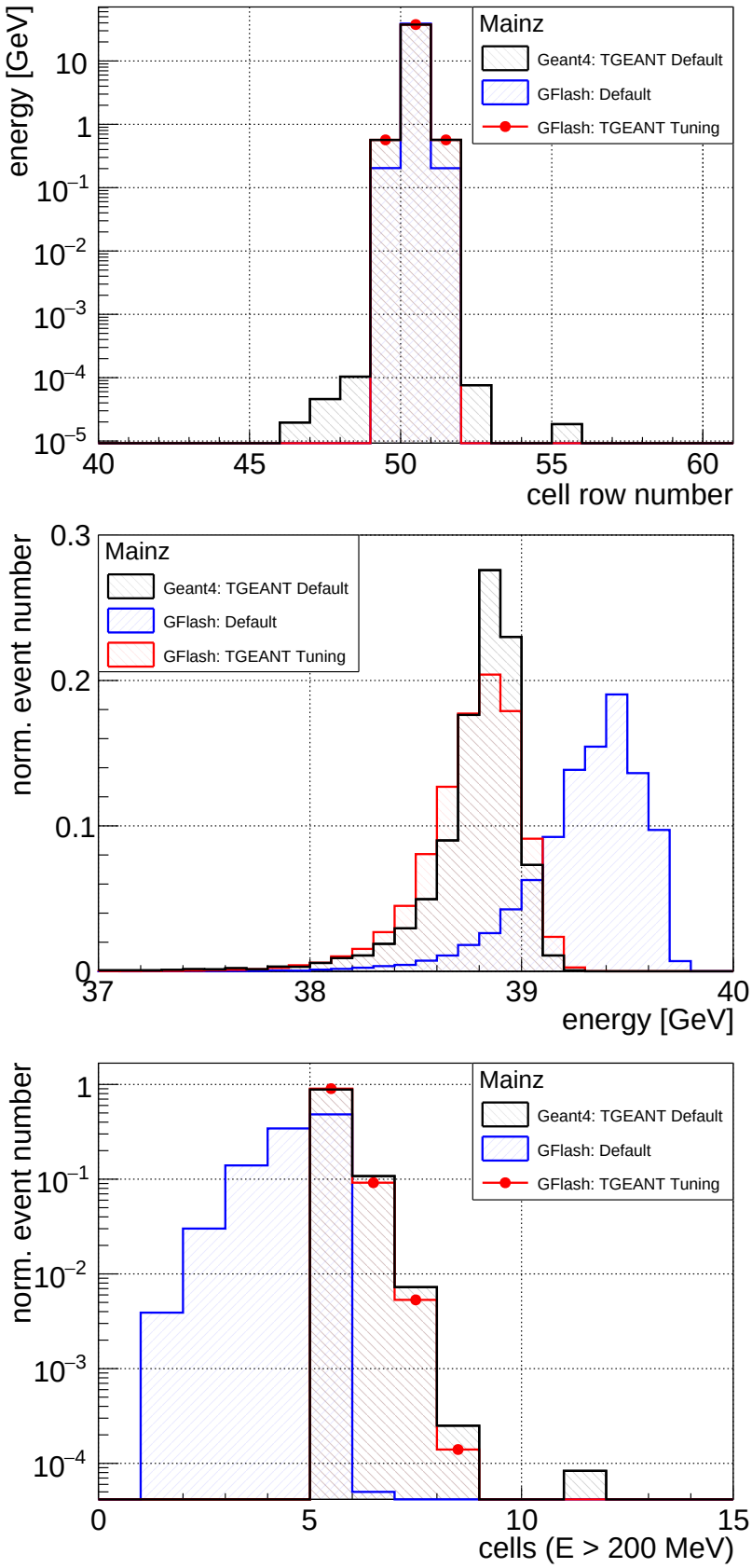

Figure C.6: Results of the GFlash tuning for Mainz modules. Top: Energy profile simulated in the test calorimeter with a 40 GeV electron beam. Center: Energy calibration. Bottom: Number of cells above the 200 MeV threshold.

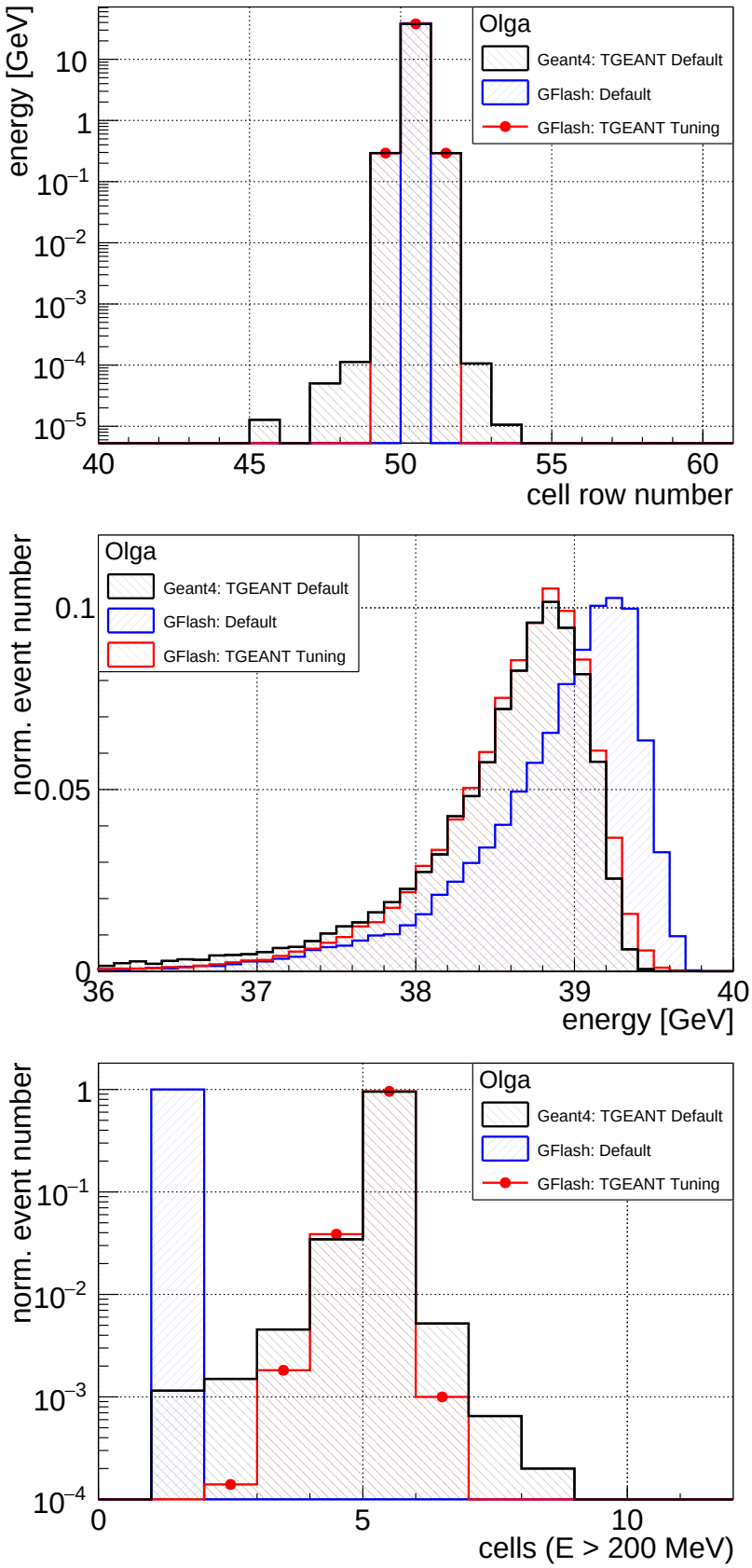

Figure C.7: Results of the GFlash tuning for Olga modules. Top: Energy profile simulated in the test calorimeter with a 40 GeV electron beam. Center: Energy calibration. Bottom: Number of cells above the 200 MeV threshold.

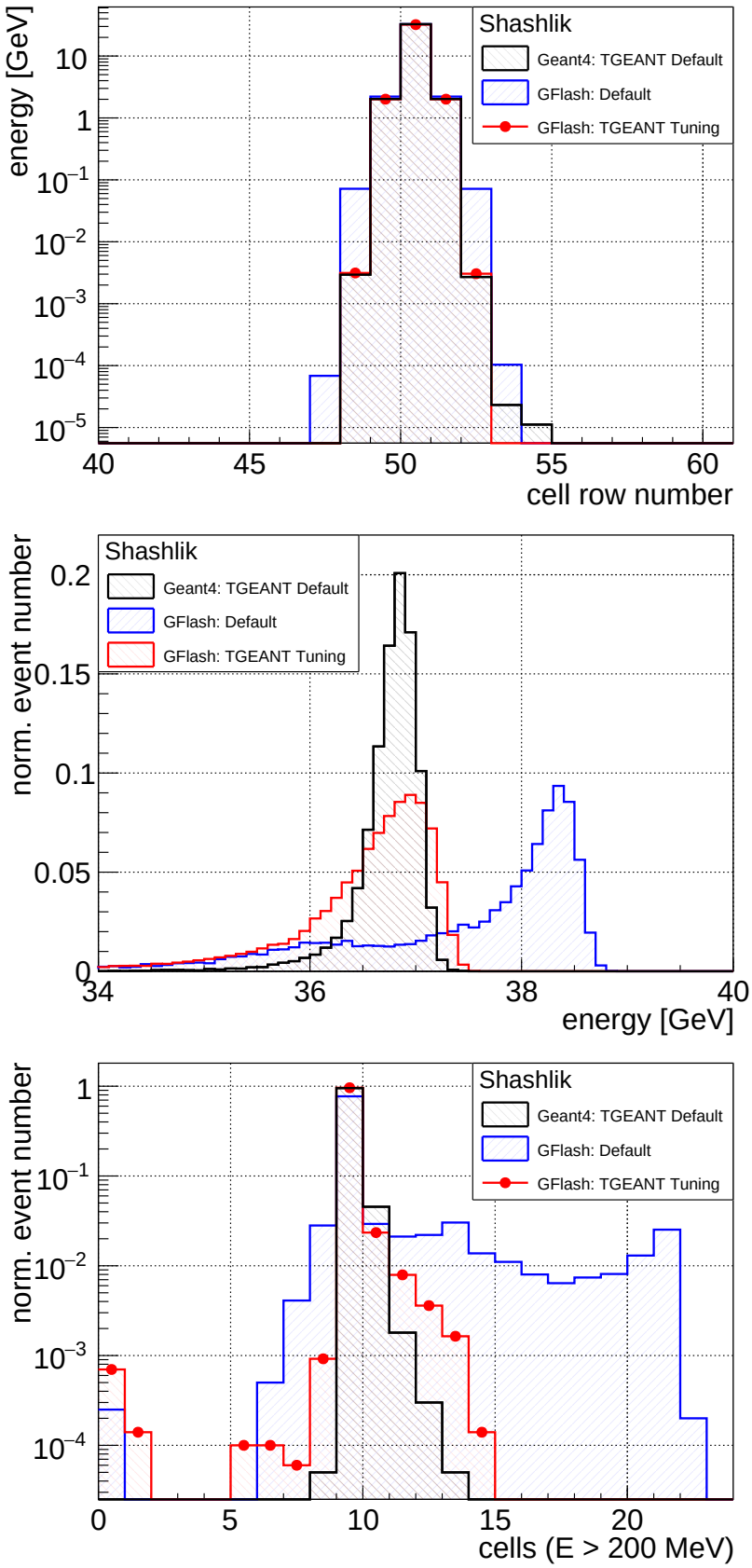

Figure C.8: Results of the GFlash tuning for Shashlik modules. Top: Energy profile simulated in the test calorimeter with a 40 GeV electron beam. Center: Energy calibration. Bottom: Number of cells above the 200 MeV threshold.

C.3 Energy Calibration

For all electromagnetic calorimeters, the energy calibration needs to be performed individually for each kind of module. The results of the new energy-dependent calibration method and comparisons with the default method for all ECAL2 modules are already presented in Sec. 5.5. The results for all other modules are shown in the following figures:

- Shashlik (ECAL0), Fig. C.9
- All modules of ECAL1, Fig. C.10
- Gams (ECAL1), Fig. C.11
- Mainz (ECAL1), Fig. C.12
- Olga (ECAL1), Fig. C.13
- Shashlik (ECAL1), Fig. C.14
- Gams (ECAL2), Fig. C.15
- GamsRH (ECAL2), Fig. C.16
- Shashlik (ECAL2), Fig. C.17

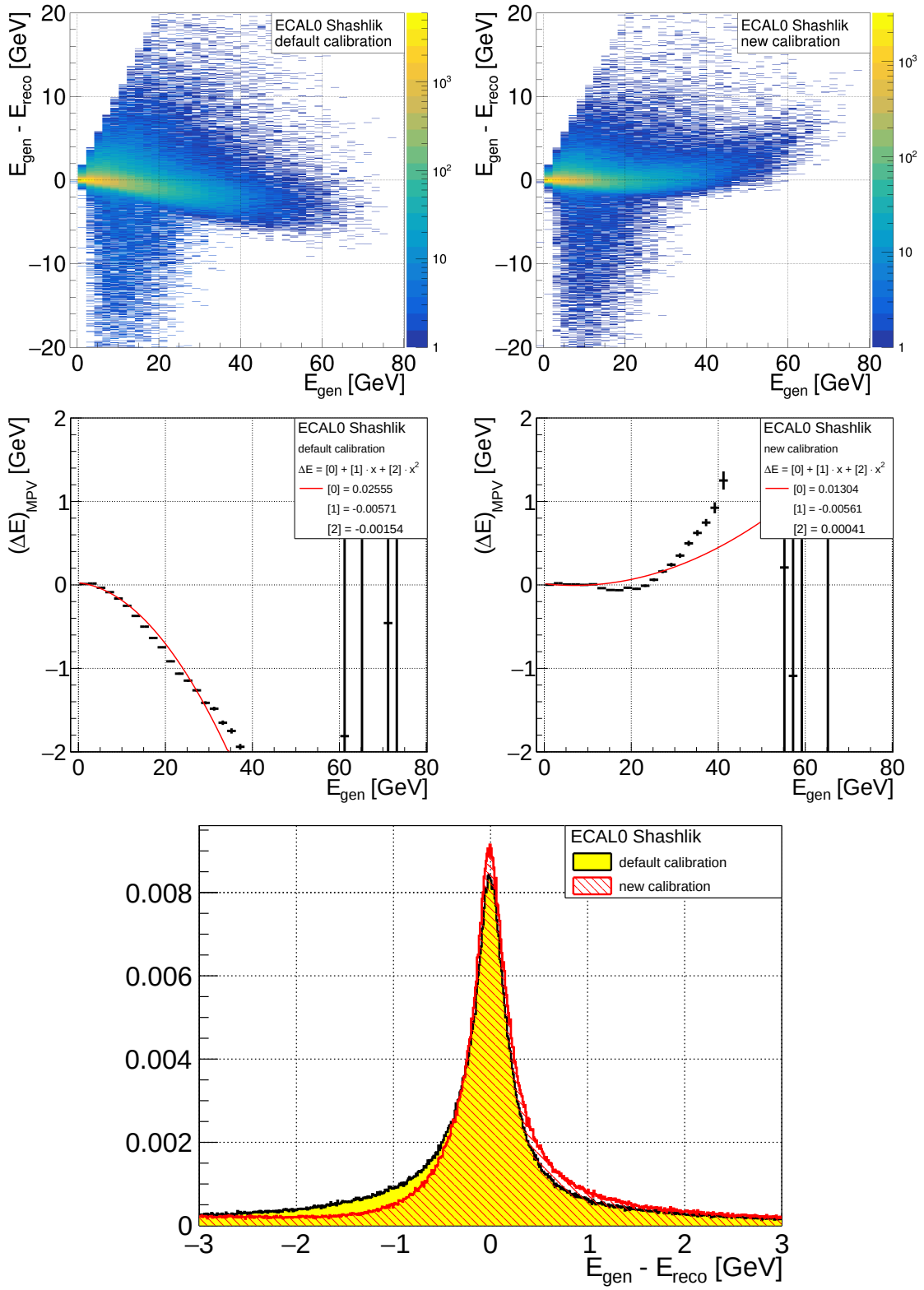

Figure C.9: Results of the new energy calibration method for ECAL0 Shashlik modules in comparison with the default energy calibration method. Top: Difference between reconstructed and generated cluster energy as a function of the generated energy. Center: Most probable values of the energy difference with the calibration fit. Bottom: Energy difference distribution of both methods in comparison.

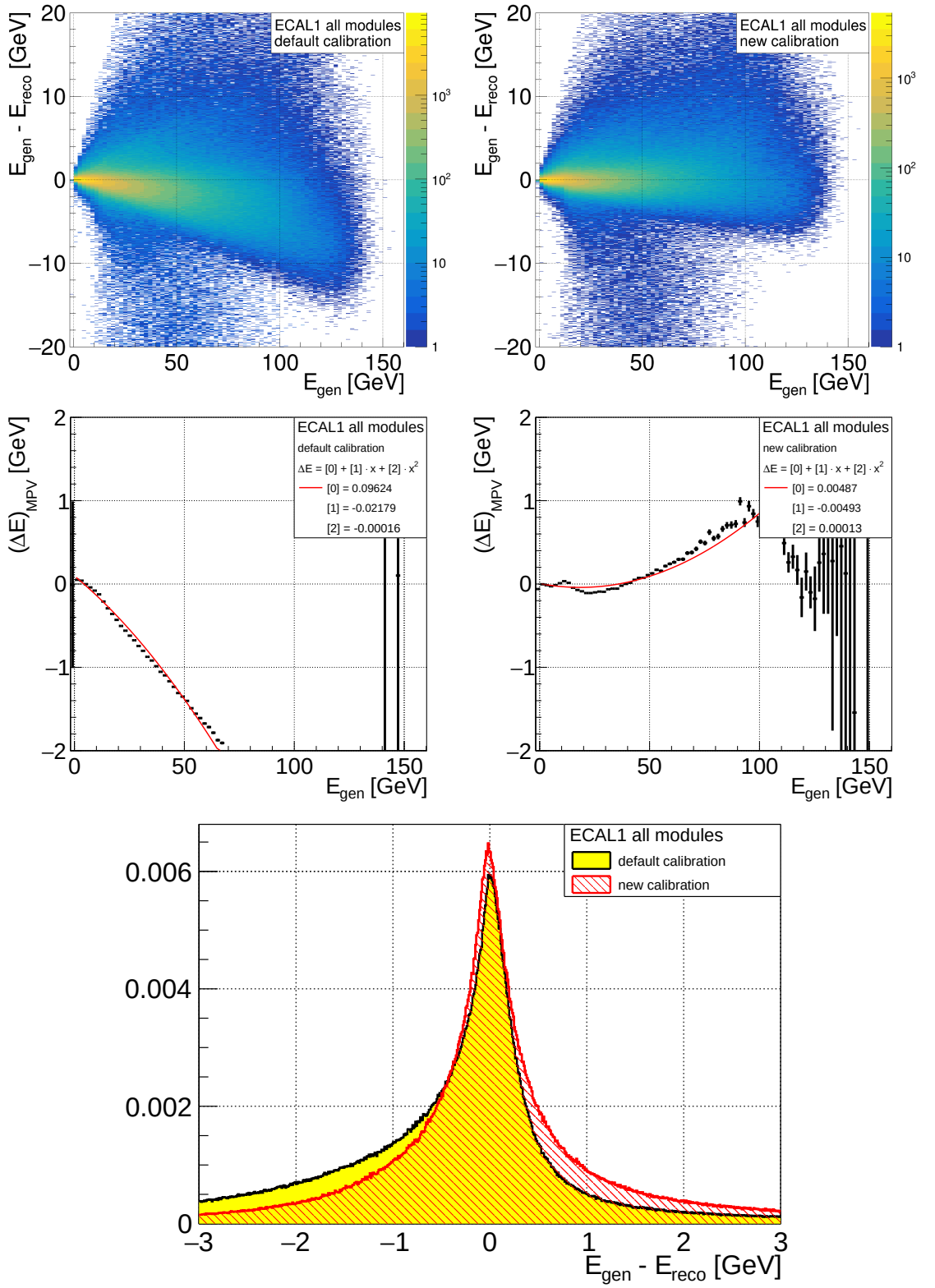

Figure C.10: Results of the new energy calibration method for all ECAL1 modules in comparison with the default energy calibration method. Top: Difference between reconstructed and generated cluster energy as a function of the generated energy. Center: Most probable values of the energy difference with the calibration fit. Bottom: Energy difference distribution of both methods in comparison.

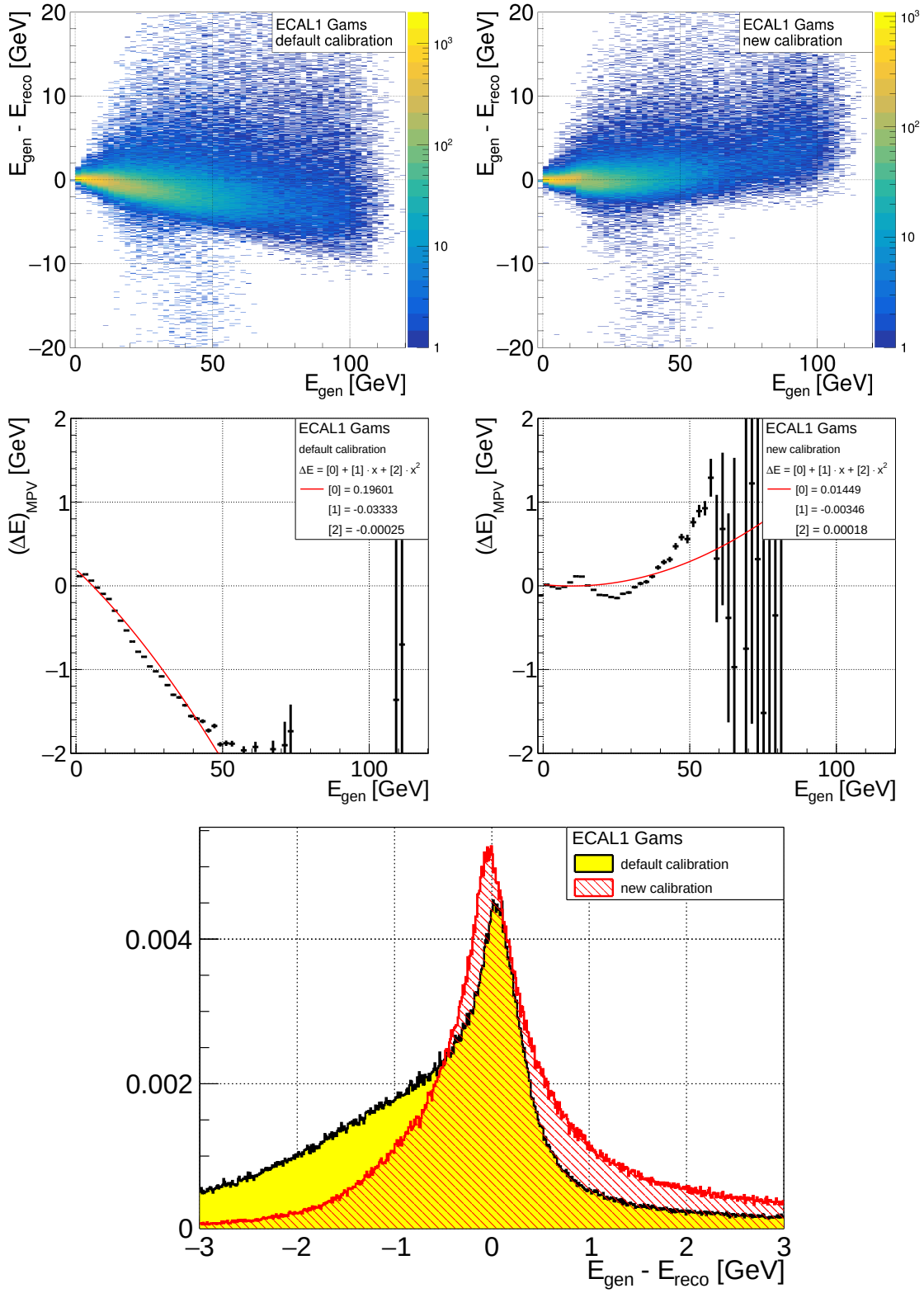

Figure C.11: Results of the new energy calibration method for ECAL1 Gams modules in comparison with the default energy calibration method. Top: Difference between reconstructed and generated cluster energy as a function of the generated energy. Center: Most probable values of the energy difference with the calibration fit. Bottom: Energy difference distribution of both methods in comparison.

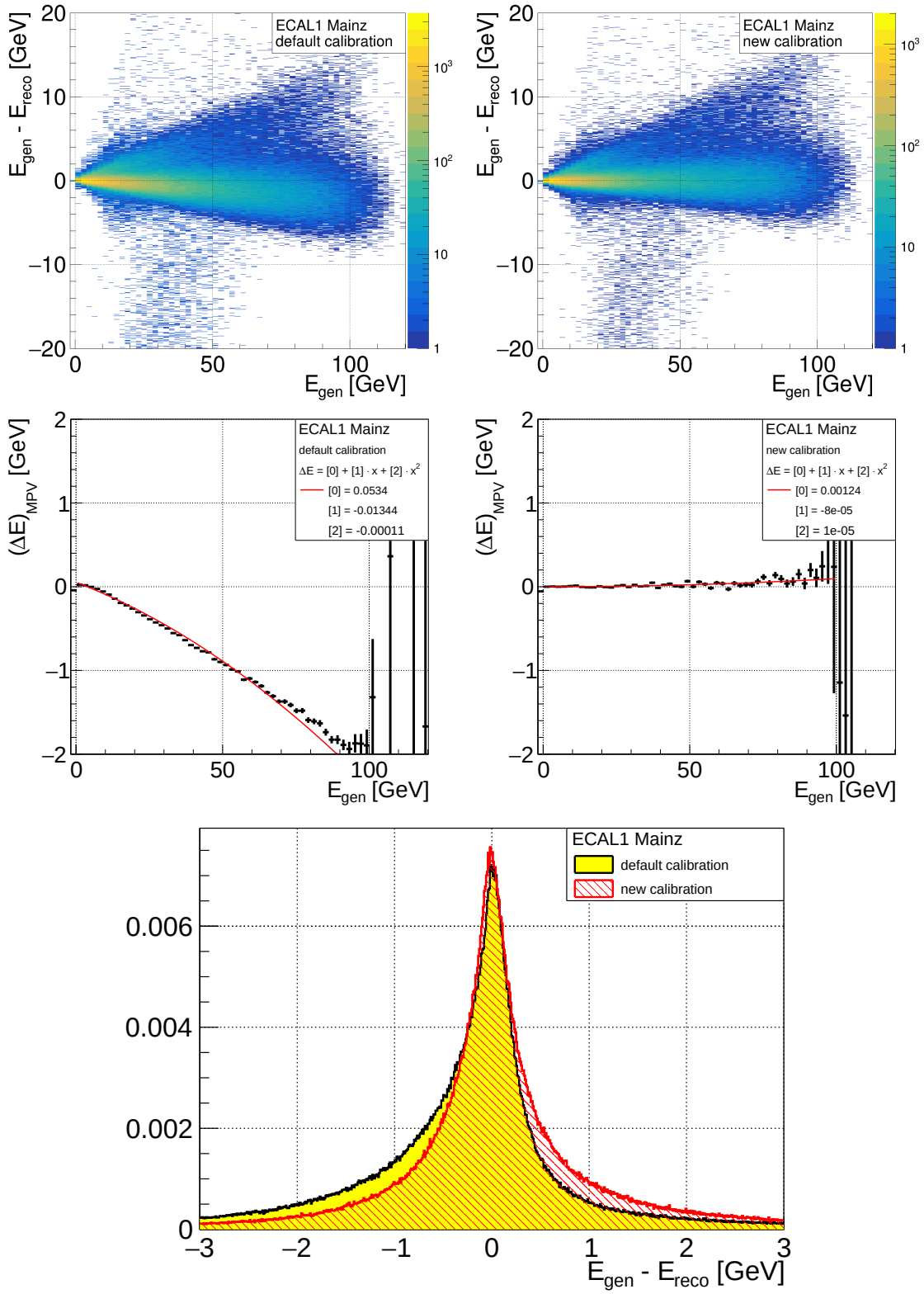

Figure C.12: Results of the new energy calibration method for ECAL1 Mainz modules in comparison with the default energy calibration method. Top: Difference between reconstructed and generated cluster energy as a function of the generated energy. Center: Most probable values of the energy difference with the calibration fit. Bottom: Energy difference distribution of both methods in comparison.

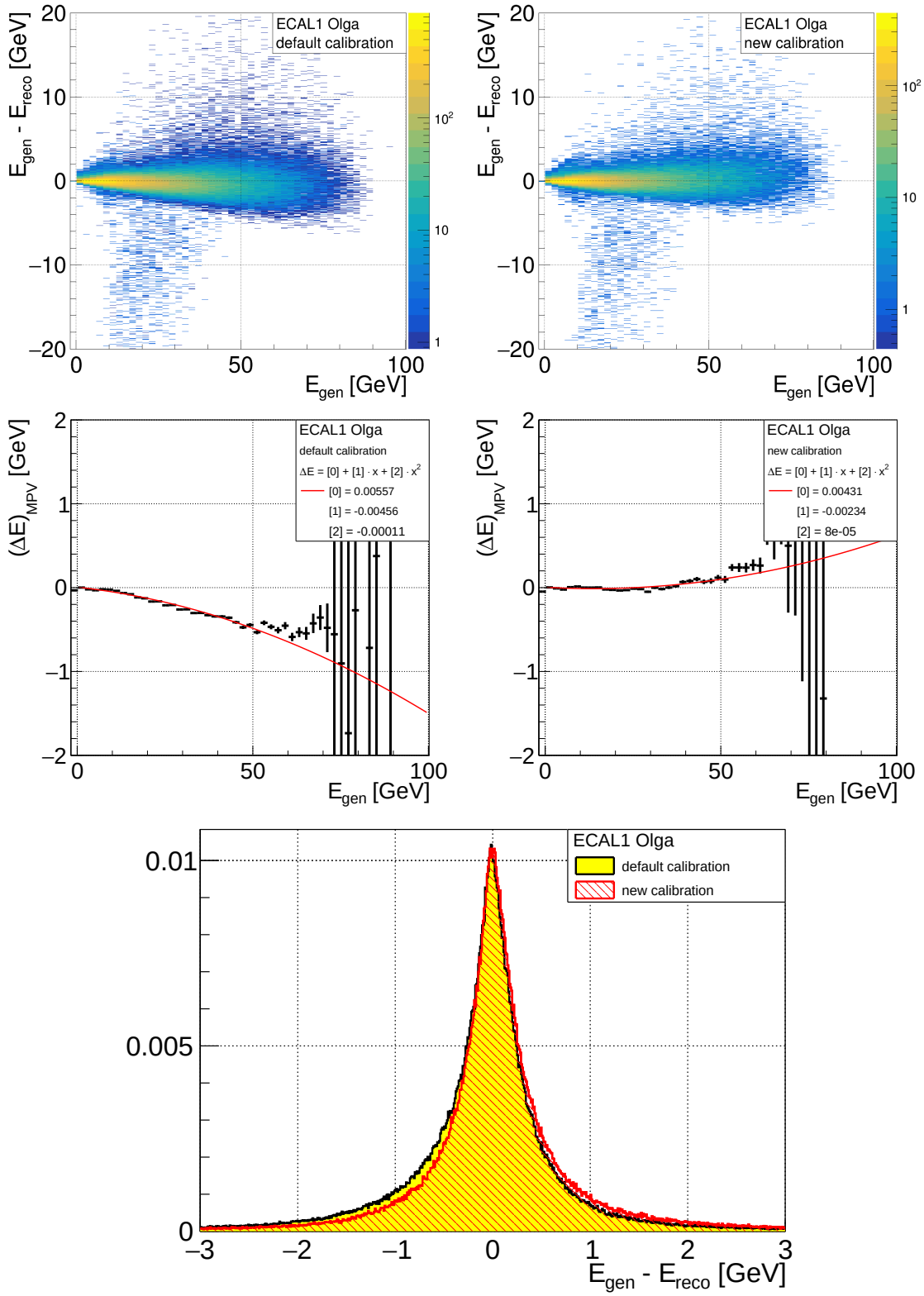

Figure C.13: Results of the new energy calibration method for ECAL1 Olga modules in comparison with the default energy calibration method. Top: Difference between reconstructed and generated cluster energy as a function of the generated energy. Center: Most probable values of the energy difference with the calibration fit. Bottom: Energy difference distribution of both methods in comparison.

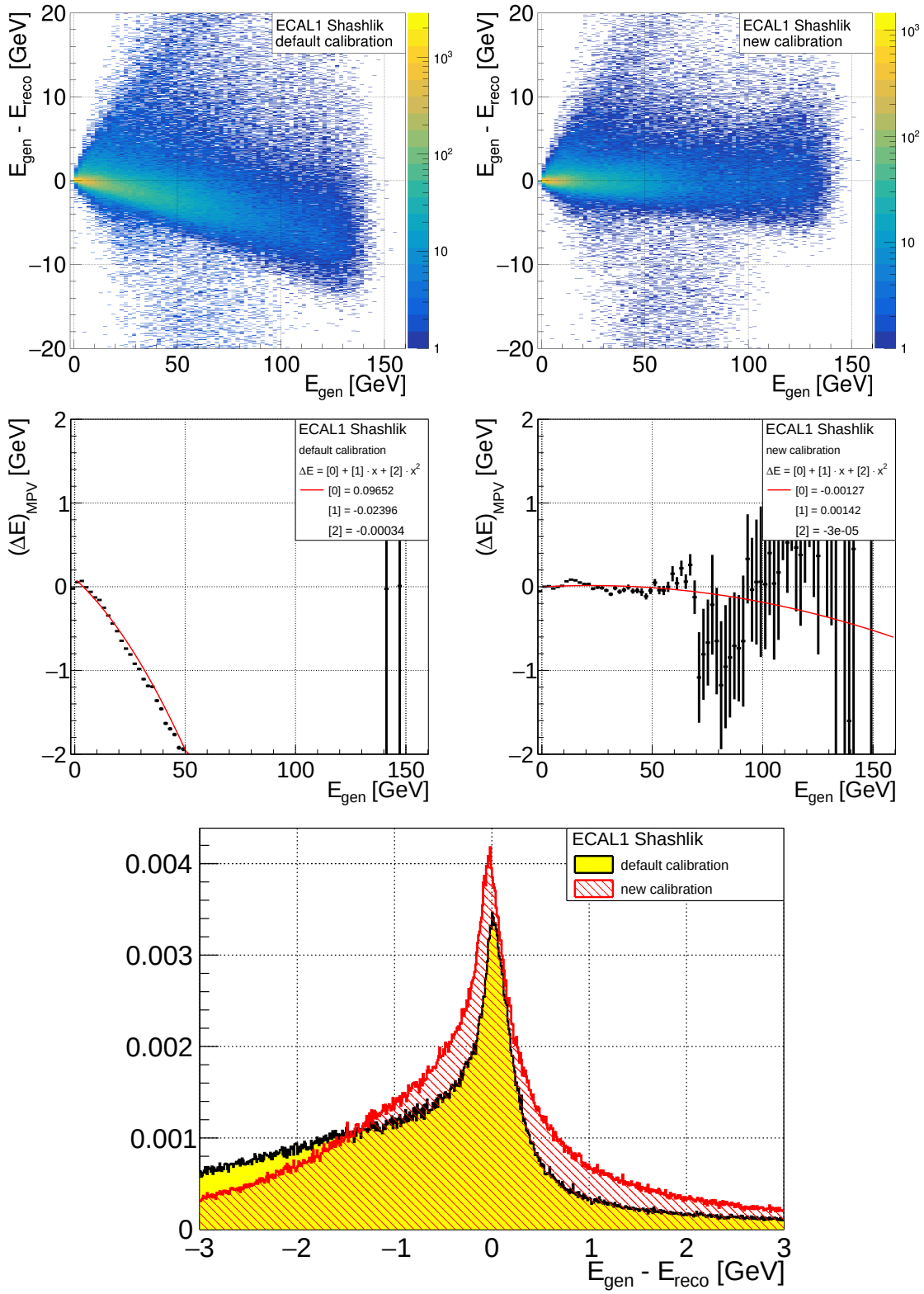

Figure C.14: Results of the new energy calibration method for ECAL1 Shashlik modules in comparison with the default energy calibration method. Top: Difference between reconstructed and generated cluster energy as a function of the generated energy. Center: Most probable values of the energy difference with the calibration fit. Bottom: Energy difference distribution of both methods in comparison.

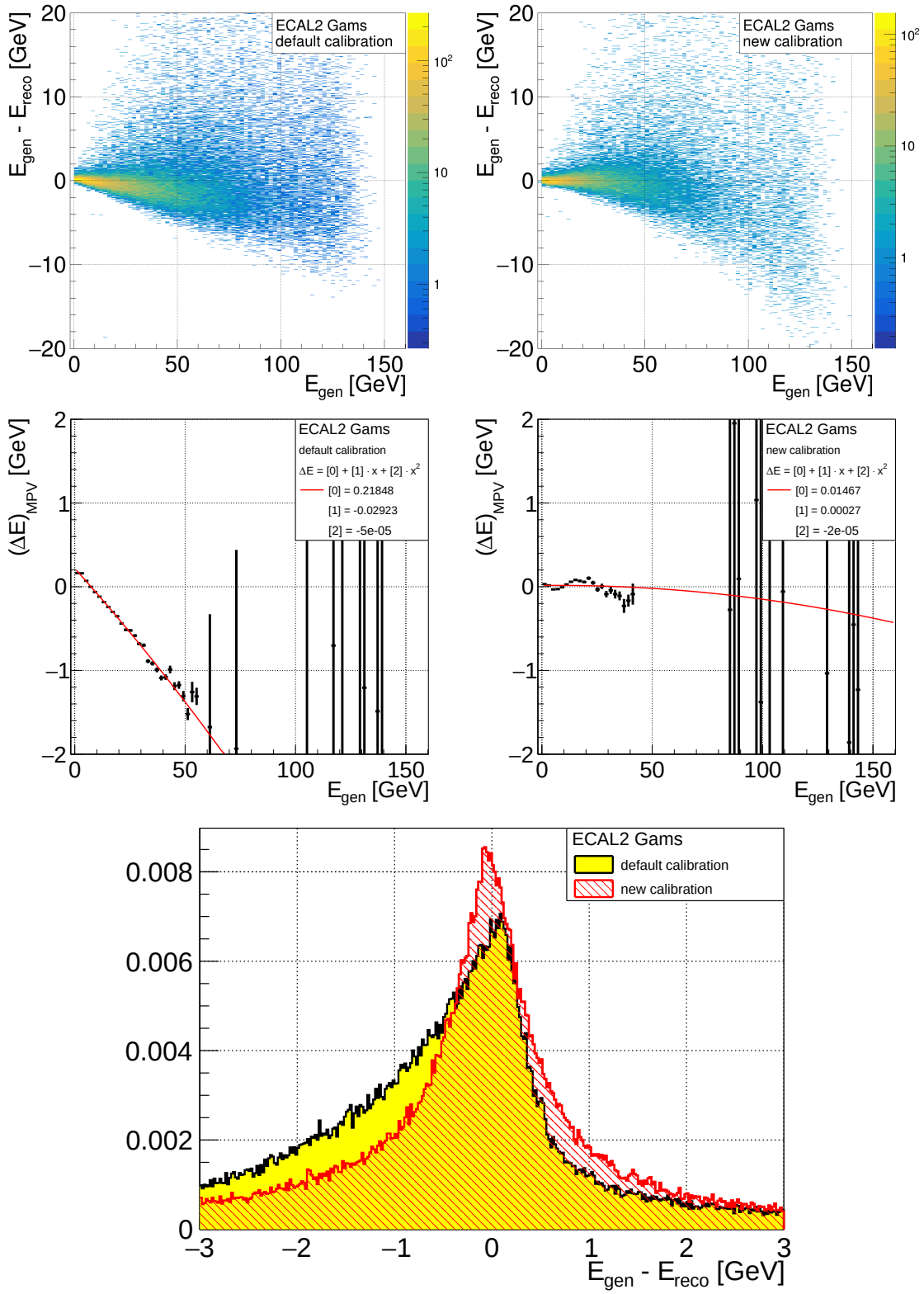

Figure C.15: Results of the new energy calibration method for ECAL2 Gams modules in comparison with the default energy calibration method. Top: Difference between reconstructed and generated cluster energy as a function of the generated energy. Center: Most probable values of the energy difference with the calibration fit. Bottom: Energy difference distribution of both methods in comparison.

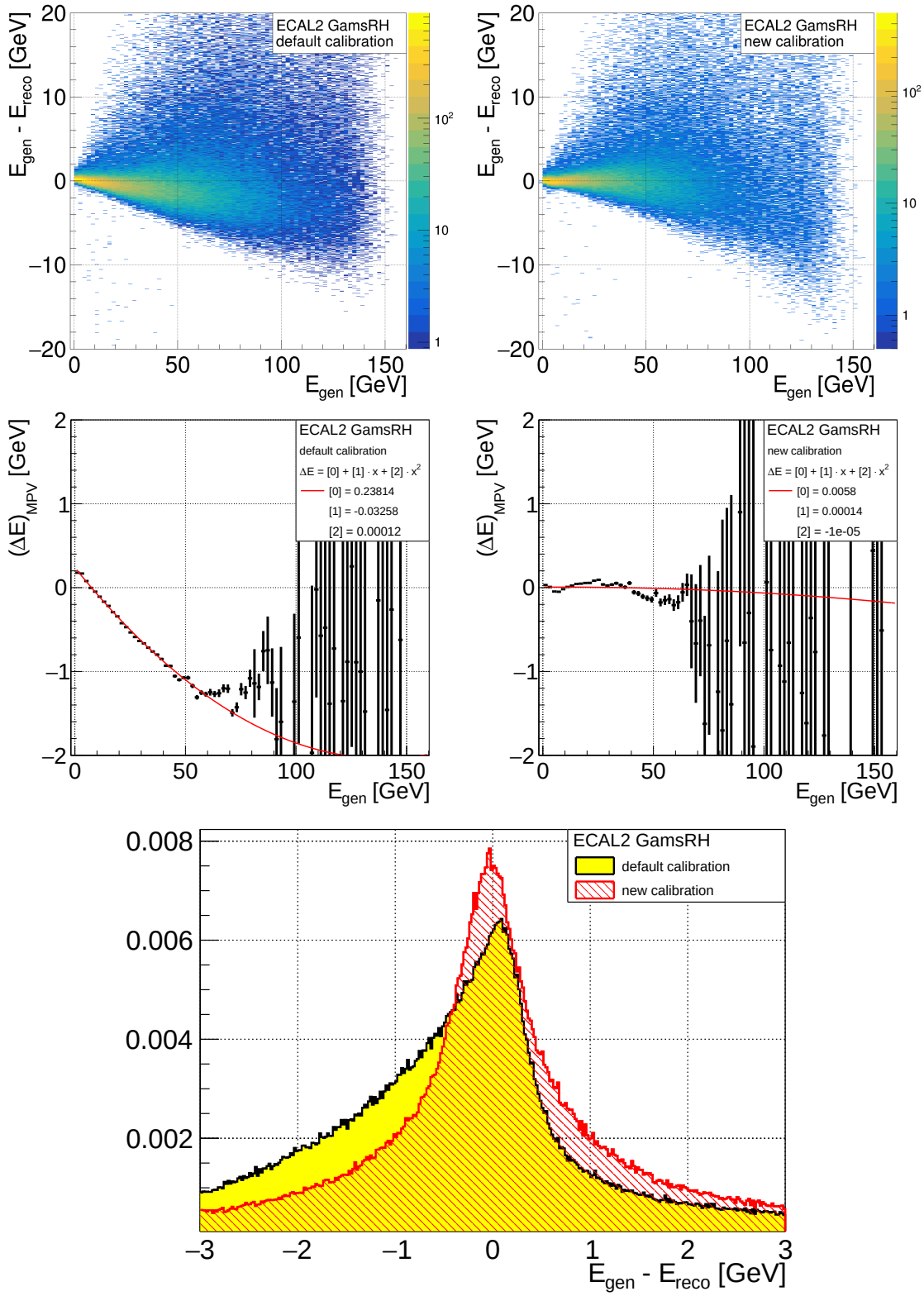

Figure C.16: Results of the new energy calibration method for ECAL2 GamsRH modules in comparison with the default energy calibration method. Top: Difference between reconstructed and generated cluster energy as a function of the generated energy. Center: Most probable values of the energy difference with the calibration fit. Bottom: Energy difference distribution of both methods in comparison.

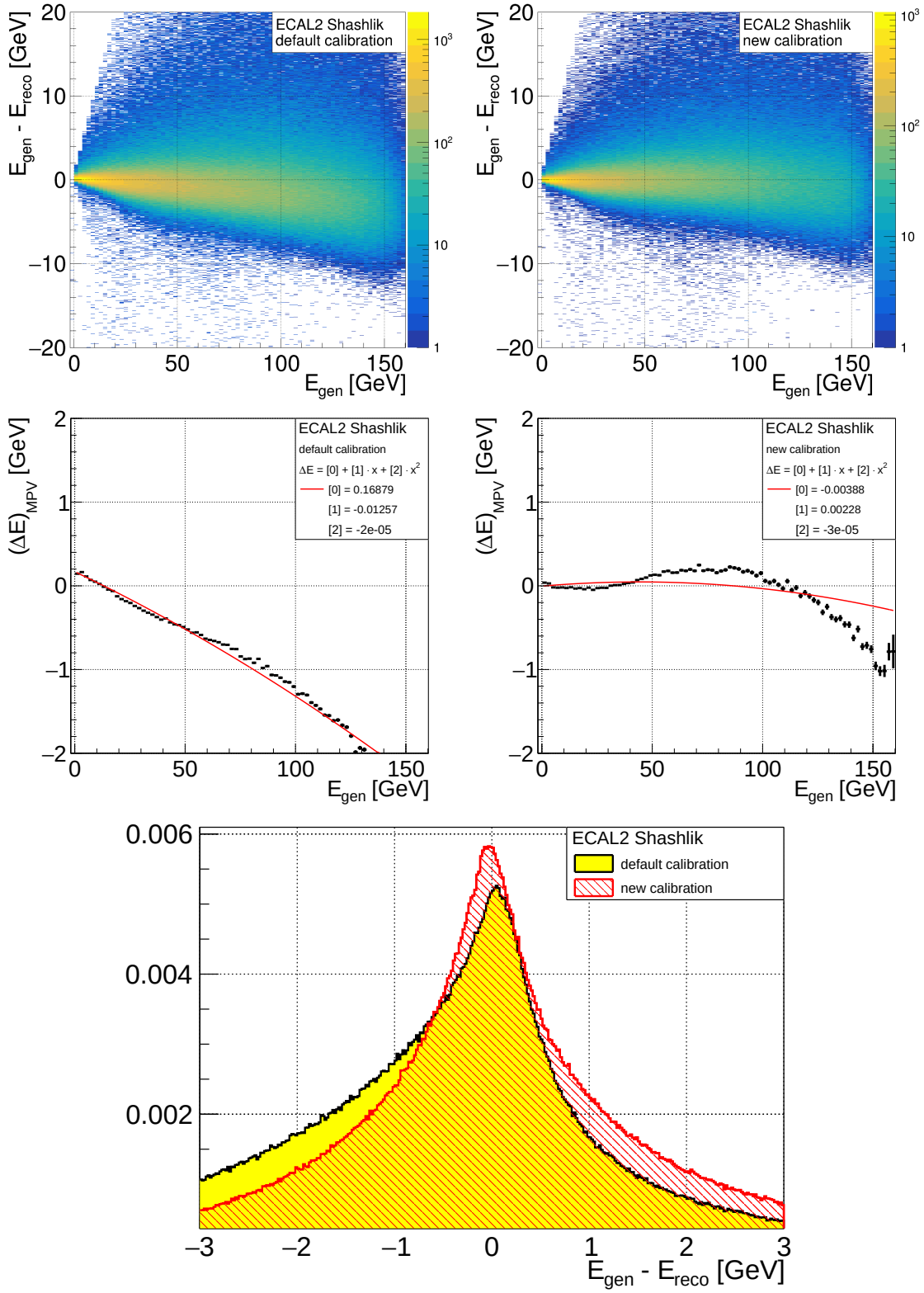

Figure C.17: Results of the new energy calibration method for ECAL2 Shashlik modules in comparison with the default energy calibration method. Top: Difference between reconstructed and generated cluster energy as a function of the generated energy. Center: Most probable values of the energy difference with the calibration fit. Bottom: Energy difference distribution of both methods in comparison.

D. Results of the Silicon RPD Monte Carlo Studies

For the sake of clarity, not all tables and kinematic distributions for modified geometries are presented in Sec. 8. The following results are presented in this appendix:

- Modification of the cavity thickness, Tab. D.1
- Modification of the cavity radius, Tab. D.2
- Modification of the thickness of the inner ring A, Tab. D.3
- Kinematic distributions and mean values using a target radius of 15 mm, Fig. D.1, and 10 mm, Fig. D.2

Table D.1: Kinematic limits and detection efficiencies for different cavity thicknesses. All other material layers remain unchanged with respect to the reference setup (cavity thickness of 0.6 mm). The survival probabilities are normalized to the generated HEPGen++ sample and are therefore dependent on the generator cuts.

Cavity Thickness	0.2 mm	0.3 mm	0.4 mm	0.5 mm	0.6 mm
$p_{\min}/(\mathrm{MeV/c})$	296.0	297.6	300.6	304.6	307.2
$-t_{\min}/(\mathrm{GeV/c})^2$	0.0866	0.0876	0.0895	0.0907	0.0917
$p+\gamma$ survival prob. norm. to gen. sample	43.2%	42.6%	42.1%	41.4%	40.8%
Luminosity factor	93.3%	93.3%	93.3%	93.3%	93.3%
Combined efficiency	40.3%	39.7%	39.3%	38.6%	38.1%

Table D.2: Kinematic limits and detection efficiencies for different cavity radii. All other material layers remain unchanged with respect to the reference setup (cavity radius of 100 mm). The survival probabilities are normalized to the generated HEPGen++ sample and are therefore dependent on the generator cuts.

Cavity Radius	70 mm	80 mm	90 mm	100 mm
$p_{\min}/(\mathrm{MeV/c})$	307.2	307.2	307.2	307.2
$-t_{\min}/(\mathrm{GeV/c})^2$	0.0917	0.0917	0.0917	0.0917
$p+\gamma$ survival prob. norm. to gen. sample	39.4%	40.0%	40.5%	40.8%
Luminosity factor	93.3%	93.3%	93.3%	93.3%
Combined efficiency	36.8%	37.3%	37.8%	38.1%

Table D.3: Kinematic limits and detection efficiencies for different thicknesses of the inner silicon ring A. All other material layers remain unchanged with respect to the reference setup (inner ring thickness of 300 µm). The survival probabilities are normalized to the generated HEPGen++ sample and are therefore dependent on the generator cuts.

Ring A thickness	200 µm	250 µm	300 µm	350 µm
$p_{\min}/(\mathrm{MeV/c})$	306.4	306.8	307.2	307.4
$-t_{\min}/(\mathrm{GeV/c})^2$	0.0913	0.0915	0.0917	0.0919
$p+\gamma$ survival prob. norm. to gen. sample	41.0%	40.9%	40.8%	40.8%
Luminosity factor	93.3%	93.3%	93.3%	93.3%
Combined efficiency	38.3%	38.2%	38.1%	38.1%

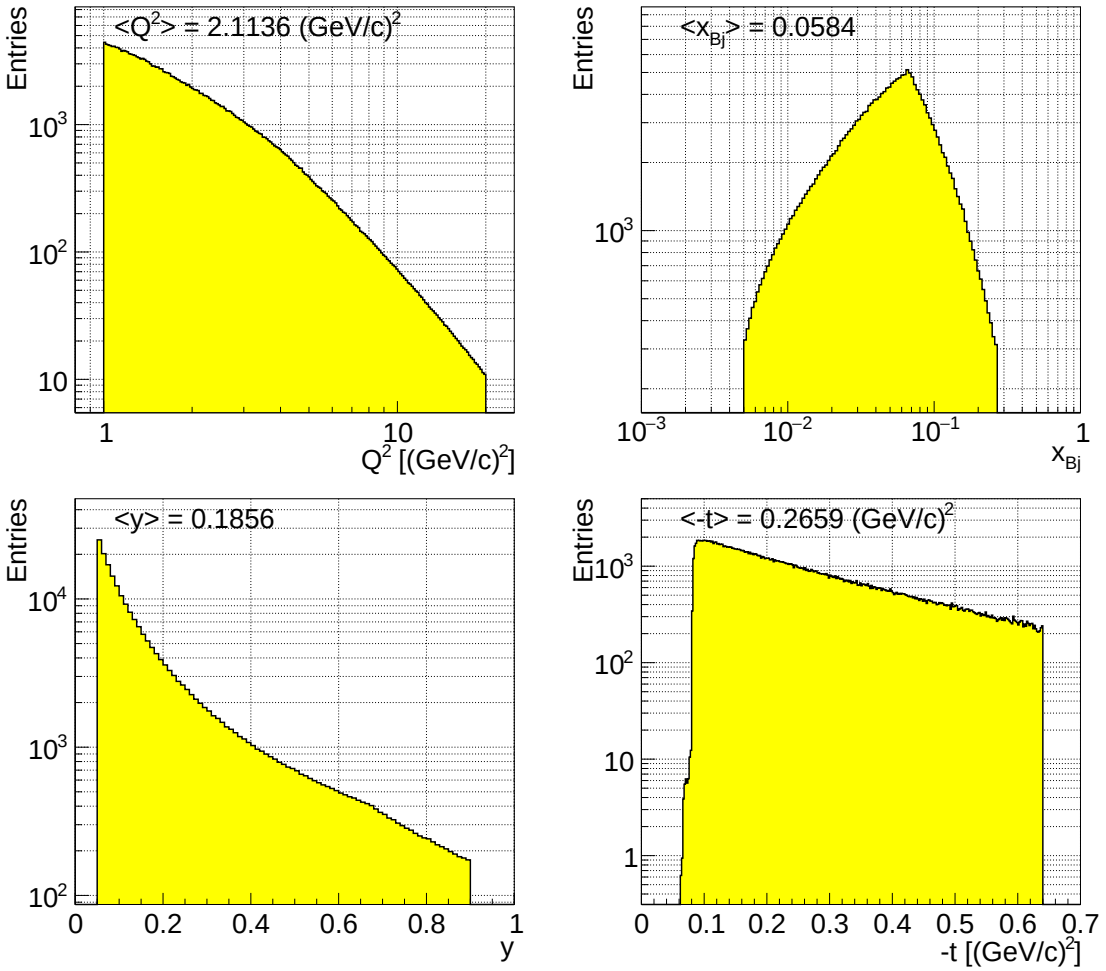

Figure D.1: Kinematical distributions and mean values of Q^2, x_{Bj}, y, and $-t$ for a target radius of 15 mm. The DVCS event generator of HEPGen++ is restricted to the kinematical limits given in Eq. (8.1). The lower limit for the generated proton momentum is $p_{\mathrm{min}} = 287.1\,\mathrm{MeV/c}$ or $-t_{\mathrm{min}} = 0.0817\,\mathrm{GeV/c^2}$.

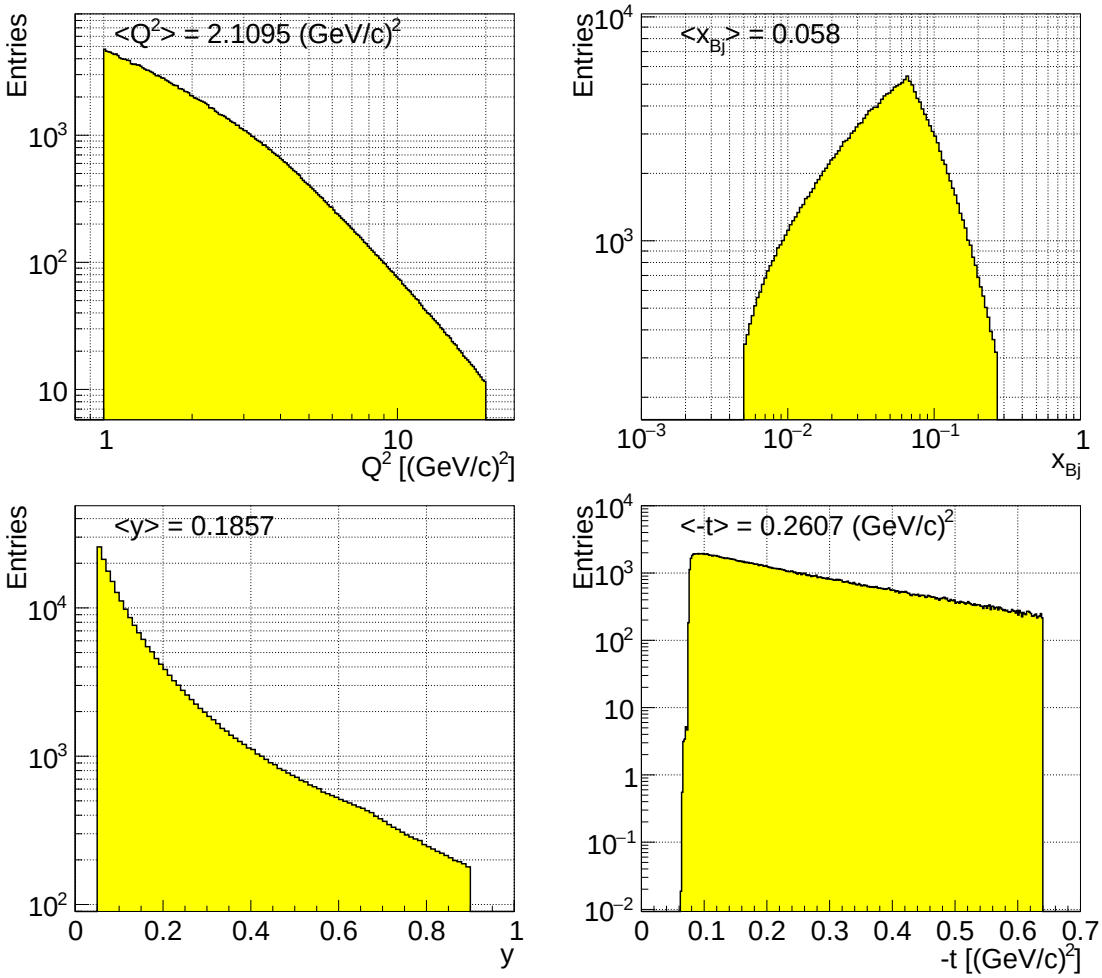

Figure D.2: Kinematical distributions and mean values of Q^2, x_{Bj}, y, and $-t$ for a target radius of 10 mm. The DVCS event generator of HEPGen++ is restricted to the kinematical limits given in Eq. (8.1). The lower limit for the generated proton momentum is $p_{\mathrm{min}} = 278.3\,\mathrm{MeV/c}$ or $-t_{\mathrm{min}} = 0.0758\,\mathrm{GeV/c^2}$.

List of Figures

List of Tables

Bibliography

[1] E. Rutherford, "The Structure of the Atom", *Philosophical Magazine Series 6* **27** (1914) 488–498.

[2] J. Chadwick, "Possible Existence of a Neutron", *Nature* **129** (1932) 312.

[3] M. Gell-Mann, "A Schematic Model of Baryons and Mesons", *Phys. Lett.* **8** (1964) 214–215.

[4] G. Zweig, "An SU_3 Model for Strong Interaction Symmetry and its Breaking", *CERN-TH-401* (1964) 1–24. `http://cds.cern.ch/record/352337`.

[5] A. Petermann, "Propriétés de l'étrangeté et une formule de masse pour les mésons vectoriels", *Nucl. Phys.* **63** (1965) 349–352.

[6] D. Griffiths, "Introduction to Elementary Particles", John Wiley & Sons, 2 ed., 2008.

[7] **EMC** Collaboration, J. Ashman *et al.*, "A measurement of the spin asymmetry and determination of the structure function g_1 in deep inelastic muon-proton scattering", *Phys. Lett. B* **206** (1988) 364–370.

[8] E. Leader and M. Anselmino, "A crisis in the parton model: where, oh where is the proton's spin?", *Z. Phys. C* **41** (1988) 239–246.

[9] **COMPASS** Collaboration, C. Adolph *et al.*, "Leading order determination of the gluon polarisation from DIS events with high-p_T hadron pairs", *Phys. Lett. B* **718** (2013) 922–930.

[10] X. Ji, "Gauge-Invariant Decomposition of Nucleon Spin", *Phys. Rev. Lett.* **78** (1997) 610–613.

[11] M. Burkardt, C. A. Miller, and W.-D. Nowak, "Spin-polarized high-energy scattering of charged leptons on nucleons", *Reports on Progress in Physics* **73** (2010) 016201. `http://stacks.iop.org/0034-4885/73/i=1/a=016201`.

[12] F. Halzen and A. D. Martin, "Quarks and Leptons: An Introductory Course in Modern Particle Physics", John Wiley & Sons, 1985.

[13] V. Barone and P. G. Ratcliffe, "Transverse Spin Physics", World Scientific, Singapore, 2003.

[14] **H1** and **ZEUS** Collaborations, H. Abramowicz *et al.*, "Combination of measurements of inclusive deep inelastic $e^{\pm}p$ scattering cross sections and QCD analysis of HERA data", *Eur. Phys. J. C* **75** (2015) 580.

[15] L. W. Whitlow *et al.*, "Precise measurements of the proton and deuteron structure functions from a global analysis of the SLAC deep inelastic electron scattering cross-sections", *Phys. Lett. B* **282** (1992) 475–482.

[16] **BCDMS** Collaboration, A. C. Benvenuti *et al.*, "A High Statistics Measurement of the Proton Structure Functions $F_2(x, Q^2)$ and R from Deep Inelastic Muon Scattering at High Q^2", *Phys. Lett. B* **223** (1989) 485–489.

[17] **E665** Collaboration, M. R. Adams *et al.*, "Proton and deuteron structure functions in muon scattering at 470 GeV", *Phys. Rev. D* **54** (1996) 3006.

[18] **NMC** Collaboration, M. Arneodo *et al.*, "Measurement of the proton and deuteron structure functions, F_2^p and F_2^d, and of the ratio σ_L/σ_T", *Nucl. Phys. B* **483** (1997) 3–43.

[19] **Particle Data Group** Collaboration, C. Patrignani *et al.*, "Review of Particle Physics", *Chinese Physics C* **40** (2016) 100001.

[20] **COMPASS** Collaboration, M. Wilfert, "New COMPASS results on the spin structure function g_1^p, and QCD fit", *PoS(DIS2014)206* (2014) 1–6. `http://pos.sissa.it/archive/conferences/203/206/DIS2014_206.pdf`.

[21] **HERMES** Collaboration, A. Airapetian *et al.*, "Measurement of the virtual-photon asymmetry A_2 and the spin-structure function g_2 of the proton", *Eur. Phys. J. C* **72** (2012) 1921.

[22] **E143** Collaboration, K. Abe *et al.*, "Measurements of the proton and deuteron spin structure functions g_1 and g_2", *Phys. Rev. D* **58** (1998) 112003.

[23] **E155** Collaboration, P. L. Anthony *et al.*, "Precision measurement of the proton and deuteron spin structure functions g_2 and asymmetries A_2", *Phys. Lett. B* **553** (2003) 18–24.

[24] M. Kaku, "Quantum field theory: A modern introduction", Oxford University Press, New York, 1993.

[25] R. Devenish and A. Cooper-Sarkar, "Deep Inelastic Scattering", Oxford University Press, New York, 2004.

[26] C. G. Callan and D. J. Gross, "High-Energy Electroproduction and the Constitution of the Electric Current", *Phys. Rev. Lett.* **22** (1969) 156–159.

[27] B. Povh, K. Rith, C. Scholz, F. Zetsche, and W. Rodejohann, "Teilchen und Kerne: Eine Einführung in die physikalischen Konzepte", Springer Spektrum, 9 ed., 2014.

[28] R. K. Ellis, W. J. Stirling, and B. R. Webber, "QCD and Collider Physics", Cambridge University Press, Cambridge, 1996.

[29] G. Baum *et al.*, "New Measurement of Deep-Inelastic $e-p$ Asymmetries", *Phys. Rev. Lett.* **51** (1983) 1135–1138.

[30] **COMPASS** Collaboration, V. Y. Alexakhin *et al.*, "The deuteron spin-dependent structure function g_1^d and its first moment", *Phys. Lett. B* **647** (2007) 8–17.

[31] **COMPASS** Collaboration, M. G. Alekseev *et al.*, "Quark helicity distributions from longitudinal spin asymmetries in muon-proton and muon-deuteron scattering", *Phys. Lett. B* **693** (2010) 227–235.

[32] **COMPASS** Collaboration, C. Adolph *et al.*, "Final COMPASS results on the deuteron spin-dependent structure function g_1^{d} and the Bjorken sum rule", *CERN-EP-2016-299* (2016) 1–16, `arXiv:1612.00620`.

[33] R. L. Jaffe and A. Manohar, "The g_1 problem: Deep inelastic electron scattering and the spin of the proton", *Nucl. Phys. B* **337** (1990) 509–546.

[34] J. C. Collins and A. Freund, "Proof of factorization for deeply virtual Compton scattering in QCD", *Phys. Rev. D* **59** (1999) 074009.

[35] M. Diehl, "Generalized parton distributions", *Phys. Reports* **388** (2003) 41–277.

[36] K. Goeke, M. V. Polyakov, and M. Vanderhaeghen, "Hard Exclusive Reactions and the Structure of Hadrons", *Prog. Part. Nucl. Phys.* **47** (2001) 401–515.

[37] A. V. Belitsky and A. V. Radyushkin, "Unraveling hadron structure with generalized parton distributions", *Phys. Reports* **418** (2005) 1–387.

[38] S. Boffi and B. Pasquini, "Generalized parton distributions and the structure of the nucleon", *Riv. Nuovo Cim.* **30** (2007) 387–448.

[39] **COMPASS** Collaboration, F. Gautheron *et al.*, "COMPASS-II Proposal", *CERN-SPSC-2010-014 SPSC-P-340* (2010) 1–125. `http://wwwcompass.cern.ch/compass/proposal/compass-II_proposal/compass-II_proposal.pdf`.

[40] A. V. Belitsky, D. Müller, and A. Kirchner, "Theory of deeply virtual Compton scattering on the nucleon", *Nucl. Phys. B* **629** (2002) 323–392.

[41] M. Burkardt, "Impact parameter dependent parton distributions and off-forward parton distributions for $\zeta \to 0$", *Phys. Rev. D* **62** (2000) 071503.

[42] M. Burkardt, "Impact Parameter Space Interpretation for Generalized Parton Distributions", *Int. J. Mod. Phys. A* **18** (2003) 173–208.

[43] M. Diehl, "Generalized parton distributions in impact parameter space", *Eur. Phys. J. C* **25** (2002) 223–232.

[44] M. Burkardt, "GPDs with $\zeta \neq 0$", `arXiv:0711.1881v2 [hep-ph]`.

[45] C. R. Regali, "Exclusive event generation at the COMPASS-II experiment at CERN and improvements for the Monte Carlo chain", PhD thesis, Albert-Ludwigs-Universität Freiburg, Physikalisches Institut, 2016.

[46] M. Diehl and S. Sapeta, "On the analysis of lepton scattering on longitudinally or transversely polarized protons", *Eur. Phys. J. C* **41** (2005) 515–533.

[47] C. A. Aidala, S. D. Bass, D. Hasch, and G. K. Mallot, "The spin structure of the nucleon", *Rev. Mod. Phys.* **85** (2013) 655.

[48] A. Bacchetta, U. D'Alesio, M. Diehl, and C. A. Miller, "High-energy hadron induced dilepton production from nucleons and nuclei", *Phys. Rev. D* **70** (2004) 117504.

[49] K. Schmidt, "Transverse target spin asymmetries in exclusive vector meson muoproduction", PhD thesis, Albert-Ludwigs-Universität Freiburg, Physikalisches Institut, 2014.

[50] **COMPASS** Collaboration, P. Abbon *et al.*, "The COMPASS experiment at CERN", *Nucl. Instrum. Meth. A* **577** (2007) 455–518.

[51] **COMPASS** Collaboration, P. Abbon *et al.*, "The COMPASS setup for physics with hadron beams", *Nucl. Instrum. Meth. A* **779** (2015) 69–115.

[52] E. Bielert *et al.*, "A 2.5 m long liquid hydrogen target for COMPASS", *Nucl. Instrum. Meth. A* **746** (2014) 20–25.

[53] A. Groß, "Extraction of cross sections for ρ^0 and ϕ muoproduction at the COMPASS experiment", Master's thesis, Albert-Ludwigs-Universität Freiburg, Physikalisches Institut, 2014.

[54] A. Ferrero, "Target Cell Position Determination for 2012", 2014. Private Communication.

[55] M. Gorzellik and P. Jörg, "CAMERA Detector Calibration", 2013. Private Communication.

[56] **COMPASS** Collaboration, P. Abbon *et al.*, "Particle identification with COMPASS RICH-1", *Nucl. Instrum. Meth. A* **631** (2011) 26–39.

[57] C. Bernet *et al.*, "The COMPASS trigger system for muon scattering", *Nucl. Instrum. Meth. A* **550** (2005) 217–240.

[58] F. Herrmann, "Development and Verification of a High Performance Electronic Readout Framework for High Energy Physics", PhD thesis, Albert-Ludwigs-Universität Freiburg, Physikalisches Institut, 2011.

[59] S. Schopferer, "An FPGA-based Trigger Processor for a Measurement of Deeply Virtual Compton Scattering at the COMPASS-II Experiment", PhD thesis, Albert-Ludwigs-Universität Freiburg, Physikalisches Institut, 2013.

[60] M. Bodlak *et al.*, "FPGA based data acquisition system for COMPASS experiment", *J. Phys. Conf. Ser.* **513** (2014) 012029.

[61] S. Gerassimov, "Physics Analysis Software Tools", 2003. `http://ges.web.cern.ch/ges/phast/`. Accessed on 11-10-2016.

[62] **COMPASS** Collaboration, A. A. Lednev, "Shower separation program for ECAL2", *COMPASS Note* (2009) 1–9. `https://wwwcompass.cern.ch/compass/notes/2009-7/2009-7.pdf`.

[63] **Geant4** Collaboration, "Geometry And Tracking", 2003. `https://geant4.web.cern.ch/geant4/`. Accessed on 11-10-2016.

[64] S. Agostinelli *et al.*, "Geant4 – a simulation toolkit", *Nucl. Instrum. Meth. A* **506** (2003) 250–303.

[65] J. Allison *et al.*, "Geant4 Developments and Applications", *IEEE Transactions on Nuclear Science* **53** (2006) 270–278.

[66] G. Ingelman, A. Edin, and J. Rathsman, "LEPTO 6.5 – A Monte Carlo Generator for Deep Inelastic Lepton-Nucleon Scattering", *Comput. Phys. Commun.* **101** (1997) 108–134.

[67] A. S. Carroll *et al.*, "Absorption Cross-Sections of $\pi^{\pm}$, $K^{\pm}$, p and $\bar{p}$ on Nuclei Between 60 and 280 GeV/c", *Phys. Lett. B* **80** (1979) 319–322.

[68] P. L. McGaughey, J. M. Moss, and J. C. Peng, "High-energy hadron induced dilepton production from nucleons and nuclei", *Ann. Rev. Nucl. Part. Sci.* **49** (1999) 217–253.

[69] R. Longo, "Reconstructed vertex distribution for the Drell-Yan setup", 2016. Private Communication.

[70] ROOT, "Data Analysis Framework", 2014–16. `https://root.cern.ch/`. Accessed on 11-10-2016.

[71] V. Behrendt, "Characterization of the CAMERA Detector at the COMPASS II Experiment", Bacherlor's Thesis, Albert-Ludwigs-Universität Freiburg, Physikalisches Institut, 2015.

[72] T. C. Szameitat and C. R. Regali, "TGEANT website", 2015. `https://na58-project-tgeant.web.cern.ch/`. Accessed on 11-10-2016.

[73] F. James, "A review of pseudorandom number generators", *Comput. Phys. Commun.* **60** (1990) 329–344.

[74] **Geant4** Collaboration, "Physics Reference Manual", 2015. `http://geant4.web.cern.ch/geant4/UserDocumentation/UsersGuides/PhysicsReferenceManual/fo/PhysicsReferenceManual.pdf`.

[75] G. Grindhammer and S. Peters, "The Parameterized Simulation of Electromagnetic Showers in Homogeneous and Sampling Calorimeters", `arXiv:hep-ex/0001020`.

[76] E. Longo and I. Sestili, "Monte Carlo calculation of photon-initiated electromagnetic showers in lead glass", *Nucl. Instrum. Meth.* **128** (1975) 283–307.

[77] C. Bernet *et al.*, "The COMPASS trigger system for muon scattering", *Nucl. Instrum. Meth. A* **550** (2005) 217–240.

[78] B. M. Veit, "Hodoscope Efficiency Determination for DVCS 2012", 2015. Private Communication.

[79] **COMPASS** Collaboration, J. Barth *et al.*, "Trigger Configuration Summary 2002–2012", *COMPASS Note* (2016) 1–20. `https://wwwcompass.cern.ch/compass/notes/2016-4/2016-4.pdf`.

[80] L. L. Frankfurt, A. Freund, and M. Strikman, "Diffractive exclusive photon production in DIS at DESY HERA", *Phys. Rev. D* **58** (1998) 114001.

[81] L. L. Frankfurt, A. Freund, and M. Strikman, "Deeply virtual compton scattering at HERA – A probe of asymptotia", *Phys. Lett. B* **460** (1999) 417–424.

[82] A. Sandacz, "Modifications to FFS model and predictions", 2009. `https://wwwcompass.cern.ch/compass/gpd/meetings/200904_april22/AS_gpd-Apr2009.ppt`.

[83] **COMPASS** Collaboration, A. Ferrero *et al.*, "Extraction of the t-slope of the pure DVCS cross section", *COMPASS Note* (2016) 1–91. `https://wwwcompass.cern.ch/compass/notes/2016-5/2016-5.pdf`.

[84] B. M. Veit, "New HO4 step design in deadzone", 2016. Private Communication.

[85] **SMC** Collaboration, B. Adeva *et al.*, "Spin asymmetries A_1 and structure functions g_1 of the proton and the deuteron from polarized high-energy muon scattering", *Phys. Rev. D* **58** (1998) 112001.

[86] **E143** Collaboration, K. Abe *et al.*, "Measurements of $R = \sigma_L/\sigma_T$ for $0.03 < x < 0.1$ and fit to world data", *Phys. Lett. B* **452** (1999) 194–200.

[87] S. Landgraf, "Luminosity Calculation for the COMPASS Experiment using the F_2 Structure Function", Master's thesis, Albert-Ludwigs-Universität Freiburg, Physikalisches Institut, 2015.

[88] E. Fuchey, "Beam Flux Determination using Random Trigger or Scalers for DVCS 2012", 2015. Private Communication.

[89] P. Jörg, PhD thesis in preparation, Albert-Ludwigs-Universität Freiburg, Physikalisches Institut, 2017.

[90] **COMPASS** Collaboration, P. Jörg, "The t-dependence of the pure DVCS cross section at COMPASS", *PoS(DIS2016)235* (2016) 1–6. `http://pos.sissa.it/archive/conferences/265/235/DIS2016_235.pdf`.

[91] **COMPASS** Collaboration, Polarized Target Group, "Technical drawing of 40 mm NH3 target", 2007. `http://wwwcompass.cern.ch/compass/detector/target/Drawings/NH3target07v01bw.pdf`.

[92] A. Abragam, "The Principles of Nuclear Magnetism", Clarendon Press, 1961.

[93] A. Magnon *et al.*, "Proposal on Common R&D Project to upgrade the COMPASS polarized target with recoil detectors", 2016. Private Communication.

[94] M. Gorzellik, PhD thesis in preparation, Albert-Ludwigs-Universität Freiburg, Physikalisches Institut, 2017.

[95] R. Longo, PhD thesis in preparation, Università degli Studi di Torino, Via Pietro Giuria 1, 10125, Torino, 2017.

[96] T. C. Szameitat, "Entwicklung einer Monte-Carlo-Simulation für das COMPASS-II-Experiment", Diplomarbeit, Albert-Ludwigs-Universität Freiburg, Physikalisches Institut, 2012.

[97] S. Gerassimov, "EPIC: π^0 mass calibration for electromagnetic calorimeters", 2014. Private Communication.

Danksagung

An dieser Stelle möchte ich mich bei all denjenigen bedanken, die zum Gelingen dieser Arbeit beigetragen haben:

- Ganz besonders möchte ich Prof. Dr. Horst Fischer danken, für die Vergabe des interessanten Themas, die umfassende Betreuung sowie seine wertvollen Ratschläge und Anregungen während der letzten Jahre.
- Prof. Dr. Kay Königsmann danke ich für die freundliche Aufnahme in seiner Abteilung und für die Chance am COMPASS-Experiment mitzuwirken.
- Ein besonderer Dank geht an Christopher Regali, für die freundschaftliche Zusammenarbeit und die zahlreichen konstruktiven Diskussionen, die wesentlich zum Gelingen dieser Arbeit beigetragen haben.
- Riccardo Longo, Christopher Regali, Stefan Sirtl und insbesondere Patricia Hofmann danke ich für das sorgfältige Korrekturlesen dieser Arbeit und für ihre konstruktive Kritik.
- Allen Mitgliedern unserer Abteilung und der gesamten COMPASS-Kollaboration danke ich für die angenehme Atmosphäre und die vielen hilfreichen Diskussionen.
- Abschließend möchte ich mich bei meiner Familie bedanken, die mich stets liebevoll unterstützt hat.